Line-Scan Spectral-Domain Optical Coherence Tomography for Cellular Resolution Structural and Vascular Imaging of Biological Tissues

by

Le Han

A thesis

presented to the University of Waterloo

in fulfillment of the

thesis requirement for the degree of

Doctor of Philosophy

in

Physics

Waterloo, Ontario, Canada, 2022

Examining Committee Membership

The following served on the Examining Committee for this thesis. The decision of the Examining Committee is by majority vote.

External Examiner	Dr. Robert Zawadzki Associate Professor, Department of Ophthalmology & Vision Science University of California, Davis
Supervisor(s)	Dr. Kostadinka Bizheva Professor, Department of Physics and Astronomy University of Waterloo
Internal Member	Dr. Melanie Campbell Professor, Department of Physics and Astronomy University of Waterloo
Internal Member	Dr. Kevin Resch Professor, Department of Physics and Astronomy University of Waterloo
Internal-external Member	Dr. Denise Hileeto Clinical Associate Professor, Department of Optometry & Vision Science University of Waterloo

Author’s Declaration

This thesis consists of material all of which I authored or co-authored: see Statement of Contributions included in the thesis. This is a true copy of the thesis, including any required final revisions, as accepted by my examiners.

I understand that my thesis may be made electronically available to the public.

Statement of Contributions

Chapter 3:

Bingyao Tan made the first design of the system and wrote the algorithm for linear-k calibration.

Kostadinka Bizheva and Bingyao Tan provided the study materials.

Le Han modified the system design, evaluated the system in Zemax, built and characterized the system, and wrote the manuscript.

Kostadinka Bizheva revised the manuscript.

Chapter 4:

Le Han, Bingyao Tan, Zohreh Hosseinaee, Lin Kun Chen, Denise Hileeto, and Kostadinka Bizheva. "Line-scan OCT for *in-vivo*, non-contact cellular resolution imaging of the human cornea and limbus," (prepare to submit to Biomedical Optics Express)

Bingyao Tan and Kostadinka Bizheva conceived the study.

Kostadinka Bizheva provided the study materials.

Bingyao Tan made the first design of the system and wrote the algorithm for linear-k calibration.

Le Han modified the system design, built and characterized the system, wrote the Labview control program and Matlab processing algorithms, and processed data.

Bingyao Tan and Kostadinka Bizheva provided valuable instructions and feedbacks about the system characterization.

Kostadinka Bizheva provided the design of the head support.

Lin Kun Chen helped with controlling the motorized translational stage.

Le Han, Zohreh Hosseinaee, Lin Kun Chen, and Kostadinka Bizheva contributed to the *in-vivo* image acquisition.

Denise Hileeto provided the histology figure.

Le Han, Zohreh Hosseinaee, and Kostadinka Bizheva prepared the figures.

Le Han wrote the manuscript draft.

Kostadinka Bizheva revised the manuscript.

All authors contributed to the final version of the manuscript.

Chapter 5:

Le Han and Kostadinka Bizheva. "Correcting the spatial-spectral crosstalk and chromatic aberrations in broadband line-scan SD-OCT," (prepare to submit to Biomedical Optics Express)

Le Han and Kostadinka Bizheva conceived the study.

Kostadinka Bizheva provided the study materials.

Le Han developed the theory, proposed the methods, performed experiments, wrote the algorithms, and processed data.

Le Han and Kostadinka Bizheva prepared the figures.

Le Han wrote the manuscript draft.

Kostadinka Bizheva revised the manuscript.

All authors contributed to the final version of the manuscript.

Chapter 6:

Le Han, Bingyao Tan, Leopold Schmetterer, and Kostadinka Bizheva. "Decorrelation-based localized transverse flow measurement by line-scan OCT," (prepare to submit to Biomedical Optics Express)

Le Han, Bingyao Tan, Leopold Schmetterer, and Kostadinka Bizheva conceived the study.

Kostadinka Bizheva provided the study materials.

Le Han developed the theory, proposed the methods, performed experiments, wrote the algorithms, and processed data.

Bingyao Tan provided valuable suggestions and feedback about the algorithms and results.

Le Han and Kostadinka Bizheva prepared the figures.

Le Han wrote the manuscript draft.

Kostadinka Bizheva revised the manuscript.

All authors contributed to the final version of the manuscript.

Abstract

Optical coherence tomography (OCT) is an optical interferometric technique for non-invasive contactless imaging of the cellular-level structures of biological tissues. However, the application of OCT for in-vivo volumetric cellular resolution imaging of the human anterior eye is challenging due to artifacts induced by involuntary eye motion and the contradictory requirements for high lateral resolution and extended depth of focus. This thesis addresses these challenges by developing: (i) a broadband line-scan (LS) spectral-domain (SD) OCT system that combines micrometer-scale spatial resolution and ultrafast image acquisition rate; (ii) an image reconstruction method for restoring the diffraction-limited lateral resolution of the LS SD-OCT system along a large depth range. In addition, a novel flow velocimetry method is developed for extending the LS SD-OCT system's functionality.

The novel LS SD-OCT system combines a broadband light source and an ultrafast area camera to achieve a nearly isotropic spatial resolution of ~2.3 μm in free space and an image acquisition rate of up to 3000 frames/second. The central sensitivity of the system is 92 dB near the zero optical delay with a 6 dB rolloff depth range of 0.78 mm. The system's performance was evaluated by imaging in-vivo a healthy volunteer's cornea and limbus. The motion artifacts are not noticeable in most volumetric images. Cornea epithelial cells, sub-basal corneal nerves, keratocytes in the stroma, cornea endothelial cells, palisaded of Vogt (POV) in the limbus, limbal epithelial cells between the POVs, and hyper-reflective line structures underneath POVs are resolved in the 3D images within a limited depth range.

Digital adaptive optics (DAO) is commonly used to correct the monochromatic wavefront aberrations in heterodyne imaging techniques. We show that interference-induced phase destruction, spatial-spectral crosstalk, and chromatic aberrations are the three primary artifacts obscuring diffraction-limited resolution restoration with standard DAO in images acquired with the broadband LS SD-OCT system. We demonstrate that phase destruction can be minimized with appropriate optics alignment. In addition, we show that spatial-spectral crosstalk and chromatic aberrations can be efficiently suppressed by registration of monochromatic aberration corrected sub-band tomograms. The image reconstruction method for recovering the diffraction-limited lateral resolution has been validated using different test objects such as standard resolution target, microbeads phantom, and different biological tissues imaged ex-vivo.

The novel decorrelation-based transverse flow velocimetry, developed specifically for LS SD-OCT, extends the current dynamic light scattering flow speed measurement techniques. We take advantage

of the phase stability within each B-scan and digitally generate a low-resolution OCT signal. By introducing the lateral resolution contrast in the temporal autocorrelation function of the OCT signals, this method allows for precisely measuring the transverse intralipid flow velocity in the low time resolution and low SNR conditions. The proposed method was validated by comparing with the phase-based OCT velocity measurement methods in phantom-based experiments.

The combination of the broadband LS SD-OCT system and the proposed image reconstruction method allows aberration-free volumetric cellular resolution imaging of biological tissues. The high image acquisition rate suppresses the motion-induced image artifacts, making high-resolution in-vivo imaging of the human eye in an extended depth of focus possible. The novel flow velocimetry can be used to monitor the flow dynamic, which extends the LS SD-OCT's functionality.

Acknowledgements

First, I would like to thank my supervisor, Dr. Bizheva, for her kind support through my PhD journey. She taught me the OCT's fundamental theory and advanced techniques in a nuts and bolts approach, which is extremely helpful to get familiar with the field. Dr. Bizheva provides a delightful atmosphere of independent research and assures maximum freedom in exploring research topics. I also appreciate the opportunities she offered to present my work at different conferences and build up my networks with the OCT community. I would also like to thank Dr. Melanie Campbell, Dr. Kevin Resch, Dr. Denise Hileeto, Dr. Gina Sorbara, and Donna Strickland for serving in my PhD committee. Their inspiring advice and constructive critique are precious to extend my knowledge.

Next, I want to thank Dr. Bingyao Tan from Nanyang Technological University for always having an open ear when I need discussions and feedback, Dr. Dierck Hillmann from VU University Amsterdam and Dr. Laurin Ginner from the Austrian Institute of Technology for introducing the digital adaptive optics and testing our data, and Hiruy Haile and Krunomir Dvorski from the University of Waterloo science shop for the assistance with the custom designs of the mechanical and electronic components of the LS SD-OCT system. I would also like to thank Dr. David Cory for the financial support and research creed he taught me. I may forget all the quantum mechanics and spin dynamics, but I will always remember the importance of integrating theory and experiment.

A huge thank you to all the friends I have made in Waterloo. There are too many to name, but your companionship is the main therapy of loneliness in a city 6731 miles away from home. Thank you for kicking me out of the room and taking me to many outdoor activities, for the most delicious food in Waterloo, and for all the insightful discussions about science and life.

A special thanks to my parents. You are the ones who have sustained me, especially in the darkest moments.

Dedication

To the ordinary souls who become their own lights after being lost in the dark.

Table of Contents

List of Figures

List of Tables

List of Abbreviations

APSO	accelerated particle swarm optimization
CMOS	complementary metal-oxide semiconductor
cPSF	coherent point spread function
CS	cuckoo search
CTF	coherence transfer function
DAO	digitally adaptive optics
DC	dispersion compensation
DLS	dynamic light scattering
DOCT	Doppler OCT
DOF	depth of focus
DSubAp	digital subaperture-based
FA	firefly algorithm
FD	Fourier-domain
FDML	Fourier domain mode-locked
FF	full-field
FFT	fast Fourier transformation
FOV	field of view
FWHM.	full width at half maximum
IVCM	in-vivo confocal microscopy
LC	limbal crypt
LLS	linear least square
LS	line-scan
LSC	limbal stem cell
MIP	maximum intensity projection
NA	numerical aperture

NIR	near-infrared
OCT	optical coherence tomography
OCTA	optical coherence tomography angiography
POV	palisade of Vogt
PSD	power spectral density
PSF	point spread function
ROI	region of interest
SA	simulated annealing
SGD	stochastic gradient descent
SD	spectral-domain
SI	swarm-intelligence
SNR	signal to noise ratio
SS	swept-source
TD	time-domain

Chapter 1
Introduction

1.1 Motivation

Corneal and limbal diseases are some of the primary causes of blindness. Currently, there are several techniques that can image the anterior segment of the eye for clinical evaluation, e.g., slit-lamp biomicroscopy, ultrasound biomicroscopy, and *in-vivo* confocal microscopy (IVCM). Slit-lamp biomicroscopy offers a non-contact approach to examining the corneal crosssection and the surface of the limbus; however, due to the low spatial resolution, it cannot be used for resolving corneal and limbal cells and the corneal layers. Ultrasound biomicroscopy has a tissue penetration depth of ~5 mm and can be used for determining the anterior chamber angle. However, since its resolution is low (up to 20 μm axially and 50 μm laterally), ultrasound biomicroscopy is only capable of imaging the morphology of the anterior eye. In addition, the physical contact of the probe with the patient's cornea may cause pain and inflammation. IVCM, in particular laser scanning IVCM, is often used for imaging the cells of the cornea and limbus in both clinical and biomedical research. Traditional IVCM also requires physical contact, and its resolution is typically ≤ 2 μm in the lateral direction and 4-25 μm in the axial direction, thanks to the large numerical aperture (typically 0.4-0.9) of the immersed microscope objective. Due to the slow depth scanning rate (~30 frames/second), *in-vivo* volumetric imaging of the cornea and limbus is challenging because of involuntary eye movements. Recently, 3D corneal images were demonstrated with a modified Rostock Cornea Module (Heidelberg Engineering GmbH), in which a concave contact cap was used to reduce saccades. Nevertheless, the low axial resolution impedes resolving the ultrafine structure in the axial direction. Non-contact designs of IVCM have also been developed with the cost of reduced resolutions.

Optical coherence tomography (OCT) is a non-contact interferometric optical imaging technique measuring the sample's scattering profile with high spatial resolution and high volumetric imaging speed. With the development over 30 years, OCT has become one of the most successful techniques for clinical imaging and biomedical research. One important application of OCT in ophthalmology is cell imaging. Visualizing changes at the cellular level helps in diagnosing and treating ocular diseases at early stages. The main motivation of this thesis is developing a broadband line-scan (LS) spectral-domain (SD) OCT system capable of *in-vivo* imaging the 3D cell structures and vasculatures of human anterior ocular tissues such as cornea and limbus. SD-OCT allows for an isotropic ~2 μm spatial resolution using broadband light sources and proper effective numerical aperture (NA). The line-scan modality enables a faster volumetric acquisition rate than the point-scan OCT, which is important for suppressing involuntary eye motions and maintaining lateral phase stability. The high lateral phase stability is critical in performing digital adaptive optics (DAO) to restore the diffraction-limited lateral resolution over a large depth range. Due to the limited time resolution and the relatively low signal-to-noise ratio (SNR) of the LS modality, phase-resolved flow measurement methods' speed detection ranges are confined and may fail in certain conditions. A novel flow velocimetry is therefore on-demand in vascular imaging with the developed LS SD-OCT system.

1.2 Human cornea and limbus

The cornea, along with the sclera, forms a structural barrier between the eye and the outside environment and protects the inner tissue against infections. A healthy cornea maintains transparency and provides two-thirds of the refraction power of the eye [2]. The central cornea thickness of normal eyes ranges from 551 to 565 μm, and the peripheral thickness is from 612 to 640 μm [3]. As shown in Figure 1.1, the cornea consists of 5 layers: corneal epithelium, Bowman's membrane, stroma, Descemet's membrane, and corneal endothelium. The corneal epithelium is ~50 μm in thickness, and it consists of 3 different types of cells: superficial cells, wing cells, and basal cells. The diameter and thickness of the superficial cells are about 40-60 μm and 2-6 μm, respectively. The basal cells form a 20 μm tall single cell layer at the bottom of the epithelium layer. The Bowman's membrane is a ~12 μm thick layer located between the corneal epithelium and the stroma. It cannot be regenerated and may form scars when injured [2]. The stroma constitutes approximately 90% of the corneal thickness. Its structure consists of collagen lamellae with keratocytes cells located between the lamellae. The collagen fibrils in the cornea are narrower and more organized than in the sclera, and both factors are essential to maintain the optical transparency of the corneal tissue[2,4]. The collagen structures in the stroma, especially in the anterior stroma, provide mechanical strength to the cornea and prevent morphology changes. The keratocytes are responsible for maintaining stromal homeostasis [2]. The keratocytes cell density is reduced from the anterior to the posterior stroma. The Descemet's membrane is a 7-10 μm collagen layer on which the endothelium cells are attached. The endothelium cells form a single cellular layer at the most posterior of the cornea. The endothelial cells are hexagonal in shape and have a diameter of about 20 μm and thickness of ~4 μm in adults. The endothelium layer functions as a barrier to the anterior chamber of the eye and regulates the flow of fluids and ions between the stroma and aqueous humor, which is essential for corneal clarity [2]. The endothelial cell density is reduced at a mean rate of ~0.6% per year in the normal adult cornea [2], whereas adults' endothelial cells have no proliferate ability [5,6]. Thus, endothelial cells tend to enlarge and migrate to cover defects in the endothelium. Corneal endothelial dysfunction results in corneal edema, blurred vision, and discomfort.

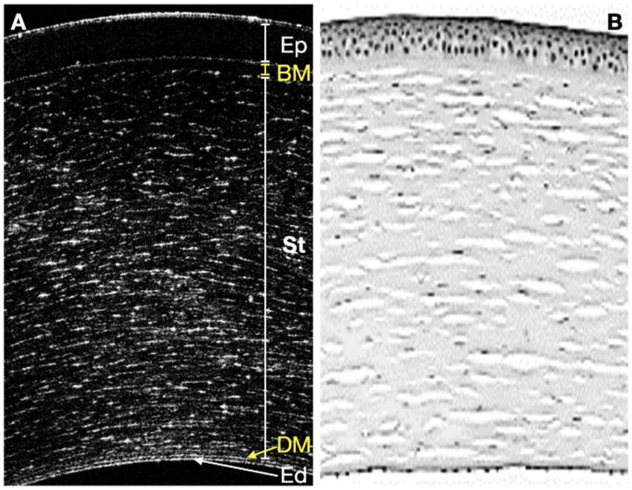

Figure 1.1 (A) *In-vivo* OCT [1] and (B) *ex-vivo* histology (reproduced with permission from Prof. Denise Hileeto) image of the human cornea. Ep, corneal epithelium; BM, Bowman's membrane; St, stroma; DM, Descemet's membrane; Ed, corneal endothelium.

The limbus is a 1-2 mm wide ring-shaped border between the cornea and sclera. The palisades of Vogt (POVs) are radially oriented structures located in the scleral limbus [7], and they are primarily found in the inferior and superior limbus. The visibility of POVs is related to the amount of melanin pigmentation [8]. Figure 1.2 shows typical radial and tangential crosssectional images of the POVs. The POVs have an undulating shape, and the blood capillaries and peripheral corneal nerves locate underneath the POVs' envelopes [9]. Limbal stem cells (LSCs) are located at the basal layer of the limbal epithelium. LSCs are responsible for the regeneration of the corneal epithelium cells [10–12]. Limbal stem cell deficiency results in loss of corneal clarity, corneal neovascularization, and conjunctivalization[13,14].

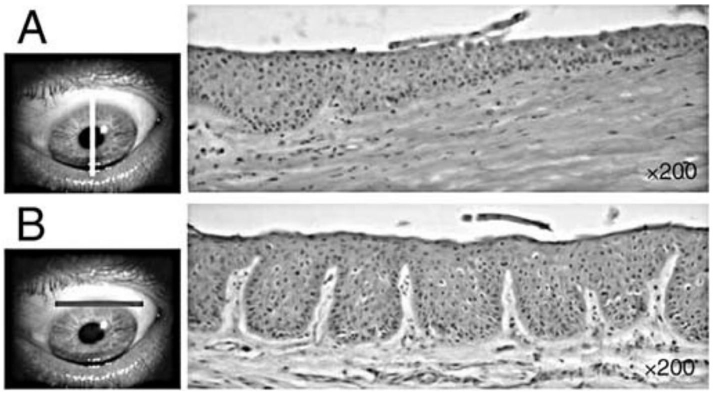

Figure 1.2 H&E stain image showing the palisades of Vogt (POVs) limbal structure [15].

In-vivo assessment of the corneal and limbal cellular structure allows for early and/or better diagnostics of potentially blinding corneal and limbal diseases. Such images can also assist ophthalmologists with the planning of the treatment, as well as the assessment of the effectiveness of the treatment. Currently, clinical *in-vivo* imaging of the human cornea and limbus cellular structures is accomplished by *in-vivo* confocal microscopy (IVCM) [7,8,16]. IVCM provides remarkable enface images with a limited field of view (typically 400×400 μm). However, its relatively low axial resolution and slow acquisition speed in the axial direction prevent the acquisition of volumetric images in the clinical environment. In addition, many IVCM instruments requires physical contact with the imaged tissue and may cause pain and inflammation. Recently, efforts have been made in *in-vivo* imaging the cellular structure of the human cornea and limbus using different OCT modalities. Point scan SD-OCT has been used for *in-vivo* imaging of both the human corneal and limbal cells [17–19]. The cellular resolution crosssectional images showed individual cells; however, with the slow imaging speed, 3D images are distorted because of eye motions. Full-field (FF) time-domain (TD) OCT records the enface image parallelly, and it is scanned in depth to extract the 3D structures. It has been used for *in-vivo* imaging of the cells in the human stroma and endothelium and the POVs structure and vasculature in the human limbus [20,21]. Nevertheless, the relatively slow scanning speed (275 frame/second) and low SNR (74 dB) prevent it from acquiring stable 3D images within a relatively large depth range and observing clear cornea and limbal epithelium cells. In addition, FF TD-OCT uses a high-power light-emitting diode with a 30 nm bandwidth as the light source, which limits its axial resolution. A thermal light source can improve the axial resolution to 1 μm [22,23], however, the SNR is limited [24]. Recently, Full-field (FF) swept-source (SS) OCT has also been demonstrated in *in-vivo* human cornea imaging [25]. The reported volumetric imaging rate is 58 Hz, which is remarkable for freezing the eye motions and allows for digital refocusing. However, its axial resolution is limited by the relatively narrow spectral range of the tunable lasers, which is insufficient for resolving the cellular details in the axial direction. Moreover, in order to visualize individual cells, multiple 3D images are averaged to compensate for the low SNR, and the effective volumetric imaging rate drops to 4 Hz.

1.3 Thesis organization

A broadband LS SD-OCT has been built, characterized, and tested for *in-vivo* imaging of the cellular structures of the human cornea and limbus. Three phenomena preventing the success of DAO in broadband LS SD-OCT are identified and resolved, and the performance of the proposed reconstruction method is demonstrated in different phantoms and biological tissues. A novel flow velocimetry method using the temporal decorrelation information was proposed and demonstrated in phantom studies. The thesis organization is as follows:

Chapter 2 presents an overview of the OCT's principle of operation, different design configurations (time-domain and Fourier domain) and image acquisition modalities (point-scan, line-scan, and full-field), as well as the key characteristics of an SD-OCT system. The techniques used in this study, e.g., DAO and Doppler OCT, are also introduced.

Chapter 3 discusses the design and characterization of the broadband LS SD-OCT system, spectrometer calibrations, dispersion compensation, axial motion-induced phase error correction, and signal reduction because of fringe washout and decorrelation.

Chapter 4 shows the *in-vivo* human corneal and limbal images acquired from healthy, normal eyes with the LS SD-OCT system.

Chapter 5 focuses on extending the broadband LS SD-OCT system's diffraction-limited lateral resolutions over an extended depth range. Three challenges, i.e., interference-induced phase destruction, spatial-spectral crosstalk, and chromatic aberrations, are addressed. A multi-band reconstruction method is proposed, and its performance is demonstrated in phantoms and in *ex-vivo* biological tissues (cucumber and animal cornea). The choice of image metrics and optimization methods for iteration-based DAO algorithms is discussed.

Chapter 6 presents a novel decorrelation-based method for measuring localized transverse intralipid flow speed using the LS SD-OCT. Dynamic light scattering (DLS) OCT theory is extended to the LS SD-OCT modality. The temporal decorrelation ratio of the original and digitally generated low-resolution OCT signals separates the transverse flow velocity along the line-illuminating direction from other perpendicular velocity components, diffusion of the flow particles, and the noise-induced distortion of the autocorrelation, therefore allowing for precise determination of the transverse flow velocity.

Chapter 7 summarizes the work presented in this thesis and discusses the future studies to extend this work.

Chapter 2

Fundamentals of Optical Coherence Tomography (OCT)

Optical coherence tomography (OCT) is an optical interferometric technique that is capable of mapping the depth-dependent backscattering profile of imaged objects volumetrically and with micrometer-scale resolution. The short coherence length of the low-coherence light source determines the axial resolution with which scatterers can be resolved along the measured optical path length. In 1988, Fercher et al. reported the first biological application of low-coherence interferometry in measuring axial eye length [26]. The name, OCT, was given by Huang et al. in a seminal publication in Science 1991 [27], in which the first *in-vivo* crosssectional human retina OCT tomogram was demonstrated.

Over the last 30 years, the design of OCT systems has seen significant development thanks to the advances in laser and camera technologies. One major revolution in the OCT design was the development of Fourier-domain (FD) OCT which offers significant sensitivity improvement over time-domain (TD) OCT [28,29]. The greater than 1000-fold signal-to-noise ratio (SNR) improvement and the parallel information acquisition in the axial direction characteristic of FD-OCT allow for a wide range of clinical and biomedical applications of the FD-OCT technology for *in-vivo* imaging. The phase information provided by the heterodyne detection configuration allows OCT to be used for acquisition of physiological and metabolic information about the imaged object. For example, phase-resolved Doppler OCT (DOCT) allows for mapping of blood vasculature and quantitative measurement of blood flow [30,31], optoretinography (ORG) and functional OCT allow for measuring physiological responses of neural tissue to external stimulation [32–37], and optical coherence elastography (OCE) can measure the biomechanical contrast [38,39]. In addition, the temporal decorrelation difference between the dynamic and static signals provides noticeable contrast, especially in the region where scattering contrast is low, enabling cell dynamic contrast imaging and blood vessel imaging with dynamic OCT and OCT angiography (OCTA) respectively [40,41]. Furthermore, with the dramatically increased acquisition speed, the diffraction-limited lateral resolution can be extended beyond the Rayleigh range with digital adaptive optics (DAO), allowing for high-resolution imaging over a relatively large field-of-view (FOV) in *in-vivo* imaging [42–45].

In this chapter, we present an overview of the principle of OCT as well as its different configurations and modalities. We will also introduce the techniques utilized in this PhD study.

2.1 Optical coherence tomography

2.1.1 Low-coherence interference

The principle of operation of OCT is based on interference of low coherent light. Figure 2.1 shows a typical Michelson interferometer powered by a low-coherence light source whose electric field can be expressed as $E_i(k) = s(k)e^{i(kz-\omega t)}$. Here, $s(k)$ is the electric field amplitude as a function of the wavenumber k. For simplification, it is assumed that the whole OCT system is in free-space. The electric fields reflected by the mirror $E_r = E_i\gamma_r(k)e^{i2kz_r}$ and scattered by the sample $E_s = E_i\gamma_s(k, z_s) \otimes e^{i2kz_s}$ interfere and generate a photocurrent at the detector which can be expressed as:

$$I(k) \propto \rho(k)\langle(E_s(k) + E_r(k))(E_s(k) + E_r(k))^*\rangle_t \tag{2.1}$$

Here ρ is the product of the power loss function of the optics and responsivity of the detector, $\langle\rangle_t$ denotes the average within the detector's response time, and $z_{r,s}$ is the optical path length of the reference/sample arm. Assuming that the amplitude reflecting/scattering profile $\gamma_{r,s}$ is wavelength-independent, and the scatters' distribution is discrete $\gamma_s(k, z_s) = \sum_{i=1}^{n}\gamma_{s,i}\,\delta(z_s - z_{s,i})$, the photocurrent can be simplified as:

$$I(k) \propto S(k)[\underbrace{\gamma_r^2 + \sum_{i=1}^{n}\gamma_{s,i}^2}_{\text{DC}} + \underbrace{2\gamma_r\sum_{i=1}^{n}\gamma_{s,i}\cos[2k(z_r - z_{s,i})]}_{\text{cross-correlation}} + \underbrace{2\sum_{i\neq j}\gamma_{s,i}\gamma_{s,j}\cos[2k(z_{s,i} - z_{s,j})]]}_{\text{auto-correlation}} \tag{2.2}$$

where $S(k) = \rho(k)|s(k)|^2$ is the effective power spectrum detected by the detector. There are 3 components in Equation (2.2). The 'DC' terms refer to the light intensities generated by the reference and sample arms if there was no interference; the 'cross-correlation' terms represent the interference between the sample and reference signals; the 'auto-correlation' terms denote the self-interference between signals generated by different scatters within the imaged object in the sample arm of the OCT system. In practice, $\gamma_{s,i}$ are much weaker than γ_r, thus the reference intensity dominates in the OCT signal, and in general, the sample intensities and the auto-correlation terms can be neglected. The cross-correlation terms, that carry information about the spatially dependent scattering profile of the imaged object, form the OCT signal I_{AC} used to generate the OCT images. Integrating over the wavenumber space, the total photocurrent generated at the detection end of the OCT system by the cross-correlation terms is:

$$\begin{aligned} I_{AC}(z_r) &= \int I_{AC}(k)dk \\ &\propto 2\gamma_r \sum_{i=1}^{n} \gamma_{s,i} \Gamma[2(z_r - z_{s_i})]\cos[2k_0(z_r - z_{s_i})] \end{aligned} \quad (2.3)$$

Here $\Gamma(z) = FT[S(k)]$ denotes the autocorrelation function of the low-coherence light source, and k_0 is the central wavenumber.

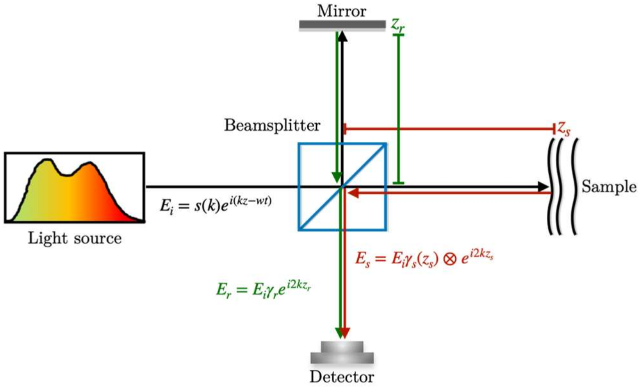

Figure 2.1 Schematic of a Michelson interferometer with a low-coherence light source. $\mathrm{s(k)}$ is the amplitude of the electric filed; γ_z and γ_s are the amplitude scattering/reflecting potentials of the reference mirror and sample, respectively.

2.1.2 Time-domain (TD) OCT vs. Frontier-domain (FD) OCT

As shown in Equation (2.3), the cross-correlation term appears only when the reference arm and sample arm's optical path lengths match because of the short coherence length of the low-coherence light source. Therefore, in order to extract the scattering profile along the depth, the reference mirror is scanned in depth to match the axial positions of the scatterers within the imaged object as shown in Figure 2.2 (A). The depth scan can be performed by translating the reference mirror with a piezoelectric actuator. Alternatively, a rapid depth scan can be achieved with the so-called Fourier-domain rapid scanning optical delay line setup [46]. This method is called time-domain (TD) OCT. Assuming $S(k)$ follows a Gaussian distribution:

$$S(k) = S_0 \exp[-(\frac{k-k_0}{\Delta k})^2] \quad (2.4)$$

The OCT signal can be rewritten as:

$$I_{AC}(z_r) \propto 2\gamma_r \sum_{i=1}^{n} \gamma_{s,i} \exp[-\Delta k^2 (z_r - z_{s,i})^2]\cos[2k_0(z_r - z_{s_i})] \quad (2.5)$$

Figure 2.3 (A) illustrates how the one dimensional (1D) signal (an axial or a depth scan) is generated in TD-OCT. The AC interference signal, with a modulating frequency of $k_0/2\pi$, appears when the optical path difference between the OCT sample and reference arms is less or equal to the coherence length l_c. In the early development of OCT, the coherence length of the light source is typically >10 μm, which is an order larger than the wavelength. Thus, the AC interference signal oscillates inside the magnitude envelope, and a low-pass filter is required for demodulation.

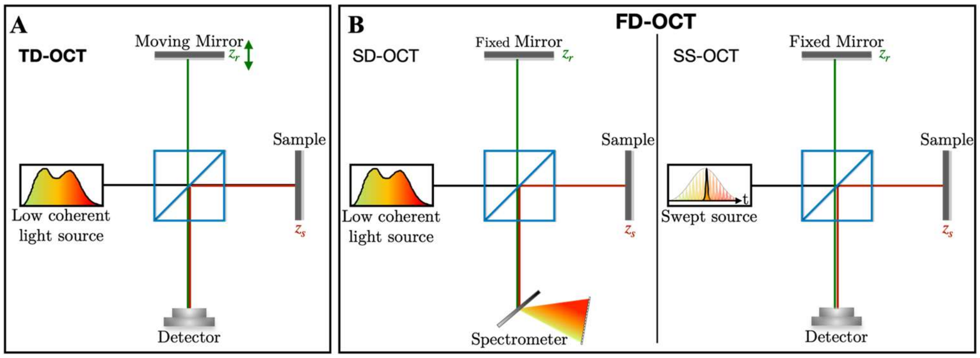

Figure 2.2 Schematics of (A) time-domain (TD) OCT and (B) Fourier-domain (FD) OCT. The TD-OCT requires a depth scan of the reference mirror, while the reference mirror's position is fixed in FD-OCT. FD-OCT has two different configurations: the SD-OCT uses a spectrometer to record the spectrum; the SS-OCT scans the wavelength or wavenumber over time.

The mechanical depth scanning configuration of TD-OCT limits the 1D data acquisition speed to a maximum of several kHz. This limit can be overcome using spectrum-resolvable configurations. Specifically, the full spectrum is divided into many narrow spectra that are detected independently. As the coherence length of each narrow spectra is much longer than that of the full spectrum, the scattering profile at different depths can be recorded simultaneously without moving the reference mirror. This method is called Fourier-domain (FD) OCT. Depending on how the spectrum is recorded, FD-OCT can be categorized into spectral-domain (SD) OCT and swept-source (SS) OCT. The latter is sometimes referred to as optical frequency domain imaging (OFDI). The simplified schematics of SD-OCT and SS-OCT are shown in Figure 2.2 (B). In SD-OCT, a continuous wavelength, broad-bandwidth, low coherence light source is used at the entrance of the OCT system. At the detection end of the system, the broad spectrum is dispersed by a grating and the narrow spectral bands are mapped over individual pixels of a line camera. In SS-OCT, a rapid tunable laser is employed as the light source, and the wavelength or wavenumber is linearly swept over time. The optical signal is recorded either by a single photodiode or as in most cases, by a pair of photodiodes (dual balanced detection). Compared to TD-

OCT, FD-OCT offers significantly higher SNR and acquisition speed [28,29], as well as the flexibility of dispersion compensation in post-processing.

The scattering profile in depth can be extracted by the Fourier transform of the interference fringe $I_{AC}(k)$:

$$\begin{aligned} I(z) &\propto FT_{k\to z}\left[2S(k)\gamma_r\sum_{i=1}^{n}\gamma_{s,i}\cos[2k(z_r-z_{s,i})]\right] \\ &=\gamma_r\Gamma(z)\otimes\sum_{i=1}^{n}\gamma_{s,i}(\delta[z+2(z_r-z_{s,i})]+\delta[z-2(z_r-z_{s,i})]) \\ &=\gamma_r\sum_{i=1}^{n}\gamma_{s,i}(\Gamma[z+2(z_r-z_{s,i})]+\Gamma[z-2(z_r-z_{s,i})]) \end{aligned} \tag{2.6}$$

The scattering profile distribution $\gamma_s(z_s)=\sum_{i=1}^{n}\gamma_{s,i}\,\delta(z_{s,i})$ is effectively reconstructed at the depth of $\pm 2(z_{s,i}-z_r)$. Here, the ambiguity of the positive and negative locations is known as the complex conjugate artifact which arises from the Fourier transform of a real sequence, and the factor of 2 is due to the phase delay corresponding to the round trip of the optical beam in the reference and sample arms of the OCT system. The mirror artifact cannot be eliminated by simple post-processing methods, however different approaches have been developed for eliminating or reducing the effect of the ambiguity to allow for development of so called full-range OCT systems [47,48]. In most cases, the interference fringes are usually processed with the Hilbert transform before the Fourier transform; thus, all energy can be displayed in the positive range. A single-pass depth $\tilde{z}=z/2$ is often used to accommodate the factor of 2.

Figure 2.3 (B) illustrates the 1D scattering profile reconstruction in FD-OCT. When the OCT imaging beam is scattered by 2 or more scatterers located at different depths along an axial scan, the interference pattern generated at the OCT detection end has a complex fringe pattern with modulated amplitude. By applying a Fourier transform to the modulated interference signal, the individual frequency components can be identified that correspond to the signals generated by different scatterers. The DC terms and auto-correlation terms usually appear near the zero optical path delay. Thus, the cross-correlation components can be separated from the DC and auto-correlation terms by adjusting the optical path length of the reference arm. In practice, the DC term is removed by subtracting the reference intensity (so called “background”) from the detected OCT signal.

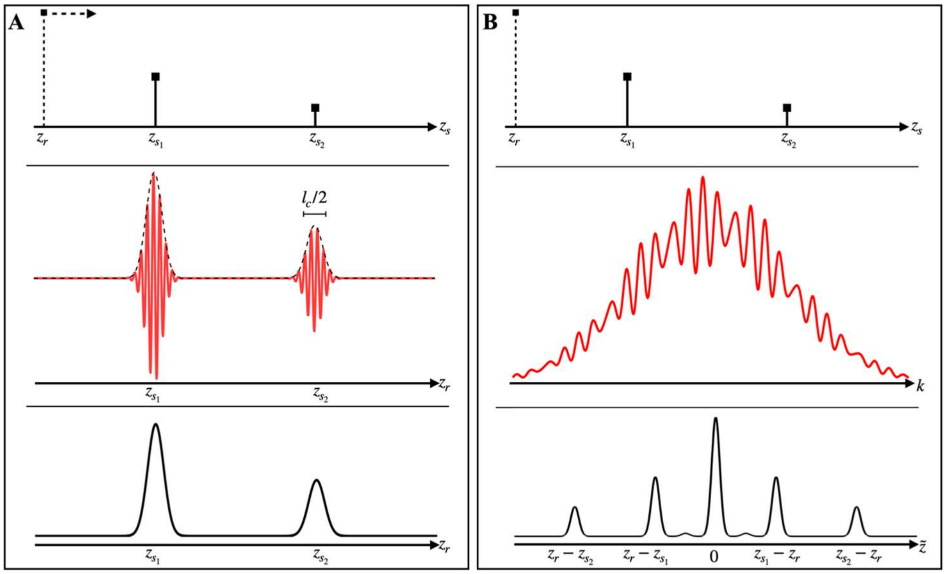

Figure 2.3 One dimensional (1D) signal formation in (A) TD-OCT and (B) FD-OCT. Top: scattering profile $\gamma(z_s)$; middle: interference signal; bottom: OCT signal.

In OCT, the 1D scattering profile reconstruction along the imaging depth (z-direction) is referred to as 'A-scan', a terminology borrowed from ultrasound imaging. The two dimensional (2D) crosssectional image consisting of successive A-scans is called a ‘B-scan', which is generated by scanning along one lateral direction (y-direction) with a galvanometric scanner. With an additional scanner, a three dimensional (3D) volumetric image can be acquired by scanning in the x-direction. Once a volumetric OCT image is recorded, image processing software can be used to select specific planes from the 3D imaging set. Enface images in the xy-plane are referred to as 'C-scans'. Here, the Cartesian coordinate (x, y, z) is used to be consistent with our line-scan configuration in the following chapters. However, the x- and y-direction choice can be arbitrary in other OCT systems.

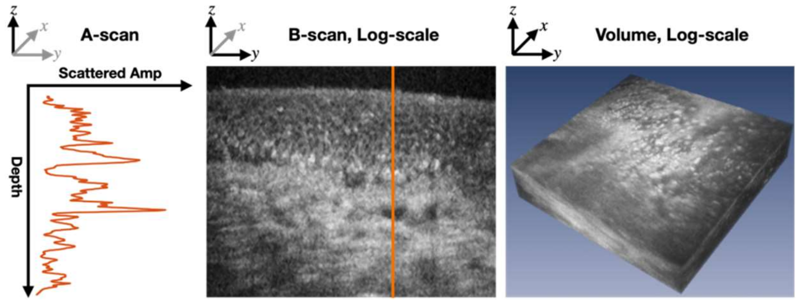

Figure 2.4 A-scan (left), B-scan (middle), and volumetric image (right) of the limbus-cornea region of a healthy volunteer.

2.1.3 OCT imaging modalities

Acquisition of volumetric images with OCT can be accomplished using different methods that have resulted in different designs of the OCT systems. Three imaging modalities are illustrated in Figure 2.5. In the point-scan design, a pair of galvanometric scanners or a 2D micro electro-mechanical system (MEMS) scanner is used for lateral scanning of the OCT imaging beam, and OCT A-scans are recorded for each position on the xy-plane. Although the acquisition speed of FD-OCT has been dramatically improved with the development of camera sensing technology, the point-scan modality is still suffering from the motion effects in *in-vivo* volumetric human ocular imaging. The A-scan rate of most commercial SD-OCT and SS-OCT systems is below 300 kHz, which is not fast enough to suppress involuntary eye motion, therefore resulting in motion artifacts in the OCT images. Higher A-scan rates can be achieved in research-grade systems. For example, the most advanced line cameras allow for a 400-600 kHz A-scan rate in SD-OCT [49,50], and the Fourier domain mode-locked (FDML) laser achieved a 5.4 MHz A-scan rate in SS-OCT [51]. However, the use of higher imaging speed (shorter image acquisition time) setups requires the use of higher power to achieve acceptable SNR in the OCT images. As exposure of biological tissue to optical beams of high power can case temporary or permanent damage to the structure and physiology of the imaged biological tissue, the trade-off between increasing the OCT imaging speed and the optical imaging power can limit the use of point-scan OCT technology for some clinical applications.

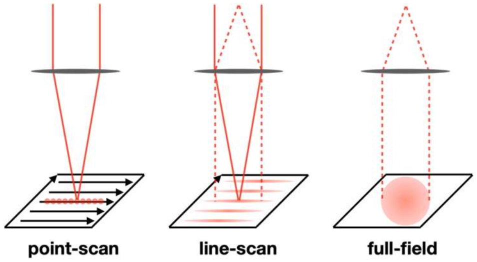

Figure 2.5 Schematics of point-scan (left), line-scan (middle), and full-field OCT (right).

Two laterally parallel image acquisition modalities of FD-OCT, namely line-scan (LS) SD-OCT and full-field (FF) SS-OCT, were demonstrated in 1999 and 2006, respectively [52,53]. With the development of fast 2D complementary metal-oxide semiconductor (CMOS) cameras, these two parallel acquisition modalities have attracted more research interest. The main advantage of the parallel modalities is the high lateral phase stability, which enables digital compensation for aberrations in *in-vivo* OCT images without complicated motion tracking systems or algorithms.

However, the two modalities have drawbacks compared with point-scan configuration. In fiber-based point-scan OCT modality, the single-mode fiber introduces a confocal gate that rejects out-of-focus signals. FF SS-OCT lacks the confocal gate thus all scattered photons are detected by the camera. A fraction of the multi-scattered signals from a location (x_1, y_1, z_1) can be misinterpreted as the OCT signal from another location (x_2, y_2, z_2). This artifact is known as spatial crosstalk, which can be suppressed with low spatial coherence light sources [54,55]. Another problem of FF SS-OCT is axial motion within the time window of a spectral scan. A typical spectral scan time is about 5-10 ms for FF SS-OCT with acceptable SNRs. Even though the axial motion of the imaged object (or subject for the case of *in-vivo* imaging) can be reduced to a micrometer level within the acquisition time window with proper mechanical supports, it still results in blurred images due to the chirping of the interference fringes. Therefore, extra efforts are needed to compensate for the motion-induced fringe chirping [56].

In LS SD-OCT, the imaging beam is shaped in the form of a line, that is projected onto the surface of the imaged object and then scanned in x-direction with a galvanometric scanner to generate volumetric OCT images. LS SD-OCT has a confocal gate in the lateral scanning direction (x-direction), while it uses a wide-field configuration along the parallel illumination direction (y-direction) and as such offers a compromise between the point-scan and full-field modalities. In principle, the LS SD-OCT should have a higher sensitivity than FF SS-OCT, and its spatial crosstalk occurs only along the y-direction. However, since LS SD-OCT simultaneously records the spatial and spectral information on a 2D camera, spatial-spectral crosstalk is inevitable, especially in an ultrahigh-resolution OCT system in which the spectral range is large. In addition, the axial motion induced fringe washout is more significant in LS SD-OCT since its camera integration time is typically about 70-400 μs, which is much longer than 2-10 μs in point-scan SD-OCT.

In parallel OCT modalities, an effective A-scan rate is often used to compare with the A-scan rate of the point-scan system. The effective A-scan rate is calculated by multiplying the complete spectral acquisition rate with the number of parallelly imaged locations. For instance, if an FF SS-OCT's spectral scanning rate is 100 spectrums/second and its lateral recording area is 500×500 pixels, its effective A-scan rate is 25 MHz. The effective A-scan rate is used to show the 2D/3D acquisition speed superiority of LS-OCT/FF-OCT over point-scan OCT; however, it does not imply an A-scan is recorded with such a high speed.

Note that the line-scan and full-field modalities have also been utilized in TD-OCT [21,57,58].

2.1.4 OCT system characteristics

In this section, we introduce the key design characteristics of an FD-OCT system based on the point-scan design.

Axial resolution

As mentioned above, the OCT's axial resolution is determined by the coherence length of the light source. Assuming the effective power spectral density distribution is Gaussian, as shown in Equation (2.4), the autocorrelation function of the electrical field can be calculated as $\mathit{\Gamma}(z) = FT[S(k)]$. Substitute the single-pass depth $\tilde{z} = z/2$, the axial point spread function (PSF) is:

$$\Gamma(\tilde{z}) = S_0 \exp\left(-\Delta k^2 \tilde{z}^2\right) \quad (2.7)$$

Therefore, for a Gaussian spectrum, the OCT axial resolution, defined as the full width of maximum half (FWMH) of the axial PSF, is:

$$\delta\tilde{z} = 2\sqrt{\ln 2} / \Delta k = \frac{2\ln 2}{\pi}\frac{\lambda_0^2}{\Delta\lambda} \quad (2.8)$$

Here λ_0 and $\mathit{\Delta}\lambda$ are the light source's central wavelength and FWMH bandwidth, respectively. It is worth pointing out that we have assumed the light source's power spectrum is Gaussian in deriving Equation (2.8), and one should calculate the axial resolution of a non-Gaussian light source following the definition of the coherence length. From now on, we will drop the tilde mark in the single-pass depth, $\tilde{z} \rightarrow z$, unless specifically noted.

Lateral resolution

Since OCT utilizes a light source with a broad spectral bandwidth, the OCT's lateral resolution is usually estimated using the central wavelength of the light source. Using a monochromic illumination beam with a circular shape and uniform irradiance, a confocal configuration's lateral PSF at the focal plane can be expressed as $I(v) = (J_1(v)/v))^4$ [24].Here $J_1(v)$ is the first-order Bessel function (first kind), and v is the rescaled lateral coordinate defined as $v = 2\pi r \sin(\alpha)/\lambda_0$. The lateral resolution is characterized with the FWMH of the lateral PSF:

$$\delta x = 0.37\frac{\lambda_0}{\mathrm{NA}} \quad (2.9)$$

where $\mathrm{NA} = \sin\alpha$ is the effective numerical aperture. When the NA is small, the expression in Equation (2.9) can be further simplified as $\mathrm{NA} = a/f$, where a is the beam radius and f is the focal length of the objective. In many applications, the illuminating beam irradiance is Gaussian instead of uniform and the objective is underfilled. Assuming that the electric field incident at the entrance aperture of the imaging lens (or objective) has Gaussian distribution $E(r) = \exp(-r^2/a^2)$, the electric field distribution at the focal plane of the imaging lens (or objective) is:

$$h_{illu}(r) \propto \exp\left[-(\frac{\pi a}{\lambda_0 f})^2 r^2\right] \tag{2.10}$$

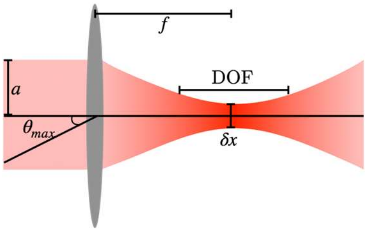

Figure 2.6 Schematic of a microscope objective in point-scan modality. a: beam radius; f: focal length; θ_{max}: maximum optical scan angle; δx: lateral resolution; DOF: depth of focus.

where a is the $1/e$ beam radius of the incoming electric field. Due to the confocal configuration and the symmetry of the illumination and detection optics, the coherence point spread function (cPSF) of the system is:

$$h_{sys}(r) = h_{illu}^2(r) \propto \exp\left[-2(\frac{\pi a}{\lambda_0 f})^2 r^2\right] \tag{2.11}$$

Here, the cPSF refers to the distribution of the electric field amplitude, while PSF denotes the distribution of the light intensity. The FWMH waist size is also $0.37\lambda_0/\mathrm{NA}$, where NA is the effective NA calculated with the $1/e$ electric field radius (equals $1/e^2$ intensity radius for Gaussian beam). However, one should note that it is referred to the lateral resolution of the cPSF, while Equation (2.9) is for the PSF. Since OCT is based on a heterodyne detection scheme, we will use cPSF to characterize the system's resolutions in the following chapters unless noted otherwise.

Depth of focus

The depth of focus (DOF), sometimes referred to as confocal parameter or axial FOV, is used to describe the depth range over which the lateral resolution is maintained at an acceptable level. In Gaussian beam convention, it is defined as twice the Rayleigh range:

$$\mathrm{DOF}^{(1)} = 2z_R = \frac{2\pi\omega_0^2}{\lambda_0} = \frac{2}{\pi}\frac{\lambda_0}{\mathrm{NA}^2} \tag{2.12}$$

where ω_0 is the $1/e^2$ beam radius of the illuminating PSF at the focal plane and NA is calculated using the $1/e^2$ irradiance radius of the incoming beam. If we follow the uniform illumination convention and define the DOF as the FWHM of the axial intensity response function of the planer reflector, then the DOF it is calculated as [24]:

$$\mathrm{DOF}^{(2)} = \frac{0.22\lambda_0}{\sin^2[\arcsin(\mathrm{NA}/2)]} = 0.88\frac{\lambda_0}{\mathrm{NA}^2} \tag{2.13}$$

In most OCT systems, the DOF is irrelevant to the axial OCT resolution, as that is defined by the coherence length of the light source; however, if the DOF and the coherence length are comparable when the effective NA is large, both parameters influence the axial resolution. Both conventions suggest that a large DOF and a high lateral resolution are contradictory to each other. Therefore, digital refocusing is necessary to restore the lateral resolution in the out of focus region.

Lateral FOV

The lateral FOV is governed by the maximum optical scan angle $\theta_{\max}$ and the focal length f in the scanning configuration:

$$\mathrm{FOV}_{\mathrm{scan}} = 2f\tan(\theta_{\max}) \tag{2.14}$$

For wide-field OCT design, it is depended on the detector dimension and the sample to camera magnification:

$$\mathrm{FOV}_{\text{wide-field}} = \mathrm{nd/M} \tag{2.15}$$

where n and d are the camera's spatial pixel number and pixel size, and M is the sample to camera magnification ratio.

Depth scanning range

In the axial direction, the depth scanning range $Z_{\max}$ of an OCT system is defined as the maximum depth an FD-OCT signal can be acquired. For the OCT system with a spectral detection range $(\lambda_{\min}, \lambda_{\max})$, the one side OCT depth scanning range is:

$$Z_{\max} = \frac{N}{4\times(1/\lambda_{\min} - 1/\lambda_{\max})} \tag{2.16}$$

where N is the number of illuminated camera pixels along the spectral direction. In the case where the spectral detection range is much shorter than the central wavelength, Equation (2.16) can be simplified as $Z_{\max} = \lambda_0^2/(4\delta_s\lambda)$, where $\delta_s\lambda$ is the average spectral sampling interval.

Digital resolutions

The digital spatial resolution is defined as the sampling interval per pixel:

$$\begin{aligned} \tilde{\delta}x &= \frac{FOV_{lateral}}{n} \\ \tilde{\delta}z &= \frac{Z_{max}}{N/2} = \frac{1}{2\times(1/\lambda_{min} - 1/\lambda_{max})} \end{aligned} \tag{2.17}$$

where n is the number of A-scan or B-scan, N is the spectral pixel number, and the tilde mask is used to differentiate the digital spatial resolutions from spatial resolutions. According to the Nyquist–Shannon sampling theorem, the digital resolution should be smaller than half of the spatial resolution to avoid aliasing.

Signal to noise ratio (SNR)

In many OCT literature, the SNR and sensitivity are used interchangeably. We will not distinguish these two terms in the following materials. The sensitivity of an OCT system is defined as $\mathrm{SNR}(z) = \langle I(z)\rangle^2/\sigma_n^2$, where $I(z)$ is the amplitude of the axial PSF and σ_n^2 is the noise variance. Assuming a single scatter in the sample arm, the interference fringe can be rewritten as:

$$I(k) = \rho(k)[I_r(k) + I_r(k) + 2\sqrt{I_r(k)I_s(k)}\cos(2k(z_s - z_r))] \tag{2.18}$$

where $\rho(k)$ is the responsivity of the detector, $I_r(k)$ and $I_s(k)$ are the reference and sample light intensities projected onto the detector. Assuming a uniform responsivity and the sample's and reference's power spectrums are the same, $I_r(k) = \gamma_r^2 S(k)$ and $I_s(k) = \gamma_s^2 S(k)$, the axial PSF's amplitude at the zero optical path delay is:

$$I(z=0) = \rho\gamma_r\gamma_s\sum_{n=1}^{N} S(k_i) \tag{2.19}$$

In the shot noise limited regime, the photon count follows the Passion distribution and the noise variance for each spectral channel is $\sigma_n^2(k) = eI(k)/\tau$, where e is a single electron charge and τ is the integration time. Assuming the reference intensity dominates, and the detection of each spectral channel is independent, the total noise variance can be approximated as:

$$\sigma_n^2 = \sigma_{sh}^2 = \frac{1}{\tau} e\rho\gamma_r^2 \sum_{n=1}^{N} S(k_i) \tag{2.20}$$

Thus, the SNR at the 0 optical path delay can be expressed as:

$$\mathrm{SNR(z=0)} = \frac{\langle I(z=0)\rangle^2}{\sigma_{sh}^2} = \frac{\rho P_s \tau}{e} = \frac{\eta P_s \tau}{h\nu_0} \tag{2.21}$$

where P_s is the sample arm power projected onto the detector, η is the mean quantum efficiency of the detector, h is the Planck constant, and ν_0 is the central frequency of the light source.

SNR rolloff

Due to the finite spectral resolution and spectral sampling interval, the amplitude of the A-scan degrades along depth. This phenomenon is called SNR rolloff or sensitivity rolloff in the OCT field. For an SD-OCT system, the detected power spectrum can be expressed as: $I(k) = G(k) \otimes S(k)$, where $S(k)$ is the true power spectrum and $G(k) = \exp[-k^2/(\delta k)^2]$ comes from the diffraction limit of the grating and camera lens. Due to the finite pixel size, the digitalized interference fringe is:

$$\begin{aligned} I(k_i) & \propto \int_{k_i-\frac{\Delta k}{2}}^{k_i+\frac{\Delta k}{2}} I(k)\cos(2k\Delta z)dk \\ & = \int_{-\infty}^{\infty} H(k-k_i)[(G(k)\otimes S(k))\cos(2k\Delta z)]dk \\ & = H(k_i)\otimes[(G(k_i)\otimes S(k_i))\cos(2k_i\Delta z)] \end{aligned} \tag{2.22}$$

where $H(k) = \mathrm{rect}(k/\Delta k)$ is the rescaled rectangle function, and Δk is the spectral sampling interval in wavenumber space. Therefore, the intensity reduction ratio is:

$$R(z) = \mathrm{sinc}^2(\Delta kz)\exp[-2(\delta kz)^2] = \mathrm{sinc}^2(\Delta kz)\exp[-(\frac{2\pi\delta\lambda_{1/e^2}}{\lambda_c{}^2}z)^2] \tag{2.23}$$

Here, λ_c is the central wavelength and $\delta\lambda_{1/e^2}$ is the spectral derivation corresponding to $1/e^2$ radius of the central wavelength's PSF. It should be noted that here a constant spectral resolution δk and a spectral sampling interval Δk are assumed to simplify the model.

2.2 Digital adaptive optics

An optical imaging system can be modeled as a linear shift-invariant system. For a coherent imaging setup, the detected electric field at the image plane is:

$$u(x,y) = \int h(x,y,z)\otimes\gamma(x,y,z)\mathrm{d}z \tag{2.24}$$

where $\gamma(x,y,z)$ is the sample's amplitude scattering profile, and $h(x,y,z)$ is the 3D cPSF of the system. As OCT intrinsically detects the depth information, Equation (2.24) can be modified as:

$$u(x,y;z) = h(x,y;z)\otimes\gamma(x,y;z) \tag{2.25}$$

If the cPSF is a delta function, the image is identical to the sample; however, h has a finite size because of the limited aperture size. In addition, the wavefront aberrations result in a distorted cPSF, which further degrades the image quality.

The wavefront aberrations' influence is easier to illustrate using the angular spectrum representation:

$$U(k_x,k_y;z)=H(k_x,k_y;z)\Gamma(k_x,k_y;z) \tag{2.26}$$

where U and Γ are the transverse 2D Fourier transforms of the image and sample fields. H is the coherence transfer function (CTF), which is a complex function:

$$H(k_x,k_y;z)=P(k_x,k_y;z)e^{i\phi(k_x,k_y;z)} \tag{2.27}$$

The phase $\phi(k_x,k_y;z)$ is consist of the optical wavefront aberrations that need to be corrected. In principle, if a counter phase mask, $\alpha(k_x,k_y;z)=-\phi(k_x,k_y;z)$, is digitally applied on both sides of Equation (2.26), the wavefront aberration is canceled. However, this requires accessing the phase information of the imaged structure. Since OCT utilizes a heterodyne detection configuration, the phase information is preserved if not degraded by the motion of the imaged object.

2.3 Flow measurement

2.3.1 Doppler OCT (DOCT)

In addition to imaging the structure of the imaged object (3D scattering profile), OCT can also be utilized to detect flow velocity by using the Doppler effect. Here, the Doppler effect denotes the modulation frequency change of the TD-OCT signal. In Figure 2.3, the 1D TD-OCT is plotted as a function of the reference mirror position. Since the reference mirror is scanned over depth in a time series, the TD-OCT signal can be rewritten as:

$$I_{AC}(t)=2\gamma_r\gamma_s\Gamma[2(z_{r,0}+v_rt-z_s(t))]\cos[2k_0(z_{r,0}+v_rt-z_s(t))] \tag{2.28}$$

where v_r is the reference mirror's scanning speed. For a static scatter, the modulation frequency is $f_r=2v_r/\lambda_0$. If the scatter moves with an axial speed $v_{s,z}$, the modulation frequency becomes $f_s=2(v_r-v_{s,z})/\lambda_0$. The Doppler frequency shift associated with the scatter's motion can be expressed as $f_D=f_r-f_s=2v_{s,z}/\lambda_0$, which can be used to estimate the scatter's speed since λ_0 is known.

Note that the phase term $\phi(t)=2k_0\Delta z(t)$ can be measured directly in both TD-OCT and FD-OCT [30,59]. the localized axial velocity can be determined by the phase difference of two successive A-scans:

$$v_z(z)=\frac{\Delta\phi(z)}{2k_0\tau} \tag{2.29}$$

where τ is the time interval between two A-scans and k_0 is the central wavenumber in the medium. Nevertheless, the name 'Doppler OCT' is used, and the Doppler frequency shift is linked with the phase difference as $f_D = \Delta\phi/2\pi\tau$.

In a single-beam point-scan OCT system design, the phase change $\Delta\phi$ is only related to the axial motion. The phase change induced by the motion of a scatter can be expressed as:

$$\Delta\phi = (\vec{k}_s - \vec{k}_i)\cdot\vec{v}\tau \tag{2.30}$$

where $\vec{k}_{i,s}$ are the illuminating and scattering wave vectors and $\vec{v}$ refers to the scatter's velocity. In a 2D simplified scenario, as shown in Figure 2.7, the phase differences generated by the off-axis scattering vectors $\vec{k}_s^{(2),(3)}$ are $\Delta\phi_s^{(2),(3)} = (k_z v_z \pm k_x v_x)\tau$. However, the lateral velocity information is averaged out because of symmetry.

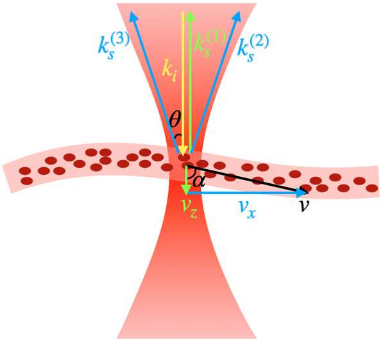

Figure 2.7 Schematic of the illuminating and scattering beams in Doppler OCT (DOCT).

The magnitude of the flow velocity can be determined with the knowledge of the Doppler angle α as $|v| = v_z/\cos\alpha$. However, accurately determining α is challenging since it requires a recovery of the full 3D refractive index map. In addition, small axial velocity itself can be distorted by the presence of phase noise, especially when the blood vessels are perpendicular to the beam propagating direction. To overcome this limitation, multi-beam DOCT and its digital version, digital subaperture-based (DSubAp) DOCT, are used to extract the lateral induced phase difference[60–63]. In DSubAp DOCT, symmetrical off-axis scattering vectors are digitally filtered. Therefore, the phase changes induced by $\vec{k}_s^{(2),(3)}$ are separable, and the lateral velocity component can be determined by:

$$v_x = \frac{\Delta\phi^{(2)} - \Delta\phi^{(3)}}{2k_x\tau} = \frac{\Delta\phi^{(2)} - \Delta\phi^{(3)}}{2k_0\tan\theta\tau} \tag{2.31}$$

where θ is the angle between the illuminating beam and scattering vectors of the subapertures.

2.3.2 OCT angiography (OCTA)

OCT Angiography (OCTA) utilizes the temporal motion contrast to separate the blood flow from the static surroundings. Since the scatter distribution keeps changing, the speckle signal of the blood flow varies rapidly; in contrast, the speckle signal of the static tissues should be constant without bulk motions. As shown in Figure 2.8, a simple but effective method to extract the motion contrast is calculating the accumulated signal difference:

$$\mathrm{OCTA}(x,y,z)=\sum_{i=1}^{n-1}\left|I(x^{(i+1)},y,z)-I(x^{(i)},y,z)\right| \tag{2.32}$$

where $x^{(i)}$ denotes the ith repeated scan at position x.

Both DOCT and OCTA require acquisition of repeated A-scans or B-scans, however the scan time intervals are different. In DOCT, the two successive signals should be well correlated; otherwise, the phase information may correspond to totally different scatters and the phase difference is meaningless. For OCTA, the flow signals between two scans should be well decorrelated such that the signal difference is large enough to separate the vessels from the static tissues. Therefore, in point-scan OCT, DOCT utilizes repeated A-scans and OCTA adopts repeated B-scans protocols.

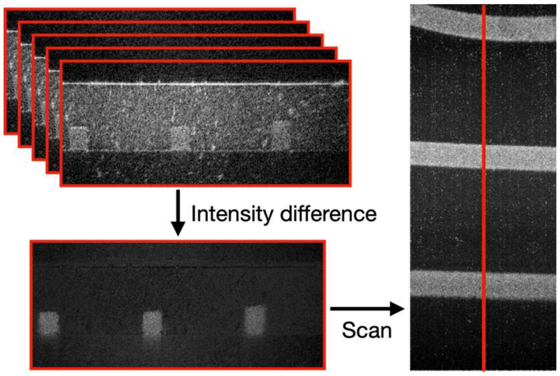

Figure 2.8 Schematic of OCT angiography (OCTA).

2.3.3 Dynamic light scattering (DLS) OCT

As discussed above, with the single-beam point-scan configuration, DOCT can only determine the axial velocity, and OCTA could distinguish the blood vessel and static tissue based on the motion contrast but provides little speed information. Dynamic light scattering (DLS) OCT is a less mature technique, which promises to fill-in the gap. DLS-OCT is based on analyzing the first-order temporal autocorrelation function of the complex OCT signals:

$$g_1(\tau) = \langle I(t+\tau)I(t)^* \rangle_t \tag{2.33}$$

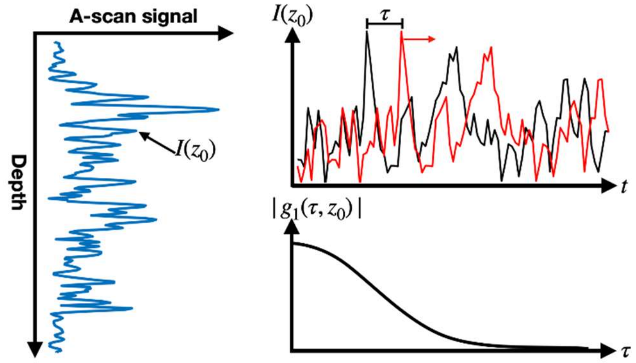

Figure 2.9 Schematic of dynamic light scattering (DLS) OCT.

Assuming the scatters are uniformly distributed, in the point-scattering and first Born approximation regime, $g_1(\tau)$ can be expressed as [64]:

$$g_1(\tau) = e^{iqv_z\tau} e^{-q^2 D\tau} e^{-(h_t^2 v_t^2 + h_z^2 v_z^2)\tau^2} \tag{2.34}$$

where $q = 2k_0$ is the change of the wave vector due to scattering, $h_{t,z}$ are the inverse of the $1/e$ radius of the transverse diffraction beam waist and axial coherence gate, and D is the diffusion coefficient. By analyzing the temporal autocorrelation's phase and magnitude change, the axial and transverse velocities can be extracted simultaneously using a simple single-beam point-scan setup.

The time resolution of DLS-OCT is about 10-20 μs. The time delay between adjacent B-scans of the point-scan OCT is typically about several milliseconds, which cannot capture the autocorrelation decay of the OCT signal. The time resolution of an LS SD-OCT system is in the range of 70-400 μs, which is in between the two time scales mentioned above. Therefore, we propose to detect the flow velocity using the temporal autocorrelation function of the repeated B-scans of the LS SD-OCT system.

Chapter 3

Broadband Line-scan (LS) Spectral-domain (SD) OCT System

3.1 Introduction

Fourier-domain OCT (FD-OCT) has been one of the most popular optical imaging techniques in ophthalmology since its development in 2002 [28,29,65–69]. It offers *in-vivo*, non-contact, volumetric imaging approach with high spatial resolution and acquisition speed. Currently, there is a growing interest in development of ultrahigh resolution, ultrahigh speed OCT technology for *in-vivo* cellular resolution imaging of the human anterior and posterior eye [17,21,25,34,44,45,54,70–75]. The combination of high spatial resolution and high acquisition rate in OCT is essential for successful imaging of the 3D cellular structure of different ocular tissues such as the retina, cornea, and limbus. The OCT's lateral resolution, like in most optical imaging techniques, is inversely proportional to the NA of the imaging optics, therefore it can be improved by increasing the effective NA. However, the OCT axial resolution is independent on the imaging optics and is primarily determined by the coherence length of light source, and therefore can be increased by using a broad bandwidth light source. OCT axial resolution of ~1 μm in biological tissues has been demonstrated with different designs of the OCT technology such as TD-OCT and SD-OCT [18,57,76–80]. In all of these cases, the OCT image acquisition rate was rather low, determined by the limited speed of the camera and scanning technologies, and was insufficient for suppressing involuntary eye motion artefacts and related image blur. The axial resolution of SS-OCT is typically limited to > 5 μm because of the limited spectral range of the tunable lasers. For the research presented in this thesis, broadband light sources such as a femtolaser and a supercontinuum laser were used in the proposed LS SD-OCT to achieve an axial resolution < 2.5 μm in free space. In some studies where priority is placed only on high resolution enface images, low axial OCT resolution is not an issue; however, it obscures morphological details in the axial direction of 3D images. For example, Auksorius et al. demonstrated enface images of human cornea epithelial cells with FF SS-OCT [25], however, the crosssectional images were blurred because of the low axial resolution.

A high OCT image acquisition rate is vital to suppress eye motion artefacts as well as motion related blur in the images. Although both head and eye motion can be reduced with the use of a head support frame, a bite bar, and a fixation target, involuntary eye motion cannot be fully suppressed. For example, saccades usually happen with a frequency of 1 to 2 Hz [81,82], which requires that a full volumetric

OCT data set is acquired in less than 0.5 seconds. Point-scan OCT can reach this volumetric rate by severely reducing the lateral FOV under study. By far the fastest commercially available spectrometer for SD-OCT records A-scans at a rate of 250 kHz. A small FOV of 310×310 (A-scan×B-scan) is needed to achieve a 2 Hz volumetric image acquisition rate, assuming a 0.8 scanning duty cycle. Otherwise, the enface images are distorted [17], and require complicated post-registration. SS-OCT can reach a A-scan rate of ~10 MHz, however, the image's SNR is reduced with increasing the imaging speed, while the unstable intensity and phase instability cause blur in the OCT images and add extra challenges in further studies. Parallelizing multiple detectors increases the effective acquisition rate of a point-scan OCT [75], however this comes at the expense of a more complex, expensive and difficult to operate system design.

Alternatively, the volumetric imaging rate can be boosted by developing OCT designs that are based on parallel signal acquisition modalities. While LS SD-OCT and FF SS-OCT were first described in 1999 and 2006, respectively[52,53]; however, their superiority in 3D imaging speed has been well acknowledged until recently with the development of fast 2D complementary metal-oxide-semiconductor (CMOS) cameras. Depending on the camera type used, the B-scan rate of an LS SD-OCT system can vary from 2 kHz to 16 kHz [34,45]. Since the camera read-out rate is dependent on the number of read-out pixels, while the number of illuminated pixels in the spectral direction is related to the axial resolution and the depth scanning range of the SD-OCT system, there is a trade-off between the axial resolution and image acquisition rate that needs to be considered when a LS-SD-OCT is designed. In the case of FF SS-OCT, the volumetric image acquisition rates that have been reported recently range from 0.1 kHz to 1 kHz [25,44,83]. The acquisition rate difference of each modality depends on the imaging FOV, spectral range, and camera's full detection speed. A major advantage of the fast volumetric imaging speed is that the lateral phase stability of the OCT signal is well maintained. This allows for successful correction of defocus and higher-order monochromatic aberrations in the LS SD-OCT/FF SS-OCT images by use of digital adaptive optics (DAO) and extension of the diffraction-limited lateral resolution to a large imaging depth of the system [25,42–45]. However, it should be noted that the higher image acquisition rate will result in lower SNR for the same illumination power, therefore requiring averaging of multiple repeated images to boost the image SNR [44].

This chapter includes a detailed description of a novel broadband LS SD-OCT system that combines an isotropic spatial resolution of $2.2\times2.3\times2.4$ μm (x×y×z) in free space and rapid image acquisition rate ≥ 2.5 kHz. From now on, I will use micrometer level resolution to refer to the spatial resolution under 2.5 μm in free space. Here I discuss in detail the design and characterization of the system, including the component choice, Zemax evaluation of the illumination and detection arms, spectrometer calibrations in wavenumber and wavelength domain, characterization of the key parameters, dispersion compensation, axial phase correction, and signal reduction due to fringe washout and decorrelation.

3.2 Design of the broadband LS SD-OCT system

The schematic of the broadband LS SD-OCT is shown in Figure 3.1. A cartesian coordinate (x, y, z) is used to describe the imaging system; x-direction refers to the beam scanning direction, y-direction is along the line illumination direction, and z-direction denotes the beam propagating direction. The system is powered by a femtosecond laser (Integral, Femtolasers GmbH) with a 790 nm center wavelength and 140 nm spectral bandwidth measured at 3 dB. A 100-meter long fiber is used to stretch the femtosecond pulses and simulate CW emission. The light is first collimated by an achromatic doublets L1 (AC127-019-B, Thorlabs), and the $1/e^2$ beam diameter of the output beam is 3.21 mm. A telecentric pair of lenses L2 (AC254-060-B, Thorlabs) and L3 (AC254-100-B, Thorlabs) form a beam expander with magnification ratio of 1.67. The beam's circular symmetry breaks after passing through an achromatic cylindrical lens CL1 (ACY254-100-B, Thorlabs). A 50:50 non-polarizing beam splitter (BS014, Thorlabs) serves as the OCT interferometer core, and it divides the optical beam into the sample and reference arms of the system.

In the sample arm, the beam is focused in yz-plane at the center of a 1-D galvanometer scanner (GVS011, Thorlabs), whose axis is along the y-direction. A telecentric pair, L4 and L5 (AC254-075-B, Thorlabs), placed after the scanner, is used to relay the beam to the entrance of a microscope objective (M Plan Apo NIR 10×, Mitutoyo). The incident power on the sample surface is 2.6 mW. The optical beam is reshaped to a circular collimated beam in the reference arm by a second cylindrical lens CL2 (ACY254-100-B, Thorlabs) and then focused onto a mirror with lens L6 (AC254-060-B, Thorlabs). A neutral density filter (NDF) controls the optical power, a pair of BK7 prisms is used for hardware dispersion compensation (HDC), and two translational stages are used to control the optical path delay and tune the reference spectrum.

Light scattered from the sample and reflected from the reference mirror meets at the beam splitter and is projected onto the custom spectrometer through a telecentric pair of lenses L7 (AC254-150-B, Thorlabs) and L8 (AC254-100-B, Thorlabs). The choice of the focal lengths, f_7 and f_8, reflects a trade-off between the is a compromising of the spectral resolution and the y-direction's sample to camera magnification: the former is proportional to the ratio f_8/f_7, while the latter is inversely proportional to it. An adjustable slit (VA100C, Thorlabs) is placed in between L7 and L8 to block stray light. The spectrometer is comprised of a volume phase holographic grating (960 l/mm @ 840nm, Wasatch Photonics), a camera lens (Planar T* 1.4/85, Zeiss), and a 2D CMOS camera (Dimax S4, PCO). The spectrum is dispersed in the spectral (horizontal) direction of the camera, and the spatial information of the sample along the y-direction is projected in the spatial (vertical) direction of the camera with a magnification of 6.38. While the full size of the CMOS sensor is 2016×2016 pixels with a pixel size of 11×11 μm^2; with the current design of the LS SD-OCT system, the projected optical beam covers a smaller area of 1920×800 (spectral$\times$spatial) pixels. This area corresponds to a maximum camera read-out rate of 2.5 kHz. While the frame rate can be increased by reducing the detection area of the camera, significantly reducing the pixel number along the spectral direction below 1920 is not practical in our case, as it will shorten the LS-SD-OCT's depth scanning range and lower the axial OCT resolution. The acquisition trigger and scanning waveform are generated and synchronized through a data acquisition (DAQ) card (PCIe-6321, NI). A custom Labview program is used to control the B-scan live display, the 3D image acquisition, and data saving.

The chosen doublets (L1-L8, CL1, CL2) and beam splitter (BS) are antireflection coated for the NIR spectral range (650 nm to 1050 nm) and $\phi1''$-sized except for the collimator. The camera lens (L9) is NIR coated as well, and the microscope objective (MO) is designed for use in the spectral range 400 nm to 1800 nm. All the mirrors (M1-M3) and the galvanometer scanner are silver protected.

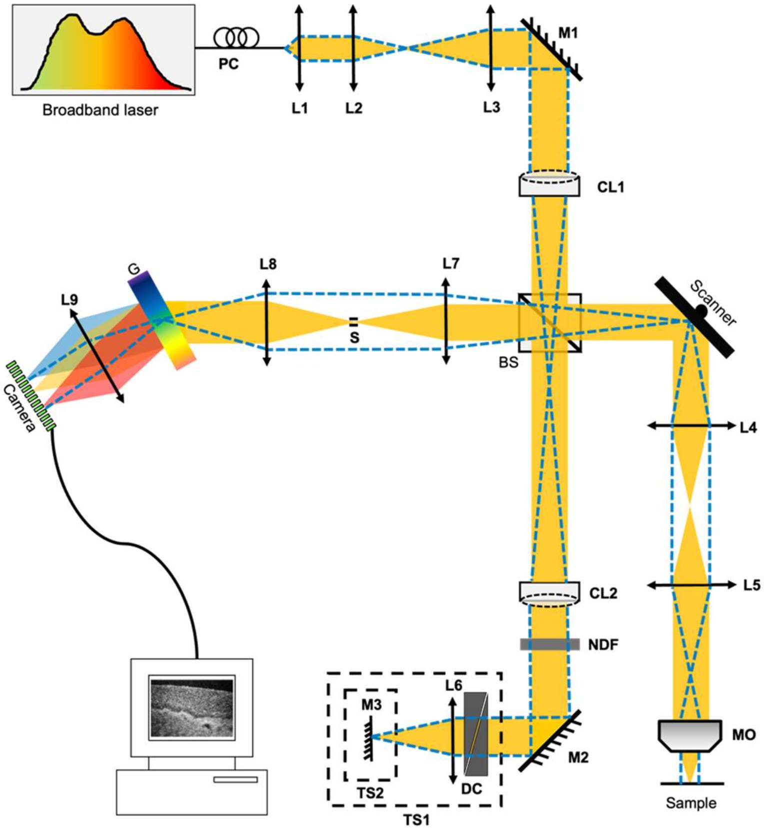

Figure 3.1 Schematic of the line-scan (LS) spectral-domain (SD) OCT system. Horizontal and vertical orientations of the optical beam are represented by the solid yellow color and the blue dashed line, respectively. BS, non-polarizing beam splitter; CL, cylindrical lens; G, transmission grating; DC, dispersion compensator; L, lens; M, mirror; MO, microscope objective; NDF, neutral density filter; PC, polarization controller; TS, translational stage.

3.2.1 Illumination arm

The illumination arm is defined as the optics from the fiber output to the sample plane. The scanner and the objective are the two components that constrain the beam size: the maximum beam diameter allowed by the scanner is 10 mm, and the back aperture of the objective is not less than 10.64 mm. The former limit is provided by the manufacturer, and the latter is determined with the objective's focal length and NA. The beam diameter ($1/e^2$) after L3 is 5.35 mm, and the 1/1000 beam diameter is 9.95 mm, thus there is no waste of the laser power in terms of optics size. The illumination arm is modeled in Zemax to evaluate the lateral scanning performance, and the ray tracing and spot diagrams are shown in Figure 3.2. Since the design specifications of the microscope objective are not available, in the Zemax model the objective was replaced by a paraxial lens with an 11 mm aperture and a 20 mm focal length, which are very close to the entrance aperture and effective focal length of the microscope objective. A 0.5° mechanical scan angle results in 0.35 mm lateral shift in the x-direction, which is the upper limit that the laser beam is not cut off by the objective's entrance aperture. Note that the 1/1000 beam diameter was used for this calculation. Since the scanning angle is small, it is safe to assume the lateral scanning position is proportional to the scanner voltage, and no additional calibration is needed. As shown in Figure 3.2 (A), the radial defocus suggests the field curvature is not negligible in the x-direction. The axial focus shift is about 15 μm at the edge of the lateral scan (0.5°), however, not evident at -0.25°. Axial chromatic aberration of the illumination arm is illustrated in Figure 3.2 (B). The spot diagrams in Figure 3.2 (C) and (D) further confirm the field curvature in both x- and y-directions and the axial chromatic aberration in the z-direction.

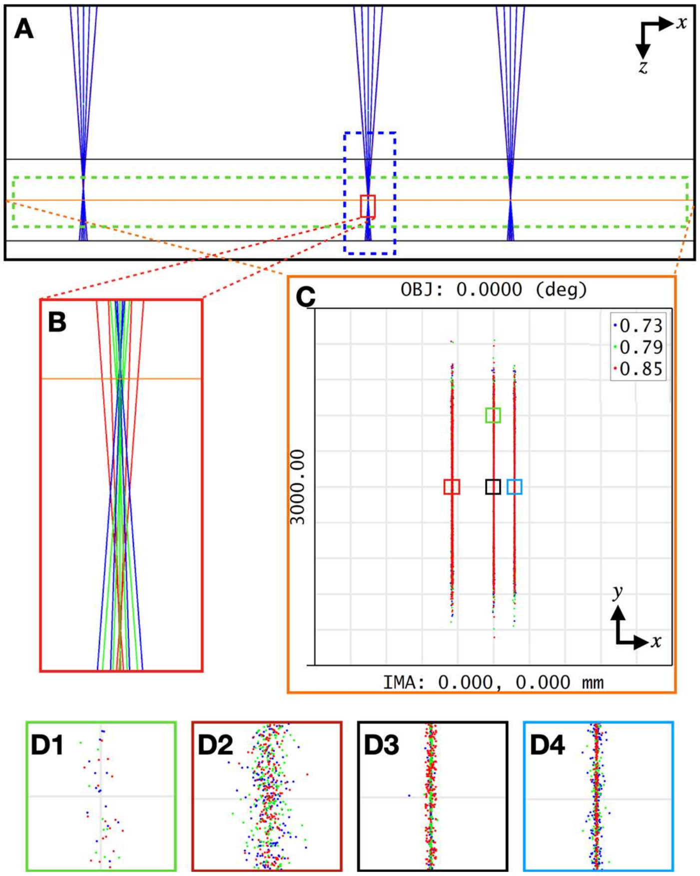

Figure 3.2 Ray tracing and spot diagram of the lateral scan of the illumination arm in Zemax. (A) Ray tracing with the mechanical scan angle of 0.5° (left), 0° (middle), and -0.25° (right), in the xz-plane. The focal plane is shown in orange, and the two black lines stand for the out of focus planes at $\pm 50\mu$m. (B) Zoomed ray tracing

near the focal plane. Three wavelengths 730 nm, 790 nm, and 850 nm, are shown in blue, green, and red. (C) Spot diagrams of the three scan angle on the focal plane. (D) Enlarged spot diagrams of the ROIs labeled in (C).

At the focal plane, the theoretical spot diameter ($1/e^2$) of the illumination beam along the x-direction, following Equation (2.10), is 1.88 μm for the wavelength 790 nm, the beam diameter ($1/e^2$) in the y-direction is 1.071 mm, and the Rayleigh length is 14.2 μm in the xz-plane. These results are confirmed with the physical optics propagation (POP) simulation in Zemax, as shown in Figure 3.3 (A, B). It should be noted that the collimated beam diameters of different wavelengths after L1 are assumed to be a constant in the simulation, whereas in practice they should be slightly different since the Gaussian mode diameter of the single-mode fiber is wavelength dependent. The broadened beam sizes in the x-direction at depth z=$\pm$50 μm, shown in Figure 3.3 (C), are expected because of defocusing, and it can be fully corrected with digital refocusing assuming the reference conjugate focal plane coincides with the illumination focal plane. However, the field curvature illustrated in Figure 3.3 (D) is not desired since the radical defocus results in phase destruction because of the virtual interference pinhole effect (see Chapter 5), unless the field curvature of the illumination and detection optics are perfectly matched. The size difference of irradiance distribution along y-direction is not significant across the imaging volume. It is worth pointing out that the system's lateral resolution δx cannot be determined by the illumination beam waist alone. The detection arm’s coherence point spread function (cPSF) and the interference between the sample and reference signals must be considered.

Since the beam’s power distribution is Gaussian in our system, we will describe the beam radius and diameter in the $1/e^2$ convention in the following materials unless further notice.

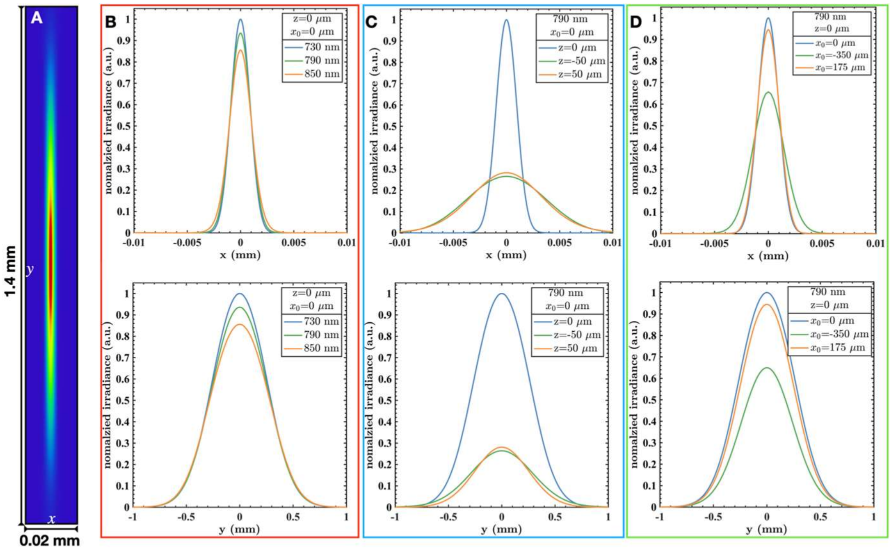

Figure 3.3 Gaussian line illumination simulation with physical optics propagation (POP) in Zemax. (A) 2D relative irradiance distribution of the central wavelength 790 nm at the focal plane with 0° scan angle. (B) Crosslines along x- and y-directions of the 2D irradiance distributions of wavelength 730 nm, 790 nm, and 850nm, at the focal plane with 0° scan angle. (C) Crosslines along x- and y-directions of the 2D irradiance of wavelength 790 nm at different depths with 0° scan angle. (D) Crosslines along x- and y-directions of the 2D irradiance of wavelength 790 nm at the focal plane with different scan angles.

3.2.2 Detection arm

The detection arm is defined as the optics from the sample plane to the camera, in which the most vital component is the spectrometer. The customized spectrometer is comprised of a transmission diffraction grating, a camera lens, and a 2D CMOS camera. The spectrum is recorded in the horizontal direction of the camera, and the spatial information along the y-direction is projected over the vertical direction. The grating groove density (G = 960 l/mm) and the focal length of the camera lens (f = 85 mm) are chosen to cover the spectrum of the femtolaser, which is centered at 790 nm with a span of 230 nm. Figure 3.4 shows a typical transmission grating based spectrometer geometry; the incidence and diffraction angles, α and β, of the central wavelength are usually set to be equal. Thus, α and β can be estimated following the grating equation:

$$d(\sin\alpha + \sin\beta) = m\lambda_c \qquad (3.1)$$

where $d = 1/G$ is the spatial period of the grating, λ_c is the central wavelength, and m is the diffraction order. In our setup, λ_c and m are set as 790 nm and 1, respectively. Substitute $\alpha = \beta$, we can get $\alpha =$

$\beta = 22.3^{\circ}$. The wavelength λ_n of the light that reaches the nth (n=0 at the middle of the camera) pixel follows the equation:

$$\sin\alpha + \sin\left(\beta + \arctan(na/f)\right) = \lambda_n / d \qquad (3.2)$$

where a is the pixel size (11 μm in our system) and f is the focal length of the camera lens. The minimum and maximum wavelength can be estimated by substituting n=±960, resulting a detectable spectrum range of (668nm, 906 nm).

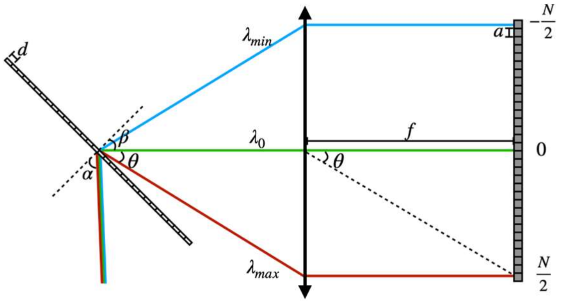

Figure 3.4 Geometrical optics diagram of the transmission grating based spectrometer. α and β are the incidence and diffraction angles of the central wavelength λ_0, θ is the deviation of the diffraction angle of an arbitrary wavelength from that of λ_0. d is the spacing period of the grating, a is the size of the camera pixel, and f is the focal length of the camera lens. The central wavelength λ_0 is assumed to be projected on the center of the camera, and the range of the detectable spectrum is limited by the camera's size.

Figure 3.5 shows a 3D rendering of the reference arm in Zemax. Since manufacturer's design data about the microscope objective and the camera lens are not available, these optical components were replaced by two paraxial lenses in the Zemax design of the LS SD-OCT system. The beam splitter and the cover glass of the transmission grating are neglected since they are passed by a parallel beam thus the parfocal point does not change. The ray tracing starts from the location $(0, y_0)$ of the sample plane, which corresponds to the 0° scan angle in Figure 3.2. Three wavelengths, 730 nm, 790 nm, and 850nm, are dispersed by the grating and reach different horizontal locations of the camera, as illustrated in the zoomed insert in Figure 3.5 (A). Since the camera lens is placed one focal length away from the transmission grating, the beams of different wavelengths are all perpendicular to the camera plane. The full aperture size of the camera lens is 60.7 mm, which is much wider than the dispersed beam size; thus, there is no cut off of the optical beam at the camera lens. The distance between the grating and camera lens is optimized in terms of the 9 (3×3) spot sizes along the spectral direction. The defocus in the y-direction, as shown in Figure 3.5 (C), is acceptable as it can be digitally corrected with DAO.

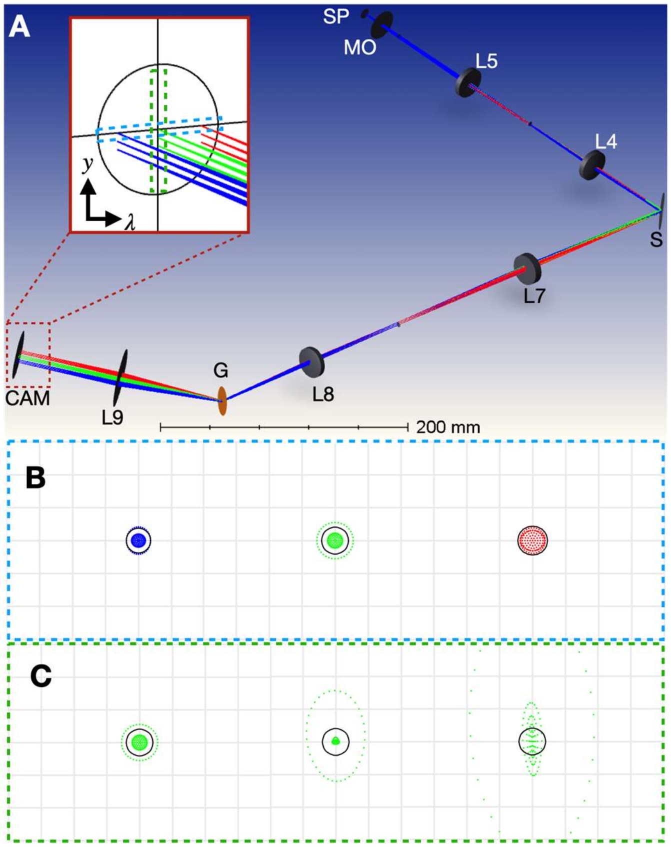

Figure 3.5 Ray tracing and the spot diagrams of the detection arm in Zemax. (A) The 3D layout of the optics. The rays' origins (x_0, y_0) on the sample plane are set as (0, 0) μm, (0, 200) μm, and (0, 400) μm. Three wavelengths, 730 nm, 790 nm, and 850nm, are labeled in blue, green, and red, respectively. Insert: zoomed ray tracing near the camera. (B) Spot diagrams of the 3 wavelengths from the origin (0, 0) μm. (C) Spot diagrams of 790 nm from different origins on the sample plane. The black circles represent airy disks. Grid size: 20×20 μm. SP, sample plane; MO, microscope objective; L, lens; S, scanner; G, transmission diffraction grating; CAM, camera.

The spectral resolution and the beam radius in the spectral direction are estimated according to the Huygens PSFs simulated in Zemax. As shown in Figure 3.6, the spatial separation between the PSFs of the two wavelengths with a 0.2 nm gap is large enough to distinguish the two spots for all 9 configurations. Thus, we can safely claim the spectral resolution is around 0.2 nm in our customized spectrometer. The beam radius along the spectral direction at the y-direction edge (y_0 = 400 μm) is broader than that at the middle (y_0 = 0) and would result in a more rapid SNR rolloff. Nevertheless, the SNR rolloff should be reasonably constant over a relatively large FOV (-200, 200) μm in the y-direction. For an ideal design, the beam size (FWMH) is expected to be below 1/2 of the pixel size.

However, in our design, the beam size (FWMH) of 790 nm is about 10.5 μm in the spectral direction, and the beam spot can be just covered by a single pixel. Thus, the SNR rolloff is dominated by the diffraction limit of the optics instead of the pixel size, as can be seen in Chapter 3.5. In theory, the spectral resolution can be improved by enlarging the beam diameter before entering the transmission grating. This can be achieved by simply increasing the ratio f_8/f_7;however, this would result in a reduced sample to camera magnification ratio along the y-direction.

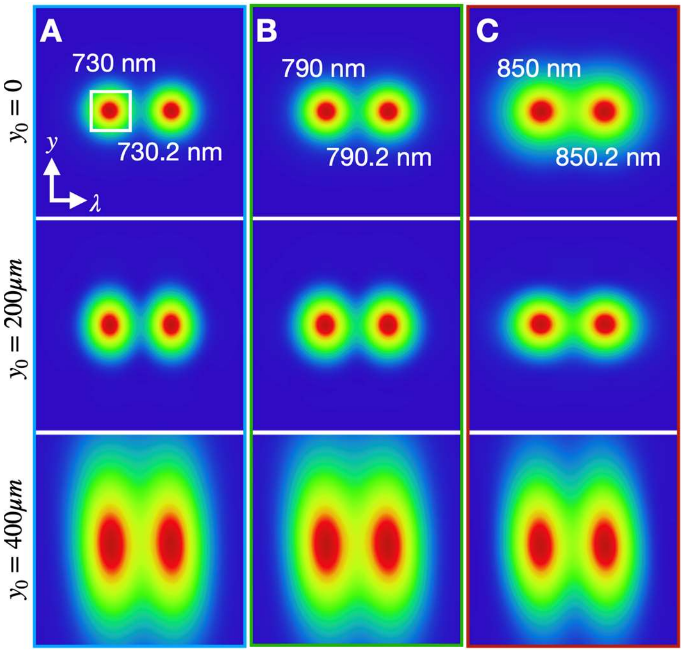

Figure 3.6 Huygens PSFs of adjacent wavelengths with a spacing of 0.2 nm from different sample plane origins at (A) 730 nm, (B) 790 nm, and (C) 850 nm. From left to right, the distances of the two peaks are 17.2 μm, 17.6 μm, and 18.2 μm, and the beam radiuses along the spectral direction are 8.2 μm, 8.9 μm, and 11.9 μm ($y_0 = 0$). The white box in (A) represents the size of a single camera pixel (11×11 μm).

3.3 Spectrometer calibration

3.3.1 Linear-k interpolation

In practice, FD-OCT uses FFT to determine the scattering distribution $I(z)$ from the interference fringe $I(k)$. Since the camera pixel number p is not linear to the wavenumber k, the curve $k(p)$ needs to be determined for linear-k interpolation before FFT. The calibration is based on the phase of interference fringe [84]. A thin coverslip is positioned at the focal plane of the sample arm. The reference arm is blocked such that no reference signal arrives at the camera, and the laser power is reduced to avoid saturation. The interference fringe $I(p, y)$ of the two air-glass interfaces at $y_0 = 0$ is used for calibration, and it can be expressed in the wavenumber space as:

$$\begin{aligned} I(k) &= I_1 + I_2 + 2\sqrt{I_1 I_2}\cos\left([2k(z+\Delta z)+\phi_{sys}]-[2k(z)+\phi_{sys}]\right) \\ &= I_1 + I_2 + 2\sqrt{I_1 I_2}\cos(\phi(k)) \end{aligned} \tag{3.3}$$

where Δz is the optical path delay of the coverslip and $\phi(k) = 2k\Delta z$ is the phase difference between the two interfaces. Since there is only a constant depth signal, the fringe $I(k)$ should have only a single frequency.

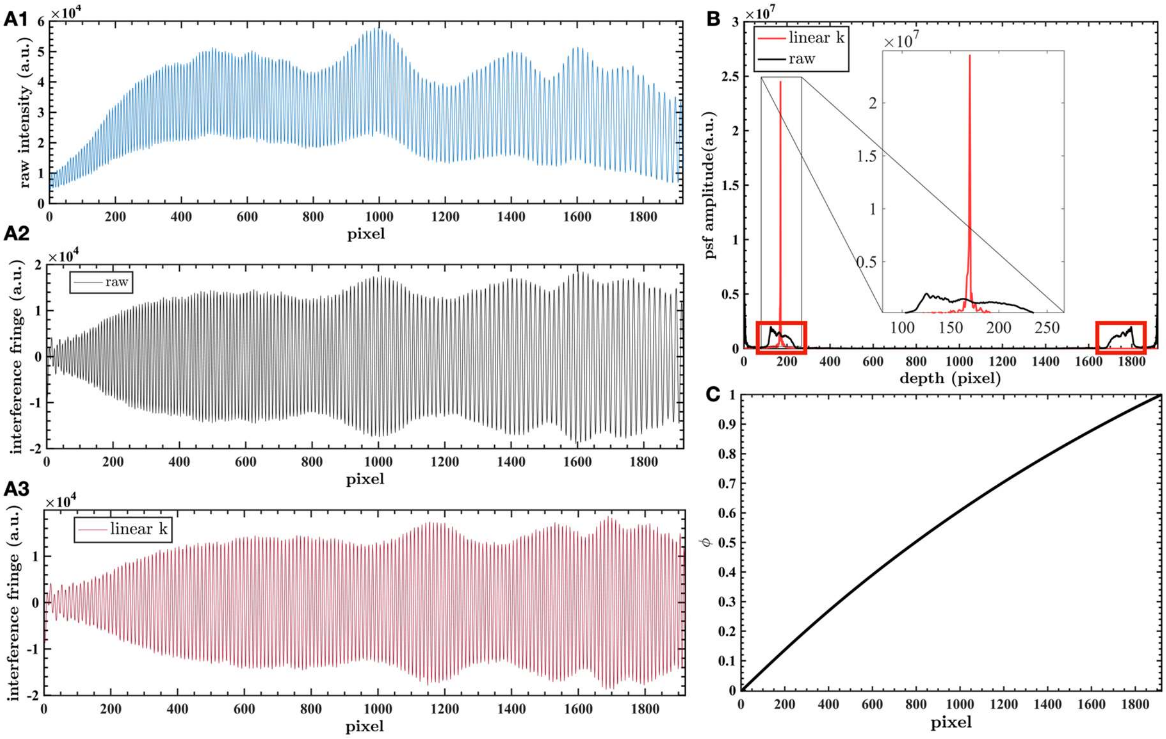

Figure 3.7 Spectrometer calibration in wavenumber space. (A) Original (top), background-subtracted (middle), and linear-k interpolated (bottom) interference fringes of a coverslip. (B) Original (black) and calibrated (red) axial PSFs determined with the fringes in (A1) and (A3), respectively. (C) Fitted $\phi(p)$ curve, which is used for linear-k interpolation.

However, as can be seen in Figure 3.7 (A), the nonlinear relationship of p and k leads to chirping of $I(p)$. Thus, directly apply the FFT to $I(p)$ results in a broadened axial PSF, as shown in Figure 3.7 (B, black line). The constant component $(I_1 + I_2)$ in $I(p)$ is filtered out by inversely FFT of the band-filtered PSF (Figure 3.7 (B, red boxes)), and the phase information $\phi(p)$ is retrieved with Hilbert transform. The phase curve is then normalized and fitted to a polynomial function up to 4th order, as shown in Figure 3.7 (C). Since ϕ is linear to k, the fitted $\phi(p)$ can be used as a lookup table to perform the linear-k interpolation. The redistributed fringe and the corresponding axial PSF are shown in Figure 3.7 (A3) and (B, red line), respectively.

It should be noted that we have used a broader light source (NKT+Superlum) to determine the lookup table. This is because the spectrum of the femtolaser is vanishing at the two edges, which can result in significant uncertainties when determining the phase near the upper and lower spectrum limit.

3.3.2 Spectrum calibration

The $\phi(p)$ curve calculated above cannot be directly used to determine the laser spectrum since $k(p)$ is only linear to, but not the same as $\phi(p)$:

$$k(p) = a\phi(p) + b \tag{3.4}$$

where a and b are the slope and offset that need to be determined. Seven narrowband filters (centered at 720nm, 760nm, 780nm, 800nm, 820 nm, 840 nm, and 860nm, respectively) were inserted after the collimator and their corresponding reference spectrums $I_i(p, y)$ were collected separately. The reference spectrums are averaged over 10 spatial pixels around the center of y-dimension and then redistributed with linear-k interpolation, as shown in Figure 3.8 (A). The normalized $\tilde{I}_i(\phi)$ is then used to calculate the weighted centers, ϕ_i, of each narrow spectrum. Since $1/\lambda$ is linear to ϕ, seven data points, $(\phi_i, 1/\lambda_i)$, are linearly fitted, and the spectrum can be calibrated with:

$$\lambda(\phi) = \frac{1}{a'\phi + b'} \tag{3.5}$$

where a' and b' are the fitted slope and offset. The entire reference spectrum is recorded and linear-k interpolated, and the calibrated spectrum is shown in Figure 3.8 (B). The laser spectrum detected by the camera has a weighted central wavelength of 783 nm with a bandwidth (FWMH) of 129 nm. The original bandwidth of the femtolaser is about 140 nm; however, it is reduced because of the nonlinear absorption of the 100-meter long fiber, as well as the nonlinear quantum efficiency and diffraction efficiency of the detector and the grating, respectively.

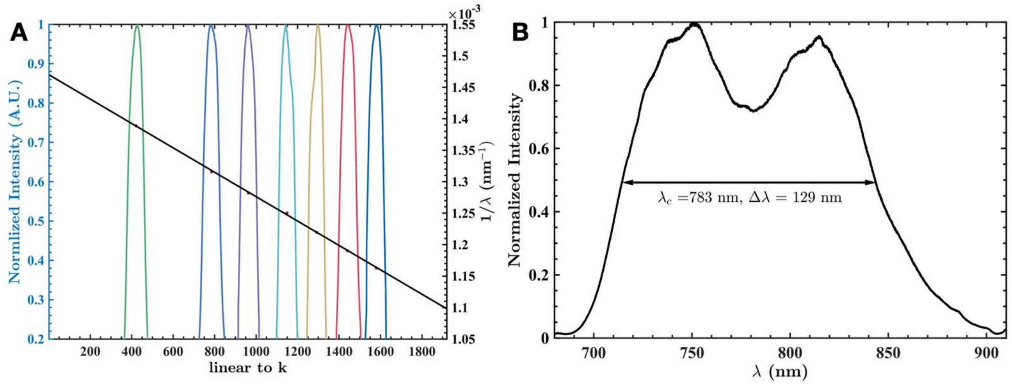

Figure 3.8 Spectrum calibration in wavelength space. (A) Normalized and linear-k interpolated spectrums of narrowband filters with central wavelengths of 720 nm, 760 nm, 780 nm, 800 nm, 820 nm, 840 nm, and 860 nm, respectively. The weighted center of each narrowband, ϕ_i, is used for the linear fitting. (B) Calibrated reference spectrum.

A comparison between the calibrated wavelengths and the central wavelengths of the narrowband filters is shown in Table 3.1. As can be seen, the central wavelengths and calibrated wavelengths are well correlated, and all the differences are within the uncertainty ranges. However, it is still hard to determine the accuracy of this calibration method. The largest uncertainty comes from the estimation of the narrowband's center since the location and shape of the narrowband spectrum are highly dependent on the orientation of the filter. In addition, the center of the narrowband might be slightly shifted from its design wavelength. Moreover, as the spectrum calibration needs linear-k interpolation, it cannot be more accurate than linear-k interpolation itself. Nevertheless, the spectrum calibration is still very meaningful. For example, the lower and upper limits of the spectrum range are determined as 680 nm and 911 nm, respectively. Thus, the digital axial resolution is estimated as 1.34 μm according to Equation (2.16), and the depth scanning range is 1.29 mm.

Table 3.1 Comparison of preset and calibrated wavelengths.

experiment(nm)	720	760	780	800	820	840	860	min	max
estimation(nm)	720.2 ±1.3	759.8 ±1.4	779.2 ±1.5	801.6 ±1.6	819.9 ±1.7	839.7 ±1.8	859.3 ±1.8	680.4 ±1.2	910.8 ±2.1

3.4 Dispersion compensation

Apart from the $k(p)$ nonlinearity, chromatic dispersion in the medium is another source that broadens the axial PSF and must be compensated for in optical design and post-processing. A BK7 prism pair is usually placed in the reference arm. The dispersion can be reduced by adjusting the thickness of the prism pair. Here, I focus on describing how the dispersion is compensated in post-processing. In a single medium, the accumulated phase of a monochromatic light scattered at the depth z is $\phi(k, z) = 2n(k)kz$, where k is the wavenumber of the light in vacuum, and $n(k)$ is the wavenumber-dependent refractive index in the medium. Alternatively, it can be expressed as $\phi(k, z) = 2\beta(k)z$, where $\beta(k) = n(k)k$ is the propagation constant and sometimes is called dispersion constant [85]. For a low coherence light, the propagation constant can be expressed in the Taylor series [86]:

$$\begin{aligned}\beta(k) &= \beta(k_0) + [n(k_0) + n^{(1)}(k_0)k_0](k-k_0) + \frac{1}{2}\frac{d}{dk}[n(k) + n^{(1)}(k)k]|_{k=k_0}\ (k-k_0)^2 + \ldots \\ &= \beta(k_0) + \sum_{m=1}^{\infty}\frac{n_g^{(m-1)}(k_0)}{m!}(k-k_0)^m \\ &= \sum_{m=0}^{\infty} b_m(k_0)(k-k_0)^m\end{aligned} \tag{3.6}$$

where k_0 is an arbitrary wavenumber (usually set as the central wavenumber), $n_g(k) = n(k) + kn^{(1)}(k)$ is the group refractive index and (m) in the superscript denotes the mth order of derivative. The 1st term (m=0) and the 2nd term (m=1) of the propagation constant lead to a constant phase and the group delay of the OCT signal, respectively; the higher orders (m>1) result in broadening of the axial PSF.

Considering multiple mediums scenario, the phase of the sample and reference signal can be written as:

$$\begin{aligned}\phi_s(k) &= \sum_{i=1} 2\beta_i^s(k)z_i^s \\ \phi_r(k) &= \sum_{i=j} 2\beta_j^r(k)z_j^r\end{aligned} \tag{3.7}$$

where $\beta_{i,j}^{s,r}(k)$ is the medium-specific propagation constant of the sample and reference arms and $z_{i,j}^{s,r}$ is the corresponding length of the medium. The phase difference between the two arms is:

$$\begin{aligned}\phi(k) &= \phi_s(k) - \phi_r(k) \\ &= 2\sum_{p=0}^{\infty}(k-k_0)^p[\sum_i b_p^s(k_0)z_i^s - \sum_j b_p^r(k_0)z_i^r)] \\ &= 2\sum_{p=0}^{\infty} a_p(k-k_0)^p\end{aligned} \tag{3.8}$$

To cancel the influence of the higher order dispersion terms, a phase mask $\tilde{\phi}(k) = \sum_{n=2}^{N} a_n\,(k-k_0)^n$ is applied to the complex OCT fringes after the Hilbert transform, where a_n is the dispersion coefficient of order n. Typically, up to 3rd order dispersion compensation is good enough to correct the axial PSF if the hardware dispersion compensation has been performed properly and the residual dispersion mismatch is not significant. However, it is important to note that a_p is, in general, location dependent. It does not only relate to the location under study, but also depends on the trajectory the light travels. Thus, the compensation phase mask can only correct a user-selected ROI well, and its performance in other regions might not be as well as in the selected ROI.

The dispersion coefficients $\{a_n\}$ can be manually tuned until the OCT image is sharpest. However, it is highly person-dependent as the 'sharpest' image is subjective, especially when the image local contrast is low. In principle, the dispersion coefficients can be estimated with the local derivative of $\phi(k)$ [56]. In the proposed method, the entire spectrum is split into sub-bands with user-selected windows before FFT, and each sub-band is centered at k_i ($i = 1,2,\ldots,N$). Assuming the higher order dispersions within each sub-band are negligible, the phase difference of each sub-band can be written as:

$$\phi_i(k) = 2z[\beta(k_i) + \beta^{(1)}(k_i)(k-k_i) + \mathcal{O}((k-k_i)^2)] \tag{3.9}$$

The wavenumber dependent $\beta^{(1)}(k_i)$ results in an axial shift of each sub-band OCT image after FFT. The relative shifts can be determined with the correlation of the sub-band images and then are used to estimate the compensation phase mask. This method is similar to the noniterative sub-aperture DAO algorithm[43], although the physics behind is very different.

Alternatively, the dispersion coefficients can be estimated iteratively by optimizing an image metric function relating to the image sharpness [67,87], and we adopt this method in digital dispersion compensation. The image metric is defined as:

$$S(a_2, a_3) = \sum_{(y,z)\in D} \tilde{I}(y, z; a_2, a_3)^{1.1} \tag{3.10}$$

where $\tilde{I}(y, z; a_2, a_3) = |I(y, z; a_2, a_3)|^2 / \Sigma_{(y,z)\in D} |I(y, z; a_2, a_3)|^2$ is the normalized OCT intensity after applying a phase mask controlled by (a_2, a_3), and D is a user-selected ROI. Many different optimizing algorithms can be used to find the global minimum of $S(a_2, a_3)$. Three popular categories are the gradient-based method, swarm-intelligence method, and simulated annealing (SA) method. As the first two approaches will be introduced in Chapter 5, we use a SA algorithm to determine the dispersion coefficients. In short, the SA algorithm generates a new solution using a random guess. A good trial is 100% accepted, and a bad trial is accepted with a possibility controlled by the metric difference and a scheduled cooling parameter. The acceptance of worse results prevents SA from getting trapped in local minima, thus it can reach the global minimum with a slow convergence rate. The slow convergence rate is acceptable since a frame-by-frame dispersion correction is not necessary. Figure 3.9 shows an example of the automatic dispersion compensation. A B-scan image is digitally dispersed on purpose and then automatically corrected with two different ROIs separately. The differences between the two corrected images are not obvious, as shown in Figure 3.9 (B, C); however, the PSFs in Figure 3.9 (E) show that the dispersion is only well compensated in the selected ROIs and the residual dispersion mismatch leads to broader PSFs in other regions. The PSFs have been upsampled 5-fold to increase the digital axial resolution with zero padded interference fringes. The same upsampling ratio will be applied in the following materials unless further notice.

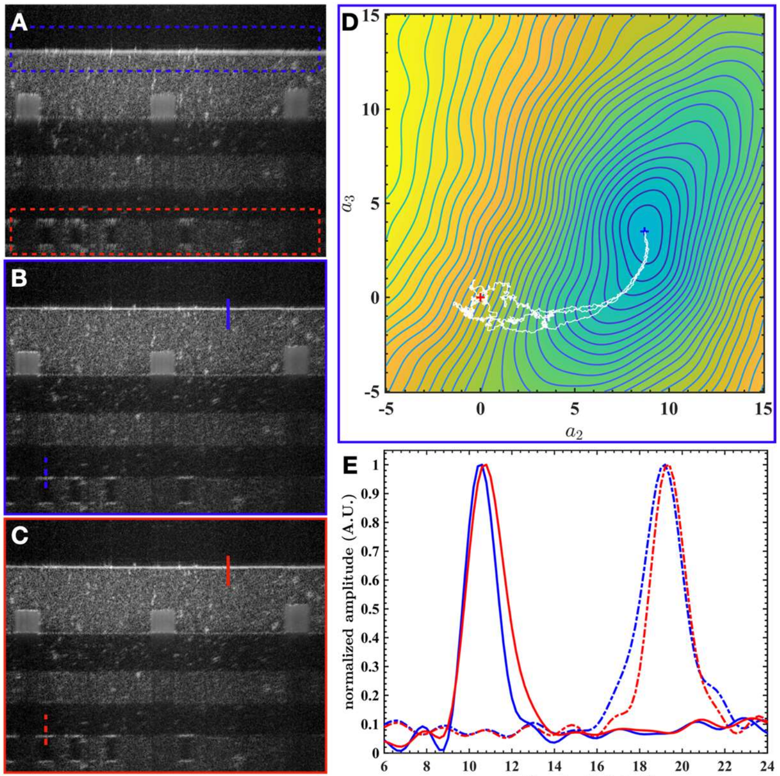

Figure 3.9 Automatic digital dispersion compensation by optimizing an image sharpness metric. (A) Digitally dispersed B-scan image. (B, C) B-scan images after digital dispersion compensation based on the blue and red boxed ROIs in (A). (D) The image metric of the blue boxed ROI in (A). Three typical trajectories of the SA optimization process are shown in white, and the red and blue cross marks denote the start and end locations. (E) The axial PSFs at locations indicated in (B) and (C).

3.5 System characterization

3.5.1 Axial resolution, SNR, and SNR rolloff, and depth scanning range

The axial resolution is determined by measuring the FWMH of the axial PSF of a mirror positioned at the focal plane. The reference arm is adjusted to introduce a 100 μm optical path delay, and the input laser power is reduced to avoid signal saturation. The axial PSF is first digitally dispersion compensated. Its FWMF is measured as 2.4 μm in air, corresponding to a 1.7 μm axial resolution in biology tissue, assuming the refraction index is 1.38. The theoretical PSF is generated with FFT of the reference spectrum in wavenumber space. Figure 3.10 (A) shows that the two PSFs are well correlated apart from the sidelobes.

The theoretical SNR at the center of the line illumination and the zero optical path delay is estimated as 92.5 dB, following Equation (2.21). The exposure time is 0.38 ms with the current design. The average exposure power of the line illumination on each pixel is $2.6 \times 1/310$ mW, where 310 (pixels) is the diameter of the Gaussian line, and the peak exposure power at the center is twice of the average. The average quantum efficiency of the camera is about 0.35, and the average diffraction efficiency of the transmission grating is assumed to be 0.8. We also assume a 75% energy loss because of the beam splitter and other optics. The two SNR rolloff terms origin from the finite pixel size and the diffraction limit are plotted separately in Figure 3.10 (B). The Δk in Equation (2.23) is assumed to be a constant which equals to $2\pi/1920 \cdot (1/\lambda_{\text{min}} - 1/\lambda_{\text{max}})$, λ is used as the central wavelength 790 nm, and $\delta\lambda_{1/e^2}$ is estimated as 0.202 nm using the beam radius of 790 nm determined by Huygens PSFs simulation in Chapter 3.2.2. Since the FWMH of the diffraction spot size is comparable with the pixel size, the diffraction limit of the grating and camera lens is the main contributor to SNR rolloff. Figure 3.10 (C) shows the SNRs measured at different optical path delays. The optical path delay is changed by adjusting the axial position of the reference mirror and its focusing lens together, and the sample mirror is kept at the focal plane. In practice, the SNR is first determined with the axial PSF's peak amplitude and the standard deviation of the noise floor, after which a 40 dB SNR floor is added back because of signal attenuation. The measured SNRs are fitted with Equation (2.23) with a larger spectral resolution ($\delta\lambda_{1/e^2}$ = 0.272 nm). The worse spectral resolution might come from alignment errors of the system.

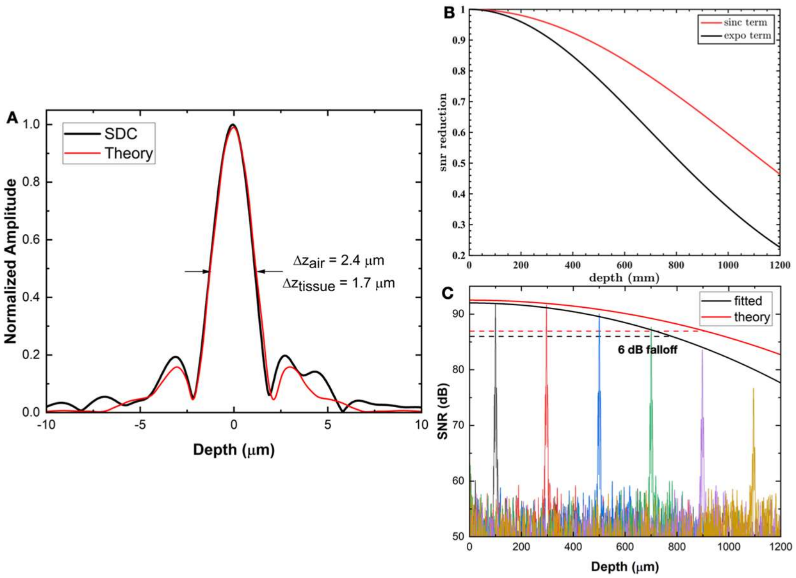

Figure 3.10 Axial resolution and SNR. (A) Theoretical and digitally dispersion compensated axial PSFs. The two PSFs are shifted to the same depth for better comparison. (B) Theoretical SNR reductions due to finite pixel size and diffraction limit. (C) Measured SNRs at different optical path delays. The theoretical and fitted rolloff curves indicate that the 6 dB rolloff ranges are 0.91 mm and 0.78 mm, respectively.

3.5.2 Lateral field of view (FOV) and resolutions

The lateral FOV and digital resolutions are determined by imaging a positive grid distortion target with a 10 μm spacing. The grid target is positioned at the focal plane and orientated perpendicular to the axial direction. A typical enface image is shown in Figure 3.11. The image is comprised of 500×500 pixels (A-scan×B-scan) with a ±0.2 V scan voltage. The two labeled lines with flat arrows are used to determine the lateral digital resolutions:

$$\begin{aligned} \tilde{\delta}x &= \frac{n_x}{p_x}\cdot 10\mu m \\ \tilde{\delta}y &= \frac{n_y}{p_y}\cdot 10\mu m \end{aligned} \tag{3.11}$$

where $n_{x,y}$ are the grid number along the x- and y-directions and $p_{x,y}$ are the corresponding pixel numbers. In order to reduce the measurement uncertainty because of blur lines at the edges, each digital resolution is calculated with 5 lines at different locations:

$$\begin{aligned} \tilde{\delta}x &= 1.120\pm0.002\ \mu m \\ \tilde{\delta}y &= 1.723\pm0.005\ \mu m \end{aligned} \tag{3.12}$$

The lateral FOV is thus 0.56×0.86 mm (x×y). Another scan protocol is used in Chapter 4, and its enface image is comprised of 800×600 pixels (A-scan×B-scan) with a ±0.25 V scan voltage in the x-direction. Assuming the scanner is linear, that configuration's FOV is 0.70×1.38 mm (x×y).

The angle between the two labeled lines is measured as $90.06 \pm 0.10^\circ$, which confirms the orthogonality of the x- and y-directions. We have also noticed the field curvature, as shown in the zoom-in images. Thus, DAO needs to be applied in different ROIs independently for defocus correction.

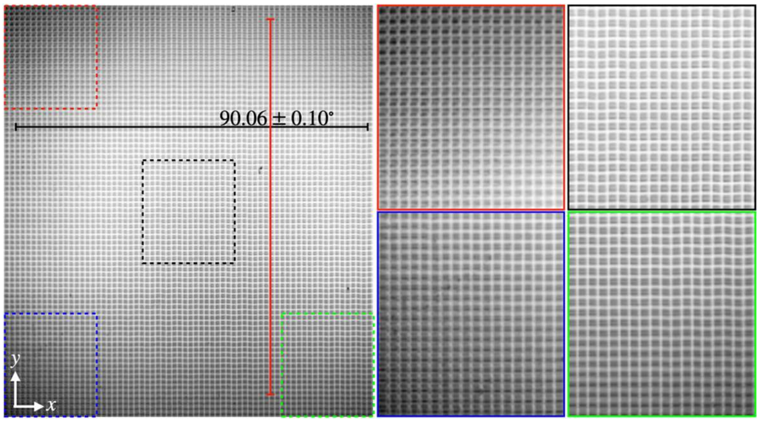

Figure 3.11 A typical enface image of a grid distortion target.

Eight USAF 1951 resolution target tomograms placed at different depths are used to determine the lateral resolutions in x- and y-directions. Each enface image is digitally refocused first, following the method developed in Chapter 5. The coherence edge spread functions (cESFs) along the x- and y-direction, $e(x)$ and $e(y)$, are then extracted at the locations labeled in Figure 3.12 (B). The coherence line spread functions (cLSFs) can be calculated using the derivative of the cESFs:

$$\begin{aligned} l(x) &= \frac{d}{dx} e(x) \\ l(y) &= \frac{d}{dy} e(y) \end{aligned} \tag{3.13}$$

The cLSF radiuses ($1/e$) are estimated with Gaussian curve fitting and then averaged as $\sigma(x)$ =1.17±0.17 pixels and $\sigma(y)$ = 0.81± 0.03 pixels. Thus, the lateral resolutions, defined as the FWMH of the cPSF, are δx=2.23±0.34 μm and δy=2.33±0.08 μm, respectively. We calculate the lateral resolutions using refocused images at different depths because the phase destruction due to the virtual interference pinhole might broaden the PSF in the x-direction. Thus, the average results are more suitable to represent the overall image resolutions after DAO. The virtual pinhole effect will be explained in Chapter 5. In principle, the digital resolution needs to be less than half of the physical resolution according to the Nyquist sampling theorem. However, the lateral digital resolutions in the current configuration are not high enough in the y-direction. However, a better digital resolution in the y-direction requires decoupling of the spectral resolution and sample to camera magnification.

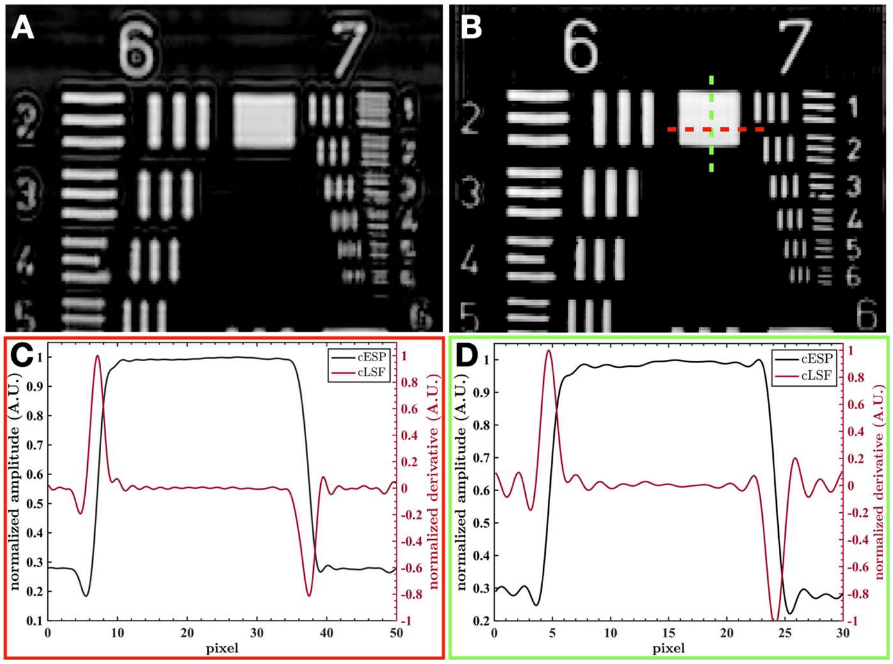

Figure 3.12 Lateral resolutions calibration with USAF 1951 resolution target. (A) A typical defocused enface image of the resolution target. (B) Digitally refocused enface image. (C, D) The cESPs and the corresponding cLSFs of the dash lines labelled in (B).

3.6 Axial motion-induced phase error correction and DOCT

Phase stability is vital in analyses where complex OCT signal is used. Although phase noise itself cannot be avoided, extra phase error because of bulk axial motions should be compensated. The bulk axial motion comes from saccade, breathing, heartbeat, and even the mechanical vibration of the head support. Uncompensated phase errors lead to distorted velocity, failure of DAO, and faster signal decorrelation. Assuming the motion within one time resolution (the time period of a B-scan) is smaller than the resolution thus the adjacent B-scans are well correlated, the axial phase errors can be determined as:

$$\Delta\phi_n(y,z) = \arg[I(x_n, y, z) I^*(x_{n+1}, y, z)];\ n = 1, 2, \ldots, N-1 \tag{3.14}$$

where $I(x_n, y, z)$ is the complex signal of the nth B-scan and $[*]$ denotes the complex conjugate. Since the LS OCT records a B-scan simultaneously, the phase error induced by axial motions is spatially invariant. The weighted phase error is:

$$\Delta\phi_n = \arg[\sum_{(y,z)\in D} I(x_n, y, z) I^*(x_{n+1}, y, z)];\ n = 1, 2, ..., N-1 \qquad (3.15)$$

where D is a user-selected region away from moving particles since they carry additional phase information other than bulk motions. The axial motion-induced phase error is then compensated according to:

$$I_{corr}(x_n, y, z) = I(x_n, y, z) \prod_{i=1}^{n-1} \exp(i\Delta\phi_i);\ n = 2, ..., N \qquad (3.16)$$

Figure 3.13 shows an example of how the axial motion-induced error affects the DOCT results. The camera is running at a frame rate of 2.95 kHz with a detection area of 1920×500 pixels, and the B-scans are collected at the same location without scanning. The flow rate is controlled by a single syringe pump and is set as a constant. The phase error between adjacent B-scans determined with the air-phantom interface is illustrated in Figure 3.13 (D). The mechanical vibrations generate an oscillating phase error in the range of (-0.4, 0.4), which is about 1/8th of the full phase detection range ($-\pi$, π). As can be seen in Figure 3.13 (E), the phase error leads to distorted phases and velocities if not appropriately compensated. The full phase detection range corresponds to an axial velocity range of (-0.43, 0.43) mm/s. If the speed of axial bulk motion is beyond this limit, the phase error cannot be corrected. Phase unwrapping has been utilized to extend the velocity detection limit in DOCT, assuming the velocity distribution is smooth in the blood vessel. However, since the axial bulk motions are random, phase unwrapping cannot be used here.

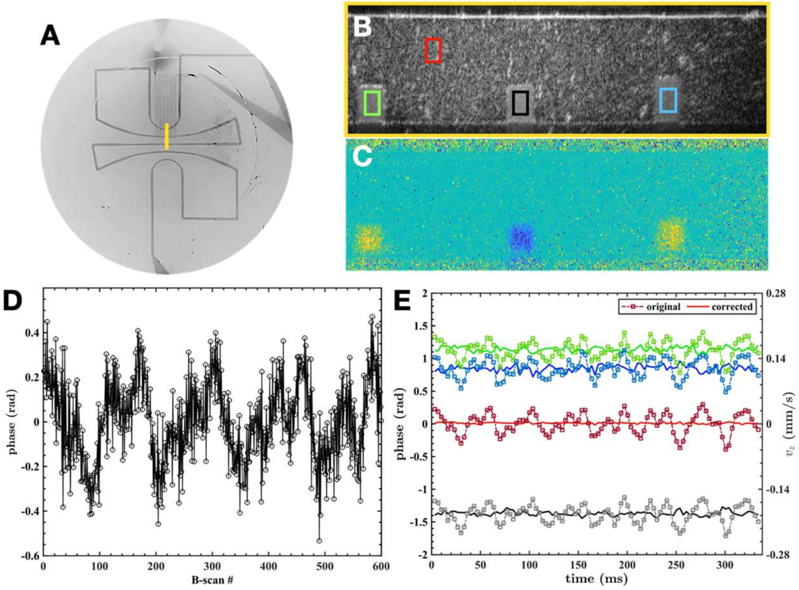

Figure 3.13 DOCT with and without axial motion-induced phase error correction. (A) Schematic of a microfluidic phantom filled with black ink. The yellow line indicates the location of the B-scan. (B) Log-scale B-scan image of the phantom filled with intralipid. (C) The phase difference between 2 adjacent B-scans after axial phase error correction. 20 phase difference distribution are used for averaging to reduce phase noise. (D) Axial phase errors determined with the air-phantom interface. (E) Phases and the corresponding velocities of the intralipid flow in the ROIs labeled in (B).

Axial motion does not only result in phase instability between B-scans, but it can also lead to signal loss because of dephasing within a single integration time. This artifact is known as fringe washout [88]:

$$I(k) \propto \cos(2nk\Delta z)\mathrm{sinc}(2nkv_z\tau) \tag{3.17}$$

where τ is the exposure time of the detector. The sinc function leads to a degradation of the fringe amplitude and thus the OCT signal. The influence of the decorrelation on the OCT signal is often neglected in point-scan modality, whereas it is not negligible even at low speed in LS OCT because of the long exposure time. Figure 3.14 shows the plots of the 5% intralipid OCT signal's amplitude and adjacent B-scans' phase difference at different intralipid flow rates, which were controlled with a syringe pump. The amplitude reduces with an increase in the flow speed. However, the axial velocity is not the sole contributor to the signal loss. As shown in Figure 3.14 (C), the attenuation compensated OCT signal amplitude is not systematic. The extra signal loss at the bottom might come from decorrelation. In Figure 3.14 (B) and (D), DOCT fails to produce reasonable results because of the randomness of the phase difference at higher flow rates. This randomness comes from the signal loss induced SNR degradation as well as the signal decorrelation. However, it is hard to determine which is more significant as the decorrelation is affected by SNR. Nevertheless, the failure of DOCT in the detectable range brings up the need to develop new velocimetry methods in LS OCT.

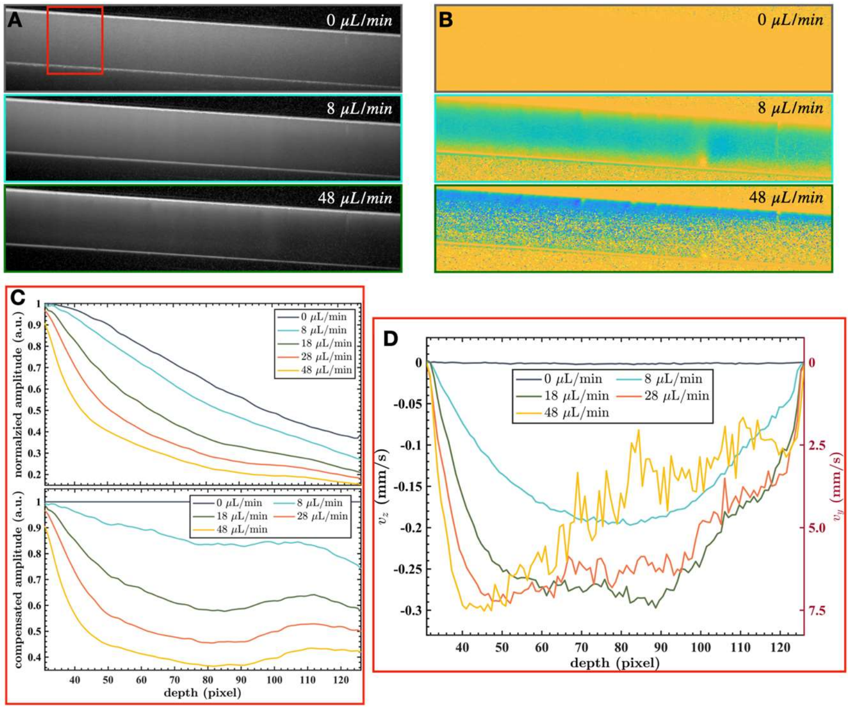

Figure 3.14 OCT signal amplitude and phase degradation at different intralipid flow rates. (A) Log-scale B-scan images. (B) The phase difference between 2 adjacent B-scans after axial phase error correction. (C) Averaged original and attenuation compensated amplitudes vs. depth. (D) Averaged DOCT velocities vs. depth. The lateral velocities are calculated using the Doppler angle. 100 B-scans are used for averaging for all images. Both (C) and (D) are averaged along y-direction within the ROI labeled in (A) after flattening.

3.7 Conclusion

We have developed a broadband LS SD-OCT system with isotropic micrometer level resolution of 2.2×2.3×2.4 μm (x×y×z) in free space. The lateral resolution is achieved with a 10× objective, and the axial resolution is achieved with a stretched femtosecond laser with a 790 nm center wavelength and 140 nm FWMH bandwidth. The camera operates at a B-scan rate of 2.5 kHz with an effective detection area of 1920×800 (spectral×spatial) pixels, and the equivalent A-scan rate is 2 MHz. The SNR at the center of the Gaussian illumination line is measured as 92 dB 100 μm away from the zero optical delay, and its 6 dB rolloff range is about 0.78 mm. The combination of the high spatial resolution and rapid acquisition speed allows for *in-vivo* revealing the 3D structures of human cornea and limbus cells in a relatively large FOV with fewer motion artifacts. Axial motion induced phase error is noticeable even though the axial displacement between adjacent B-scans is in the ~100 nm scale. Therefore, additional axial motion induced phase error correction is necessary for the study where the phase or complex value of the OCT signal is used. The axial velocity detection range of DOCT in the LS SD-OCT system is significantly lower than that of the point-scan FD-OCT because of the limited time resolution, and the fringe washout and fast decorrelation of the OCT signal further reduce the effective detection range. Therefore, novel flow velocimetry is in demand for measuring the flow speed in LS SD-OCT.

Chapter 4

In-vivo Imaging of the Human Cornea and Limbus

4.1 Introduction

Corneal and limbal inherited, degenerative, and infectious pathologies constitute the 4th leading cause of blindness worldwide after cataract, glaucoma, and age-related macular degeneration [89]. The accurate and early diagnostics of corneal and limbal pathologies and the effective planning of therapies are strongly dependent on the ability of imaging technologies to visualize, identify, and characterize the tissue cellular structure *in-vivo.* Currently, the only clinical imaging method that can image corneal and limbal cells *in-vivo* is In-vivo Confocal Microscopy (IVCM) [90]. However, IVCM has a number of limitations: a) in order to generate high resolution enface images, many IVCM instruments require physical contact with the corneal epithelium that necessitates corneal anesthesia, and significantly increases the risk of corneal infections and abrasions; b) limited field of view (FOV ~400 µm × 400 µm); and c) difficulty generating high resolution volumetric images due to depth location ambiguity associated with poor axial resolution, as well as slow scanning in the axial direction compared to fast axial eye motion.

Compared to IVCM, optical coherence tomography (OCT) offers the advantages of *in-vivo,* non-contact, high-resolution, high-speed, volumetric imaging of the cornea [91,92]. OCT technology with different optical designs has been used to image *in-vivo* the cellular structure of the human and animal cornea. Point-scan spectral-domain (SD) OCT can achieve axial resolution in the order of 1 µm in corneal tissue by using broadband lasers [1,18,77,93–95]. Although *in-vivo* volumetric SD-OCT images of the corneal cellular structure have been reported in the past from anesthetized animals [95,96], where anesthesia was used to reduce image artifacts induced by involuntary eye motion, *in-vivo* imaging of the human cornea remained problematic due to the limited acquisition speed of the linear array camera. Recently, *in-vivo* volumetric SD-OCT images of the human cornea acquired with a 250 kHz linear array camera and showing the cellular structure of all corneal layers were reported [17], however, motion artifacts were still noticeable in the 3D images.

Full-field (FF) time-domain (TD) OCT utilizes a different scanning approach where enface images are acquired rapidly while the imaged object is scanned slowly in the axial direction [57,97,98]. The relative insensitivity of the images to optical aberrations, combined with a transverse resolution of ~1 µm, allows FF TD-OCT to image the cells in the human corneal stroma and endothelium both *ex-vivo*

[79,99,100] and *in-vivo* [21,101]. However, the limited dynamic range of the area camera used in FF TD-OCT, resulting in limited SNR, prevented *in-vivo* visualization of cells in the corneal epithelium and the limbal crypts [21]. Furthermore, the image acquisition rate of FF TD-OCT is limited by the speed of the mechanically scanned reference mirror.

FF swept-source (SS) OCT technology was introduced recently for *in-vivo* human corneal imaging [25]. FF SS-OCT uses a rapidly tunable light source and offers better sensitivity and a significantly faster volumetric acquisition rate. Although the concept of FF SS-OCT was published a while ago [53], it took many years of development of fast area cameras before FF SS-OCT could be developed for *in-vivo* imaging of the human eye [25,44,54,102–104]. One major advantage of FF SS-OCT is the high phase stability in the enface images, which allows for wavefront aberration correction with digital adaptive optics (DAO) [42,43,105–107]. However, the fairly narrow spectral range of the tunable lasers currently limits the FF SS-OCT axial resolution in corneal tissue to ~5 μm, which is insufficient for visualization of cellular details in the axial direction.

Line-scan (LS) SD-OCT offers an alternative design to point-scan SD-OCT, that utilizes line instead of point illumination optical beam projected onto the imaged object, an area camera instead of a linear array camera, and 1D scanning instead of 2D scanning to achieve image acquisition rates higher than 2,000 fps. LS SD-OCT generates B-scan images of the imaged object by sampling the lateral structure of the object along the vertical direction (y-direction) of the 2D camera while encoding the axial structure of the object by projecting spectral information along the horizontal direction (x-direction) of the camera, followed by Fourier transformation of the spectral data into the spatial domain. Therefore, the B-scan rate of LS SD-OCT is determined by the frame rate of the 2D camera, while the spatial resolution of LS SD-OCT is determined by the spectrum of the light source (axial direction) and the imaging optics (lateral direction). Because LS SD-OCT utilizes a spatially extended light source, the optical power of the imaging beam can be increased safely by ~4× compared to the optical imaging power used in point-scan SD-OCT for *in-vivo* human cornea imaging. This safe increase of the optical power compensates partly for the loss of sensitivity in LS SD-OCT resulting from the faster image acquisition rates. Although the concept of LS SD-OCT was published nearly 2 decades ago [52], the use of this technology for *in-vivo* imaging of the human retinal structure and blood flow [45] and the retinal response to visual stimulation [34] was only reported recently. However, the LS SD-OCT technology used in those studies offered limited axial OCT resolution of ~ 6.2 μm in air, which is insufficient to visualize cells and sub-cellular structures in the axial direction.

Here we present a novel design of an LS SD-OCT system that combines a 2 × 3 × 1.7 μm (x × y × z) resolution in biological tissue with an acquisition rate of ~2,500 fps and a depth scanning range of ~1.3 mm. We also demonstrate the ability of the system to image *in-vivo*, volumetrically, and without contact with the tissue surface, the cellular structure of the human cornea and limbus.

4.2 Methods

4.2.1 System design

The LS SD-OCT system design is discussed in detail in Chapter 3.2.

4.2.2 Imaging procedure

Images of the human central cornea and corneoscleral limbus were acquired *in-vivo* with the LS SD-OCT system from healthy subjects. The imaging sessions were approved by the research ethics committee of the University of Waterloo, and informed consent was obtained from the subjects. A custom head support frame, mounted on XYZ translation stages, was used to stabilize the subject's head during the imaging procedure and align ocular locations of interest with respect to the OCT imaging probe. A fixation target was used for additional eye alignment with respect to the imaging beam and for reducing involuntary eye motion. Volumetric (800 A-scans × 600 B-scans × 1920 pixels) images were acquired. The system design and scanning protocol allowed for the acquisition of a single 3D tomogram with a field of view (FOV) of 0.7 mm × 1.4 mm (x × y) and 1.3 mm depth scanning range in free space. The maximum camera frame rate for this setting was 2461 fps, resulting in an equivalent B-scan rate of ~2.5 kHz and volumetric data acquisition time of 0.24 s. Because of the microscope objective's limited depth-of-focus, the anterior and posterior cornea were imaged separately, and the reference optical path length was adjusted accordingly.

4.2.3 Image processing

Images were generated from the raw OCT data and numerically dispersion compensated up to the 4th order with a custom MATLAB algorithm. The B-scan and enface images shown were averaged over 3 adjacent images and convoluted with a Gaussian filter if necessary for better visualization. The volumetric images were generated with Amira (Thermo Fisher Scientific).

4.2.4 Maximum permissible exposure for *in-vivo* anterior segment ocular imaging

During the *in-vivo* image acquisition, the imaging beam forms a line shape along the y-direction (vertical) on the cornea or limbus, and the line is scanned in the x-direction (horizontal). The line-shaped optical beam projected onto the cornea will generate an elliptical power distribution at the retina, whose minor axis in the y-direction is much shorter than its major axis in the x-direction. The ellipse's shift in x-direction during scanning is negligible compared to the length of its major axis, and the exposure should be considered static at the retinal surface. Therefore, we limit the exposure time to no longer than 10 seconds, which is a typical time period between successive blinks for normal blinking rate in the healthy eye.

According to the ZEMAX model of the LS SD-OCT system described in Chapter 3.2, the $1/e^2$ beam diameter of the light intensity distribution at the objective's focal plane is 3.8 μm in the x-direction and 1.00 mm in the y-direction. According to the American National Standards Institute (ANSI) guidelines, ANSI Z80.36-2016 [108], the Group 1 unweighted anterior segment visible and infrared radiation irradiance limit value (E_{VIR-AS}^{MPE}) for a continuous wave is:

$$E_{VIR-AS}^{MPE} = \sum_{380}^{1200} = E_{\lambda} \times \Delta\lambda = 4\,\mathrm{W/cm^2} \tag{4.1}$$

The average irradiance of the system at the anterior segments is:

$$E_{VIR-AS} = \frac{P}{A} = \frac{2.6\mathrm{mW}}{\frac{\pi}{4}1\mathrm{mm}^2} = 0.33\,\mathrm{W/cm^2} \tag{4.2}$$

where A is the area of a circle with diameter of 1.0 mm. Thus, the unweighted anterior segment irradiance is only 1/12 of the group 1 maximum permission exposure (MPE) at the worst scenario of continuous illumination.

Assuming that the human eye's focal length in healthy normal adults is ~17 mm and there are no optical aberrations, the $1/e^2$ diameter of the light intensity distribution on the retina is about 19.9 µm in the y-direction. As it is smaller than 0.03 mm, we use 0.03 mm as the minor axis length. We estimate the length of the major axis at the retinal surface is ~5.1 mm based on a Zemax simulation of the LS SD-OCT system and an eye model provided by Zemax [109]. The limit of weighted retinal visible and infrared radiation irradiance (E_{VIR-R}^{MPE}) for time-limited instruments in the time range (0.25 s, 200 s) is:

$$E_{VIR-R}^{MPE} = \sum_{380}^{1400} E_{\lambda} \times R(\lambda) \times \Delta\lambda = 6t^{-1/4}\,\mathrm{W/cm^2} \tag{4.3}$$

The weighted maximum permissible exposure for duration of 10 seconds is:

$$P_{VIR-R}^{MPE}\,|_{t=10\,\mathrm{s}} = E_{VIR-R}^{MPE}\,|_{t=10\,\mathrm{s}} \times A = 4.0\ \mathrm{mW} \qquad (4.4)$$

where A is the area of an ellipse with a minor and major length of 0.03 mm and 5.1 mm. In addition, the energy of light source used in the LS SD-OCT system is confined in the spectral range of (700 nm, 900 nm), in which the thermal hazard weighting function $R(\lambda)$ is less than one, so the power limit should be higher than 4.0 mW.

With a stricter standard [110], for a non-circular exposed retinal field, the maximum permissible radiant power (in Watts) is calculated as:

$$MP\Phi = 6.93\times10^{-4}\,C_T(\lambda)C'_E\,P^{-1}(\lambda)t^{-1/4} \qquad (4.5)$$

Here, $C_T(\lambda) = 10^{0.002(\lambda-700)}$ and $P(\lambda) = 1$ in the wavelength range (700 nm,1050 nm), and $C_T(\lambda) = 1$ and $P(\lambda) = 10^{-0.0074(\lambda-700)}$ in the range (600 nm, 700 nm). $C'_E = 8\alpha_L/\pi(\alpha_{\min} + \alpha_{\max})$ is a parameter for a slit field, where $\alpha_{\min}$=1.5 mrad, $\alpha_{\max}$=100 mrad, and α_L=300 mrad. Since both $C_T(\lambda)$ and $P^{-1}(\lambda)$ is not less than 1 in most regions of the spectrum, maximum permissible radiant power for duration of 10 seconds is:

$$MP\Phi < 6.93\times10^{-4}\,C'_E\,10^{-1/4} = 2.9\times10^{-3}\ \mathrm{W} = 2.9\ \mathrm{mW} \qquad (4.6)$$

For the *in-vivo* human imaging studies described here, the imaging power of the LS SD-OCT system was set to 2.6 mW, which is below the limits calculated above.

4.3 Results

4.3.1 System’s resolution and sensitivity

Performance test results of the LS SD-OCT system are summarized in Figure 4.1. Figure 4.1 (A) shows the normalized sample and reference spectra measured at the detection end of the LS SD-OCT system by using a silver-protected mirror as the test sample. The spectra were averaged over 50 consecutive frame recordings to reduce temporal fluctuations. Since the cylindrical lens (CL1) generates a line with Gaussian power distributions along and across the line, for consistency, the system's axial point spread function (PSF) and signal to noise ratio (SNR) were evaluated at the central position of the line. Figure 4.1 (B) shows the theoretical axial PSF (red line) and the axial PSF with hardware dispersion compensation only (blue line) and after additional software dispersion compensation (black line) up to the 4th order. The measured axial resolution is 2.4 μm in air, which corresponds to 1.7 μm in biological tissue, assuming an average refractive index of 1.38. Figure 4.1 (C) shows the depth-dependent SNR measurement results. For 2.6 mW power incident on the imaged sample, the system provides an SNR of ~92 dB at an imaging depth of 100 µm away from the zero-delay and a 6dB SNR rolloff over a range of ~0.78 mm. The system's lateral resolution was evaluated by imaging a standard United States Air Force resolution target Figure 4.1 (D), and the measured LS SD-OCT resolution was ~2 µm in the x-direction and ~3 µm in the y-direction.

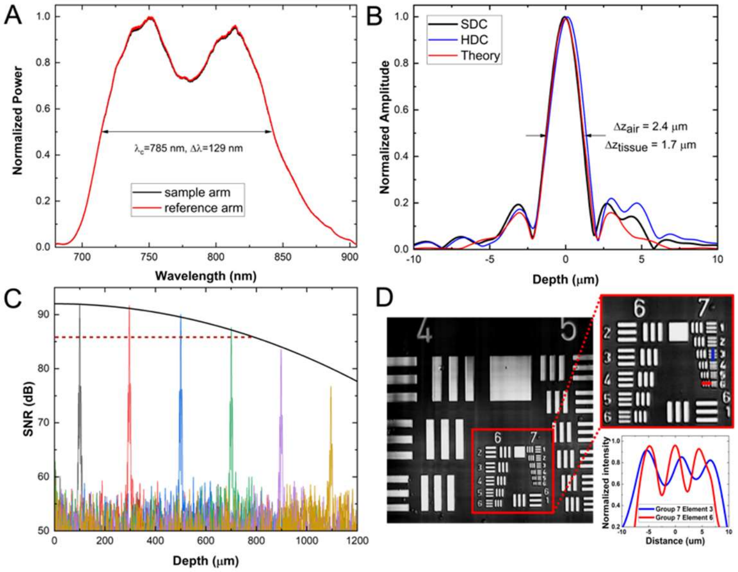

Figure 4.1 System characterization of the LS SD-OCT system. (A) Reference (red) and sample (black) arm spectra measured at the detection end of the system. (B) Theoretical axial PSF and the axial PSF measured at a depth of 100 µm in free space with hardware (HDC) and software dispersion compensation (SDC). (C) Depth-dependent SNR and the fitted SNR rolloff. (D) Image of a USAF resolution target with intensity analysis (insert).

4.3.2 Cornea images

Anterior cornea images were acquired from a location slightly inferior relative to the corneal apex to avoid the strong back-reflections in the OCT images from the corneal surface. Posterior cornea images were acquired near the corneal apex. Representative images from the anterior and posterior cornea are shown in Figure 4.2. A custom algorithm was used to flatten the images to correct the curvature of the anterior cornea. A volumetric image of the anterior human cornea (Figure 4.2 (A)) shows the cellular structure of the corneal epithelium and stroma and the reflective structures in the tear film (orange arrows) that could be cellular debris, mucin clusters, or dust particles. A representative B-scan from the 3D image stack is shown in Figure 4.2 (B), where the cellular structure of the epithelium is visible. This

B-scan image and following enface images were generated by averaging 3 adjacent images for better visualization. A cross-section of a sub-basal nerve (red arrow) located at the interface of the basal cell layer of the corneal epithelium and the Bowman's membrane, as well as reflections from keratocytes (blue arrows) in the anterior stroma are also visible. A representative Haemotoxylin and Eosin histological image of the human cornea that was acquired from a healthy normal donor human cornea postmortem (Figure 4.2 (C)) shows similar features. An enface image of the corneal epithelium (Figure 4.2 (D)) shows the cellular structure of that layer over a FOV of 700 µm × 700 µm. Figure 4.2 (E) and Figure 4.2 (F) show zoomed views of the regions of interest (ROIs) in the corneal epithelial layer marked with blue and red dashed lines.

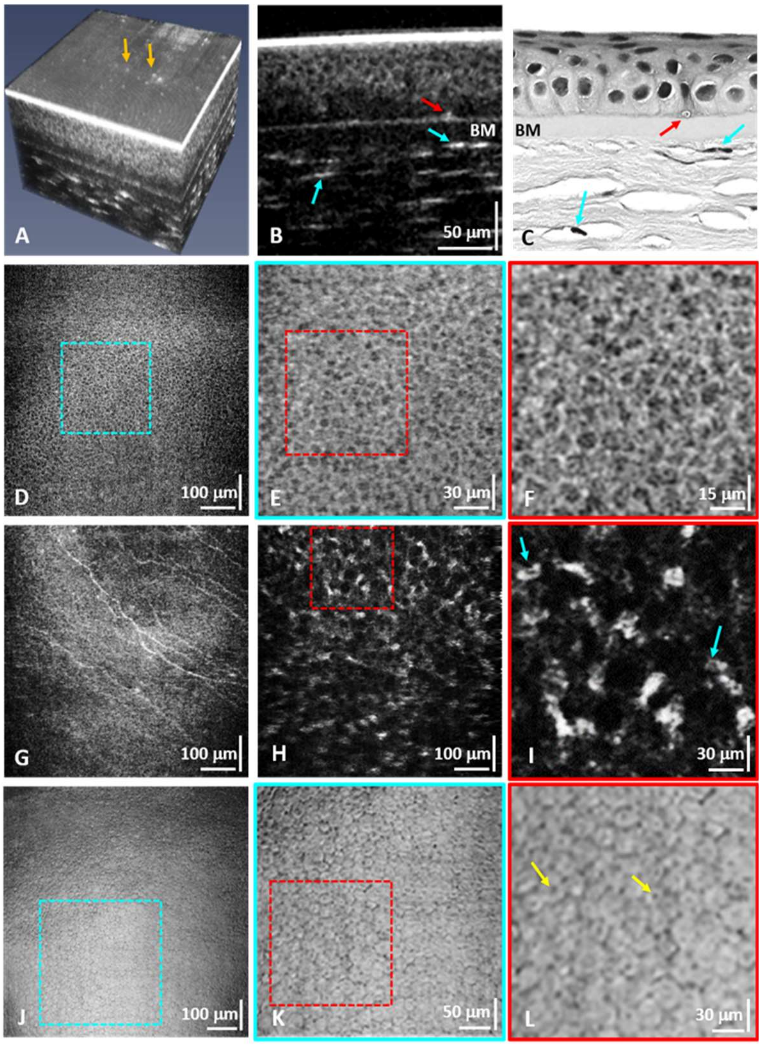

Figure 4.2 *In-vivo* imaging of the anterior and posterior cornea of a healthy volunteer. (A) Flattened 3D LS SD-OCT image of the anterior cornea from a healthy volunteer. (B) Crosssectional image of the anterior cornea showing the cellular structure of the epithelium, crosssection of sub-basal corneal nerves (red arrow), the Bowman's membrane, and keratocyte nuclei in the anterior stroma (blue arrows). The same morphological features are resolved in the crosssectional H&E corneal histology *ex-vivo* (C). (D) Enface image of the corneal epithelium with magnified views (E, F) of the regions of interest (ROIs) marked with the blue and red dashed lines that show individual epithelial cells. (G) Enface images of sub-basal corneal nerves. (H, I) Enface images of the anterior stroma showing keratocyte nuclei. (J) Enface maximum intensity projection image of the corneal endothelium. (K, L) Zoomed ROIs showing individual endothelial cells.

Figure 4.2 (G) shows an enface image of the sub-basal corneal nerves located between the epithelial basal cell layer and the Bowman's membrane. Figure 4.2 (H) and Figure 4.2 (I) show a large FOV and the magnified ROI of the anterior stroma, respectively. The hyperreflective structures observed in the images correspond to keratocyte nuclei that are located in between the collagen lamellae of the corneal stroma.

Figure 4.2 (J) shows a large FOV (700 µm × 700 µm) enface image of the corneal endothelium generated by using maximum intensity projection. The cellular mosaic of the endothelial layer is clearly visible. Figure 4.2 (K) and Figure 4.2 (L) show magnified views of the ROIs in the corneal endothelium images marked with the blue and red dashed squares. The hexagonal shape of the endothelial cells is clearly visible in Figure 4.2 (K) and Figure 4.2 (L). The dark spots observed inside the endothelial cells in Figure 4.2 (L) (yellow arrows) most likely correspond to reflections from the cellular nuclei.

4.3.3 Limbus images

Volumetric images of the healthy human limbus were also acquired with the LS-SD-OCT system from the inferior limbus. The corneoscleral limbus is about a 1-2 mm wide ring-shape region of tissue that separates the peripheral cornea anatomically from the conjunctiva and sclera. The limbus has a rich and complex morphology [14,111,112] with dense innervation [113] and vascularization [114,115], that provides a unique environment for housing the limbal stem cells (LSCs), which is responsible for the regeneration of the corneal epithelium, as well as progenitor cells [115–117]. The limbus contains radially oriented fibro-vascular ridges, known as the palisades of Vogt (POVs) that are interspaced by the limbal crypts (LC).

A volumetric image of the inferior limbus (Figure 4.3 (A)) shows the finger-like POVs (orange arrows) and the cellular structure of the limbal crypts. The vascular network in the underlying sclera is also visible. A representative B-scan from the volumetric stack (Figure 4.3 (B)) shows crosssections of the POVs and the LC. A magnified view of the ROI marked with the red dashed line in Figure 4.3 (B) is shown in Figure 4.3 (C). The cellular structure of the limbal crypt is visible. Hyperreflective structures (yellow arrow) are visible along parts of the inner surface of the limbal crypts, which most likely correspond to clusters of melanocytes located along the interface between the POVs and the LC. Another type of hyper-reflective structure is visible in crosssections of the POVs, marked with red arrows in Figure 4.3 (B, C). These structures appear as thin, reflective lines located under the folds of the POVs and oriented vertically along the length of the POVs. A magnified view of the ROI marked with the yellow dashed line in Figure 4.3 (B) is shown in Figure 4.3 (D). Cells of smaller size (blue arrow) are observed close to the walls of the limbal crypts compared to cells populating the central part of the crypts.

Enface images of the limbus at different depths from the same volumetric stack are shown in Figure 4.3 (E-H). A magnified view of the ROI marked with the red dashed line in Figure 4.3 (E) is shown in Figure 4.3 (F). The cellular structure of the limbal crypt is clearly visible. Hyper-reflective linear morphological features located under the folds of the POVs and extending radially along the POVs are observed in Figure 4.3 (E-G) (red arrows). According to anatomy data these reflective structures may correspond to blood vessels or peripheral corneal nerves. Focal stromal projections (vertical type of POVs) are observed at the interface between the limbus and the peripheral cornea (Figure 4.3 (G), green arrow). The image in Figure 4.3 (H) corresponds to a depth location at the base of the POVs and the interface of the underlying scleral tissue. It shows similar hyperreflective liner structures along the POVs, which may also correspond to peripheral vessels or nerves.

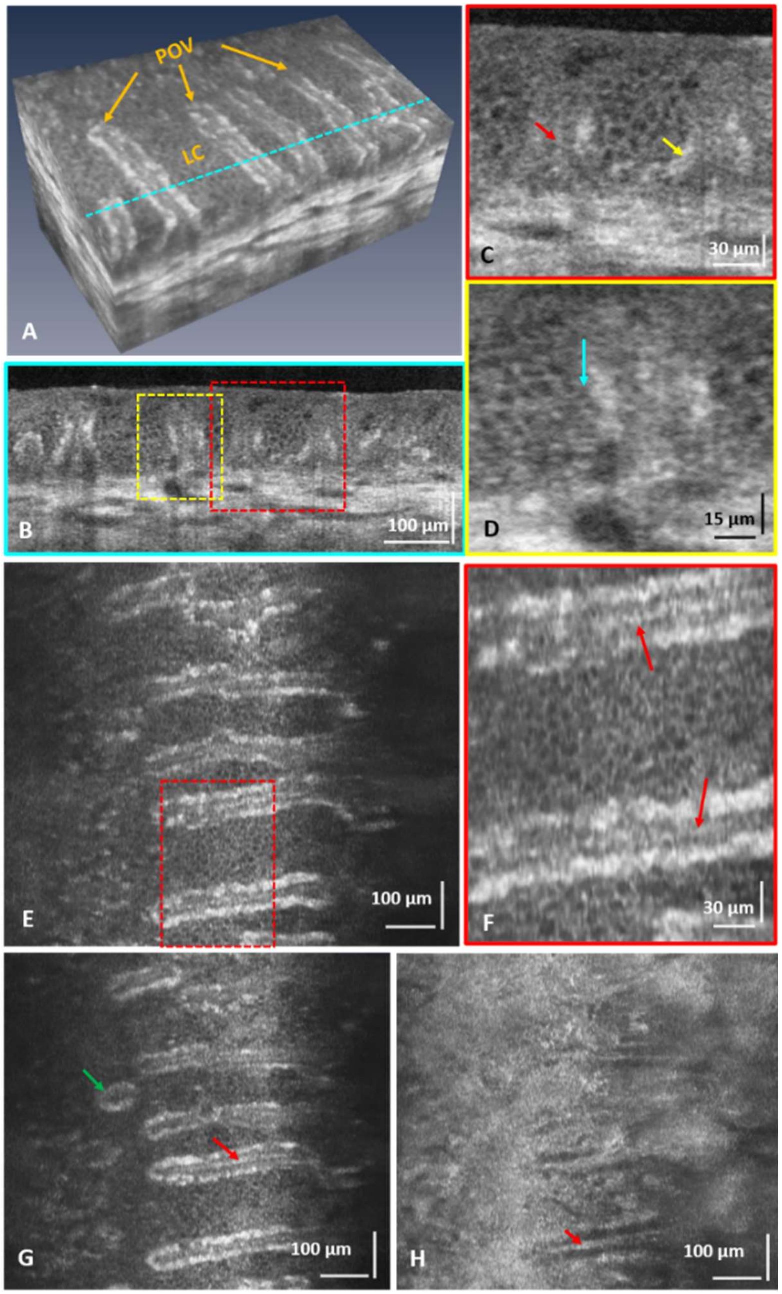

Figure 4.3 *In-vivo* imaging of the limbus of a healthy volunteer. (A) Flattened volumetric image of the healthy inferior human limbus showing the palisades of Vogt (POVs) and the cellular structure of the limbal crypts (LC). Crosssectional image of the POVs and the LC corresponding to the location in (A) marked with the blue dashed line. (C, D) Zoomed images of the ROIs marked in (B) that show pigmented cells along the inner borders of the limbal crypts (yellow arrow), hyperreflective structure under the POVs (red arrow), and small sized cells, probably limbal stem cells or transient amplifying cells, located along the crypt walls (blue arrow). (E, G, and H)

Enface images of the POVs and LC acquired at different depth locations. (F) Zoomed view of the ROI marked in (E). These images show a focal stromal projection (green arrow) and hyperreflective line structures, possibly blood vessels or nerves, located under the POVs (red arrows).

4.4 Discussion

Different OCT modalities have been used to image the corneal cells of human or animals. For example, the point-scan micro-OCT showed excellent *ex-vivo* images of the corneal epithelial cells, keratocytes, and endothelial cells of animals [118], and the image quality is close to that achieved with IVCM. The major limitation of point-scan SD-OCT for *in-vivo* imaging of the human corneal and limbal cells stems from the fact that the slow image acquisition rate cannot suppress the involuntary eye motion (e.g., saccades), even using the fastest commercially available or research-grade linear array cameras [17,49,119]. Therefore, it can only be used to image small FOV otherwise the cellular structure in the OCT images shows blur due to eye motion. FF TD-OCT has been used to image *in-vivo* the sub-basal nerves, keratocytes, and endothelial cells of the human cornea [21,101], and its variant, termed curved-field OCT, extended the lateral FOV to 1.13×1.13 mm in imaging the endothelium layer [73]. However, low axial resolution (~7 μm) and enface image acquisition rate (275 frames/second) limit its application for *in-vivo* 3D imaging, and the low SNR (74 dB after image averaging) prevented visualization of the corneal epithelial cells. FF SS-OCT has also been used to *in-vivo* image the human cornea [25,55], and digital refocusing was applied to extend the depth of focus. Currently, the main limitation of FF SS-OCT is the low axial resolution associated with the relatively narrow spectral range of tunable laser technology. As an alternative design, the LS SD-OCT proposed in this study combines a high spatial resolution, fast imaging speed, and relatively large FOV. Therefore, it may be more suitable for *in-vivo*, non-invasive, contactless, volumetric imaging of the cellular structure of human cornea and limbus.

In the B-scan image of the corneal epithelium (Figure 4.2 (B)), only the wing cells were resolved while the superficial cells and basal cells were not resolved. The superficial cells were overwhelmed by the strong reflection signal of the interface of air and tear film, which can be reduced by asking the imaged subject to wear a contact lens. While the contact lens material will introduce additional dispersion in the OCT images, that can be easily compensated in post-processing. The missing of basal cells might be because the scattering coefficient is low [120], and the focal plane is away from the basal cell layer. Visualization of the basal cells may be achieved by improving the image SNR through averaging of multiple B-scans or 3D volumes, applying despeckle algorithms or other image enhancement algorithms, and applying digital refocusing. While the image SNR can also be increased by reducing the image acquisition rate or increasing the optical power of the imaging beam, these approaches are not advisable, as the current imaging power is already close to the MPE limit and slowing down the camera will introduce more image blur and eye motion artefacts.

In the magnified enface images of the corneal endothelium (Figure 4.2 (K, L)), dark spots were observed inside the endothelial cells. These dark dots most likely correspond to cellular nuclei. One might expect that since the refractive index of the endothelial nuclei is higher than the one of the cytoplasm, the nuclei will appear as “bright” rather than “dark” spots. However, the images shown in Figure 4.2 (J-L) are generated by MIP from the 3D image stack and include the highly reflective interface between the posterior surface of the corneal endothelium and the fluid of the anterior eye chamber. Since the specular reflection from that layer is stronger than the scattering from the cellular nuclei, the image contrast of the nuclei is reversed, and they appear as “dark” spots over a more reflective background.

In both the B-scan and enface images of the limbus, hyper-reflecting line structures were identified under the POVs. Anatomically, both blood vessels, extending along the POVs, as well as peripheral nerves, are located under the folds of the POVs, and both can reflect light strongly compared to the surrounding tissue. Further studies utilizing motion detection approaches such as Doppler OCT or optical micro-angiography (OMAG) to resolve moving particles from static scatterers are required to identify the nature of these reflective morphological features. Furthermore, limbal stem cells and early transient amplifying cells are characterized by significantly smaller size and tend to line up against the LC walls, compared to limbal epithelium cells which are larger in size and populate the bulk of the LC. Therefore, we speculate that the cells marked with the blue arrow in Figure 4.3 (D) are most likely limbal stem cells and/or early transient amplifying cells, though further studies are required to prove this hypothesis.

Although the novel LS SD-OCT system has shown excellent research potential in clinical and biomedical imaging, there are still several limitations that need to be addressed in the future. First, the effective lateral FOV shown is ~700×700 μm, whereas the optical design allows ~1400 μm FOV in the y-direction. The reduced FOV is related to 2 factors: a) the optical power of the imaging beam has a Gaussian intensity distribution along the illumination line, which results in spatially dependent SNR within each B-scan, where the SNR is lower at the 2 ends of the frame relative to the central position along the line; b) the curved surface of the cornea results in lower image contrast at the 2 ends of the

B-scan relative to the center, as less of the backscattered light is coupled into the NA of the imaging objective for locations where the curvature is stronger. The former problem can be improved by shaping the Gaussian line into a uniformly illuminated line by use of a Powell lens. This approach will ensure constant SNR across the lateral FOV and allow for use of the full FOV. [121,122]. The latter problem can be compensated by correcting the defocus aberration, using a zero power contact lens over the cornea, or applying a curved scanning pattern of the corneal surface.

Next, in the current setup, both the digital resolution in the y-direction and the spectral resolution are not sufficiently high, according to the Nyquist sampling theorem. The low digital spatial resolution may cause aliasing, and the low spectral resolution results in a reduced OCT signal at a large depth. However, these two parameters cannot be increased simultaneously because of the contradiction of the sample to camera magnification in the y-direction and beam size entering the spectrometer in the x-direction. This paradox can be resolved by replacing the doublets before the transmission grating with a pair of perpendicularly oriented cylindrical achromatic lenses [123]. Replacing the transmission grating, camera lens, and camera may also help resolve this problem.

Another problem we have not addressed is the multi-scattering induced spatial crosstalk within a B-scan. The confocal gate of the point-scan OCT intrinsically rejects the multi-scattering signal, while FF TD-OCT and FF SS-OCT reduce the crosstalk using the spatial incoherence light generated by light-emitting diode [101], random deformable mirror [54], or multimode fiber [55,124]. Spatially incoherence light generated with the multimode fiber and sparse sampling using a digital micromirror device might be two promising solutions to suppress the spatial crosstalk in LS SD-COT [125].

4.5 Conclusion

In conclusion, we have developed a novel LS SD-OCT system that combines high spatial resolution and fast image acquisition, which is necessary for *in-vivo*, non-contact imaging of the cellular structure of the human cornea and limbus. We also show for the first time volumetric images of the cellular structure of the limbal crypts and the POVs acquired *in-vivo* and without contact from the healthy human limbus. When adopted for clinical use, the LS SD-OCT can aid the diagnosing of potentially blinding corneal and limbal pathologies, monitoring the effectiveness of various treatments, and assist ophthalmic surgeons with pre-operative planning.

Chapter 5

Restoring Diffraction-limited Lateral Resolution in Broadband LS SD-OCT

5.1 Introduction

Optical coherence tomography (OCT) allows for *in-vivo*, contactless, non-invasive volumetric imaging of scattering biological tissues with cellular level resolution and high image acquisition speed. While the axial OCT resolution is defined only by the coherence length of the light source [76], as in other optical imaging techniques, the diffraction-limited OCT lateral resolution is determined by the numerical aperture (NA) of the microscope objective and the beam waist of the optical beam incident on it. The OCT lateral resolution can be enhanced by increasing the effective NA; however, this approach results in a significant reduction in the depth of focus (DOF), which is inversely proportional to the square of effective NA. Therefore, the optical design of an OCT system includes a compromise between the system's lateral resolution and DOF, depending on the application the system is designed for. In cases that prioritize imaging morphological details of size larger than a single cell, a low NA optical design is used to maintain a relatively uniform lateral resolution over a large imaging depth range [18,78]. In cases where the priority is imaging the cellular structure of biological tissue, high NA imaging optics is typically used [17,25], and depth scanning is performed when the regions of interest (ROIs) are larger than the limited DOF and volumetric OCT images acquired at different depths are merged using image post-processing algorithms [126].

Different methods have been developed to overcome the tradeoff between lateral resolution and DOF in OCT. The DOF can be physically extended by reshaping the incident plane wave. For example, one approach is to use an axicon lens to generate a Bessel beam illumination that can sustain a uniform lateral OCT resolution over a large depth range [127,128]. Another approach is to use a phase mask with a delicate pattern to generate multiple foci along the imaging depth [129]. Both methods can extend the DOF over 10-fold; however, the low SNR prohibits the use of such OCT technology for *in-vivo* human ocular imaging. Alternatively, optical coherence refraction tomography (OCRT) generates an isotropic synthesized point spread function (PSF) that depends only on the coherence length of the OCT light source by synthesizing multiple conventional OCT crosssectional images acquired with at different angles [130,131]. However, OCRT requires multi-angle imaging, which limits the image acquisition speed and cannot be directly applied in *in-vivo* human ocular imaging. Another approach is digital refocusing, which compensates the defocus phase in the Fourier space [132–134]. It requires no modification of the optical design of conventional OCT systems or imaging procedure and can achieve spatial invariant lateral resolution over 10-fold of the DOF in the post-processed OCT images.

Aside from defocus, higher-order wavefront aberrations due to imperfect optics and the inhomogeneous structure of the imaged biological tissue can also deteriorate the lateral OCT resolution. Hardware adaptive optics (HAO) OCT utilizes a deformable mirror to compensate for wavefront aberrations, and aberration-free images of nerve fibers and photoreceptors in the human and animal retina have been acquired *in-vivo* using this approach[71]. However, HAO-OCT systems are associated with significantly higher cost, complex and bulky optical design, and difficulty with optimal optical alignment. Furthermore, depth scanning or digital refocusing is required for HAO-OCT images when the ROI is larger than its limited DOF. Digital adaptive optics (DAO) OCT estimates and corrects the wavefront aberrations in post-processing. Based on how the wavefront aberrations are reconstructed, different DAO algorithms can be categorized into two groups: iteration-based methods and hardware-inspired methods [43,44,135,136]. Iteration-based methods estimate the aberration coefficients by optimizing image metric functions. However, there is little theoretical proof that the metric minimum or maximum corresponds to aberration-free images. Moreover, the optimization process can be trapped at local optima. Hardware-inspired methods, i.e., subaperture correlation and digital lateral shearing, are non-iterative and are digital versions of the Shack-Hartmann and lateral shearing wavefront sensors. However, independent speckle patterns lead to inaccurate estimation in the subaperture correlation method, while the digital lateral shearing method requires single point scatter filtering, which is not present in many biological tissues. All DAO methods require high lateral phase stability of the OCT signal, which is related to the OCT image acquisition rate and is also dependent on the natural motion of the imaged biological tissue (ocular saccades in the eye, heart rate, breathing rate, etc.) [137,138]. For *in-vivo* human ocular imaging, it is suggested that OCT image acquisition rate greater than 10 volumes/second is required for effective suppression of motion artefacts in the OCT images induced by natural eye motion [136]. Due to this requirement, a phase-stable point-scan OCT can only image a small field of view (FOV) or requires an additional motion tracking system [139,140]. Parallel acquisition OCT modalities, e.g., line-scan (LS) spectral-domain (SD) OCT and full-field (FF) sweep source (SS) OCT, have also demonstrated DAO to compensate aberrations in human retinal images acquired *in-vivo* [44,45]. Nevertheless, all current DAO methods are restricted to correction of monochromatic aberrations. Since high axial OCT resolution is achieved by use of broadband low coherent light sources, development of novel method for compensation for chromatic aberrations is essential for achieving lateral OCT resolution close to the diffraction limit over an extended DOF.

This paper describes a novel method of recovering OCT resolutions for images acquired with a broadband LS SD-OCT system. The broadband LS SD-OCT offers nearly isotropic spatial resolution of 2.2 × 2.3 × 1.7 μm in air and can be used in a variety of clinical and biomedical studies where *in-vivo* volumetric cellular resolution imaging of biological tissue is required. The parallel acquisition configuration and the ultrafast area camera used in the LS SD-OCT system allow for a fast volumetric imaging rate which can suppress the motion-induced lateral phase instability in i*n-vivo* imaging. In general, there are three major artifacts that impede diffraction-limited OCT resolution recovery by use of standard DAO algorithms, i.e., phase destruction, spatial-spectral crosstalk, and chromatic aberrations. The phase destruction was effectively suppressed with proper optics alignment. Localized monochromatic aberrations in different sub-bands were independently corrected with an iteration-based DAO method, and lateral registering aberration corrected sub-band tomograms reduce the spatial-spectral crosstalk and chromatics aberrations. The axial resolution is restored with phase registration of the sub-bands' interference fringes. The proposed novel reconstruction method was validated by imaging a standard resolution target, a microbeads phantom, and biological tissues such as cucumber and animal cornea.

5.2 Factors that degrade the OCT resolution in LS SD-OCT images

5.2.1 Virtual interference pinhole effect

In this work, x-direction is the scanning direction of the LS SD-OCT system, z-direction is the light propagation direction, and y-direction is the direction orthogonal to the xz-plane. Location (x, y, z) represents the center position of the optical volume under study, and (x_1, y_1, z_1) and (x_2, y_2) denote the coordinates of the imaged sample volume and the camera detection plane respectively.

Considering the light scattered back from the sample, when it reaches the camera detection plane, the electrical field can be expressed as:

$$E_{det}(x_2, y_2 \mid x, y, z) = \int h_i(x_1, y_1, z_1) s(x_1 - x, y_1 - y, z_1 - z) h_d(x_2 - x_1, y_2 - y_1, z_1) dx_1 dy_1 dz_1 \quad (5.1)$$

where $h_i(x, y, z)$ and $h_d(x, y, z)$ are the coherent point spread functions (cPSFs) of the illuminating and detecting optics and $s(x, y, z)$ is the scattering distribution function of the sample. Here, the light rejected by the slit aperture is not taken into consideration since the slit is much wider than the beam waist. Note that this formula describes the single scattering regime case.

Since the OCT signal is generated by interference of the electrical fields backscattered from the imaged object and reflected from the reference mirror, the reference electrical field acts as a virtual pinhole along the x-direction under the assumption that its spot size on the detection plane is the same for all wavelengths (Figure 5.1 (A)). Incorporating the virtual pinhole in the x-direction and the camera pixel size confinement in the y-direction as $p(x, y, Z)$, where Z is the axial shift of the reference focus from the detection plane, the effective electrical field backscattered from the position (x, y, z) is:

$$\begin{aligned} E_s^{eff}(x,y,z) &= \iint h_i(x_1,y_1,z_1)s(x_1-x,y_1-y,z_1-z)h_d(x_2-x_1,y_2-y_1,z_1)dx_1dy_1dz_1 \\ &\qquad p(x_2,y_2,Z)dx_2dy_2 \\ &= \int s(x_1-x,y_1-y,z_1-z)h_i(x_1,y_1,z_1)[\int h_d(x_2-x_1,y_2-y_1,z_1) \\ &\qquad p(x_2,y_2,Z)dx_2dy_2]dx_1dy_1dz_1 \\ &= s(x,y,z)\otimes[h_i(x,y,z)[h_d(x,y,z)\otimes p(x,y,Z)]] \end{aligned} \tag{5.2}$$

where $\otimes$ denotes convolution. Under the assumption that the pinhole is infinitely small, i.e., $p(x, \mathrm{y}, Z) = \delta(x, z - Z)\delta(y)$, and the illuminating and detecting optical beams are underfilled such that the cPSFs are separable $h(x, y, z) = h(x, z)h'(y, z)$, E_s^{eff} can be simplified as:

$$E_s^{eff}(x,y,z) = s(x,y,z)\otimes[h_i(x,z)h_d(x,z-Z)h_i'(y,z)h_d'(y,z)] \tag{5.3}$$

Here, $h_{i,d}$ and $h'_{i,d}$ refer to the illumination and detection cPSFs in x- and y-direction, respectively, considering that the beam waists and focus positions can be different in these two transverse directions. Since the illuminating beam radius along y-direction is much broader than that of the detecting (420 μm vs. 1.5 μm), the effective cPSF of the scattering light can be further simplified as:

$$h_s(x,y,z) = h_i(x,z)h_d(x,z-Z)h_d'(y,z) \tag{5.4}$$

It is clear from Equation (5.4) that the effective detection focal plane in the xz-plane is axially shifted due to the reference signal, while it is not affected in the yz-direction.

The virtual interference pinhole acts as a confocal gate in the x-direction and reduces the necessity of deploying physical apertures; however, it results in phase loss if the focal planes are miss-aligned. For simplification, we only consider the effective cPSF of the scattering light in the xz-plane and assume the illumination and detection cPSFs are Gaussian with the same beam waist and focal position. The virtual pinhole's focal plane is shifted axially, leading to a shift in the effective detection focal position (Figure 5.1 (B)). The coherence transfer function (CTF), $H_{i,d}(k_x, z)$, which is the Fourier transform of the cPSF, can be represented as $H_{i,d}(k_x,z)=\frac{\omega}{\sqrt{2}}exp(-\frac{\omega^2}{4}k_x^2+i\frac{z}{2k}k_x^2)$. The CTF of $h_s(x,z)$ is:

$$\begin{aligned}H_s(k_x,z) &= H_i(k_x,z)\otimes H_d(k_x,z-Z)\\ &= \begin{cases}\sqrt{\frac{\pi}{2}}\omega\frac{e^{-\frac{\omega^2-i\frac{2z}{k}}{8}k_x^2}}{\sqrt{1-i\frac{2z}{k\omega}}}, & |z|\gg Z\\ \sqrt{\frac{\pi}{2}}\omega e^{-\frac{\omega^2+\frac{Z^2}{k^2\omega^2}}{8}k_x^2}, & z=\frac{Z}{2}\end{cases}\end{aligned} \tag{5.5}$$

It can be seen that when $|z|\gg Z$, $H_s(k_x,z)$ is irrelevant with the focus separation Z and its phase information is well preserved; however, the completely lost phasor at $z=Z/2$ leads to a failure of DAO (Figure 5.1 (D)).

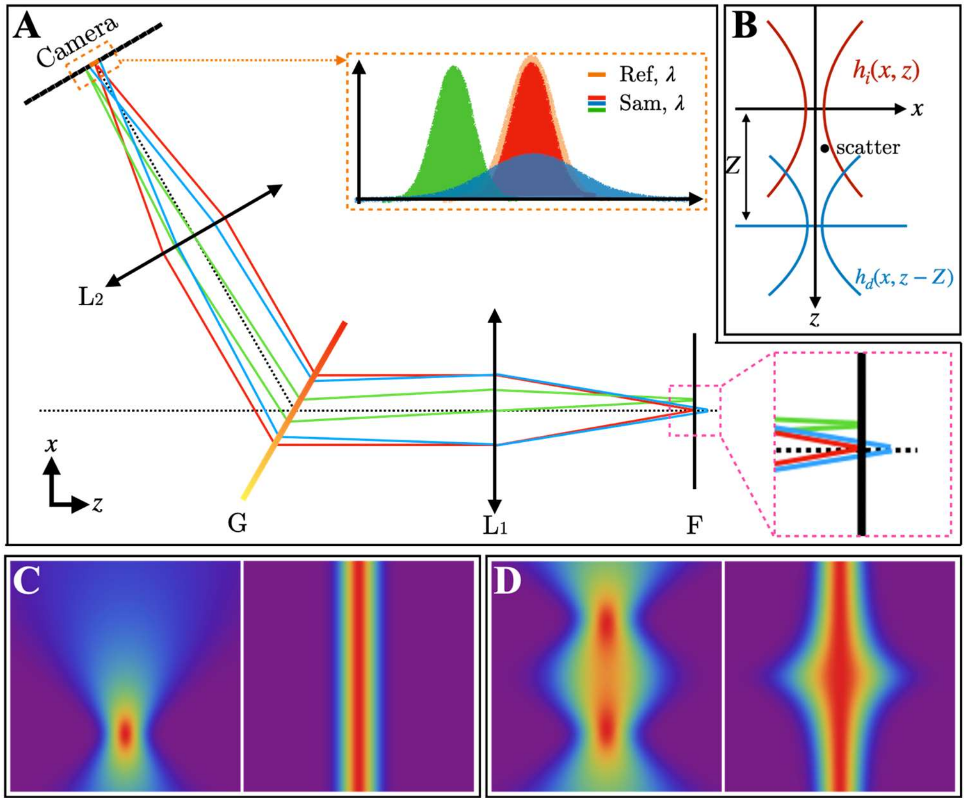

Figure 5.1 Virtual interference pinhole effect. (A) Schematic of the simplified detection optics of the LS SD-OCT system. The orange envelop in the upper-right box represents the spot of the reference light, while the light spots backscattered from the sample are labeled in red, green, and blue. The reference spot confines the region within

which the interference signal is collected. The interference signal reaches the highest when the reference light interferes with the sample light scattered within the conjugation volume of the reference focus. (B) Schematic of the illuminating cPSF $h_i(x,z)$ and shifted effective detecting cPSF $h_d(x,z-Z)$. (C) Original cPSF $h_s(x,z)$ (left) and refocused cPSF $\tilde{h}_s(x,z)$ (right) when the illuminating and effective detecting focal planes are overlapped ($Z=0$). The refocused $\tilde{h}_s(x,z)$ maintains the waist of $h_s(x,z)$ at all depths since phase information is preserved. (D) Original cPSF $h_s(x,z)$ (left) and refocused cPSF $\tilde{h}_s(x,z)$ (right) when the illuminating and effective detecting focal planes are separated ($Z \neq 0$). $\tilde{h}_s(x,z)$ cannot recover the diffraction-limited resolution in the middle of the two focal planes because phase information is lost.

Aligning the illumination, detection, and reference focal planes at the same axial position would be ideal such that phase of the OCT signal is lossless. However, it is impractical to fulfill this requirement for a broadband light source given the fact that the axial achromatic aberration is not negligible. Nevertheless, the failure of the DAO to properly compensate the monochromatic aberrations is significant only when $|Z| > z_R$ (Figure 5.9 (A))., where z_R is the Rayleigh range. The beam size of the refocused cPSF $\tilde{h}_s(x,z)$ will not be distorted significantly if the separation Z of the focal planes is less than z_R for all wavelengths (Figure 5.9 (B)). We determined that the Rayleigh range of the LS SD-OCT system used in this study was ~7.9 μm by fitting the axial PSF peaks of a reflecting mirror with the theoretical axial amplitude response function of a Gaussian beam (Figure 5.10).

5.2.2 Spatial-spectral crosstalk

In LS SD-OCT, the spatial distribution of the light backscattered from the imaged object in the y-direction and the spectrum of that light are recorded by an area complementary metal-oxide semiconductor (CMOS) camera. Because of this unique information encoding configuration, it is possible that different wavelengths scattered from the same position (y_0) on the sample plane are projected onto different y-coordinates on the camera: $I(y_0) \rightarrow I(y(y_0,k),k)$ (Figure 5.2 (B)), which is called spatial-spectral crosstalk in this work. The spatial-spectral crosstalk can be caused by the tilted optical axis of the grating with respect to the plane of the camera sensor, chromatic aberrations in the lateral direction, multi-scattering from the imaged object, etc. The discussion in this work focuses only on the relative alignment between the diffraction grating and the camera sensor, and the chromatic aberrations. On one hand, the spread of y_0 to $y(y_0,k)$ reduces the lateral resolution in the y-direction (Figure 5.2 (D)); on the other hand, the distorted spectrum (Figure 5.2 (C)) results in a broader axial PSF (Figure 5.2 (E)).

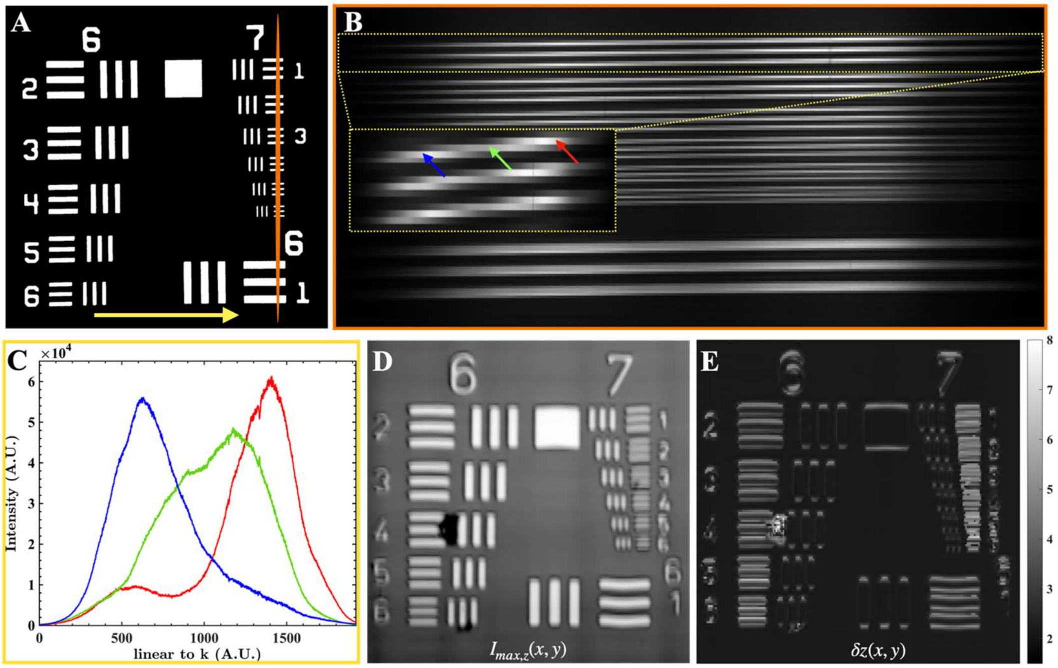

Figure 5.2 Spatial-spectral crosstalk in LS SD-OCT. (A) Schematic showing the illuminated region (orange) of an USAF resolution target placed at the detection focal plane. (B) Raw data recorded by the camera. The image pattern corresponds to the light reflected by the resolution bars of Group 7. In the case of perfect optical alignment, the reflective lines on the sensor plane should be parallel to the pixel rows. Tilted lines (yellow box) suggest the existence of spatial-spectral crosstalk. (C) Distorted spectra corresponding to the locations in the camera plane marked with the colored arrows in (B). (D) Log-scale maximum intensity projection (MIP) enface image of the USAF target. The resolution in the y-direction is affected significantly by the spatial-spectral crosstalk. (E) Axial resolution distribution. The axial PSF at the chrome pattern's horizontal edges is much broader than the rest due to the distorted spectrum shown in (C).

5.2.3 Chromatic aberrations

Chromatic aberrations in both the axial and lateral directions are not negligible in imaging systems with broadband light sources and cannot be corrected with HAO/DAO. Achromatizing lens has been utilized to correct axial chromatic aberration in retinal imaging with AO-UHR-OCT [70,141]. However, chromatic aberrations have not been addressed for imaging anterior human eye (cornea and limbus) in UHR-OCT [17,18,95,142]. The axial chromatic focal shift from the minimum to maximum wavelength in our LS SD-OCT system is larger than 15 μm in free space (Figure 5.11 (A, B)), which is about twice the Rayleigh range. The chromatic aberrations in the lateral direction introduce dependency of the spatial-spectral crosstalk on the measured location. (Figure 5.11 (C, D)). Therefore, characterizing the spatial-spectral crosstalk and correcting the spatial-spectral information before imaging are impractical.

5.3 Methods

5.3.1 Broadband LS SD-OCT system

The broadband LS SD-OCT system setup used in this study was similar to the one previously reported for *in-vivo* imaging of human cornea and limbus [143]. However, there are two main differences between the two systems. Firstly, we replaced the femtolaser with a combination of a supercontinuum laser (SuperK, NKT Photonics) and a superluminescent diode (cBLMD-T-850-HP, Superlum). The two light sources were coupled using a 60:40 fiber coupler (2×2, Gould Fiber Optics) and the combined emission spectrum covered the spectral range from 680nm to 910 nm with an effective full width at half maximum (FWHM) bandwidth of ~200 nm. The FWHM axial resolution was measured as 1.7 μm in air. Secondly, the effective detection area of the camera was reduced from 1920×800 (spectral×spatial) to 1920×500 as the edge signal is weak because of the Gaussian distribution of the optical power along the line illumination. One benefit from reducing the detection area is that the camera readout frame rate is increased from 2.5 kHz to 3.0 kHz, which is close to the 3.2 kHz B-scan rate suggested to maintain phase stability for *in-vivo* human ocular imaging [45]. The sample power measured after the imaging objective was 2.1 mW. System's signal to noise ratio (SNR) was measured as 89 dB with an exposure time of 320 μs at the center of the Gaussian illuminating line near the zero optical delay. All 3D images consisted of 500 B-scans. The system design and scanning protocol allowed for the acquisition of a single 3D tomogram with a lateral field-of-view (FOV) of ~ 0.86 mm × 0.56 mm (x × y) and 1.29 mm (z) depth scanning range in free space within 0.17 seconds.

5.3.2 Sample preparation

The proposed method for correction of the spatial-spectral crosstalk and chromatic aberrations was tested on images of an USAF resolution target, a microbeads phantom, as well as biological tissues such as cucumber and a post-mortem rat cornea, acquired with the LS SD-OCT. The microbeads phantom was prepared by mixing polystyrene microspheres with agar-based gel. The agar gel was prepared by mixing water and agar powder (Sigma Aldrich) at a weight ratio of 20:1. The agar powder was first dissolved in water at temperature $80 \sim 90\ ^{\circ}C$ and the agar gel was cooled down to $70\ ^{\circ}C$ before dispersing polystyrene microbeads with a diameter of 3 μm (Polybead, Polysciences).

A Spague-Dawley female rat was euthanized, and volumetric images of its cornea were acquired with the LS-SD-OCT system immediately after euthanasia. *Ex-vivo* imaging of the rat cornea was necessary due to COVID-19 related restrictions that prohibited research studies on live animals at the time these experiments were carried out. The post-mortem animal imaging procedure was approved by the University of Waterloo Office of Research Ethics. Glass coverslips were placed on the surface of the microbeads phantom, cucumber, and the rat cornea during the imaging procedure in order to reduce the specular reflection from the surface of the imaged object and to allow for axial phase correction and registration.

5.3.3 OCT signal reconstruction procedure

The virtual interference pinhole effect described in Chapter 5.2.1 requires better optical alignment of the LS SD-OCT system. It cannot be corrected digitally because of the phase information loss. In contrast, spatial-spectral crosstalk and chromatic aberrations can be digitally compensated by independently correcting the monochromatic aberrations in the sub-band and sub-region tomograms and registering them afterward. The procedure of the OCT signal reconstruction is described in Chapter 5.5.4. In short, the raw data was first split into three sub-bands after background subtracting and wavenumber interpolation, and three corresponding tomograms were obtained through the standard OCT image processing procedure. Axial phase correction was applied to each sub-band OCT image before dividing it into sub-regions (typically 4×4). For each 3D sub-band and sub-region image, the aberration coefficients at different depths were estimated using an iteration-based DAO algorithm, and aberration-free tomograms were generated by applying the aberration phase mask according to the smoothed aberration coefficients. Next, the three sub-band images of the same sub-region were laterally registered according to the correlation of their intensity. Each sub-band image was then inverse Fourier transformed along the axial direction to perform the phase registration, and the final OCT tomogram was generated by Fourier transforming the phase registered fringes along the wavenumber space.

5.3.4 Iteration-based DAO

As the enface images of the sub-regions were small, typically 112×112 pixels in this study, the wavefront aberrations were determined via an iteration-based optimization algorithm instead of using the relative lateral shifts of the subaperture images. The wavefront error is expressed as:

$$\phi(k_x, k_y) = \sum_{n=2}^{N} \sum_{i=0}^{n} a_{n,i} k_x^i k_y^{n-i} \tag{5.6}$$

where (k_x, k_y) is the coordinate of the Fourier plane, n refers to the radical order of the aberration, and N denotes the maximum radical order considered. The cartesian coordinate was used instead of Zernike polynomials because the digital resolutions of the spatial frequencies in the x- and y-direction are different, and the asymmetrical system configuration induces defocusing phase difference, such as phase loss along the two lateral directions. The OCT signal corrected by the guessed wavefront error is:

$$\tilde{I}(x,y)\,|_{\{a_{n,i}\}} = FT^{-1}_{k_x,k_y}\left[FT_{x,y}[I(x,y)]\exp(i\phi(k_x,k_y))\right] \tag{5.7}$$

where $\{a_{n,i}\}$ refers to the set of aberration coefficients, and $FT_{x,y}$ and $FT^{-1}_{k_x,k_y}$ denote the 2D Fourier transform and inverse Fourier transform along the lateral directions respectively.

An appropriate metric as a function of the aberration coefficients is essential to the optimization process. Such a metric should be associated with the image quality, and its global minimum or maximum is supposed to correspond to the fully aberration-corrected image. Different image metric functions were compared (see Chapter 5.5.5), and the image metric functions of the scattering and reflecting OCT signals are chosen as:

$$\begin{aligned} S_{\text{scat}}\,|_{\{a_{n,i}\}} &= \sum_{x,y} -\hat{I}^{0.9}(x,y) \\ S_{\text{ref}}\,|_{\{a_{n,i}\}} &= \sum_{m=1}^{256} -p_m \log p_m \end{aligned} \tag{5.8}$$

Here $\hat{I}(x,y) = |\tilde{I}(x,y)|^2 / \sum_{x,y} |\tilde{I}(x,y)|^2$ is the normalized intensity of the enface OCT signal; the interval $\left(0, \hat{I}_{\max}|_{\{0\}}(x,y)\right)$ is divided into 256 equally spaced bins, and p_m is the normalized counts that $\hat{I}(x,y)$ falls into the mth bin.

Another critical element of a successful optimization process is the iteration algorithm which should be robust to local minima and maxima. The gradient descent algorithm and its variants can reduce the cost function efficiently by updating the parameters according to the gradient or the accumulated gradient of the function [144]. Despite the overwhelming popularity in machine learning, gradient-based methods have problems with finding the global minimum of a non-convex function. Pattern search and downhill simplex are two examples of gradient-free algorithms that are insensitive to the gradient and may get rid of some local minima [145,146]. However, both methods are deterministic, and their iteration results are highly dependent on the initial parameters; thus, their global searching ability is relatively weak. The gradient-based and gradient-free algorithms, e.g., resilient backpropagation (Rprop) and downhill simplex, have been applied in DAO to correct the aberrations of OCT [44,135]; however, there is little reports of the reliability so far. Unlike deterministic algorithms, stochastic algorithms use randomization to avoid solutions being trapped at local minima. For example, simulated annealing (SA) accepts worse random walk attempts with probability based on the Boltzmann distribution such that the iteration can escape from the local minimal traps [147]. Although it has been proven that SA can find the global minimum [148,149], its converging rate is very slow in practice. Swarm-intelligence (SI) is another category of stochastic algorithms that utilize multiple agents to collectively explore the parameter space and share information before the next iteration. The stochastic random walk enhances the exploration ability of the entire parameter space, and the information sharing ensures convergence. In this study, the performance of gradient-based and SI-based algorithms was compared (see Chapter 5.5.6) and the cuckoo search (CS) algorithm was determined to be the optimal one for processing the LS SD-OCT imaging data.

5.4 Results

5.4.1 3D resolution recovery in resolution target and microbeads phantom images

The recovery of the diffraction-limited lateral resolutions and ultra-high axial resolution in the LS SD-OCT images was first demonstrated in an USAF resolution target (Figure 5.3) and a microbeads phantom (Figure 5.4). Metric S_{ref} was used in the DAO procedure when correcting the aberrations of the resolution target image. Only the sub-region containing groups 6 and 7 patterns is presented in Fig. 3. The enface and B-scan images of the original, full-spectrum corrected, sub-bands corrected and lateral registered with and without axial phase registration OCT tomograms of the resolution target are shown in Figure 5.3 (A-D). The aberration coefficients of the enface image with the maximum intensity were determined to the 5th order and were then applied to the whole 3D tomogram. The enface image shown in the figure corresponds to the imaging depth at which the OCT signal reached its peak, and the B-scan images correspond to Group 7's horizontal patterns indicated by the black line in Figure 5.3 (A).

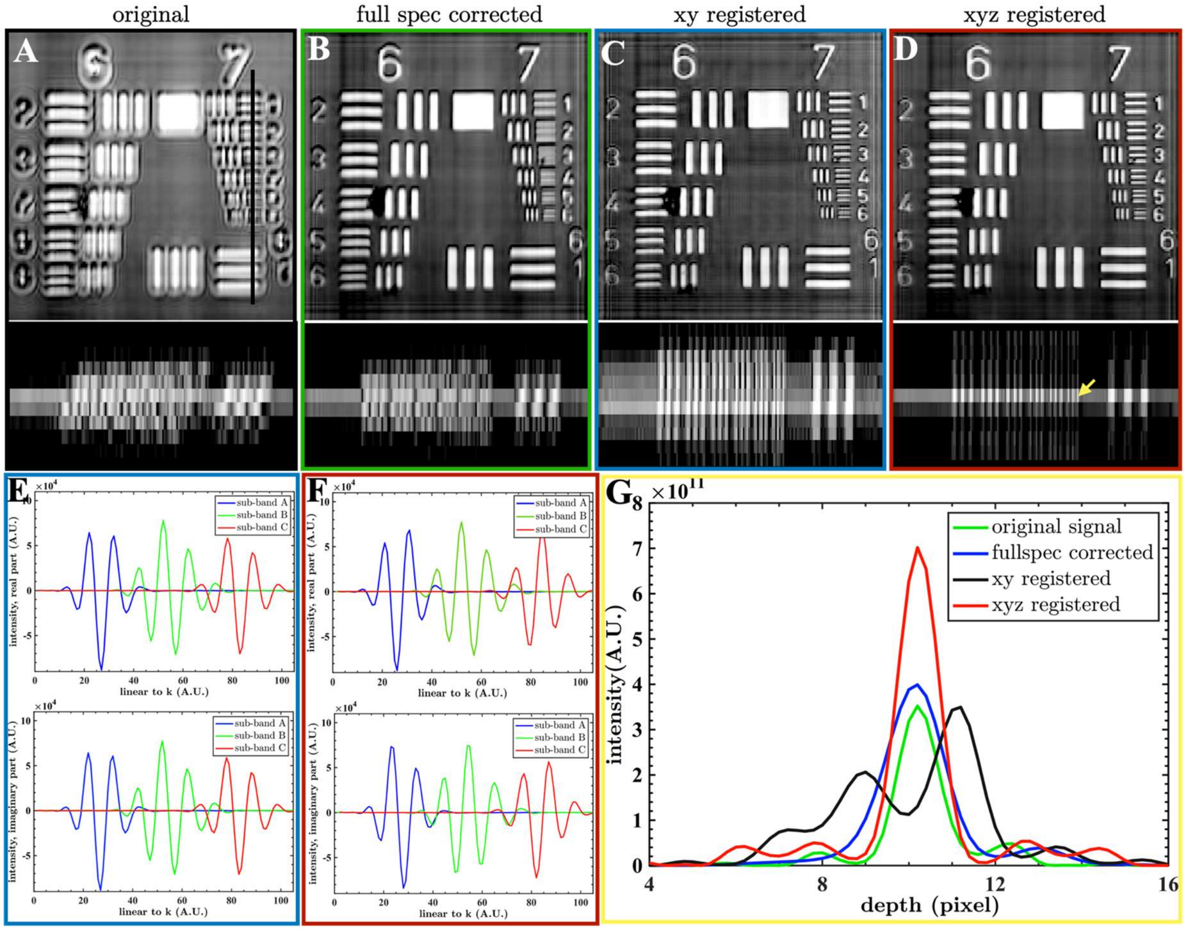

Figure 5.3 Three dimensional (3D) recovery of the OCT diffraction-limited lateral resolution and coherence length confined axial resolution in the resolution target image acquired with the LS SD-OCT system. (A-D) Log-scale enface and B-scan images of the original, full-spectrum corrected, sub-bands corrected and lateral registered with and without axial phase registration OCT tomograms of the resolution target. The B-scan was taken at the location of Group 7's horizontal patterns indicated by the black line in (A). (E) The real and imaginary part of the interference fringes at the Group 7 Element 6, indicated by the yellow arrow in (D). (F) Phase registered interference fringes at the same location of (E). (G) The intensity of the OCT A-scan PSF signal at the location labeled in (D).

The spatial-spectral crosstalk impacts the full-spectrum corrected result in both the lateral and axial directions. In the y-direction, the impact is shown as the blurred horizontal patterns in the enface image. In z-direction, the impact is shown as the broadened signal distribution and the lateral shifts of the signal pattern at different depths in the B-scan image. The broadening of the signal corresponds to the distorted spectrum (Figure 5.2 (C)), and the lateral shifts might be generated by changes in the optical path length when the light traveled to neighboring pixels in the y-direction. Direct summation of the three laterally registered sub-band tomograms results in a reduced depth resolution because of the narrower bandwidth of each band and axial shifts of the A-scan if the dispersion is not fully compensated (Figure 5.3 (G), black line). With proper phase registration (Figure 5.3 (F)), the ultra-high axial resolution can be recovered. The intensity of the A-scan signals, $\hat{I}(z) = |E_r E_s(z)|^2$, from the chroma pattern of group 7 element 6 is compared in Figure 5.3 (G). The proposed method achieved similar FWMH with the original signal, with a much higher peak intensity.

Metric S_{scat} was used in the DAO procedure when correcting the aberrations of the microbeads image. Typical B-scans of the original, full-spectrum corrected, and fully corrected OCT images are compared in Figure 5.4 (A), and a selected ROI near the focal plane was zoomed for better visualization in Figure 5.4 (B). The axial PSFs of the microbead labeled by the green line are shown in Figure 5.4 (C). The tilted crosssection of the microbeads away from the focal plane (Figure 5.4 (B1)) shows the spatial-spectral crosstalk artifact again on the OCT image quality. The full-spectrum correction improved the lateral resolution to some extent, while its axial resolution is much larger than the coherence gate of the light. Our proposed method achieved the best image quality with the highest spatial resolutions. The proposed method produced noticeable sidelobes in the axial PSF, which resulted in the ghost pairs around the true microbeads (Figure 5.4 (B3)). This should be avoided by carefully reshaping the spectrum after the OCT signal reconstruction procedure if necessary.

The enface images of the three tomograms at the labeled depth (Figure 5.4 (A1), yellow dash line) are shown in Figure 5.4 (D), and the selected ROIs were enlarged and shown in Fig. 4E. The full-spectrum corrected image showed a decent image quality improvement (Figure 5.4 (D2)), however, still not as good as the proposed method (Figure 5.4 (D3)). In addition, due to the spatial-spectral crosstalk, a single microbead can be split into two in the full-spectrum corrected images, as indicated by the yellow arrow, while the proposed method showed the true distribution. The lateral cPSFs of the labeled microbead (Figure 5.4 (E1), green lines) along the x- and y-directions were shown in Figure 5.4 (F). The cPSF generated by the proposed method shows the narrowest waist in both lateral directions.

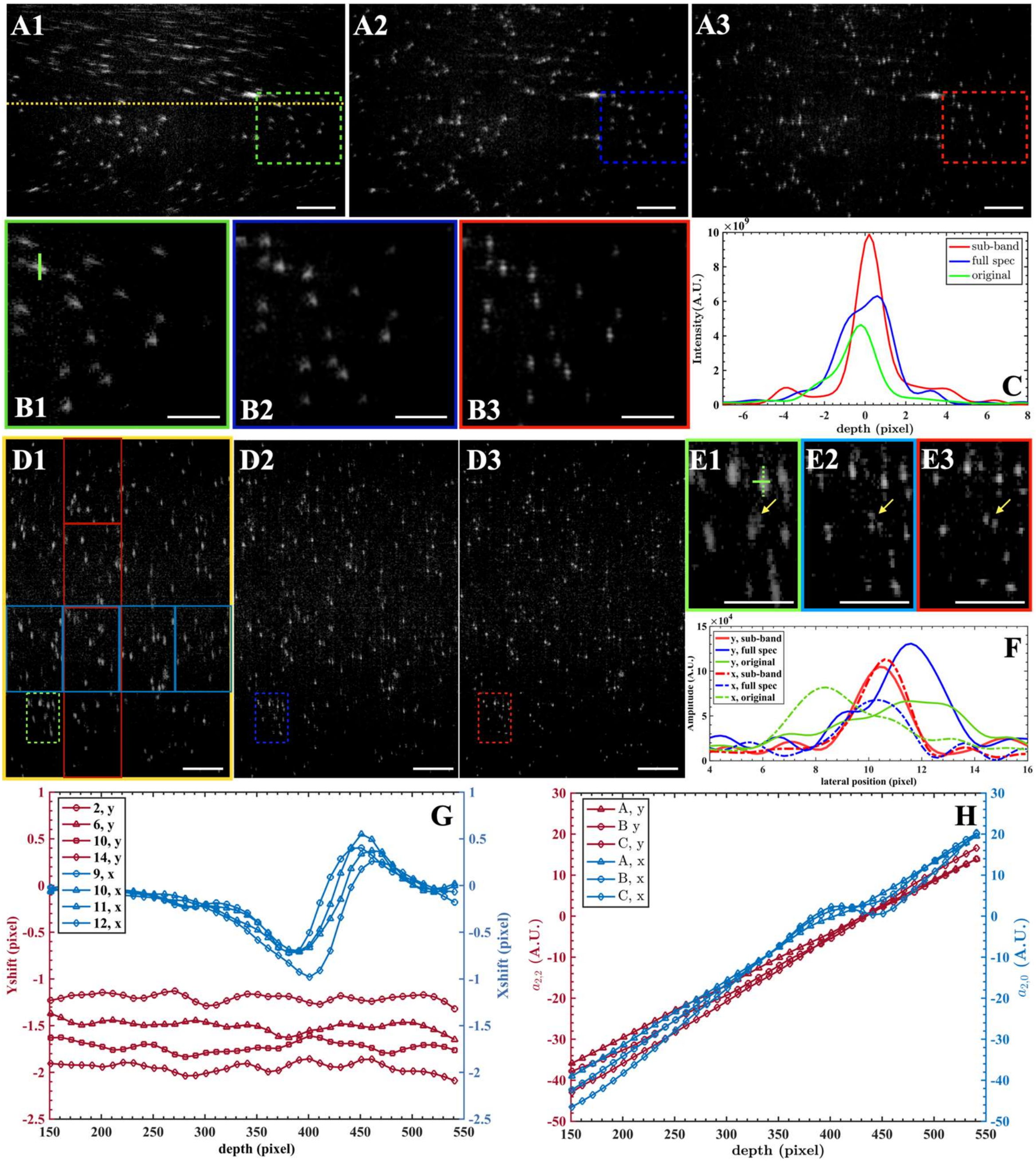

Figure 5.4 3D resolution recovery in the microbeads phantom images. (A) Log-scale B-scan image of the original, full-spectrum corrected, and sub-bands corrected and fully registered OCT images. (B) Enlarged microbeads images of the ROIs labeled in (A). (C) The intensity of the axial PSF scattered by the microbead labeled by the green line in (B1). (D) Enface image of the original, full-spectrum corrected, and sub-bands corrected and fully registered OCT images at the depth (z=360 pixel) labeled by the yellow dash line in (A1). (E) Zoomed ROIs selected in (D). (F) Amplitude of OCT signals in x- and y-directions scattered by the microbead labeled (green

solid and dash lines) in (E1). (G) Lateral shifts between sub-band A and B at different sub-regions labeled (red and blue boxes) in (D1). The labeled number indicates the index of the sub-region. (H) The refocusing coefficients, $a_{2,2}$ and $a_{2,0}$, of the three sub-bands at sub-region 10. Both the enface and B-scan images were coherently averaged with 2 adjacent neighborhoods. The lateral shifts and refocusing coefficients were smoothed along depth. Scale bars are 100 μm (original size) and 50 μm (zoomed).

The depth-dependent lateral shifts between sub-band A and B at different sub-regions are shown in Figure 5.4 (G). The y-shifts are from the 2nd column sub-region 2, 6, 10,14 (Figure 5.4 (D1), red boxes); while the x-shifts are from the 3rd row sub-region 9, 10, 11,12 (Figure 5.4 (D1), blue boxes). The y-shifts of the 4 sub-regions are well separated from each other across the whole depth range, and each y-shift's variance is small compared with the gaps. The x-shifts are about 0 at the depth far away from the focal plane; however, there are significant changes near the focal plane. The level structure of the y-shifts conveys the chromatic aberration in the y-direction. However, the reasons for the irregular but distinct pulse of the x-shifts observed around the focal plane are unclear, and further investigation is necessary. Nevertheless, the x- and y-shift curves suggest that. the sub-region division and frame-by-frame lateral shift registration are essential for reconstruction of the OCT signal in the broadband LS SD-OCT system. Figure 5.4 (H) shows the refocusing coefficients, $a_{2,2}$ and $a_{2,0}$, of the three sub-bands at sub-region 10. The obvious differences between the refocusing coefficients of three sub-bands reinforce the importance of applying DAO within narrow sub-bands instead of the full spectrum. As expected, curves of $a_{2,0}$ are straight since the system's cPSF along y-direction only depends on the detection optics, and its defocusing phasor is proportional to $z\lambda$. However, due to the influence of the virtual pinhole in the x-direction, the curves of $a_{2,2}$ are not straight, particularly in sub-band C.

5.4.2 *Ex-vivo* imaging of biology tissues

The proposed correction approach was also tested on biological tissues (cucumber and rat cornea). The original and reconstructed OCT images are presented in Figure 5.5-Figure 5.8. Metric S_{scat} was used in the DAO procedure. To balance the processing time and image quality, the aberrations were corrected to the 2nd order in DAO.

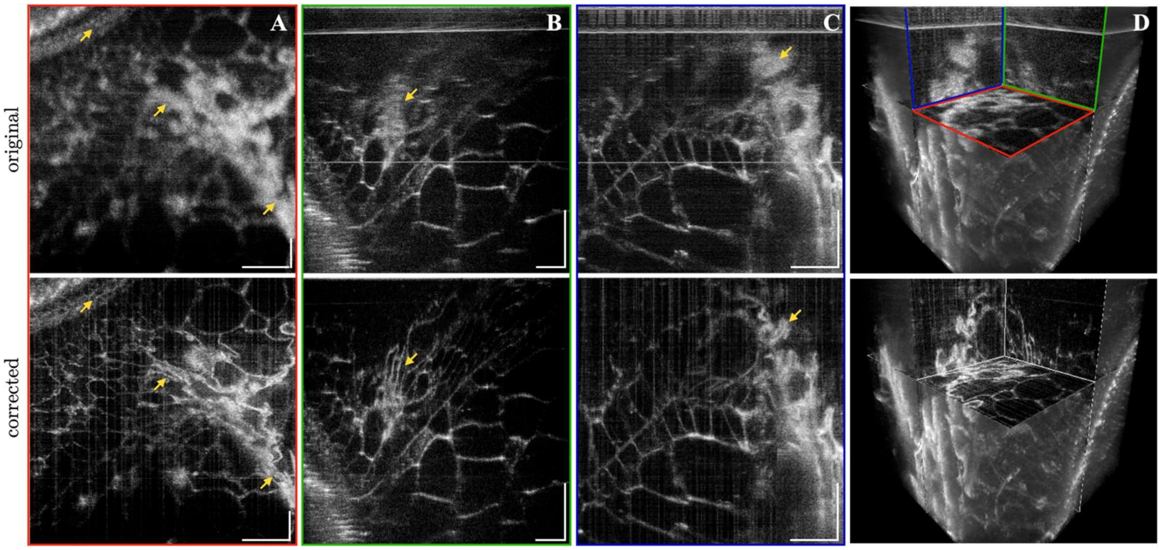

Figure 5.5 Large cucumber cells and structures of the original (top) and corrected (bottom) OCT images. (A) Enface images (xy-plane). (B) B-scan images (yz-plane). (C) Side view projections (xz-plane). (D) 3D images. All images were generated with Amira software. The 2D images were incoherently averaged with two adjacent neighborhoods. The locations of the three orthogonal planes' projection images are labeled by the boxes in (D). Scale bars are 100 μm.

For the case of imaging of the large cucumber cells and structures (Figure 5.5), the proposed reconstruction method achieved remarkable image quality improvement. The visualization of cucumber cells and delicate structures (yellow arrows), which are not resolved in the original images, indicates the resolution recovery at the depth away from the focus. Unlike in the resolution target and microbeads phantom images, the axial sidelobes of the reconstructed OCT images are not evident in Figure 5.5 (B, C). Frame-by-frame comparisons of the two tomograms enface and B-scan images can be found in Supplementary videos 5.1 and 5.2, respectively. These videos were generated using the Amira software.

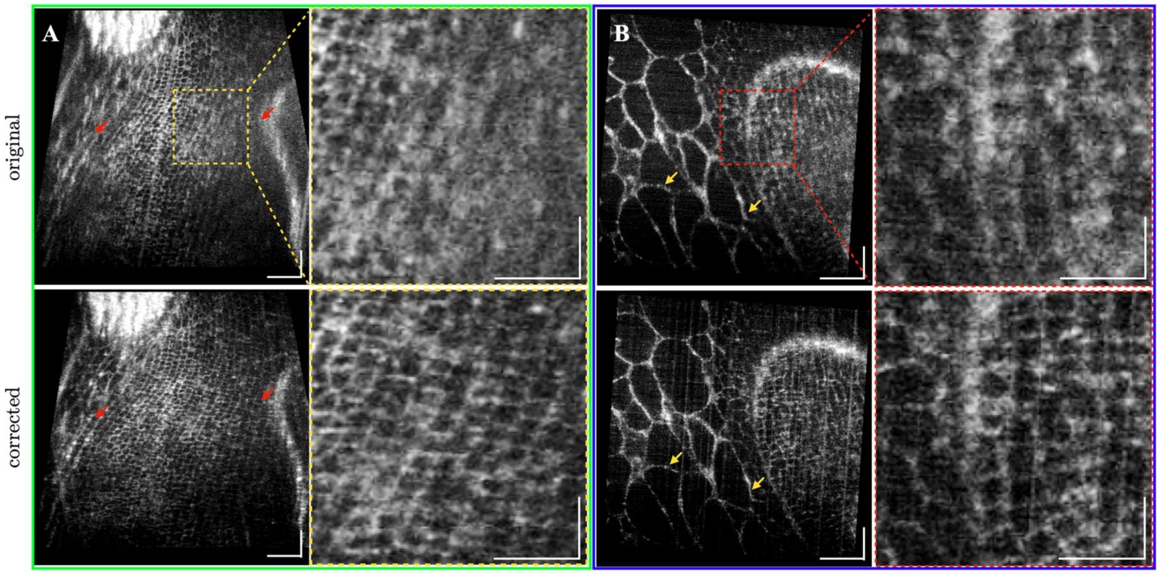

Figure 5.6 Immature cucumber cells of the original (top) and corrected (bottom) OCT images. (A) Tilted projection images with the zoomed ROIs (yellow box). (B) Tilted projection images of a different seed and the enlarged ROIs (red box). All images were generated with Amira software. Each image was incoherently averaged with two adjacent neighborhoods. Scale bars are 100 μm (original size) and 50 μm (zoomed).

Besides the large cells and structures, the LS SD-OCT system with micrometer level resolution can also resolve the small immature cells underneath the cucumber seed surface. The diameter of these immature cells is typically about 10 μm, which is smaller than the epithelium cells of the human cornea. However, due to the limited DOF and the orientation of curved surface of the cucumber seeds, only a small fraction of the immature cells can be resolved (Figure 5.6 (A), top). The proposed reconstruction method has successfully refocused the images, and the small cells in the regions indicated by the red arrows and yellow box can be resolved (Figure 5.6 (A), bottom). Figure 5.6 (B) shows a slightly tilted enface projection of another cucumber seed with a different orientation. Although the large cells can be resolved in the original image, the correct one shows thinner boundaries (yellow arrows). In addition, the small immature cells are better visualized in the corrected image, as shown in the zoomed ROI.

In the case of *ex-vivo* rat cornea imaging, the imaging focal plane was first positioned at a depth near the boundary between the epithelium layer and the Bowman's membrane (Figure 5.7). All the five layers of the rat cornea can be resolved in the B-scan images of the original OCT tomogram (Figure 5.7 (A), top). The image quality improvement in the corrected B-scan image (Figure 5.7 (A), bottom) is not as noticeable as in the microbeads phantom images and the cucumber seeds images because of the lack of small morphological structures. Nevertheless, the reduced crosssection of the stromal nerve (yellow arrows) located in the middle of the stroma is clear evidence of the effectiveness of the proposed reconstruction method. In the enface images, the superiority of the corrected image is more apparent. The local contrast has been enchanted in the enface image near the focal plane (Figure 5.7 (B)), while the resolution is recovered in the out-of-focus enface image (Figure 5.7 (C)).

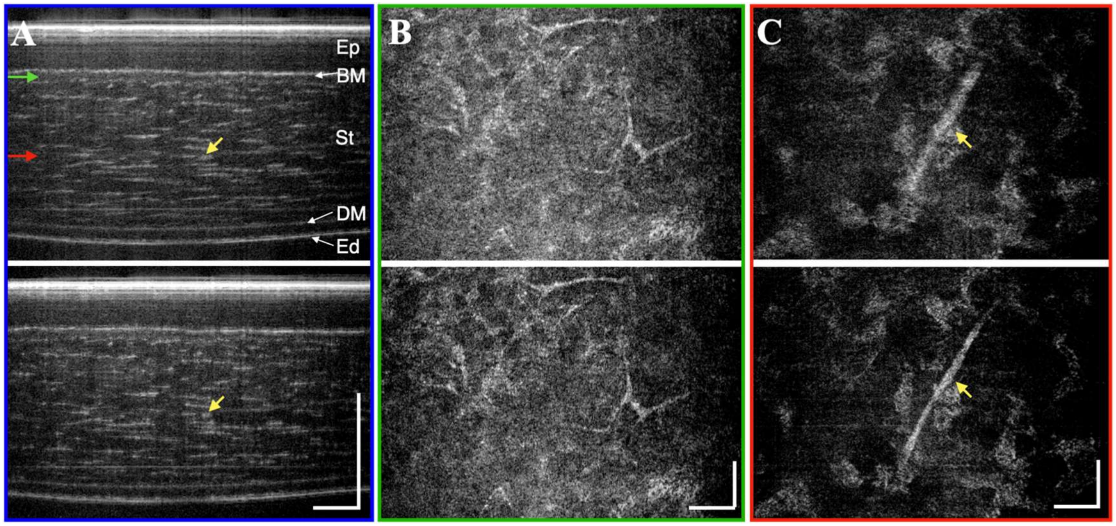

Figure 5.7 Original (top) and corrected (bottom) OCT images of *ex-vivo* rat cornea. (A) A typical B-scan image of the rat cornea. (B) The enface image underneath the boundary of the epithelium layer and Bowman's membrane. (C) Enface image in the middle stroma. All images were generated with Amira software. Each image was incoherently averaged with two adjacent neighborhoods. Ep: epithelium; BM: Bowman's membrane; St: stroma; DM: Descemet's membrane; Ed: endothelium layer. Scale bars are 100 μm.

Figure 5.8 shows the MIP images of the rat corneal endothelium layer. The focus position was shifted to the posterior end of the cornea. However, due to the title and curvature of the endothelium layer, only a small fraction was in focus. The endothelium layer was first corrected based on the extrapolation of the aberration coefficients determined within the stroma, followed by a flattening algorithm that shifted the endothelium surface to the same depth with the sub-pixel resolution. Both the high and low frequencies in the 3×3 sub-regions were then filtered out with a bandpass filter, and the contrasts of the 9 sub-regions were adjusted to the same level. The reconstructed images reveal the boundaries of the polygonal endothelial cells, which is blurred or missing in the original images.

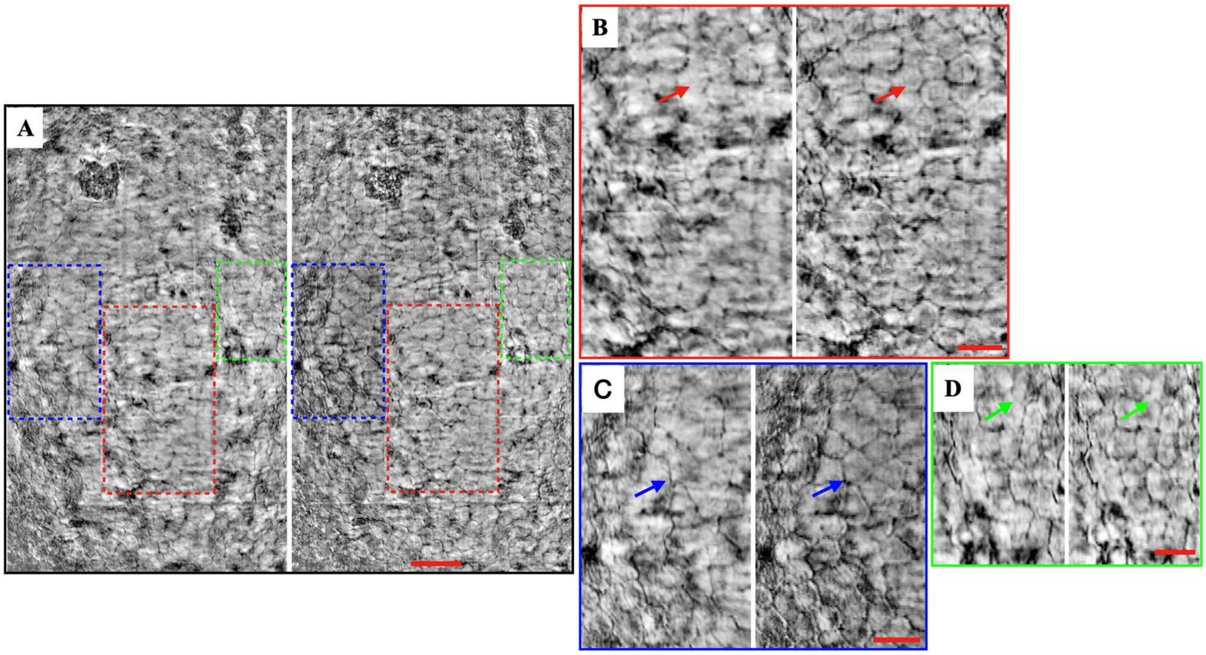

Figure 5.8 Flattened endothelium layer of *ex-vivo* rat cornea. (A) Original (left) and corrected (right) enface maximum intensity projection (MIP) of the endothelium layer. (B-D) Enlarged endothelium images of the selected ROIs labelled in (A). Scale bars are 100 μm (original size) and 50 μm (zoomed).

5.5 Supplement information

5.5.1 Virtual interference pinhole affects DAO's performance in x-direction

The virtual interference pinhole results in phase information loss when the illuminating and effective detecting focal planes are mismatched, which leads to the DAO corrected cPSF's beam radius above diffraction limitation in the middle of the two focal planes. According to Equation (5.5), the extent of the distortion is dependent on the separation of the two focal planes. Here, we show the distortion is acceptable if the separation Z is small. The OCT images of a resolution target were collected at different depths with large and small Z. A Gaussian filter is digitally applied to reduce the affection of spatial-spectral crosstalk and chromatic aberrations, and the effective spectrum is centered at ~800 nm with a bandwidth of 50 nm. For each OCT image, sample signal $E_s E_s^*(x, y)$ and interference signal $E_r E_s^*(x, y)$ are separated, and the interference signal is corrected to the 5th order using iteration-based DAO to generate the aberration-free signal $E_r \tilde{E}_s^*$. According to group 7 element 6's local contrast in $E_s E_s^*(x, y)$ and $E_r E_s^*(x, y)$, the separation Z is about 110 μm in Figure 5.9 (A) and less than 40 μm in Figure 5.9 (B). The difference of corrected resolutions in the x-direction is noticeable: Figure 5.9 (A3), all group 7's vertical bars are blurred at depth -10 μm and 10 μm; while in Figure 5.9 (B3), all elements can be clearly resolved.

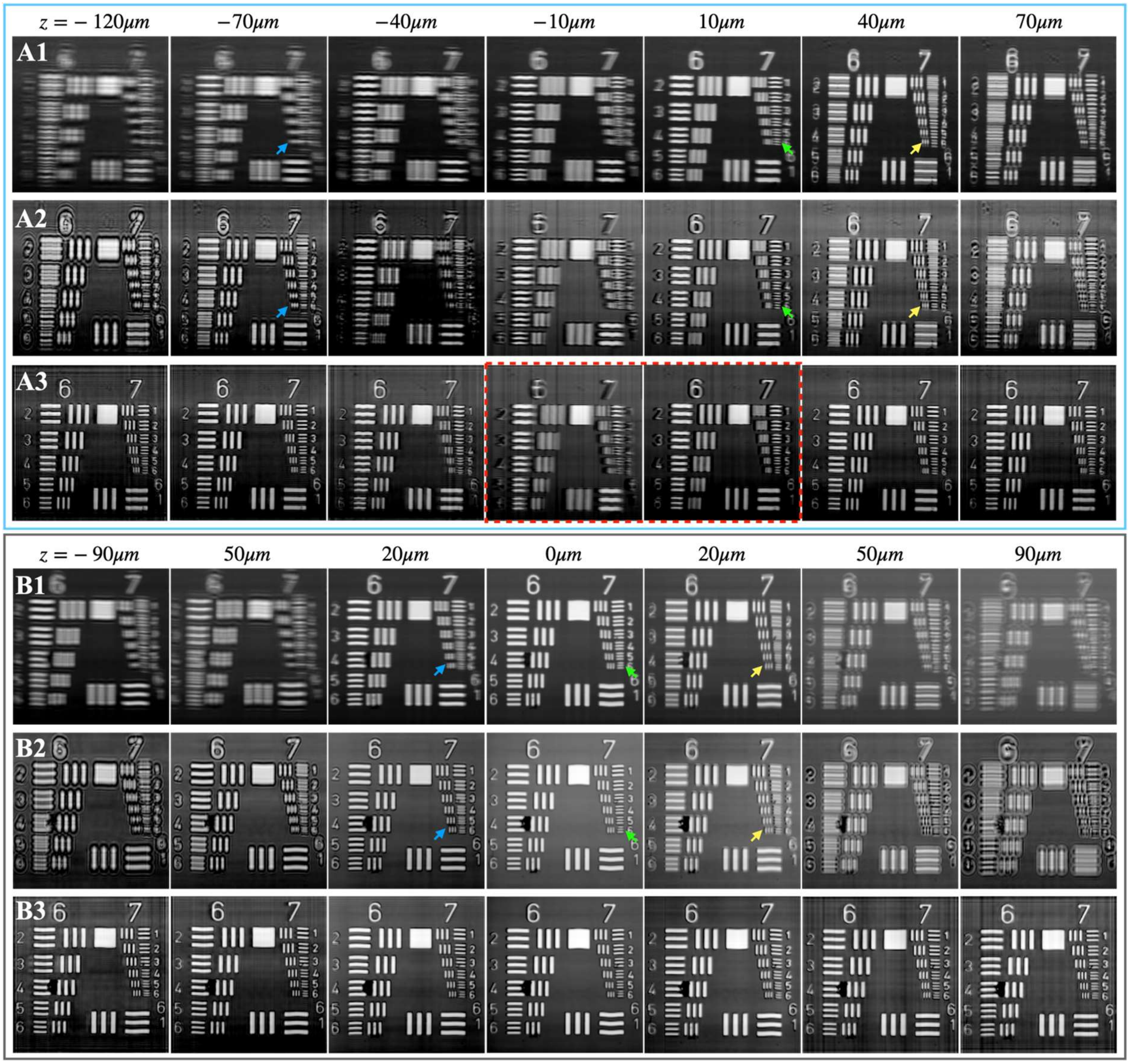

Figure 5.9 DAO's performance is affected by focal planes' separation Z. (A) Log-scale enface images of groups 6 and 7 of a positive USAF 1951 target with large Z at different depths: sample signal $E_sE_s^*$ (top), interference signal $E_rE_s^*$ (middle), and aberration-corrected interference signal $E_r\tilde{E}_s^*$ (bottom). The illuminating, detecting, and reference focal planes are at depths about 40 μm (yellow arrow), 10 μm (green arrow), and -70 μm (blue arrow), respectively. At depth -10 μm and 10 μm, all group 7's vertical bars cannot be resolved by DAO (red box)

since the phase information is lost. (B) Log-scale enface images of groups 6 and 7 with small Z at different depths: sample signal $E_s E_s^*$ (top), interference signal $E_r E_s^*$ (middle), and aberration-corrected interference signal $E_r \tilde{E}_s^*$ (bottom). The illuminating, detecting, and reference focal planes are at depth about 20 μm (yellow arrow), 0 μm (green arrow), and -20 μm (blue arrow), respectively. All elements are resolved with DAO.

5.5.2 Rayleigh range of $\boldsymbol{h_s}(\boldsymbol{x}, \boldsymbol{z})$

The measurement of sample light intensity $I_s(z)$ and OCT axial PSF $h_z(z)$ with two different slit widths was performed with the same alignment as in Figure 5.9 (B). A silver mirror was used as the sample. The sample light and interference signal were recorded separately at the same depth, and each was consisted of 100 repeated B-scans. I_s and h_z were averaged according to:

$$\begin{aligned} I_s \quad &= \left\langle \Sigma_{p,n} I_s(y,p,n) / N \right\rangle_{y \in [Y_0-5, Y_0+5]} \\ h_z(z) \quad &= \left\langle \Sigma_n \, | h'_z(y,z,n) | / N \right\rangle_{y \in [Y_0-5, Y_0+5]} \end{aligned} \qquad (5.9)$$

where p is the pixel number along the spectral coordinate, n represents the B-scan number, $|\cdot|$ returns the absolute value, and Y_0 denotes the center of Gaussian distribution in the y-direction. Here, $h'_z(y,z,n)$ is the axially registered PSF with sub-pixel resolution; otherwise, the averaged PSF is distorted by inevitable mechanical motions. The slit widths were set as 1000 μm and 200 μm, both are much larger than the $1/e^2$ beam diameter (21 μm). Despite there being a significant difference in I_s between the two slit widths, their axial PSFs are close to each other. This result confirms that the interference acts as a confocal gate and the physical slit is just utilized to block the stray light. Since the maximum of the ith axial PSF h_z^i is proportional to the amplitude of the effective cPSF, $h_s(x,z)$, at depth z_i, the Rayleigh range of the effective cPSF can be calculated by fitting $\left(z_i, \max(h_z^i)\right)$ with function:

$$h_s(x=0,z) = \frac{h_0}{\left(1 + \left(\frac{z - z_0}{z_R}\right)^2\right)^{\frac{1}{4}}} \qquad (5.10)$$

where the effective cPSF $h_s(x,z)$ is assumed to follow the electric field's distribution of a Gaussian beam. The power index $1/4$ instead of $1/2$ comes from the symmetry break of x- and y-direction. z_R is determined as 7.92 μm, corresponding to a $1/e$ beam radius of 1.42 μm of the effective cPSF.

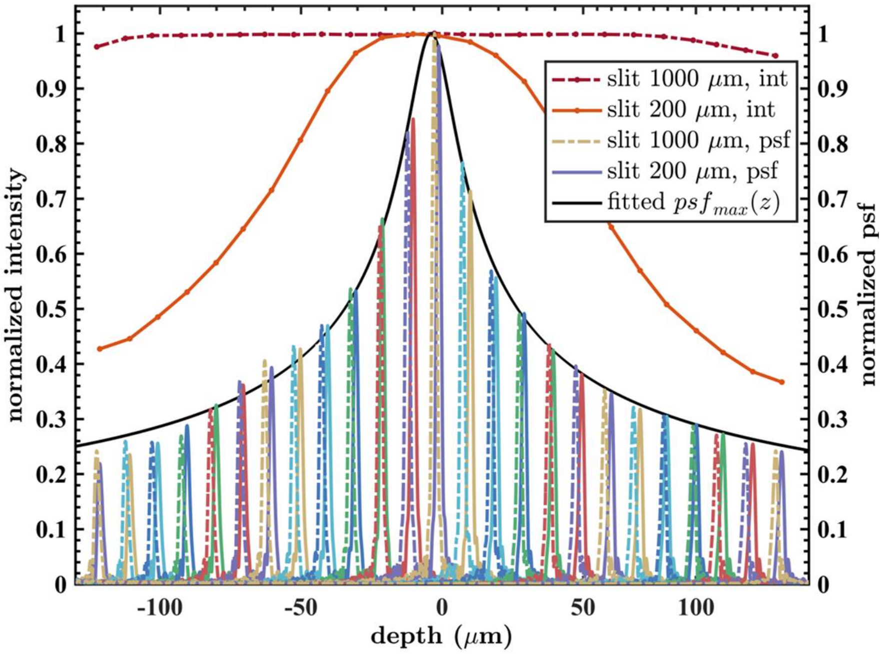

Figure 5.10 Sample light intensity I_s and OCT axial PSF h_z vs. depth with different slit widths. The dashed lines represent the intensity I_s and PSF h_z measured with slit width 1000 μm. The solid lines denote the I_s and h_z measured with slit width 200 μm. The black line shows the fitted function $h_s(x=0,z)=h_0\left(1+\left(\frac{z-z_0}{z_R}\right)^2\right)^{-1/4}$.

5.5.3 Chromatic aberrations in free space

Here, we show the existence of the chromatic aberrations of the LS SD-OCT system in free space. The resolution target was first imaged at the center of the FOV but at two different depths. The spectrum lines corresponding to group 7's horizontal chrome pattern are shown in Figure 5.11 (A). The axial chromatic focal shift of the two wavelengths labeled in blue and red is about 15 μm. The axial chromatic is not negligible since it is twice as large as the Rayleigh range determined in Chapter 5.5.2. Then we imaged the resolution target at the same depth but two different y-positions. The spectrum line pattern difference (Figure 5.11 (D)) suggests that the chromatic aberration in the lateral direction is associated with the spatial-spectral crosstalk and affects both the lateral and axial resolutions.

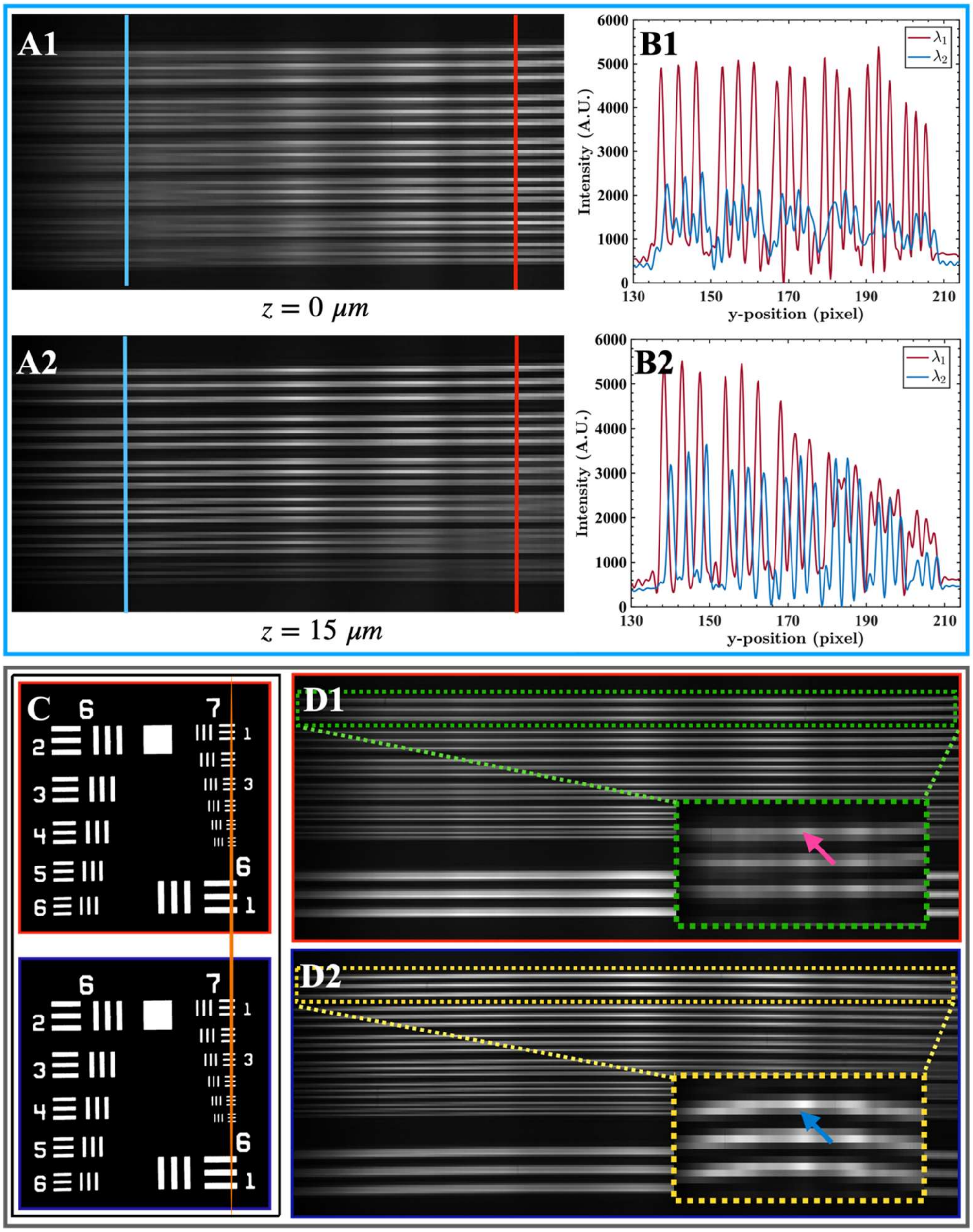

Figure 5.11 Chromatic aberrations of the LS SD-OCT in axial (top) and lateral (bottom) direction. (A) Spectrum lines of the resolution target group 7's horizontal chrome patterns. The longer wavelength is focused at z=0 μm (A1), and the shorter wavelength is focused at z=15 μm (A2). (B) Line profiles of $I_\lambda(y)$ of the two wavelengths labeled in (A). (C) Schematic showing the resolution target was imaged at the same depth but different lateral positions. The orange line represents the line illumination along the y-direction. (D) Spectrum lines of the chrome patterns. The shapes of spatial-spectral crosstalk patterns (green and yellow box) are location dependent.

5.5.4 OCT signal reconstruction procedure

The flowchart in Figure 5.12 illustrates the OCT signal reconstruction procedure in this study. The interference fringes of three sub-bands, $I_{A,B,C}(x,y,k)$, were first obtained by applying three Gaussian filters on the background-subtracted and spectrum resampled signal. Each sub-band fringe was dispersion compensated, and then Fourier transformed to generate the OCT signal $I'_{A,B,C}(x,y,z)$. The weighted average of phase difference between adjacent B-scans due to sub-micrometer involuntary axial motion was calculated as:

$$\Delta\phi_n = \arg\Big[\sum_{(y,z)\in D} I'(x_{n-1},y,z)I'^*(x_n,y,z)\Big]; n = 2,3...,N \tag{5.11}$$

where D is a user-selected region of the static area in the B-scan image, and the asterisk denotes the complex conjugate. The axial motion-induced phase error was then compensated by multiplying the OCT signal with a phasor, $\Delta\Phi_n = \sum_{i=2}^{n} \Delta\,\phi_i$, which was the accumulated phase difference of the nth B-scan with respect to the first. The three phase compensated sub-band OCT signals were then laterally split into M sub-regions: $I_{A,B,C}(x,y,z,m), m \in [1,M]$.

For each sub-band and sub-region OCT image, the aberration coefficients of the wavefront error at every 5 depth locations were estimated with an iteration-based DAO method. At each depth, the enface image was first coherently averaged with 4 adjacent enface images:

$$I_{A,B,C}(x,y,z_k,m) = \frac{1}{5}\sum_{i=k-2}^{k+2} I_{A,B,C}(x,y,z_i,m) \tag{5.12}$$

The mean enface signal was then transformed into the Fourier space. Next, the spatial frequency representation was multiplied by an aberration phase mask, and inversely Fourier transformed back to its spatial representation. The iteration was repeated until the image metric (see Chapter 5.5.5) stopped improving or the iteration number reached its maximum value. The estimated aberration coefficients were then smoothed along depth using the robust locally estimated scatterplot smoothing (RLOESS) method [150]. Next, the aberration-free tomograms were generated as:

$$\tilde{I}_{A,B,C}(x,y,z,m) = FT^{-1}_{k_x,k_y}\left[FT_{x,y}[I_{A,B,C}(x,y,z)]\exp(i\phi_{A,B,C}(k_x,k_y,z,m))\right] \tag{5.13}$$

where $FT_{x,y}$ and $FT^{-1}_{k_x,k_y}$ denote the Fourier transform and inverse Fourier transform along the lateral directions, and $\phi_{A,B,C}$ refers to the wavefront aberration estimated with the smoothed and aberration coefficients.

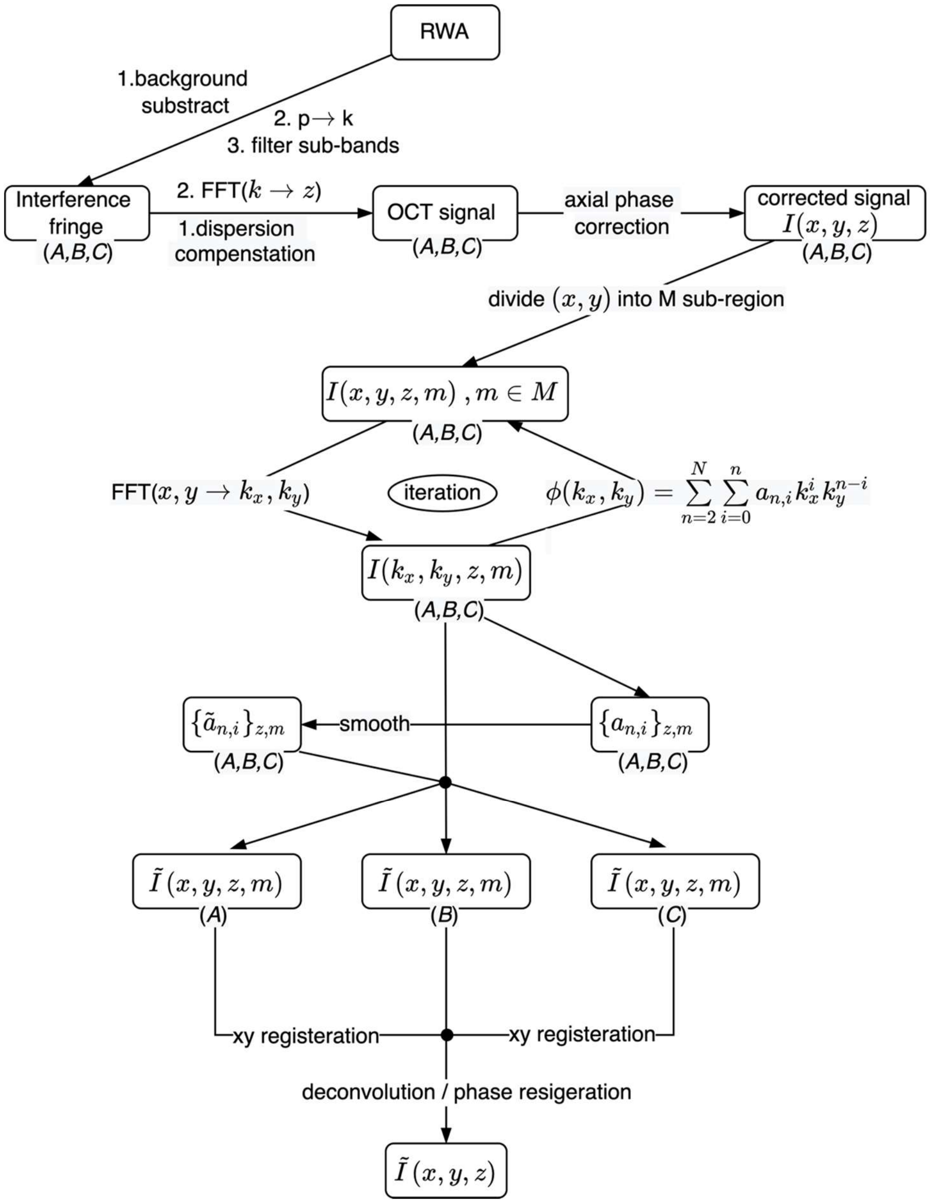

Figure 5.12 Flowchart of the OCT signal reconstruction procedure.

For each sub-region, the enface images of sub-band A and C were registered with those of sub-band B according to the amplitude correlation using the single-step DFT algorithm [151]. The translational shifts along x- and y-direction was first cursorily estimated via the maximum peak location of the correlation:

$$\max\left(\left| FT^{-1}_{k_x,k_y}\left[FT_{2,x,y,m}[\langle\tilde{I}_{A,C}(x,y,z_k,m)\rangle]FT_{2,x,y}{}^{*}[\langle\tilde{I}_{B}(x,y,z_k,m)\rangle]\right]\right|\right)\rightarrow(s_x,s_y)_{A,C,z_k,m} \quad (5.14)$$

where FT_2 denotes Fourier transform with an upsampling factor of 2, and $\langle \tilde{I}_{A,B,C}(x, y, z_k, m)\rangle$ represents the incoherent average of 5 adjacent enface images about depth z_k. The refined searching of the lateral shifts $(\tilde{s}_x, \tilde{s}_y)$ was then performed on the 50-fold upsampled correlation function within a small neighborhood around (s_x, s_y). Instead of calculating the correlation function with FFT, the 50-fold upsampled correlation inside the 1.5×1.5 pixels neighborhood was generated by the matrix-multiply DFT method [152]. This is because FFT needs to calculate the entire upsampled matrix and wastes computing resources considering we are only interested in the region around the peak.

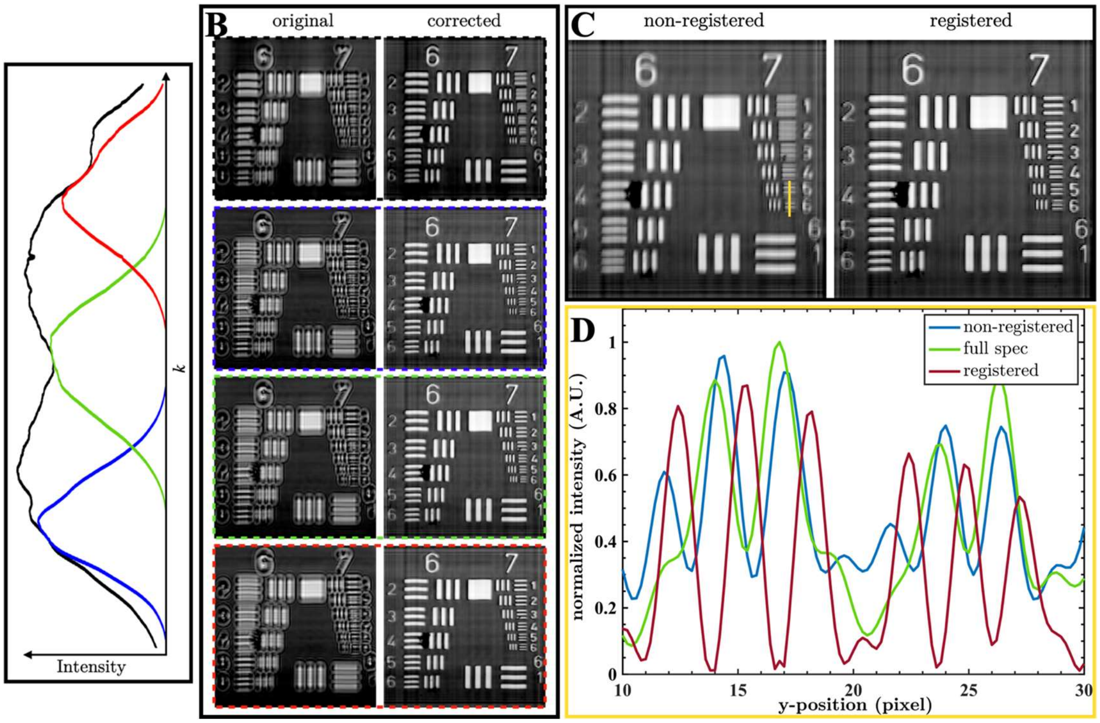

Figure 5.13 Lateral resolution restoration with the lateral registration of the monochromatic aberration corrected sub-band enface images. (A) Full spectrum (black) of the light source and the three digitally filtered sub-bands A (blue), B (green), and C (red). (B) Original and aberration-corrected (to the 5th order) enface images of the full spectrum (black box), sub-band A (blue box), sub-band B (green box), and sub-band C (red box) resolution target tomograms. All the elements are clearly resolved in the three corrected sub-band images. In contrast, the full-spectrum corrected images can only resolve the horizontal pattern up to group 7 element 2. (C) Incoherently averaged enface image of the three sub-bands with (right) and without (left) lateral registration. (D) The normalized signal of the full-spectrum corrected, and the registered and non-registered enface images along the line labeled in (C).

Once the sub-pixel lateral shifts were smoothed along the axial direction, the sub-band A and C were digitally shifted and registered with sub-band B:

$$\tilde{I}^{s}_{A,C}(x,y,z,m) = FT^{-1}_{k_x,k_y}\left([FT_{x,y}[\tilde{I}_{A,C}(x,y,z,m)]\exp(-i(k_x\tilde{s}_x^{A,C,z,m} + k_y\tilde{s}_y^{A,C,z,m}))\right) \quad (5.15)$$

The main reason that depth-dependent lateral shifts are required is that the chromatic aberration in x-direction varies with depth (Figure 5.4 (G)). A comparison of the full-spectrum aberration correction of an enface image and incoherent average of the three sub-bands' aberration-corrected images with and without lateral registration is shown in Figure 5.13. The overlapping of sub-bands AB and BC (Figure 5.13 (A)) is necessary for phase registration. The enface images of the three sub-bands were all corrected successfully by the DAO method (Figure 5.13 (B)); however, the spatial-spectral crosstalk becomes an obstacle for applying the DAO algorithm to the full-spectrum image. The lateral registration of the three corrected sub-bands enface images is the key to remove the crosstalk; otherwise, their averaged image is still blurred in the y-direction (Figure 5.13 (C, D)).

Once the lateral registration was done, the corrected interference fringes were generated via inverse Fourier transform of the three sub-band tomograms along the z-direction:

$$\tilde{I}^{s}_{A,B,C}(x,y,k) = FT^{-1}_{5,z}[\tilde{I}^{s}_{A,B,C}(x,y,z)] \quad (5.16)$$

Because of the inevitable residuals of the dispersion, the phase of the corrected inference fringes of the three sub-bands are discontinuous (Figure 5.3 (E)). In order to determine the phase discontinuities, the interference fringe of the top air-glass interface was isolated:

$$\tilde{I}^{s,g}_{A,B,C}(x,y,k) = FT^{-1}_{5,z\in Z}[\tilde{I}^{s}_{A,B,C}(x,y,z)] \quad (5.17)$$

where Z represents the depth region near the interface. The phase difference was obtained at the wavenumber, k_m, at which the fringes' overlapping hit its maximum:

$$\phi_{AB,CB}(x,y) = \arg\left(\tilde{I}^{s,g}_{A,C}(x,y,k_m)\tilde{I}^{s,g\,*}_{B}(x,y,k_m)\right) \quad (5.18)$$

The phase registration was performed as:

$$\tilde{I}^{s}(x,y,k) = \tilde{I}^{s}_{A}(x,y,k)\exp(i\phi_{AB}(x,y)) + \tilde{I}^{s}_{B}(x,y,k) + \tilde{I}^{s}_{C}(x,y,k)\exp(i\phi_{CB}(x,y)) \quad (5.19)$$

Finally, the corrected OCT tomogram was generated vis Fourier transform of the phase registered full interference fringes.

5.5.5 Image metric functions

According to Parseval's theorem, Fourier transform is unitary:

$$\int |I(x,y)|^2 \, dx dy = \int |FT_{x,y}[I(x,y)]|^2 \, dk_x \, dk_y \tag{5.20}$$

Since the DAO only applied a phase mask to the spatial frequency representation: $FT_{x,y}[I(x,y)] \rightarrow FT_{x,y}[I(x,y)]\exp\left(i\phi(k_x,k_y)\right)$, the intensity integrals of the original and corrected OCT signals are the same. Thus, the enface OCT signal is similar to an isolated system in thermodynamics: each pixel is like a particle, and the conserved pixel number and intensity integral corresponds to the isolated system exchanges no particle and energy with environment, while changing the phase mask corresponds to the system evolution. As stated in the second law of thermodynamics, the entropy of an isolated system does not decrease, it is natural to use the Shannon entropy defined in Equation (5.8) as an image metric. It is rewritten here for convenience: $S_e|_{\{a_{n,i}\}} = \sum_{m=1}^{256} -p_m \log p_m$, where p_m is the probability that the normalized intensity $\hat{I}(x,y)$ is in the mth bins. Two other commonly used image metrics in aberration correction of OCT signal are:

$$\begin{aligned} S_{de}|_{\{a_{n,i}\}} &= \sum_{x,y} -\hat{I}(x,y)\log\left(\hat{I}(x,y)\right) \\ S_p|_{\{a_{n,i}\}} &= \sum_{x,y} \mathrm{sgn}(p-1)\hat{I}^p(x,y) \end{aligned} \tag{5.21}$$

where sgn(x) is the sign function. S_{de} is so-called 'entropy' or 'Shannon entropy' in the study of synthetic aperture radar (SAR) [153,154]; however, one should not be confused with the true Shannon entropy in information theory. The power index of S_p was set as $p = 0.9$ in this study.

The three image metrics were tested with two different defocused OCT signals; one was scattered from the microbeads phantom (Figure 5.14 (A)), the other was reflected from the resolution target (Figure 5.14 (C)). In order to reduce the influence of phase destruction, spatial-spectral crosstalk, and chromatic aberrations, the OCT signals were limited in a single sub-band. Only the two defocusing aberration coefficients, $a_{2,0}$ and $a_{2,2}$, were considered, and they were determined by grid searching of the global valley of $S(a_{2,2}, a_{2,0})$. The contour plots of the image metrics of the microbeads image are shown in Figure 5.14 (B, top). From left to right, the image metrics are S_{de}, S_e, and S_p, respectively. The landscapes of the three metrics are similar except that the scales are different and S_e is noisier. The unusual number of local minima due to the noise in S_e might be related to the SNR of the signal and the number of bins used and make it challenging to apply gradient-based algorithms and SA. The grid searching result via S_e is (17.8, 23), which is slightly different from (17.4, 22.2) determined by S_{de} and S_p; although there is no noticeable difference between the three refocused images (Figure 5.14 (B, bottom)). The metrics' performances are completely different in the case of reflecting signals. The noise in S_e disappeared (Figure 5.14 (D, middle)), and the resolution target image was successfully refocused with the valley result (15.8, 19.8). However, both S_{de} and S_p failed to represent the image quality (Figure 5.14 (D, left and right)). The global minimums of these two metrics are located at (22.6, 31) and (22.6, 31.4), respectively, whereas the actual defocusing coefficients are located at smooth slopes of the two metrics, not even local valleys. From the comparison, we can see that the Shannon entropy metric S_e can correctly represent the image quality of both the scattering and reflecting signal, although the noisy landscape in the scattering case is not suitable for some optimization algorithms. On the opposite, S_{de} and S_p work well only in the scattering case, although they are smooth and compatible with all optimization algorithms.

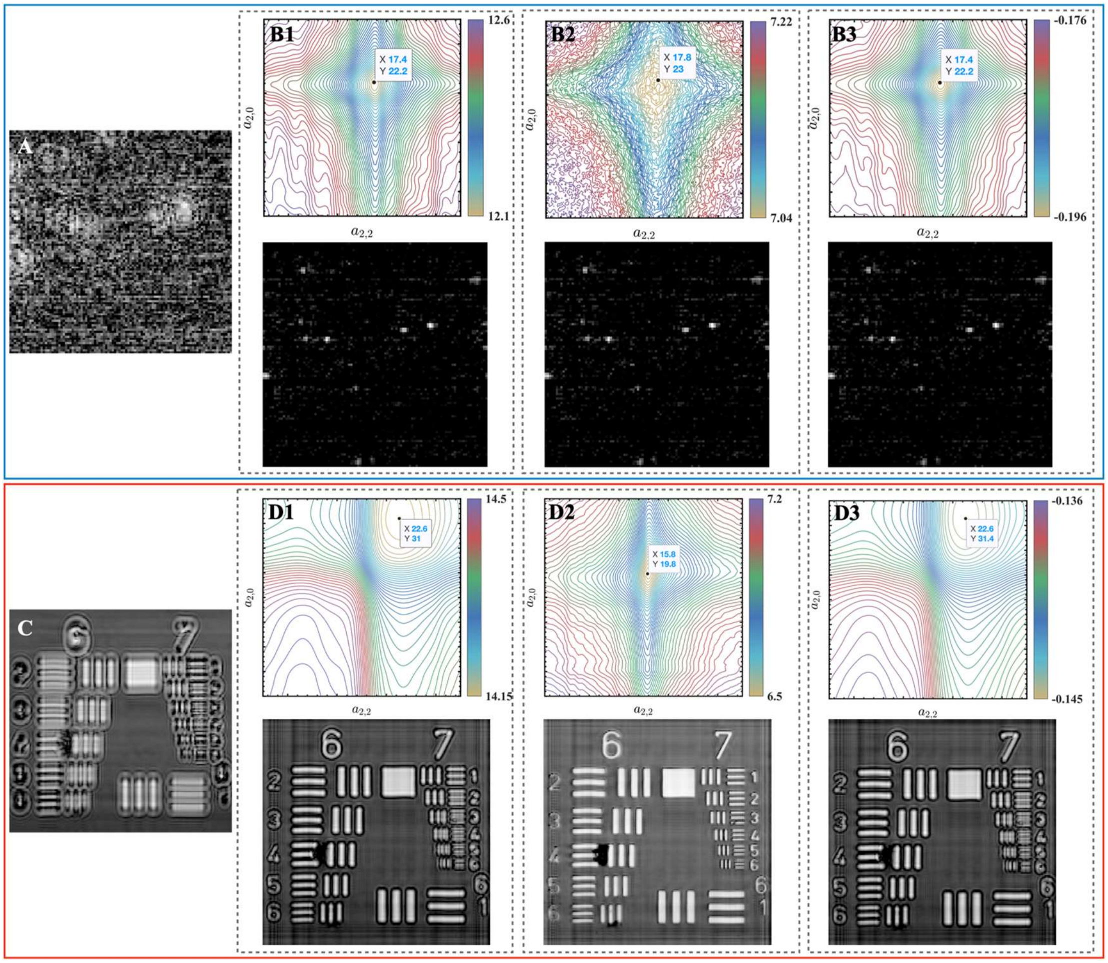

Figure 5.14 Correction of the defocused scattering (top) and reflecting (bottom) OCT signals with grid search. (A) A typical log-scale enface image of the defocused microbeads. (B) Contour plot of the image metric (top) and

the corresponding refocused image (bottom) using the coordinates of the global valley. From left to right, the three results correspond to S_{de}, S_e, and S_p, respectively. (C) A typical log-scale enface image of the defocused resolution target. (D) Contour plot of the image metric (top) and the corresponding refocused image (bottom) using the coordinates of the global valley. (D1) and (D3) were not fully refocused since the global minimums of S_{de} and S_p are both away from the actual defocusing coefficients.

5.5.6 Optimization algorithms

We first summarize the five algorithms compared here. Two gradient-based methods are standard gradient descent algorithm and adaptive moment estimation (Adam) [144,155], while the three SI-based algorithms are accelerated particle swarm intelligence (APSO), firefly algorithm (FA), and cuckoo search (CS) [156–158]. As there is only one image data during the optimizing process in this study, there is no difference between batch gradient descent and stochastic gradient descent (SGD). In this section, we use SGD to refer to the standard gradient descent algorithm. SGD updates the parameters in the opposite direction of the metric function's gradient:

$$\vec{a}_{t+1} = \vec{a}_t - \eta \nabla S(\vec{a}_t) \tag{5.22}$$

where $\vec{a}_t$ refers to the aberration coefficients' vector $\{a_j\}$ at the tth iteration, η is the learning rate, and $\nabla S(\vec{a})$ denotes the metric's gradient. Here, we use j in the subscript of the aberration coefficients instead of $\{n, i\}$ for convenience. In practice, the gradient can be calculated as:

$$\nabla_{a_j} S(\vec{a}_t) = \frac{1}{\delta}(S(\vec{a}_t + \vec{I}_j\delta) - S(\vec{a}_t)) \tag{5.23}$$

where ∇_{a_j} is the partial derivative of the mth element in $\vec{a}$, $\vec{I}_j$ is a vector whose elements are all zero with the exception of one at the jth element. SGD's convergence rate is highly dependent on the chosen learning rate, and a reasonable learning rate is usually cost function dependent. In addition, it lacks the ability to escape from shallow local minima and may even get stuck at the saddle points [144].

Adam uses adaptive learning rates that are different for each parameter. The historical gradient and its square are recorded by:

$$\begin{aligned} \vec{m}_{t+1} &= \beta_1 \vec{m}_t + (1-\beta_1)\nabla S(\vec{a}_t) \\ \vec{v}_{t+1} &= \beta_2 \vec{v}_t + (1-\beta_2)(\nabla S(\vec{a}_t))^2 \end{aligned} \tag{5.24}$$

where $\vec{m}_t$ and $\vec{v}_t$ are both initialized as zero. The parameter vector $\vec{a}_t$ is updated following:

$$\vec{a}_{t+1} = \vec{a}_t - \frac{\eta}{\sqrt{\hat{\vec{v}}_t + \epsilon}} \hat{\vec{m}}_t \tag{5.25}$$

where $\widehat{\overrightarrow{m}}_t = \overrightarrow{m}_t/(1-\beta_1^t)$ and $\hat{\vec{v}}_t = \vec{v}_t/(1-\beta_2^t)$. In practice, Adam can escape from the saddle points and some shallow local minima; thus, it has been one of the best overall optimization algorithms in machine learning. Nevertheless, Adam cannot guarantee a global minimum.

APSO is a variant of standard particle swarm intelligence that uses a group of agents to explore the parameters space with stochastic and deterministic components. The update rule of APSO is:

$$\vec{a}_{t+1}^{(k)} = \vec{a}_t^{(k)} + \beta(\vec{g}^* - \vec{a}_t^{(k)}) + \alpha\theta^t \vec{\epsilon}_t^{(k)} \tag{5.26}$$

where (k) in the superscript refers to the kth agents, $\vec{g}^*$ denotes the historical lowest position, and $\vec{\epsilon}_t$ is a vector of random numbers drawn from a Gaussian distribution. The deterministic update $\left(\vec{g}^* - \vec{a}_t^{(k)}\right)$ guarantees the convergence of the iteration, and its converge rate is controlled by β. The stochastic update increases the diversity of the solution searching, and its random searching region is controlled by a slowly reducing parameter $\alpha\theta^t$. The $\vec{a}_t^{(k)}$ is initialized with a random location drawn from the uniform distribution such that the agents can sample across the whole parameters space in a relatively uniform manner. The problem with APSO is that the only deterministic component may lead an aggressive converge to the current best solution $\vec{g}^*$ which can differ from the global best.

FA introduces the influence of other agents in the deterministic update, and the parameters are updated following:

$$\vec{a}_{t+1}^{(k)} = \vec{a}_t^{(k)} + \sum_{l \neq k} H(S(\vec{a}_t^{(k)}) - S(\vec{a}_t^{(l)}))\beta e^{-\gamma r_{k,l}^2}(\vec{a}_t^{(l)} - \vec{a}_t^{(k)}) + \alpha\theta^t \vec{\epsilon}_t^{(k)} \tag{5.27}$$

where $H(x)$ is a Heaviside step function, and $r_{k,l}$ is the Cartesian distance of the two agents. The agent is attracted by others with lower metric values, and the attractive strength depends on the distance of the two agents. The benefit is that the agents can automatically divide into sub-groups and explore different local minima simultaneously, increasing the chance to find the global minimum.

The update rule of CS has two phases: a global random walk and a local random walk. The global random walk combines stochastic Lévy flights and a deterministic attraction to the global best location:

$$\vec{a}_{t+1}^{(k)} = \vec{a}_t^{(k)} + \alpha\tilde{L}\vec{\epsilon}_t \cdot (\vec{g}^* - \vec{a}_t^{(k)}) \tag{5.28}$$

where $\tilde{L}$ refers to the step size of the Lévy flights, $\vec{\epsilon}_t$ is the direction of the Lévy flights drawn from the uniform distribution, and α is a scaling factor of the step size. Lévy flights can generate both near-field and far-field randomization. The near-field randomization explores the space like Gaussian randomization in APSO and FA, although it is biased to the global best location; the far-field randomization pushes the agents away from current locations, preventing them from getting trapped in local minima. The local random walk is performed with the possibility p_a:

$$\vec{a}_{t+1}^{(k)} = \vec{a}_t^{(k)} + \beta s H(p_a - \vec{\epsilon}'_t) \cdot (\vec{a}_t^{(m)} - \vec{a}_t^{(l)}) \tag{5.29}$$

where s and $\vec{\epsilon}'_t$ are a randomized scalar and vector drawn from the uniform distribution, β denotes the step size scaling factor, and $\vec{a}_t^{(m)}$ and $\vec{a}_t^{(l)}$ are two solutions of other agents that are randomly selected. CS employs a prudent update strategy that each agent adopts its update only if the metric function drops; otherwise, the agent keeps its current location and waits for the next update. The same user-defined boundary was used for all algorithms to prevent the iteration from producing impractical solutions.

The five algorithms are tested with two scattering microbeads enface images. The two enface signals are from the same OCT tomogram but at different depths and have different aberration coefficients and SNRs. The broadened microbeads can still be recognized at the depth 75 μm away from the focal plane (Figure 5.15 (A1)), whereas the microbeads are almost overwhelmed by noise at depth 150 μm (Figure 5.15 (A2)). Data 1 and data 2 are used to refer to the enface images of the two depths in the following discussion. The refocusing coefficients, $(a_{2,2}, a_{2,0})$, are determined with the grid searching method (Figure 5.15 (C)), and the corresponding refocused images are shown in Figure 5.15 (B). It can be seen that there are much more shallow local minima and saddle points in the metric landscape of data 2, even though just in 2 degrees of freedom. These local minima and saddle points may come from the noise, and it is expected there will be more in a higher dimension.

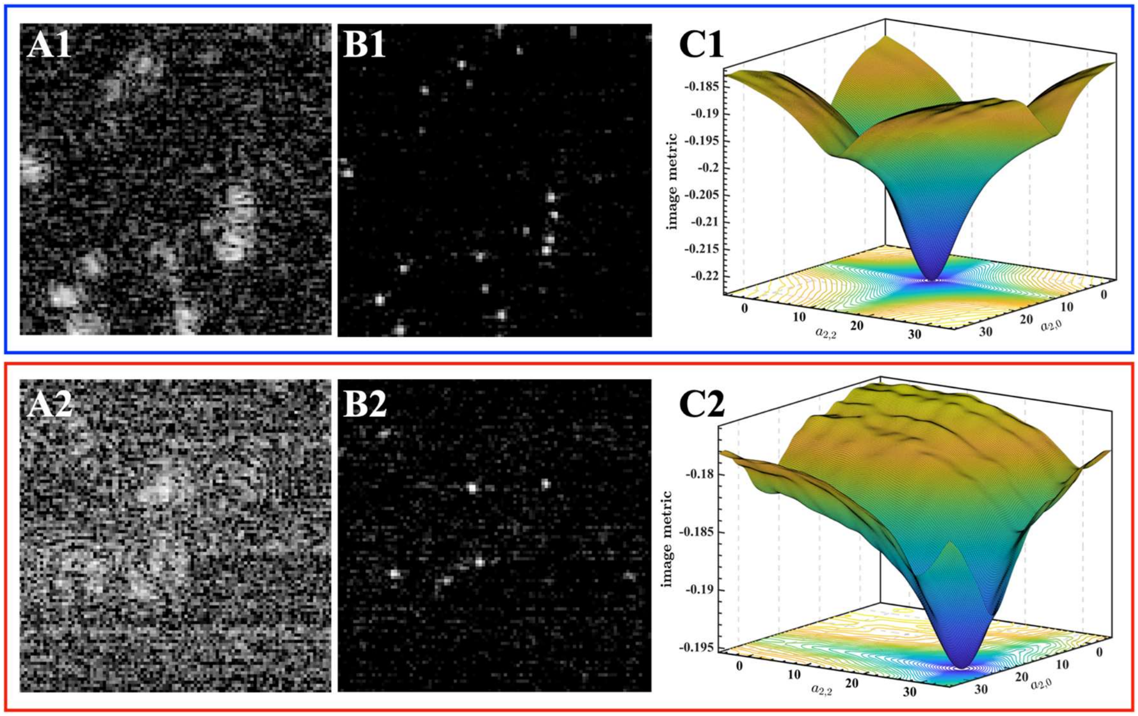

Figure 5.15 OCT signals of the microbeads phantom at two different depths. (A) Log-scale enface images of the original OCT signal. (B) Refocused enface images. (C) Image metric $S_p(a_{2,2}, a_{2,0})$.

We compared the performance of the algorithms in low order and high order aberration correction. For low order correction, the images were corrected to the 2nd order with 3 degrees of freedom; for high order correction, they were corrected to 5th order with 18 degrees of freedom. APSO, FA, and CS employed (15, 15, 15) agents in low order correction and (40 40 20) agents in high order correction. All algorithms were performed 100 times and the image metric convergence curves are shown in Figure 5.16. The grey curves show individual optimization trials, and the black line represents the mean value. The relative convergence rate and the accuracy of the five algorithms are summarized in Table 5.1.

Table 5.1 Relative convergence rate and accuracy of different optimization algorithms. d: data; n: highest radial aberration order.

algorithm	relative convergence rate				accuracy			
	d1n2	d1n5	d2n2	d2n5	d1n2	d1n5	d2n2	d2n5
SGD	-	-	-	-	0.84	0.04	0.05	0
Adam	12	1	-	-	1	0.84	0.63	0.35
APSO	7.6	0.12	7.8	0.14	1	0.52	0.99	0.42
FA	2.8	0.23	1.7	0.14	1	0.92	0.83	0.53
CS	1.7	0.09	2.3	0.11	1	0.95	1	0.74

The relative converge rate is inversely proportional to the function evaluation number at which the mean convergence curve reaches the critical value set as 99% minimum. If the mean curve is above the critical value, it does not have a meaningful relative convergence rate. The gradient-based algorithms' evaluation numbers are equal to the iteration numbers, while the function evaluation number per iteration should be multiplied with the iteration number to determine the total evaluation number for the SI-based algorithms. The accuracy was calculated as:

$$\text{accurancy} = \frac{N_{S<(S_{min}+0.001)}}{N_{total}} \tag{5.30}$$

where $N_{S<(S_{min}+0.001)}$ is the number of trials whose image metric converged below $S_{\min} + 0.001$, and $S_{\min}$ denotes image metric's global minimum. As expected, SGD fails in all tests (Figure 5.16 (A1-D1)) except for low order correction of data 1. Only several trials found the global minimum in higher-order correction of data 1 and low order correction of data 2, and no trials succeed in high order correction of data 2. Adam, APSO, FA, and CS perform very well in low order correction of data 1 (Figure 5.16 (A2-A5)). All trials of each algorithm found the global minimum. The only difference is their convergence rate. When it comes to high order correction of data 1 (Figure 5.16 (B2-B5)), FA and CS outperform Adam and APSO in terms of accuracy. The aggressive convergence strategy contributes to the low accuracy of APSO. A considerable performance difference of the four algorithms appears in correcting data 2, which has lower SNR and more local minima. 37% and 17% trials of Adam and FA do not find the global minimum in low order correction of data 2, while nearly all trials of APSO and CS succeed (Figure 5.16 (C2-C5)). As for the high order correction of data 2, only CS maintains an acceptable accuracy above 70% (Figure 5.16 (D2-D5)).

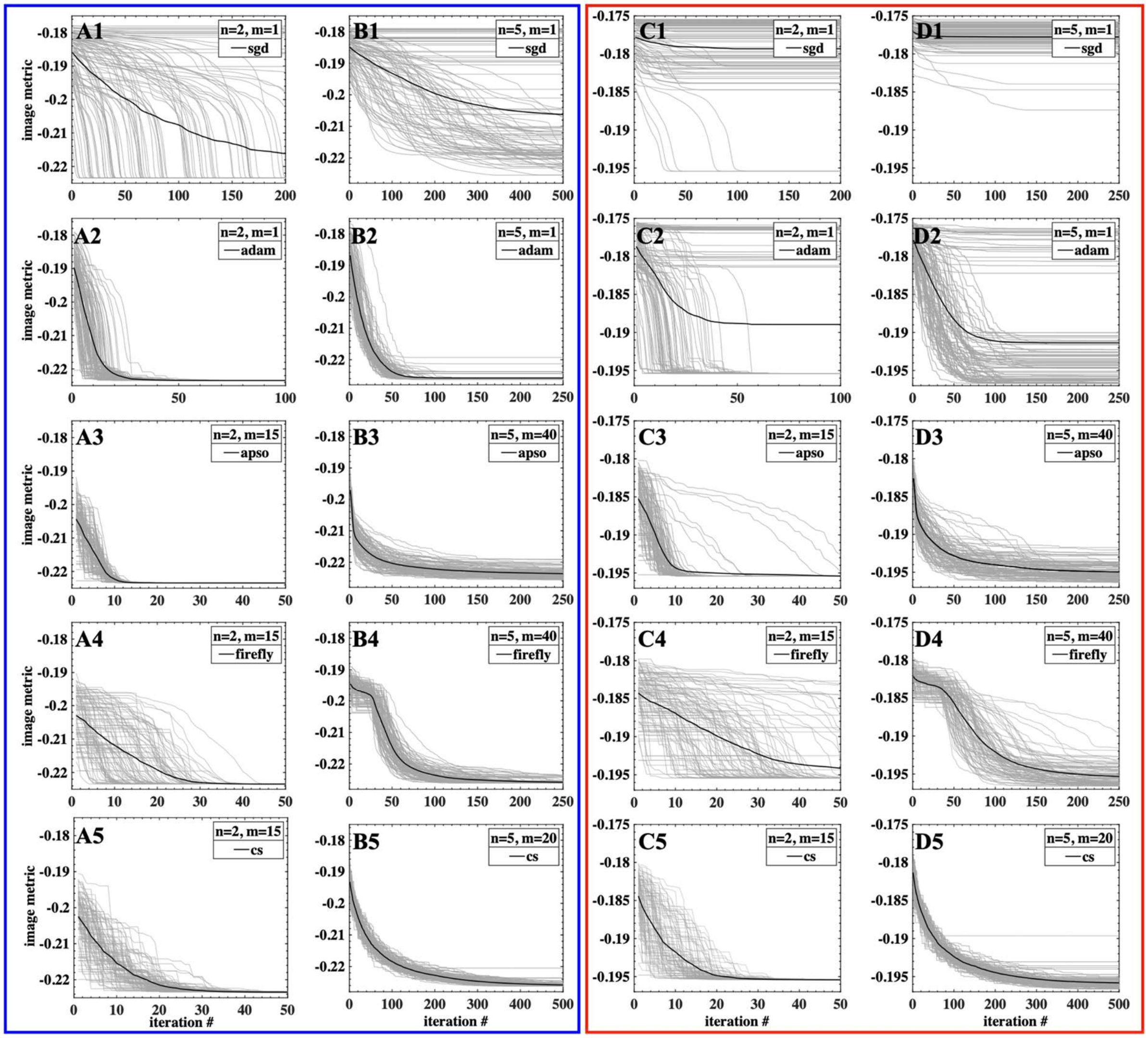

Figure 5.16 Convergence comparison of different optimization algorithms. (A) Low order aberration correction of data 1. (B) High order aberration correction of data 1. (C) Low order aberration correction of data 2. (D) High order aberration correction of data 2. Each optimization trial is shown in grey, while the mean value is presented in black.

The accuracy defined above shows the percentage of trials that successfully find the global minimum but not the accuracy of the aberration coefficients. The first three aberration coefficients, $(a_{2,0}, a_{2,1}, a_{2,2})$, determined by different algorithms and the corresponding final image metric values are shown in Figure 5.17. The abnormally large uncertainties of the three coefficients in all four test scenarios suggest that SGD cannot predict reliable results (Figure 5.17 (A)), which is consistent with the convergence curves in Figure 5.16 (A1-D1). Adam produces acceptable mean values in correcting the aberrations in data 1, although the results in high order correction were not precise enough; however, it does not produce trustable results in data 2, whose SNR was low (Figure 5.17 (B)). The mean values of the aberration coefficients generated by APSO are decent in all four test scenarios, whereas the standard deviations in correcting high order aberrations of data 1 and data 2 are both relatively large (Figure 5.17 (C)). With the same standard, FA produced reliable results when correcting the aberrations in data 1(Figure 5.17 (D)), and CS generated the most precise results in all four cases (Figure 5.17 (E)). In conclusion, Adam only works well in low order aberration correction of images with high SNR, APSO is suitable in low order correction scenarios, FA is eligible to deal with high SNR image, and CS is the only one that works well in all four cases.

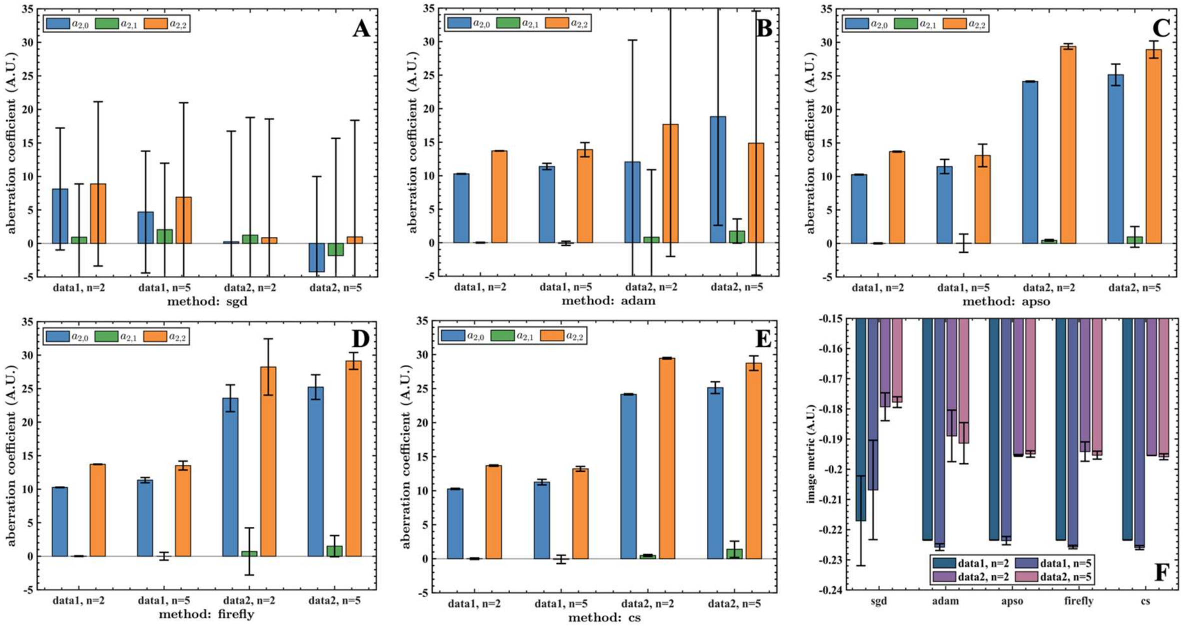

Figure 5.17 Aberration coefficients determined by different optimization algorithms and the corresponding image metric values. (A-E) Mean and standard deviation of $(a_{2,0}, a_{2,1}, a_{2,2})$ determined by SGD, Adam, APSO, FA, and CS, respectively. (F) Mean and standard deviation of the final image metric values.

5.6 Discussion

This study investigated three factors that cause degradation in the spatial resolution of volumetric images acquired with a broadband LS SD-OCT system and impede the success of DAO algorithms to restoring the diffraction-limited lateral resolution across a large imaging depth range. These three factors are associated with the system's optical design, alignment, and the broadband nature of the low coherent light source necessary to ensure high axial OCT resolution. The oversimplified virtual interference pinhole model predicts the phase information loss in the x-direction, which is unique among different configurations of OCT. In point-scan OCT systems, the fiber system separates the light collection process from the interference process. Its cPSF is determined by the optics in the sample arm, and the symmetry of the illumination and detection arms guarantees no mismatch between the two focal planes. In a free-space LS SS-OCT design, the spectral information is encoded in time instead of space. Therefore, it is the pixel size of the linear camera that confines the region at which the interference signal is collected. The axial shift of the reference focal position does not result in an axial shift of the effective collecting cPSF $h_d(x, z)$. FF SS-OCT deploys a wide-field configuration in both lateral directions; thus, its effective cPSF is just the detecting cPSF and free from phase destruction. In the broadband LS SD-OCT system, it is impossible to align the illumination, detection, and reference focal planes at the same axial position for all wavelengths, considering the axial chromatic aberrations of the three paths can be different from each other. In practice, if the separation is within the Rayleigh range, the resolution loss in x-direction due to the phase destruction is not evident (Figure 5.9 (B)). However, imaging in the medium may lead to additional separation; thus, a strategy that can quickly measure and tune the separation of focal planes under different imaging scenarios is desired and needs further development.

The spatial-spectral crosstalk results directly from the mismatch between the optical axis orientations of the camera detection array and transmission grating. The angle between the two axes in our broadband LS SD-OCT system is typically less than 7.2 arc minutes but is not negligible. Due to the mechanical drift of the camera, a perfect alignment is unrealistic. Moreover, the crosstalk curves are location-dependent because of the chromatic aberration in y-direction; thus, pre-calibrating the crosstalk before each imaging session is strenuous and impractical.

The chromatic aberrations have not been widely addressed in imaging anterior eye or other shallow biology tissue with OCT. The distortion caused by chromatic aberrations might be insignificant in OCT systems with narrowband light sources, especially in morphology studies where lateral resolution (> 10 μm) is not a limitation. However, the chromatic aberrations cannot be ignored in our ultrahigh resolution LS SD-OCT system with nearly isotropic ~2 μm resolution in all three dimensions. In our system, the axial chromatic aberration induced focal shift between the maximum and minimum wavelengths was larger than 15 μm in free space, about twice the Rayleigh length. Here, it is assumed that the axial chromatic aberration and the Rayleigh length are at the same level in the xz-plane and yz-plane. The chromatic aberrations in x- and y-directions behave differently; the former was depth dependent while the latter was not. The lateral shift in the y-direction might be caused by dispersion of the beam splitter and grating's cover glass, while the lateral shift in x-direction might be related to the interaction of the illuminating and detecting focal planes as it was only away from 0 in the depth range near the focus. The maximum lateral shifts induced by chromatic aberration were about 3 μm and 2 μm in x- and y-direction respectively, comparable with the diffraction-limited resolutions. A custom achromatizing lens has been used in retina imaging with point-scan AO-OCT to compensate for the axial chromatic aberration [70,141]. A similar design can be applied in our system, although the required amount of the wavelength-dependent defocus induced by the achromatizing lens is not on the same scale. However, unlike the dual-pass configuration in the point-scan system, the illumination and detection optics are not symmetric in the LS system, and their axial chromatic aberrations may need to be compensated separately by different achromatizing triplets. By far, there have been no simple optics elements to correct the chromatic aberrations in lateral directions; thus, digital alignment is needed to compensate for the lateral shifts [159].

Apart from the phase destruction, the other two problems, i.e., spatial-spectral crosstalk and chromatic aberrations, can be resolved by independently registering the aberration-corrected sub-band OCT images in different sub-regions. Anisotropic aberrations across the lateral FOV have been observed and separately corrected in different studies[44,106,160]; however, these studies have been limited in the monochromatic regime. We take a further step to split the full spectrum into different sub-bands. Correcting the monochromatic aberrations of each sub-band tomogram and registering them afterward results in a reduction in chromatic aberrations. Since both the spatial-spectral crosstalk and the achromatic aberration in y-direction result in the spectrum split along the y-direction, registration of sub-band images compensates the crosstalk as well. Since the defocusing phase is proportional to the wavelength, a fully defocus correction should be wavelength dependent. To our best knowledge, Interferometric synthetic aperture microscopy (ISAM) is the only method by far to account for that Ewald sphere curvature [133]. Nevertheless, a comparison study showed no significant difference between the improvement generated by ISAM and monochromatic refocusing algorithms in a narrowband OCT system [105]. Thus, we treat the defocus aberration as monochromatic in each sub-band. We have noticed that theoretical analysis shows that the LS OCT's 3D coherence transfer function (CTF) is not separable in the two transverse spatial frequencies [161]. However, since our system's effective NA is relatively small (~0.13), we assume this limitation does not critically affect our analysis and algorithm in each sub-band. As the reconstruction results of the resolution target, microbeads phantom, and different biology tissues show significant improvement compared with the original images, the separable cPSF approximation is still valid from a practical point of view.

In this study, an iteration-based method was used to find the phase mask that produces the sharpest image in the localized monochromatic aberration correction process. Many image intensity based metrics have been proposed [153]; however, the common assumption that the metric's global minimum or maximum corresponds to the aberration-free image has not been validated. For example, the intensity-based metrics failed in predicting the defocus phase mask of a reflecting signal reflected from the resolution target. Instead, the Shannon entropy is a good indicator for the reflecting signal. However, the Shannon entropy of the scattering signal is noisy, which prevents it from becoming a universal metric. By far, many studies have shown intensity-based metrics work in the scattering regime. However, a good coincide of its global optimum and the aberration-free limit is still questionable at low SNR conditions, and further investigation is necessary.

Another problem that prevents generating an aberration-free image via metric optimization is the unpredictable local minima. Gradient-based algorithms are intrinsically easy to get trapped in local minima. In principle, the global minimum can be reached with infinite trials from different randomized initial positions; however, the lack of knowledge about the local traps' number and distribution makes it difficult to choose a proper trial number. The SI-based algorithms, particularly the CS method, show a better convergence to the global minimum at the cost of increased function evaluation numbers. Lacking scattering contrast, saturation or self-interference artifacts, or a mix of scattering and reflecting signals can result in failures of the DAO algorithm. In order to reject the fake results, a smoothing algorithm along the imaging depth was applied to each aberration coefficient. It works well when the abnormal aberration coefficients are sparsely distributed; however, in the case that the abnormal region spans a relatively large depth range, the smoothing algorithm may lead to a wrong correction. Thus, an image content related method should be developed to distinguish the normal and abnormal aberration coefficients. The DAO algorithm only corrects the wavefront aberrations, and the resolution can be restored but not improved. Appropriate amplitude deconvolution methods can increase the resolutions [162]; however, noise can be amplified in deconvolution and distort the corrected signal. The relationship between the resolution improvement and the SNR gain through averaging repeated images is beyond the scope of this work.

Incompletely compensated dispersion results in the axial shifts of the three sub-band tomograms. Phase registration is necessary to correct the phase discontinuity between sub-bands. Predicting the phase differences from the full depth's interference fringe of an A-scan is challenging since it contains different frequencies with varying amplitudes. Thus, the phase differences were calculated based on the interference fringe of the air-glass interface, which contains a single frequency because of the spatial isolation from other scattering or reflecting objects. We have assumed the dispersion is depth invariant and the phase discontinuity is constant across the whole depth range. However, this assumption does not hold in theory as the dispersion is depth dependent. Nevertheless, in this study, evident distortions of the reconstructed axial resolution compared with the original broadened axial PSF due to residual dispersion were not observed. For future applications, the phase differences can be estimated iteratively in different depth sections by optimizing the A-scan signal quality, similar to the DAO procedure. Therefore, the depth-dependent dispersion can be quasi-corrected within each depth section. In addition, it does not require a coverslip as the phase registration reference and is easier to adapt in *in-vivo* imaging. Proper digital spectrum reshaping after the phase registration is recommended to remove the axial sidelobes of the reconstructed OCT image.

5.7 Conclusion

In summary, we have demonstrated an OCT reconstruction method that can restore the diffraction/coherence limited resolutions in a broadband LS SD-OCT system. An iteration-based DAO algorithm was independently applied to the sub-band tomograms at different sub-regions to correct the monochromatic aberrations. The spatial-spectral crosstalk and chromatics aberrations were effectively suppressed by registering the sub-band tomograms at sub-regions. Phase destruction in x-direction was significantly reduced by minimizing the axial separation of the illumination and effective detection focal planes. In microbeads phantom, the proposed reconstruction method shows superior resolutions compared with the full-spectrum monochromatic DAO method. Diffraction-limited transverse resolutions were achieved over a depth range over 300 μm, which is about 20× larger than the DOF. 3D reconstruction of biological tissue images demonstrates the ability of the proposed method to recover the scattering contrast of cells and tissues, which are indistinguishable in the original tomograms. The reconstruction method for the broadband LS SD-OCT enables fast 3D cells and tissue imaging with isotropic micrometer level resolution across a large depth range and makes it a suitable tool for functional studies, flow measurement, and dynamic signals.

Chapter 6

Decorrelation-based Localized Transverse Flow Measurement

6.1 Introduction

Optical coherence tomography (OCT) is an interferometric technique that can map the reflectivity profile of the imaged object volumetrically with micrometer scale resolution [27]. It is commonly used in biomedical and clinical studies due to its non-contact, label-free, high-resolution, high-speed, and optical sectioning advantages. Besides structure imaging, OCT is able to map blood vasculature and measure blood flow speed, as well as detect and characterize physiological and metabolic changes in biological tissues [163]. Among these extensions, one of the most important applications is blood flow imaging since it is believed to be an important biomarker of many diseases. Based on whether it generates qualitative or quantitative results, the OCT-based blood flow imaging can be classified into OCT angiography (OCTA) and OCT-based velocimetry. OCTA utilizes the intensity or phase variance difference of moving and static scatters to separate blood vessels from static tissues. However, the OCTA signal provides limited information about the flow dynamic as the time series of B-scans are completely decorrelated. The methods for measuring localized velocity of the blood flow can be divided into two categories: phase-based Doppler OCT and decorrelation-based techniques.

Since OCT is a heterodyne detection technique, the complex OCT signal contains the phase information of the scatters. Spatially resolved flow velocity measurement is possible by tracking the phase distribution as a function of time. However, conventional Doppler OCT (DOCT) is only sensitive to phase changes induced by axial motion; therefore, the measured flow velocity is dependent on the Doppler angle between the imaging beam and the flow velocity [31]. The Doppler angle cannot be measured precisely for many applications, resulting in significant uncertainty in the measured flow. In addition, in the case where the flow is nearly perpendicular to the optical beam propagating direction, the axial velocity component cannot be measured if the induced phase change is overwhelmed by the phase noise [164]. The lateral motion results in a broadened Doppler peak; therefore, it is possible to exploit the variance of the Doppler signal to determine the lateral velocity component [164]. Multi-beam OCT can retrieve phase changes caused by axial and lateral motions [60,61]; however, the multi-beam OCT technology is more complex, bulky and expensive than conventional single beam OCT. An alternative approach is to encode the backscattered light through different subapertures with different optical delays [165]; however, the drawback is a reduced depth scanning range. Recently, digital subaperture-based (DSubAp) DOCT has been proposed. This approach calculates lateral motion based on the phase differences of digitally reconstructed OCT tomograms of different subapertures [62,63]. Since DSubAp DOCT requires excellent lateral phase stability of the imaged OCT volumes, this method can only be applied to images acquired with parallelized imaging modalities such as full-field (FF) swept-source (SS) OCT and line-scan (LS) spectral-domain (SD) OCT. FF SS-OCT has a typical volumetric acquisition rate of 100-200 Hz thus its speed detection range is limited. LS SD-OCT only maintains excellent phase stability along the parallel illuminating direction, whereas the measurement of lateral flow along the scanning direction is still challenging due to phase noise associated with the jitter in the scanner and natural motion of biological tissue in in-vivo studies. Another problem impeding all the phase-based methods to precisely determine the flow speed is the extra phase due to multi-scattering of the flow particles [166]. If the backscattered photon goes through another particle in the flow, it will inevitably pick the motion information of the second particle, which is mistakenly explained as the motion of the first scatter.

Decorrelation-based methods are based on analyzing the fluctuations of the OCT signal induced by the motions of scattering particles. One representative method is dynamic light scattering (DLS) OCT which combines DLS techniques with OCT [64]. DLS analyzes the temporal fluctuations of the scattering signals and is originally used to measure the particle size distributions [167]. Recently, DLS has been used to measure the blood flow dynamic using different imaging techniques [168–170]. Here, we limit our discussion in the OCT field. Since the first-order temporal autocorrelation of the complex-valued OCT A-scan signal is dependent on both the lateral and axial velocity, DLS-OCT can resolve both terms simultaneously with the single beam point-scan modality [171]. Another approach, known as intensity-based DLS-OCT (iDLS-OCT) [164,172] utilizes the second-order temporal autocorrelation function, which overcomes the phase instability in SS-OCT [173,174]. However, there is little theoretical or experimental discussion about why iDLS-OCT is insensitive to the local beam sizes, like what has been shown in DLS-OCT [175–177]. There are several studies attempting to resolve the flow dynamic by recording repeated B-scans instead of A-scans [169,178,179]; however, due to the limited time resolution, determining the flow velocity is impossible. One main problem for the decorrelation-based methods is that resolving a credible autocorrelation function requires hundreds or thousands of repeated A-scans, which is time-consuming. Typical times for imaging a 3D dataset with DLS-OCT are over 10 mins [64,169], which prohibits DLS-OCT from being used in the *in-vivo* human ocular studies. In addition, recent studies have shown that the axial velocity gradients and multi-scattering lead to additional decorrelation, and how to compensate these contributions is still an open question.

Here, we present a novel decorrelation-based localized transverse flow measurement using a LS SD-OCT system, and the method is named DLS-LSOCT in this work. First, we theoretically verify the DLS-OCT model in line-scan modality. Then, we propose determining the transverse flow velocity along the line-illuminating direction using the ratio of the temporal autocorrelations of the original and digitally generated low-resolution OCT tomograms. Next, the novel DLS-LSOCT method was validated in a glass capillary phantom with intralipid flow. The experimental results obtained with the DLS-LSOCT method are compared with DOCT and DSubAp DOCT approaches, which serve as the ground truth for this experiment. Finally, we show that the DLS-LSOCT method can be used to detect the spatial-resolved velocity distribution in the beam illuminating plane and estimate the flow direction in the plane perpendicular to the beam propagating direction.

6.2 Theory

6.2.1 LS SD-OCT signal

According to Chapter 5.2.1, for a well aligned LS SD-OCT system, the effective electrical field backscattered from the position (x, y, z) is:

$$\begin{aligned} E_s(x,y,z) &= \iint h_i(x_1,y_1,z_1)s(x_1-x,y_1-y,z_1-z)h_d(x_2-x_1,y_2-y_1,z_1)dx_1dy_1dz_1 \\ &\qquad p(x_2,y_2)dx_2dy_2 \\ &= \int s(x_1-x,y_1-y,z_1-z)h_i(x_1,y_1,z_1)[\int h_d(x_2-x_1,y_2-y_1,z_1) \\ &\qquad p(x_2,y_2)dx_2dy_2]dx_1dy_1dz_1 \\ &= s(x,y,z)\otimes[h_i(x,y,z)[h_d(x,y,z)\otimes p(x,y)]] \end{aligned} \tag{6.1}$$

where $s(x, y, z)$ is the amplitude scattering profile, $h_{i,d}(x, y, z)$ are the 3D coherence point spread functions (cPSFs) of the illumination and detection optics respectively, $p(x, y)$ refers to the virtual pinhole generated by the interference in the x-direction and the pixel size confine in the y-direction, and $\otimes$ denotes convolution. By assuming that the pinhole is infinitely thin, i.e., $p(x, y) = \delta(x, y)$, and the illuminating and detecting optical beams are underfilled such that the cPSFs are separable in x- and y- directions, E_s can be simplified as:

$$E_s(x,y,z) = s(x,y,z)\otimes[h_i(x,z)h_d(x,z)h_i'(y,z)h_d'(y,z)] \tag{6.2}$$

Here, $h_{i,d}$ and $h'_{i,d}$ refer to the illumination and detection cPSFs in the xz and yz-planes respectively, considering that the beam waists and focus planes can be different because of symmetry break. The complex OCT signal, which is calculated by Fourier transforming the OCT interference fringe along the wavenumber space (k-space), can be expressed as:

$$\begin{aligned} f(x,y,z) &= \int s(x_1 - x, y_1 - y, z_1 - z) h_i(x_1, z_1) h_d(x_1, z_1) h_i'(x_1, z_1) h_d'(x_1, z_1) h_r(y_1) \\ &\qquad \sqrt{\eta_s(k)\eta_r(k)} e^{-i2nkz_1} d(2nk) dx_1 dy_1 dz_1 \\ &= [s(x,y,z) \otimes [h_i(x,z) h_d(x,z) h_i'(y,z) h_d'(y,z) h_r(y) h_c(z) e^{i2nk_0 z}]] \\ &= [s(x,y,z) \otimes [h(x,z) h'(y,z) h_c(z) e^{i2nk_0 z}]] \end{aligned} \tag{6.3}$$

where $h_r(y)$ refers to the reference arm's electrical field amplitude distribution along the y-direction, $\eta_s(k)$ and $\eta_r(k)$ are the camera detected spectral power densities of the sample and reference arm respectively, $h_c(z)$ is the coherence gating under the assumption that the spectrums of the reference and sample arms maintain the same for all locations, and $e^{i2k_0 z}$ comes from the optical path difference of the sample and reference arms.

Assuming that the illuminating and detecting cPSFs are Gaussian:

$$\begin{aligned} h_i(x,z) &= \sqrt{\frac{\sigma_{x,i}^2}{\sigma_{x,i}^2 + i\frac{2z}{k_0}}} \exp\left(-\frac{x^2}{\sigma_{x,i}^2 + i\frac{2z}{k_0}}\right) \\ h_d(x,z) &= \sqrt{\frac{\sigma_{x,d}^2}{\sigma_{x,d}^2 + i\frac{2z}{k_0}}} \exp\left(-\frac{x^2}{\sigma_{x,d}^2 + i\frac{2z}{k_0}}\right) \\ h_i'(y,z) &= \exp\left(-\frac{y^2}{\sigma_{y,i}^2}\right) \\ h_d'(y,z) &= \sqrt{\frac{\sigma_{y,d}^2}{\sigma_{y,d}^2 + i\frac{2(z+\Delta z)}{k_0}}} \exp\left(-\frac{y^2}{\sigma_{y,d}^2 + i\frac{2(z+\Delta z)}{k_0}}\right) \\ h_r(y) &= \exp\left(-\frac{y^2}{\sigma_{y,r}^2}\right) \end{aligned} \tag{6.4}$$

where $\sigma_{x,y}$ is the $1/e$ transverse beam waist radius of the cPSFs along the x- and y-direction, k_0 is the wavenumber of the central wavelength, $\sqrt{\sigma^2/(\sigma^2 + i\frac{2z}{k_0})}$ indicates the longitudinal amplitude as a function of depth z, the complex term inside the Gaussian function is due to the defocus effect, and the Δz in $h'_d(y,z)$ indicates that the focus depth can be different along x- and y- directions in the LS SD-OCT system. Since the illuminating beam radius ($1/e^2$) along y-direction is much broader than that of the detecting (1000 μm vs. 2.2 μm) and the DOF is much larger than the coherence length (48 μm vs. 4 μm in water), the illumination and reference amplitudes along the y-direction and the longitudinal amplitude functions can be treated as constants. Although the spectral power density of most broadband OCT systems is not Gaussian, we can apply a Gaussian filter over k-space in post-processing before the Fourier transformation of the interference fringe such that the coherence gate has a quasi-Gaussian envelope,

$$h_c(z) = \exp(-\frac{z^2}{\sigma_z^2}) \tag{6.5}$$

With further assuming that $h_i(x, z)$ and $h_d(x, z)$ are symmetric, i.e., $\sigma_{x,i} = \sigma_{x,d} = \sigma_x$, and the sample is composed by multiple point scatters:

$$s(x, y, z) = \sum_{i=1}^{N} \delta(\vec{r} - \vec{r}_i) \tag{6.6}$$

where $\vec{r} = (x, y, z)$, the OCT signal can be simplified as:

$$f(x, y, z) = \sum_{i=1}^{N} e^{i2nk_0 z_i} e^{-2\frac{x_i^2}{\sigma_x^2 + i\frac{2z_i}{k_0}}} e^{-\frac{y_i^2}{\sigma_y^2 + i\frac{2(z_i + \Delta z)}{k_0}}} e^{-\frac{z_i^2}{\sigma_z^2}} \tag{6.7}$$

6.2.2 Dynamic light scattering (DLS) in LS SD-OCT

The movement of scatters is composed of translational motion and diffusional motion. By assuming the two components are independent, the position of a particle can be expressed as:

$$\vec{r}(t) = \vec{r} + \vec{v}t + \delta\vec{r} \tag{6.8}$$

where $\vec{r}$ is the scatter position at $t = 0$, $\vec{v}$ is the translational velocity, and $\delta\vec{r}$ is the diffusion displacement with the probability density distribution:

$$\rho(\delta\vec{r}, t) = \frac{1}{(4\pi Dt)^{3/2}} e^{-\frac{|\delta\vec{r}|^2}{4Dt}} \tag{6.9}$$

Here, D is the diffusion coefficient. Since the OCT is a heterodyne detection system, we write the first-order temporal autocorrelation of the LS SD-OCT signal as:

$$g_1(t) = \langle f(x, y, z, t) f(x, y, z, 0)^* \rangle \tag{6.10}$$

where the asterisk indicates complex conjugate and $\langle\rangle$ denotes an ensemble average. As pointed out by Chowdhury et al. [180], the ensemble average is composed of two components: one over the diffusional displacement of the scatters and the other over the initial position of scatters. The above autocorrelation function can be rewritten as:

$$g_1(t) = \langle\langle f(x,y,z,t)\rangle_{\delta r} f(x,y,z,0)^*\rangle_r \tag{6.11}$$

The ensemble average of the OCT signal due to diffusion can be calculated by integrating with its probability density distribution function:

$$\begin{aligned}\langle f(x,y,z,t)\rangle_{\delta r} &= \sum_{i=1}^{N} e^{i2nk_0(z_i+v_zt)} \int e^{-2\frac{(x_i+v_xt+\delta x)^2}{\sigma_x^2+i\frac{2z_i}{k_0}}} e^{-\frac{(y_i+v_yt+\delta y)^2}{\sigma_y^2+i\frac{2(z_i+\Delta z)}{k_0}}} e^{i2k_0\delta z-\frac{(z_i+v_zt+\delta z)^2}{\sigma_z^2}} \\ &\qquad \rho(\delta x,\delta y,\delta z,t)d\delta x d\delta y d\delta z \\ &= \sum_{i=1}^{N} e^{i2nk_0(z_i+v_zt)} F_x(t)F_y(t)F_z(t)\end{aligned} \tag{6.12}$$

where we define:

$$\begin{aligned}F_{x_i}(t) &= \frac{1}{\sqrt{4\pi Dt}}\int e^{-2\frac{(x_i+v_xt+\delta x)^2}{\sigma_x^2+i\frac{2z_i}{k_0}}} e^{-\frac{\delta x^2}{4Dt}} d\delta x \\ F_{y_i}(t) &= \frac{1}{\sqrt{4\pi Dt}}\int e^{-\frac{(y_i+v_yt+\delta y)^2}{\sigma_y^2+i\frac{2(z_i+\Delta z)}{k_0}}} e^{-\frac{\delta y^2}{4Dt}} d\delta x \\ F_{z_i}(t) &= \frac{1}{\sqrt{4\pi Dt}}\int e^{i2nk_0\delta z-\frac{(z_i+v_zt+\delta z)^2}{\sigma_z^2}} e^{-\frac{\delta z^2}{4Dt}} d\delta z\end{aligned} \tag{6.13}$$

After integration, we have:

$$\begin{aligned}F_{x_i}(t) &= \frac{1}{\sqrt{1+\frac{8Dt}{\sigma_x^2+i\frac{2z_i}{k_0}}}} e^{-2\frac{(x_i+v_xt)^2}{\sigma_x^2+i\frac{2z_i}{k_0}}/(1+\frac{8Dt}{\sigma_x^2+i\frac{2z}{k_0}})} \\ F_{y_i}(t) &= \frac{1}{\sqrt{1+\frac{4Dt}{\sigma_y^2+i\frac{2(z_i+\Delta z)}{k_0}}}} e^{-\frac{(y_i+v_yt)^2}{\sigma_y^2+i\frac{2(z_i+\Delta z)}{k_0}}/(1+\frac{4Dt}{\sigma_y^2+i\frac{2(z_i+\Delta z)}{k_0}})} \\ F_{z_i}(t) &= \frac{1}{\sqrt{1+\frac{4Dt}{\sigma_z^2}}} e^{-(\frac{(z_i+v_zt)^2-i8k_0Dt(z_i+v_zt)}{\sigma_z^2}+4n^2k_0^2Dt)/(1+\frac{4Dt}{\sigma_z^2})}\end{aligned} \tag{6.14}$$

In the time scale we interest, the diffusional displacement is much smaller than the resolution of the system, i.e., $Dt \ll \sigma_{x,y,z}^2$. This can be validated by measuring the diffuse rate of 5% intralipid with no translational motion. Limit the maximum time delay as 10τ, where τ is our LS SD-OCT system's time resolution 0.339 millisecond, we get $D(10\tau) = 0.005(\mu m)^2$, which is much smaller than a typical σ^2 of 9 $(\mu m)^2$. Therefore, the ensemble average over diffusion displacement can be simplified as

$$\langle f(x,y,z,t)\rangle_{\delta r} = e^{-4n^2k_0^2Dt}\sum_{i=1}^{N} e^{i2nk_0(z_i+v_zt)} e^{-2\frac{(x_i+v_xt)^2}{\sigma_x^2+i\frac{2z_i}{k_0}}} e^{-\frac{(y_i+v_yt)^2}{\sigma_y^2+i\frac{2(z_i+\Delta z)}{k_0}}} e^{-\frac{(z_i+v_zt)^2}{\sigma_z^2}} \tag{6.15}$$

The above equation shows that the scatters' diffusional and translational motions are separable at the ensemble level. The diffusion of scatters only contributes to an exponential decay term and is unrelated to the scatters' initial position. However, it is important to note that the diffusion decay term is only valid when the objective's numerical aperture (NA) is small.

The first-order autocorrelation function can now be expressed as:

$$\begin{aligned} g_1(t) &= e^{i2nk_0v_zt} e^{-4n^2k_0^2Dt} \langle \sum_{i=1}^{N} e^{-2[\frac{(x_i+v_xt)^2}{\sigma_x^2+i\frac{2z_i}{k_0}} + \frac{(x_i)^2}{\sigma_x^2-i\frac{2z_i}{k_0}}]} e^{-[\frac{(y_i+v_yt)^2}{\sigma_y^2+i\frac{2(z_i+\Delta z)}{k_0}} + \frac{(y_i)^2}{\sigma_y^2-i\frac{2(z_i+\Delta z)}{k_0}}]} e^{-[\frac{(z_i+v_zt)^2}{\sigma_z^2} + \frac{(z_i)^2}{\sigma_z^2}]} \rangle_r \\ &= e^{i2nk_0v_zt} e^{-4n^2k_0^2Dt} e^{-(\frac{v_x^2}{\sigma_x^2}+\frac{v_y^2}{2\sigma_y^2}+\frac{v_z^2}{2\sigma_z^2})t^2} \langle \sum_{i=1}^{N} e^{-\frac{4[x_i+v_xt(\frac{1}{2}+i\frac{z_i}{k_0\sigma_x^2})]^2}{\sigma_x^2+\frac{4z_i^2}{k_0^2\sigma_x^2}}} e^{-\frac{2[y_i+v_yt(\frac{1}{2}+i\frac{(z_i+\Delta z)}{k_0\sigma_y^2})]^2}{\sigma_y^2+\frac{4(z_i+\Delta z)^2}{k_0^2\sigma_y^2}}} e^{-\frac{2[z_i+v_zt/2]^2}{\sigma_z^2}} \rangle_r \end{aligned} \tag{6.16}$$

We have neglected the contribution from two different scatters since their average should be zero, assuming the scatters are independent and uniformly distributed. The ensemble average term over scatters' initial position is, in fact, independent with the time delay, since the scatters are assumed uniformly distributed. Therefore, we can further simplify the autocorrelation as,

$$g_1(t) = A(x,y,z)e^{i2nk_0v_zt} e^{-4n^2k_0^2Dt} e^{-(\frac{v_x^2}{\sigma_x^2}+\frac{v_y^2}{2\sigma_y^2}+\frac{v_z^2}{2\sigma_z^2})t^2} \tag{6.17}$$

where $A(x,y,z)$ is a function of position, central wavelength, and system resolutions. To get rid of the influence of $A(x,y,z)$, the normalized autocorrelation function is utilized:

$$\hat{g}_1(t) = \frac{g_1(t)}{g_1(0)} = e^{i2nk_0v_zt} e^{-4n^2k_0^2Dt} e^{-(\frac{v_x^2}{\sigma_x^2}+\frac{v_y^2}{2\sigma_y^2}+\frac{v_z^2}{2\sigma_z^2})t^2} \tag{6.18}$$

The derived first-order temporal autocorrelation of OCT signal in LS SD-OCT is similar to that of point-scan modality. The decorrelation term arising from translational motion is, in principle, only characterized by the flow speed and system's spatial resolutions and irrelevant to the longitudinal position with respect to the focal plane. This is consistent with the theoretical study [175] and experiment results [176]. However, it is important to note that there are two main differences between the two modalities: (1) LS SD-OCT's two transverse resolutions are not necessarily the same since it has a confocal configuration in the x-direction and wide-field configuration in the y-direction. (2) The time resolution of LS SD-OCT is much larger than that of point-scan OCT since the LS SD-OCT records A-scans parallelly and its time resolution is actually the time interval between adjacent B-scans while point-scan OCT can measure A-scan repeatedly.

6.2.3 Noise influence on the autocorrelation function

By far, we only considered the autocorrelation of the noise-free OCT signal. By assuming the noise is a stochastic zero-mean complex Gaussian variable, the normalized autocorrelation function under noise can be expressed as [181,182]:

$$\tilde{g}_1(t) = \gamma \hat{g}_1(t) \tag{6.19}$$

where $\gamma = 1/\left(1 + \frac{\langle|s|^2\rangle}{\langle|n|^2\rangle}\right)$ and s and n denote the actual OCT signal and noise respectively. The noise contributes to additional decay of the autocorrelation function by multiplying a correction ratio which is independent with time; thus, the decay rate does not change with or without noise. Due to the fact that the OCT signal and noise are both position-dependent, the correction ratio γ is also a function of spatial position. In the point-scan modality, the noise is assumed to be dominated by the shot noise of the reference signal and can be compensated with pre-recorded reference only noise [182]. However, considering the existence of multi-scattering in LS SD-OCT, it is impractical to assume that the noise is irrelevant to the backscattered signal.

6.2.4 Resolution contrast in DLS-LSOCT

So far, the two often used methods for determining the flow velocity in DLS-OCT are: (1) fitting the autocorrelation function directly to get the diffusion rate and flow velocity simultaneously; (2) calculating the flow velocity based on the bandwidth of the power spectrum density of the autocorrelation function. The first method can be very precise when the time resolution is high enough such that there are enough autocorrelation data above the noise floor, while the second method is commonly used in the case where the translational motion is predominant such that the diffusion effect is negligible. However, due to the relatively low time resolution in LS SD-OCT (339 μs), which is much larger than that of point-scan OCT (typically 20 μs or smaller), the autocorrelation function is overwhelmed by noise within 5 time steps even at a slow flow speed. As a result, we cannot apply those methods directly. It is possible to calculate the diffusion coefficient in the absence of flow and fit the translational velocity with the diffusion compensated autocorrelation function. Unfortunately, this approach is not precise, as will be shown in the result section.

To overcome these difficulties, a low-resolution tomogram is generated digitally, taking advantage of the high phase stability of each B-scan. The Fourier translation of OCT signal along y-direction is:

$$\begin{aligned}
f(x,k_y,z) &= FT_{y\to k_y}\{\sum_{i=1}^{N} e^{i2nk_0z_i} e^{-2\frac{x_i^2}{\sigma_x^2+i\frac{2z_i}{k_0}}} e^{-\frac{z_i^2}{\sigma_z^2}} e^{-\frac{y^2}{\sigma_y^2+i\frac{2(z_i+\Delta z)}{k_0}}} \otimes \delta(y-y_i)\} \\
&= \sum_{i=1}^{N} e^{i2nk_0z_i} e^{-2\frac{x_i^2}{\sigma_x^2+i\frac{2z_i}{k_0}}} e^{-\frac{z_i^2}{\sigma_z^2}} (FT_{y\to k_y}\{e^{-\frac{y^2}{\sigma_y^2+i\frac{2(z_i+\Delta z)}{k_0}}} \otimes \delta(y-y_i)\}) \\
&= \sum_{i=1}^{N} e^{i2nk_0z_i} e^{-2\frac{x_i^2}{\sigma_x^2+i\frac{2z_i}{k_0}}} e^{-\frac{z_i^2}{\sigma_z^2}} (e^{-\frac{\sigma_y^2+i\frac{2(z_i+\Delta z)}{k_0}}{4}k_y^2} e^{ik_yy_i})
\end{aligned} \tag{6.20}$$

where $FT_{y\to k_y}$ denotes the Fourier transform along the y-direction. The low-resolution OCT signal can be generated by inverse Fourier transforming the product of $f(x,k_y,z)$ and a Gaussian filter $e^{-\frac{m^2}{4}k_y^2}$:

$$\begin{aligned}
f'(x,y,z) &= IFT_{k_y\to y}\{\sum_{i=1}^{N} e^{i2nk_0z_i} e^{-2\frac{x_i^2}{\sigma_x^2+i\frac{2z_i}{k_0}}} e^{-\frac{z_i^2}{\sigma_z^2}} [(e^{-\frac{\sigma_y^2+i\frac{2(z_i+\Delta z)}{k_0}}{4}k_y^2} e^{ik_yy_i})e^{-\frac{m^2}{4}k_y^2}]\} \\
&= \sum_{i=1}^{N} e^{i2nk_0z_i} e^{-2\frac{x_i^2}{\sigma_x^2+i\frac{2z_i}{k_0}}} e^{-\frac{y_i^2}{\sigma_{y'}^2+i\frac{2(z_i+\Delta z)}{k_0}}} e^{-\frac{z_i^2}{\sigma_z^2}}
\end{aligned} \tag{6.21}$$

where $\sigma_y{}' = \sqrt{\sigma_y^2 + m^2}$ is the reduced resolution along the y-direction. Follow the same derivation, the autocorrelation function of the low-resolution OCT signal under noise is:

$$\tilde{g}_1'(t) = \gamma' e^{i2nk_0v_zt} e^{-4n^2k_0^2Dt} e^{-(\frac{v_x^2}{\sigma_x^2}+\frac{v_y^2}{2\sigma'^2_y}+\frac{v_z^2}{2\sigma_z^2})t^2} \tag{6.22}$$

With the assumption that the two noise correction ratios are the same, the ratio of the two autocorrelation functions is:

$$G_1(n\tau) = \frac{\tilde{g}_1(n\tau)}{\tilde{g}_1'(n\tau)} = e^{-(\frac{1}{2\sigma_y^2}-\frac{1}{2\sigma'^2_y})v_y^2n^2\tau^2} \tag{6.23}$$

where n is the number of time steps and τ is the time resolution. Since G_1 is independent with the noise correction coefficient, the diffusion rate, and the translational velocity components v_x and v_z, the speed along the y-direction, v_y can be calculated as:

$$v_y = \frac{1}{n\tau}\sqrt{2ln\,|\,G_1(n\tau)\,|\,\frac{\sigma'^2_y\,\sigma^2_y}{\sigma'^2_y - \sigma^2_y}} \tag{6.24}$$

The axial velocity, v_z, can be obtained using Doppler OCT,

$$v_z = \frac{\lambda_0}{4n\pi\tau}\langle\delta\phi\rangle \tag{6.25}$$

where n is the refraction index of the sample, $\delta\phi$ is the phase difference of adjacent B-scans, τ is the time resolution, and $\langle\rangle$ denotes the average of the phase difference of adjacent B-scans imaged at the same location. If the overall translational decay term, $F = \frac{v_x^2}{\sigma_x^2} + \frac{v_y^2}{2\sigma_y^2} + \frac{v_z^2}{2\sigma_z^2}$, can be extracted, the velocity along the scanning direction, v_x, is given by,

$$v_x = \sigma_x\sqrt{F - \frac{v_y^2}{2\sigma_y^2} - \frac{v_z^2}{2\sigma_z^2}} \tag{6.26}$$

The resolution parameters $(\sigma_x, \sigma_y, \sigma_z)$ are usually considered as constants; however, because they are affected by system and sample aberrations as well as by imperfect linear interpolation at high fringe frequencies [69,182], these parameters are treated as functions of position in this study.

6.3 Methods

6.3.1 LS SD-OCT system and sample preparation

The experiment was carried out using the LS SD-OCT system reported recently with small modifications [143]. The system is based on a Michelson interferometer and is powered by a supercontinuum laser (SuperK, NKT Photonics, Birkerød, Denmark). A customized band-pass filter was utilized to select a spectral range of 600 nm – 980 nm. A narrow Gaussian filter was applied in post-processing to ensure that the autocorrelation signal is consistent with the theory and to reduce the influence of the axial velocity on the autocorrelation function. The spectrum after digital filtering is centered at 800 nm, and the effective full width at maximum half (FWMH) bandwidth is about 50 nm. The theoretical axial resolution after digital filtering is 5.6 μm in free space, which is consistent with the experiment result of 5.5 μm. An infinity-corrected 5× objective (M Plan NIR, Mitutoyo, Japan) was used, and the lateral resolutions along the two transverse directions are around 4 μm. The optical power incident on the imaged sample was 2.0 mW, but the effective power should be lower considering the digital Gaussian filter applied. The effective SNR was 83 dB at the center of line illumination and decreased at the edges because of the Gaussian intensity distribution. The interference signal is detected by a 2D CMOS camera (Dimax S4, PCO, Germany) with a detection area of 1920×500 pixels (spectral × spatial) at a 2.95 kHz frame rate, resulting in a time resolution of $\tau = 0.34$ ms. Only the central 300 A-scans were used for analyzing the velocity, and the two edges were removed because of low SNR.

Diluted 5% intralipid was pumped with a single syringe pump (NE300, Pump System Inc) into the glass capillary (QGCT0.2, Capillary Tube Supplies Ltd) or a customized polydimethylsiloxane (PDMS) microfluid phantom made using standard softlithography techniques [183]. Flow rates were set at 0, 0.6, 1.2, 1.8, and 2.4 μL/min for the glass capillary and 7.5 μL/min for the microfluid phantom. 800 repeated B-scans at the same location were recorded at a frame rate of 2.95 kHz.

6.3.2 Axial phase error correction

The interference fringe, $I(x, y, p)$, is first calculated by subtracting the background signal, $R(y, p)$, which is the optical intensity reflected from the reference mirror. After background subtraction, the interference function is interpolated from camera pixel number to wavenumber space with the calibration function $k(p)$ calibrated according to the method described in [84]. The fringe signal, $I(x, y, k)$, is Hilbert transformed and digitally dispersion compensated up to the 3rd order [67], and then Fourier transformed with respect to k and the complex OCT signal as a function of position can be retrieved as:

$$f(x,y,z) = FT_{k\to z}\{I(x,y,k)\} = A(x,y,z)e^{i\phi(x,y,z)} \tag{6.27}$$

Since the B-scan of the same scanning location (x-direction) is collected repeatedly, the OCT signal is rewritten as:

$$f(n\tau,y,z) = A(n\tau,y,z)e^{i\phi(n\tau,y,z)}, n = 1,2,3...,N \tag{6.28}$$

where n refers to the nth B-scan signal, N is the total number of B-scans, and τ is the time resolution of the LS SD-OCT system. Due to inevitable axial motions, e.g., mechanical vibration of the support stage, the OCT signal's phase information is distorted and results in wrong Doppler phase shifts and autocorrelation function. Since this additional axial displacement between adjacent B-scans is in the sub-micron range, the bulk motion-induced phase error $\Delta\phi$ can be compensated. Because of the parallel imaging configuration of LS SD-OCT and the fast frame rate, it can be assumed that the bulk axial motions of all the A-scans with in the same B-scan are the same [45]. The weighted averaged phase difference of two adjacent B-scans is:

$$\Delta\phi_n = \arg\Big[\sum_{(y,z)\in D} f(n\tau, y, z) f((n+1)\tau, y, z)^*\Big], n = 1,2,3\ldots, N-1 \tag{6.29}$$

where D is a user-selected static region without translational flow and the asterisk denotes the complex conjugate. The accumulated axial bulk motion-induced phase difference of the nth B-scan with respect to the first B-scan is:

$$\Delta\Phi_n = \sum_{i=1}^{n-1} \Delta\phi_i, n = 2,3,4\ldots, N \tag{6.30}$$

The OCT signal is then corrected by multiplying with a phasor:

$$f_{corr}(n\tau, y, z) = f(n\tau, y, z) e^{i\Delta\Phi_n} \tag{6.31}$$

6.3.3 Doppler OCT (DOCT)

The localized phase difference between two consecutive B-scans after axial phase correction is:

$$\delta\phi(n\tau, y, z) = \arg[f_{corr}(n\tau, y, z) f_{corr}((n+1)\tau, y, z)^*] \tag{6.32}$$

The axial velocity component thus is:

$$v_z(y,z) = \frac{\lambda_0}{4n\pi\tau}\langle\delta\phi(n\tau, y, z)\rangle_n \tag{6.33}$$

The transverse velocity can be calculated once the Doppler angle is determined. The Doppler angle can be calculated as:

$$\theta = \arccos[\frac{\sin(\alpha)}{n}] \tag{6.34}$$

where α is the angle between the normal direction of flow surface and the beam propagating direction in free space and can be calculated by fitting the slope of the top air-glass interface:

$$\alpha = \arctan(\eta \times \frac{\delta z}{\delta y}) \tag{6.35}$$

where η is the slope of the air-glass interface in terms of pixel and δy and δz are the digital resolutions of the LS SD-OCT system in the y- and z-direction.

6.3.4 Digital subaperture-based Doppler OCT (DSubAp DOCT)

Digital subaperture-based Doppler (DSubAp) OCT takes the advantage of the high phase stability of the parallel imaged tomogram to analyze the transverse spatial frequency distribution of the backscattered light on the Fourier plane:

$$F(n\tau, k_y, z) = FT_{y \to k_y}\{f_{corr}(n\tau, y, z)\} \tag{6.36}$$

Two symmetric subapertures, $[-k_{y,c} - \delta k_y/2,\ -k_{y,c} + \delta k_y/2]$ and $[k_{y,c} - \delta k_y/2,\ k_{y,c} + \delta k_y/2]$, are used to filter out the signals $F_l(n\tau, k_y, z)$ and $F_r(n\tau, k_y, z)$ separately. Here, $\pm k_{y,c}$ and δk_y refer to the centres and size of the two subapertures. The filtered signals are then transferred back into spatial space and generate two low-resolution tomograms of the two subapertures:

$$\begin{aligned} f_{corr,l}(n\tau, y, z) &= IFT_{k_y \to y}\{F_l(n\tau, k_y, z)\} \\ f_{corr,r}(n\tau, y, z) &= IFT_{k_y \to y}\{F_r(n\tau, k_y, z)\} \end{aligned} \tag{6.37}$$

The localized phase differences between two consecutive B-scans of the two post-processed low-resolution tomograms are,

$$\begin{aligned} \delta\phi_l(n\tau, y, z) &= \arg[f_{corr,l}(n\tau, y, z) f_{corr,l}((n+1)\tau, y, z)^*] \\ &= (2nk_z v_z - k_{y,c} v_y)\tau \\ \delta\phi_r(n\tau, y, z) &= \arg[f_{corr,r}(n\tau, y, z) f_{corr,r}((n+1)\tau, y, z)^*] \\ &= (2nk_z v_z + k_{y,c} v_y)\tau \end{aligned} \tag{6.38}$$

Since the objective's NA is small, the approximation $k_z = k_0$ is valid in most OCT systems. The velocity along y-direction is:

$$v_y = \frac{\delta\phi_r(n\tau, y, z) - \delta\phi_l(n\tau, y, z)}{2k_{y,c}\tau} \tag{6.39}$$

It is important to note that the above equation is valid only if the subapertures' size δk_y is small in comparison to the system's full aperture size $\Delta k_y = \frac{2\pi}{\delta y}$. The reason is that the amplitude distribution of the backscattered light over the spatial frequency space is not constant. In general, the amplitude decreases with increasing k_y. The average phase difference of the two subapertures is:

$$\delta\phi_r - \delta\phi_l = 2\arg[\int_{k_{y,c}-\frac{\delta k_y}{2}}^{k_{y,c}+\frac{\delta k_y}{2}} A(k_y) exp(ik_y v_y \tau) dk_y] \tag{6.40}$$

where $A(k_y)$ is the amplitude of the backscattered light. Since the contribution of different spatial frequency varies, the assumption $\delta\phi_r - \delta\phi_l = 2k_{y,c} v_y \tau$ does not hold if the subapertures' size is large.

It is suggested that the amplitude-weighted average of the spatial frequency should be used in a dual-angle point-scanning OCT system [165],

$$\tilde{k}_{y,c} = \frac{\int_{k_{y,c}-\frac{\delta k_y}{2}}^{k_{y,c}+\frac{\delta k_y}{2}} A(k_y) k_y dk_y}{\int_{k_{y,c}-\frac{\delta k_y}{2}}^{k_{y,c}+\frac{\delta k_y}{2}} A(k_y) dk_y} \tag{6.41}$$

However, this approximation holds only if the backscattered light is confined in a small aperture, or the flow velocity is well below the velocity detection range limited due to phase wrapping. Here, we confined the subaperture size to be 1/10 of the full aperture $\delta k_y = \frac{\Delta k_y}{10}$.

Although the small subaperture leads to smaller signal SNR thus higher phase noise, averaging the phase difference $N-1$ times can improve the accuracy as N is in the order of several hundred:

$$\begin{aligned} \delta\phi_l(y,z) &= \arg[\sum_{i=1}^{N-1} f_{corr,l}(n\tau,y,z) f_{corr,l}((n+1)\tau,y,z)^*] \\ \delta\phi_r(y,z) &= \arg[\sum_{i=1}^{N-1} f_{corr,r}(n\tau,y,z) f_{corr,r}((n+1)\tau,y,z)^*] \end{aligned} \tag{6.42}$$

The central locations of the subapertures are chosen by balancing the signal's SNR, the ratio of motion-induced phase difference to the phase noise, and the maximum detectable velocity. If the two subaperture are too close to the center, the motion-induced phase change is too small despite the signal's SNR is relatively high thus phase noise is low. On the contrary, if they are near the edges of the full aperture, the signal's SNR is low thus the phase noise is high, and the motion-induced phase difference exceeds $\pm\pi$ even at low flow speed. In this study, the centers of the two subapertures are set to be 1/4 of the full aperture $\pm k_{y,c} = \pm\frac{\Delta k_y}{4}$. Therefore, Equation (6.39) can be rewritten as,

$$v_y = \frac{\delta y}{\pi\tau}[\delta\phi_r(y,z) - \delta\phi_l(y,z)] \tag{6.43}$$

It has been pointed out that when the scatters are out of focus, the axial motion gradient induces additional phase change that can be misinterpreted as lateral motions [62,184]. Since digital refocusing of the flow signal is challenging because of the lack of distinguishable structures in the phantoms, we use DSubAp DOCT as a gold standard only when there is no axial motion.

6.3.5 DLS-LSOCT

According to the Wiener–Khinchin theorem, the first order autocorrelation of a function is the Fourier transform of its power spectral density (PSD). The temporal autocorrelation of the axial phase corrected OCT signal can be calculated more efficiently using its PSD than following the definition:

$$g_1(n\tau) = IFT_{\omega \to n\tau}\{|FT_{n\tau \to \omega}\{f_{corr}(n\tau, y, z)\}|^2\} \tag{6.44}$$

The normalized autocorrelation function is thus $\tilde{g}_1(n\tau) = \frac{g_1(n\tau)}{g_1(0)}$.

A low-resolution OCT signal is generated by applying a Gaussian filter to the transverse spatial frequency distribution function of the original OCT dataset, followed by inverse Fourier transforming back to spatial space,

$$f'_{corr}(n\tau, y, z) = IFT_{k_y \to y}\{FT_{y \to k_y}\{f_{corr}(n\tau, y, z)\} \times exp(-\frac{2k_y^2}{(a\Delta k_y)^2})\} \tag{6.45}$$

where a controls the size of the applied Gaussian filter, and Δk_y is the full bandwidth of the transverse spatial frequency. In this study, the size of the filter is set as $a = \frac{1}{4}$ as a compromise of the resolution reduction and translational motion induced decay contrast.

Once the localized resolutions σ_y and ${\sigma_y}'$ are determined, the velocity component v_y, in principle, can be calculated following Equation (6.24). The result is supposed to be independent with the time delay, as long as $\tilde{g}_1(n\tau)$ is above the noise floor. However, we find that the result using different time delay steps varies, and all of them differ from the gold standard to some extent. Thus, linear least squared (LLS) fitting is performed on all time delay steps at which $\tilde{g}_1(n\tau)$ is above a user-selected threshold. If the noise correction ratios of the original and low-resolution tomograms slightly differ, Equation (6.23) should be corrected as:

$$G_1(n\tau) = \tilde{\gamma} e^{-(\frac{1}{2\sigma_y^2} - \frac{1}{2\sigma'^2_y}) v_y^2 n^2 \tau^2} \tag{6.46}$$

where $\tilde{\gamma} = \frac{\gamma}{\gamma'}$ is an unknown factor that can be get rid of by taking the logarithm of both sides:

$$\ln[G_1(n\tau)] = ln[\tilde{\gamma}] - (\frac{1}{2\sigma_y^2} - \frac{1}{2\sigma'^2_y}) v_y^2 \tau^2 n^2 \tag{6.47}$$

As it can be seen, $\ln[G_1(n\tau)]$ is a linear function of n^2. Once the linear slope η is fitted, the v_y can be calculated by:

$$v_y = \sqrt{\frac{2|\eta|}{\tau^2(\frac{1}{\sigma_y^2} - \frac{1}{\sigma'^2_y})}} \tag{6.48}$$

In this work, $n = 1,2, \ldots, m-1$, where m is the first time delay point at which $\tilde{g}_1(n\tau) < 0.15$ and is confined in the range of $[3,15]$. The lower limit is set to ensure the LLS fitting works properly. If $m < 3$, there are two possible situations: (1) the flow speed is too fast such that none or only one time delay is above noise level; (2) there is no scattering signal but noise. Both cases will result in an inaccurate result. The data processing steps of DLS-LSOCT are illuminated in Figure 6.1.

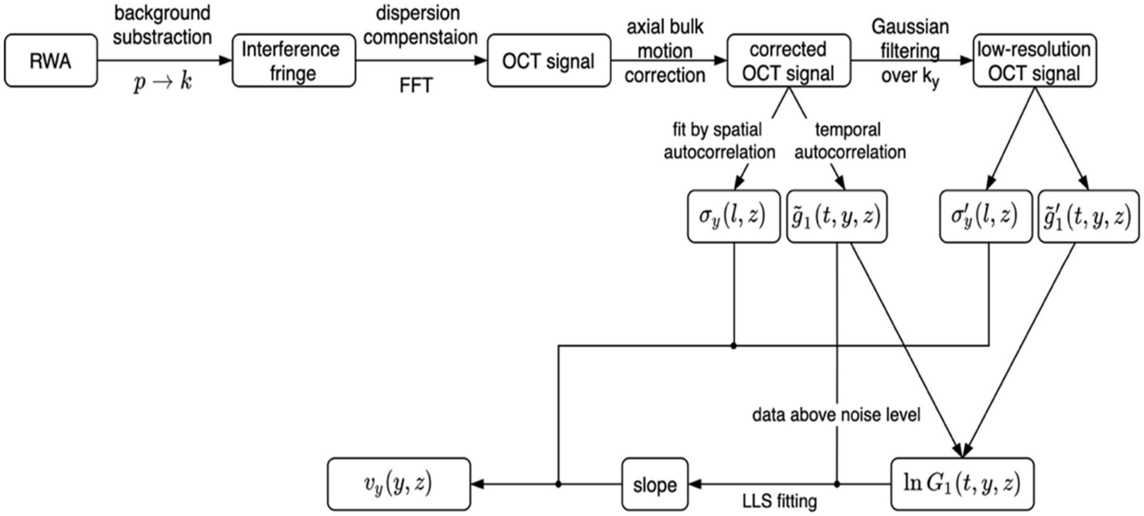

Figure 6.1 Flowchart of the data processing steps in DLS-LSOCT.

6.3.6 Localized resolutions

Conventionally, the resolution parameter $\sigma_y(y, z)$ is treated as a constant for all locations in different datasets, using the results measured in free space or calibrated with known flow velocity [64,171,176]. However, this assumption holds only when the illuminating and detecting beams are both in fundamental transverse Gaussian mode and free of any other system and sample aberrations. It has also been pointed out that the speckle induced by multi-scattering from the same imaging volume might change the autocorrelation function because of departing from the assumption of fully developed speckle. As a result, it is necessary to determine the localized resolution parameters, $\sigma_y(y, z)$ and $\sigma'_y(y, z)$ for each dataset.

In this study, these two parameters are measured by determining the spatial autocorrelation of the B-scan signal in terms of lateral shift [182]. If the B-scan signal is digitally shifted in the y-direction, there is no diffusional motion and translational motion in the xz-plane. Therefore, the normalized spatial autocorrelation of a B-scan and its digitally shifted counterpart is:

$$\tilde{g}_1(pdy,z) = \gamma e^{-(\frac{pdy}{2\sigma_y})^2} \tag{6.49}$$

where dy and p are the size and number of the digital translation steps. Again, $\ln\left(\tilde{g}_1(pdy,z)\right)$ is a linear function of p^2.

In practice, considering the resolution across the lateral direction can be different, we evenly divide each B-scan into 12 columns： $f_{\mathrm{corr}}(n\tau,y,z) \to f_{\mathrm{corr}}(n\tau,l,y,z)$, where $l = 1,2,\ldots,12$. For each sub-tomogram, the OCT signal is upsampled 5-fold along y-direction by inverse Fourier transforming its zero-padded spatial frequency representation. In this study, the zero-padding array size is set as 4 times as large as the original signal size. The autocorrelation function is then averaged over all B-scans:

$$\tilde{g}_1(l,pdy,z) = \langle \tilde{g}_1(n\tau,l,pdy,z) \rangle_n \tag{6.50}$$

$\sigma_y(l,z)$ is then determined using LLS fitting of the logarithmic version of Equation (6.49). Similarly, $\sigma'_y(l,z)$ can be calculated using the post-processed low-resolution OCT signal. The transverse resolutions are treated as constants along the y-direction within each sub-tomogram but variables along the z-direction because that a certain amount of data is required to calculate the spatial autocorrelation. Nevertheless, they still vary for different sub-tomograms, which is better than treating them as constants within the whole B-scan.

6.3.7 Power spectral density of the repeated B-scan series

Besides the phase noise, which can be suppressed by averaging repeated measurements, the Doppler phase is also broadened by the axial and lateral motions. The broadening of the Doppler phase is inevitable and can be used to estimate the lateral velocity [164,185]. Based on the assumption that the translational motion takes place only in the y-direction, the normalized temporal autocorrelation of the OCT signal is:

$$\tilde{g}_1(t) = e^{i2nk_0v_zt} e^{-4n^2k_0^2Dt} e^{-\frac{v_y^2}{2\sigma_y^2}t^2} \tag{6.51}$$

Assuming the diffusional motion is much smaller than the translational motion, the power spectral density can be written as:

$$s(\omega) = FT_{t\rightarrow\omega}\{\tilde{g}_1(t)\} \propto e^{-\frac{\sigma_y^2}{2v_y^2}(\omega-2nk_0v_z)^2} \qquad (6.52)$$

Therefore, the translational velocity, v_y, can be calculated by fitting the power spectral density function with a Gaussian distributional model. Since the autocorrelation function decays into noise level rapidly, its power spectral density is calculated by:

$$s(\omega, y, z) = | FT_{n\tau\rightarrow\omega}\{f_{corr(n\tau,y,z)}\} |^2 \qquad (6.53)$$

The uncertainty of the power spectral density at a single spatial point is at the same level as the signal itself in our LS SD-OCT system. In order to ensure the fitted results are more robust, we again divided the B-scan into 12 columns and laterally averaged the normalized power spectral density within each column:

$$s(\omega, l, z) = \langle \frac{s(\omega, y, z)}{s(0, y, z)} \rangle_{y\in Y_l} \qquad (6.54)$$

6.3.8 Diffuse compensation

In the case that the diffusional motion is not negligible, both exponential and Gaussian decay terms need to be considered. In point-scan OCT, the diffusion coefficient and translational velocity can be fitted either separately or simultaneously [176]. However, in LS SD-OCT, only the first method is possible as the autocorrelation decays too fast because of the low time resolution. The diffusion coefficient is first measured without flow. The B-scan is divided into 720 blocks and the autocorrelation function is averaged within each block before fitting. An averaged diffusion coefficient is used in the following calculation under the assumption that the diffusion coefficient is uniformly distributed across the whole volume. The diffusion decay term can be compensated following:

$$\tilde{g}_{1,dc}(t) = \tilde{g}_1(t)e^{4n^2k_0^2\bar{D}t} \qquad (6.55)$$

The translational velocity can then be determined by fitting the diffusion compensated autocorrelation function with the Gaussian decay curve.

6.4 Results

6.4.1 Validation of DLS-LSOCT performance without axial velocity gradient

In this experiment, we evaluated the performance of the DLS-LSOCT without axial velocity gradient. We start by determining the localized transverse resolution parameters, $\sigma_y(z)$ and $\sigma_y{}'(z)$, based on the spatial (y-direction) autocorrelation of the B-scan signal. Figure 6.2 shows the measurement of the localized resolution parameters of the diluted intralipid at a flow rate of 2.4 uL/min. As shown in Figure 6.2 (A), the glass capillary was placed parallel to the beam illumination plane and perpendicular to the beam propagation direction to ensure the flow velocity is along the y-direction. The illumination plane is slightly mismatched with the center of the glass capillary to avoid self-interference and signal saturation. Figure 6.2 (B) shows a typical log-scale B-scan image of the flow phantom. The red box indicates the selected region of interest (ROI), which is the 7th column of the 12 evenly divided areas. The axial position of the glass capillary was set ~ 50 μm away from the location at which the top glass-intralipid interface's signal reached to the highest. Figure 6.2 (C) shows the normalized OCT signal amplitude as a function of depth. The amplitude was laterally averaged within the selected ROI. The origin of the axial axis locates at the top glass-intralipid interface. As it can be seen, the OCT signal attenuates rapidly from the top to the bottom due to beam defocusing and medium scattering. The local contrast drops from 10 at the top to 2 at the bottom which leads to higher uncertainties for both phase-based and autocorrelation-based flow speed measurements. The localized resolution parameters of the selected ROI are shown in Figure 6.2 (D), estimated following the method described in Chapter 6.3.6.

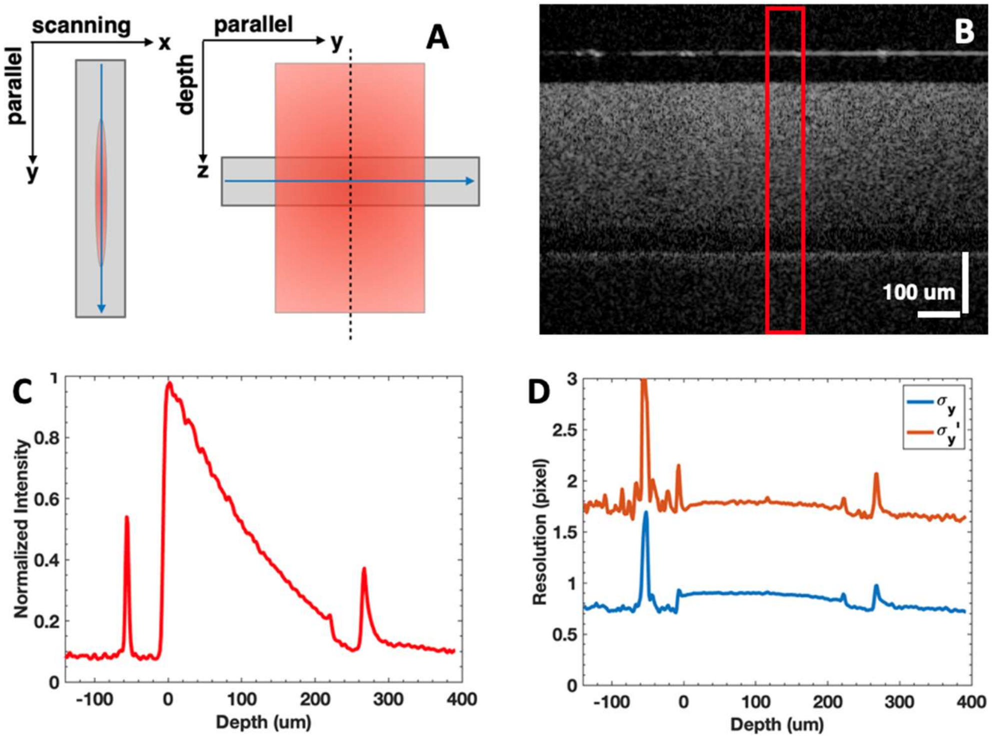

Figure 6.2 Measurement of the localized resolution parameters of the diluted intralipid at a flow rate of 2.4 uL/min. (A) Schematic of the flow orientation. (B) A typical log-scale B-scan image of the flow capillary. The red box indicates the selected region of interest (ROI) within which the signal amplitude and localized resolutions are analyzed. (C) OCT signal amplitude attenuation. The amplitude was averaged along the y-direction. (D) Estimated localized resolution parameters, $\sigma_y(z)$ (blue) and $\sigma_y{}'(z)$ (orange).

The blue and orange lines represent the resolution parameters along the y-direction of the original and digitally generated low-resolution OCT images respectively. The 4 peaks correspond to the 4 interfaces of different mediums. As expected, the resolution parameters of the scattering intralipid are larger than those of the noise and smaller than those of the specular reflection from the interfaces. This is because the estimated resolution parameters are negatively correlated with the autocorrelation function. The resolution of the scattering sample was reported to be independent of the position [175,176]. However, our result shows that the resolution parameters at the bottom of the sample is slightly smaller than those at the top. This might come from the fact that the low SNR and accumulated multi-scattering at the bottom region result in additional decorrelation.

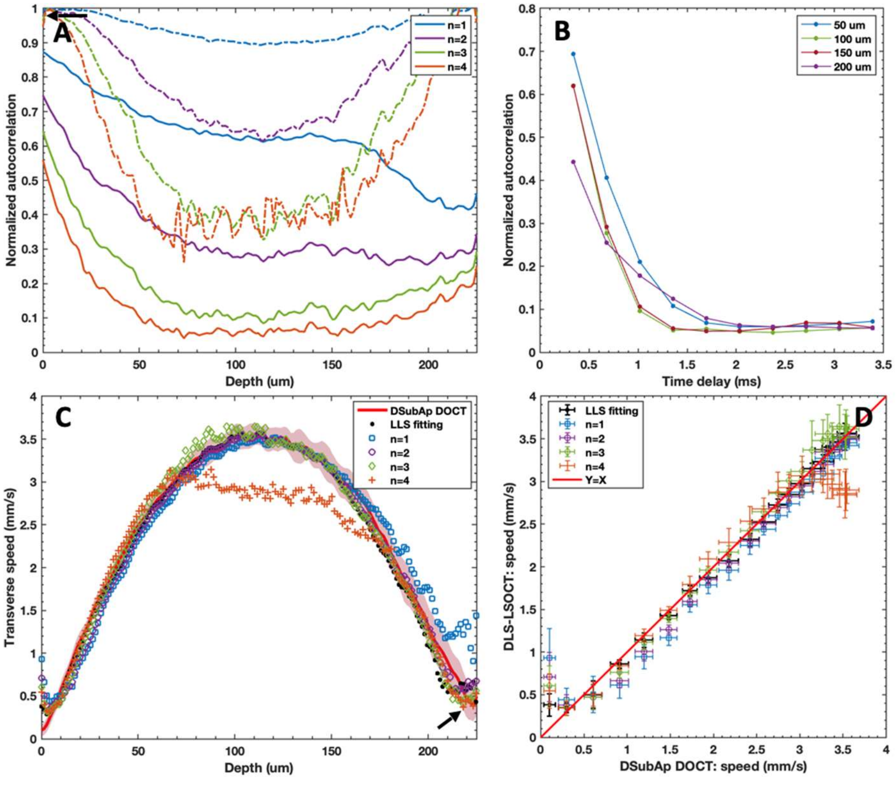

Figure 6.3 Comparison of the DLS-LSOCT results determined by single time delay and linear least squared (LLS) fitting. The dataset is the same with that of Figure 6.2. (A) Autocorrelation at different time delay steps ($n\tau$) as a

function of depth. The solid line and dosh line indicate the autocorrelation function of the original OCT signal $\tilde{g}_1$ and the ratio of the autocorrelation of the original and low-resolution signal $G_1 = \tilde{g}_1/\tilde{g}_1{}'$, respectively. (B) Autocorrelation of the original OCT signal $\tilde{g}_1(n\tau)$ at depth 50 μm, 100 μm, 150 μm, and 200 μm. (C) Measured transverse flow velocity v_y as a function of depth. The scatter plots are the results of DLS-LSOCT using LLS fitting and different time delay steps. The result of digital subaperture-based (DSubAp) DOCT is indicated by the red line and its 3-sigma uncertainty is shown by the red-with-opacity area. (D) Depth by depth comparison of the speeds determined by DLS-LSOCT and DSubAp DOCT. $z \in [0,110]$ μm. The solid red line indicates the reference at which the two measured speeds are equal.

Once the $\sigma_y(z)$ and $\sigma_y{}'(z)$ are determined, we can calculate the transverse velocity v_y following the methods described in Chapter 6.3.5. Figure 6.3 (A) shows the autocorrelation at different time delay steps ($n\tau$) as a function of depth. The solid line indicates the normalized autocorrelation of the original OCT signal $\tilde{g}_1$ and the dosh line represents the ratio of the autocorrelations of the original and low-resolution signal $G_1 = \tilde{g}_1/\tilde{g}_1{}'$. Both $\tilde{g}_1$ and G_1 were averaged along y-direction within the selected ROI shown in Figure 6.2 (B). If there is no noise, the autocorrelation decays $\tilde{g}_1(n\tau)$ with the same translational velocity are supposed to be the same. Since the speed distribution $v_y(z)$ of the laminar flow in a circular pipe is parabolic, the noise-free autocorrelation $\hat{g}_1(n\tau, z)$ should be spatially symmetric. However, the noise breaks this symmetry, as shown by the solid lines. The noise influence on the autocorrelation function is modeled as a linear correction ratio which is dependent on the SNR [181,182]. In our proposed method, both autocorrelation $\tilde{g}_1(n\tau, z)$ and $\tilde{g}'_1(n\tau, z)$ suffer similar, if not the same, reduction such their ratio, $G_1(n\tau, z)$, recovers the spatial symmetry, which is shown by the dash line. In the depth range $z \in [60,170]$ μm, $G_1(4\tau, z)$ shows randomly oscillations because $\tilde{g}_1(4\tau, z)$ reaches the noise level.

It is worth noting that the ratio $G_1(n\tau, z)$ is supposed to be 1 at the depth of 0 μm at which the translational speed is 0. However, $G(n\tau, 0)$ is lower than 1, as indicated by the black arrow in Figure 6.3 (A). This might be due to the specular reflection breaks the single scattering assumption. The noise-free upper flow speed detection limit for can be estimated as follows. For the LLS fitting method, since at least two time delay steps are required, the n = 2 lines are used. The solid line shows the diffusion decay term at $t = 2\tau$ is about 0.74 since the SNR at depth 0 μm is high and the noise correction ratio is negligible. The dash line indicates the translational motion decay term $\exp\left(-\frac{4\tau^2 v_y^2}{\sigma_y^2}\right)$ is estimated as

0.54 at a speed of 3.5 mm/s, using the average resolution parameters determined in Figure 6.2 (D) and assuming the noise correction ratios are the same. Thus, v_y can increase to 6.3 mm/s at which $g_1(2\tau)$ reaches the noise level of 0.1. Similarly, the upper limit using a single time decay step is 13.5 mm/s. In practice, due to the existence of noise, the maximum detectable flow speed can be smaller than the upper limits. Figure 6.3 (B) shows the plot of $\tilde{g}_1(n\tau)$ at 4 different depths, at which the autocorrelation functions all decay into the noise floor within 5 time delay steps. Due to the affection of noise differs at different SNRs, $\tilde{g}_1(n\tau)$ at depth 100 μm and 150 μm is almost indistinguishable, despite the translational velocities at these two depths are different. This implies the estimation of the flow speed based on $\tilde{g}_1$ itself is not trustable using the LS SD-OCT system. Figure 6.3 (C) shows the comparison of the results of DLS-LSOCT estimated by LLS fitting and different time delay steps. The flow speed and its 3-sigma uncertainty determined by DSubAp DOCT are shown by the red line and red-with-opacity area. It has been theoretically proven that the DSubAp DOCT result is distorted when the axial velocity gradient and defocus aberration exist simultaneously [184]. Nevertheless, since there was no translational velocity in z-direction in this experiment, the reported distortion should not exist and the averaged DSubAp DOCT result can be used as a gold standard. In the range $z \in [60{,}170]$ μm, there is a significant difference between the speed estimated by $G_1(4\tau, z)$ and the reference speed as $\tilde{g}_1(4\tau, z)$ is overwhelmed by the noise. In order to provide a quantitative correlation of the results of the DLS-LSOCT and the gold-standard reference, we define the fidelity of the two results as:

$$F = 1 - \frac{\sum_i |v_y(z_i) - v_{y,r}(z_i)|}{\sum_i |v_{y,r}(z_i)|} \tag{6.56}$$

where $z_i \in [0{,}110]\mu$m. The bottom half area is excluded since the phase of OCT signal picks up extra motion signal due to multi-scattering thus the speed distortion at the bottom is larger than the top. One evident is that at the bottom intralipid-glass interface, where translational motion does not exist, the result of DSubAp DOCT is well above 0, as indicated by the blue arrow. The fidelities of the results determined by LLS fitting and single time delay steps (n = 1, 2, 3 ,4) are 0.980, 0.933, 0.961, 0.959, and 0.906 respectively. Figure 6.3 (D) shows the depth by depth comparison of the speeds determined by DLS-LSOCT and DSubAp DOCT. Data is taken at every 4 steps from depth 0 to 110 μm. In general, the black dot is closer to the red line, which means the LLS fitted speeds are more precise. One possible explanation that the LLS fitting method has better performance is that the noise correction ratio γ is not exactly the same for the original and low-resolution OCT dataset, and the single time delay step method cannot compensate for it. In the following study, the LLS fitting method is used unless further notice.

Figure 6.4 shows the comparison of the performance of the proposed DLS-LSOCT method with the two other DLS-OCT based methods described in Chapter 6.3.7 and 6.3.8. Figure 6.4 (A) shows the OCT signal's power spectral density $s(\omega, z)$ of the selected ROI in Figure 6.2 (B). Since there is no translational motion in the axial direction, the Doppler peak was located at 0 frequency. The blue and red lines indicate the depths at which the power spectral density fitted in Figure 6.4 (B). The bandwidth of the fitted Gaussian curve is utilized to calculate the flow speed, as shown in Figure 6.4 (E). The diffusion coefficient of the diluted intralipid is determined without translational motion. The scattering intralipid signal is evenly divided into 30×24 ($x \times z$) blocks and the temporal autocorrelation is averaged within each block before fitted with model $\tilde{g}_1(t) = \gamma e^{-4n^2 k_c^2 Dt} + b$. Figure 6.4 (C) shows the mean value and standard deviation of the diffusion coefficient at different depths. A typical fitting of the $\langle \tilde{g}_1(\tau) \rangle$ averaged within one block is displayed in Figure 6.4 (D). The diffusion coefficient of the intralipid averaged over all the blocks is 1.56 ± 0.02 μm^2 /s. The diffusion compensated autocorrelation is calculated according to Equation (6.55) and the transverse velocity v_y is determined by LLS fitting with the model of $\ln\left(\tilde{g}_{1,dc}(n\tau)\right) = \ln(\gamma) - \frac{v_y^2 \tau^2 n^2}{2\sigma_y^2}$. Only the data above the noise level were select for the fitting, following the method described in Chapter 6.3.5. Figure 6.4 (E) and (F) compare the transverse speeds estimated by DLS-LSOCT, DLS-OCT power spectral density (PSD), and DLS-OCT diffusion compensation (DC). The results are first calculated using the laterally averaged temporal autocorrelation within the 12 sub-tomograms and then averaged over the sub-tomograms. As can be seen, only the DLS-LSOCT results show a good correlation with the gold standard. It is expected that the DLS-OCT PSD method does not agree with the reference speed since it did not take the diffusion effect into consideration.

In the case where the flow speed is high and the particle size is large, the diffusional decay is usually ignored since the translational decay dominates. However, in this experiment these two decays are comparable. For instance, at the first time delay step, the decay due to the diffusional motion and translational motion are 0.79 and 0.85 respectively, estimated using the averaged diffusion rate D=1.56 μm^2/s, the resolution parameter σ_y = 2.15 μm, and a translational flow speed of 3.5 mm/s. It has been reported that due to the diffusional motion, the power spectral density has a Lorentzian line shape instead of a delta function when the flow rate is set to zero [186]. This explains why the estimated speed is larger than 0 near the top glass-intralipid interface. In fact, the speed estimated by DLS-OCT PSD is a parameter indicating the dynamic of the flow but not the translational velocity. The result of DLS-OCT DC is not precise as well. One possible reason is that the estimated diffusion coefficient is not accurate. The model, Eq(6.18), assumes a 180° scattering angle which is not always valid with an objective whose NA is 0.15. This can be improved by using a smaller effective NA; however, the impact of translational velocity on the autocorrelation function is reduced due to a larger beam waist, leading to a reduced sensitivity of low velocity. In addition, the particle size of intralipid might not be well confined within a certain range thus the measured diffusion coefficient is just an ensemble average. For example, it has been shown by transmission electron microscopy that the diameter of the intralipid varied from 20 nm to 700 nm [187]. Another factor leading to the inaccurate results of DLS-OCT DC is that the noise-induced ratio correction model might not be valid when the SNR is low, especially with multi-scattering noise.

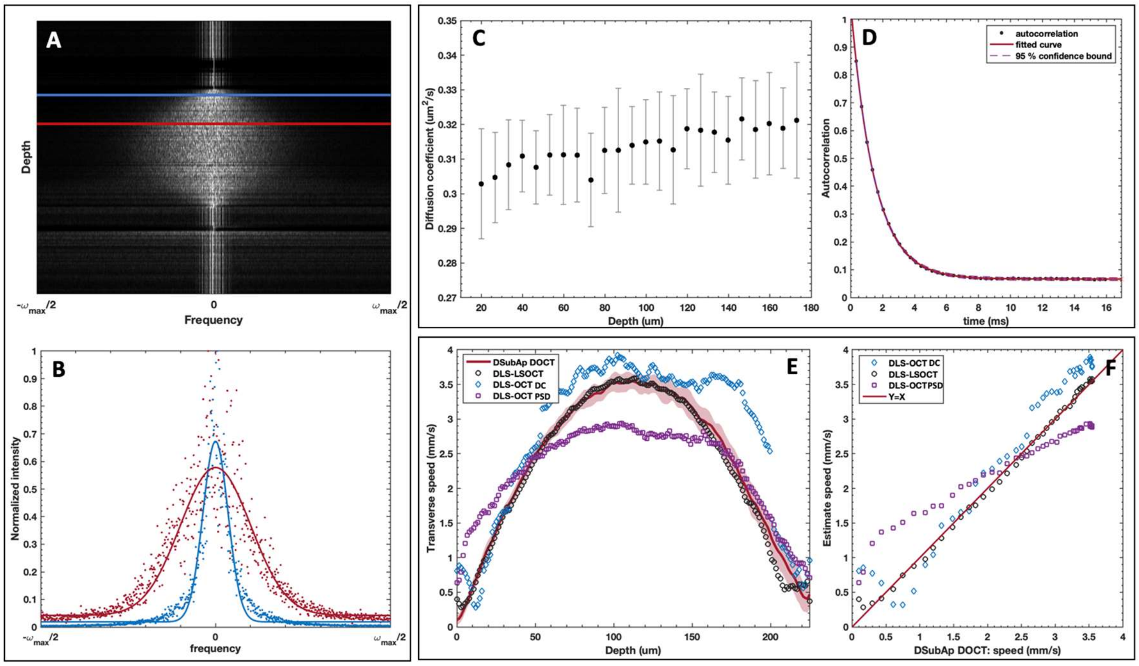

Figure 6.4 Comparison of the transverse speed determined by DLS-LSOCT, DLS-OCT PSD, and DLS-OCT DC. The dataset is the same as that of Figure 6.2. (A) Depth resolved power spectral density $s(\omega, z)$ of the ROI selected in Figure 6.2. (B) Scatter plots and the fitted Gaussian curves of the power spectral density at depths labeled by the blue and red lines in (A). (C) Diffusion coefficient measured in the absence of flow. (D) A typical averaged autocorrelation $\tilde{g}_1(\tau)$ and its fitted curve. The dash line shows the 95% confident bound. (E) Transverse flow velocity v_y as a function of depth. The scatter plots show the results determined by DLS-LSOCT, DLS-OCT

power spectral density (PSD), and DLS-OCT diffusion compensation (DC). The result of DSubAp DOCT is shown as the gold standard reference. (F) Depth by depth comparison of the speed determined by DLS methods and DSubAp DOCT.

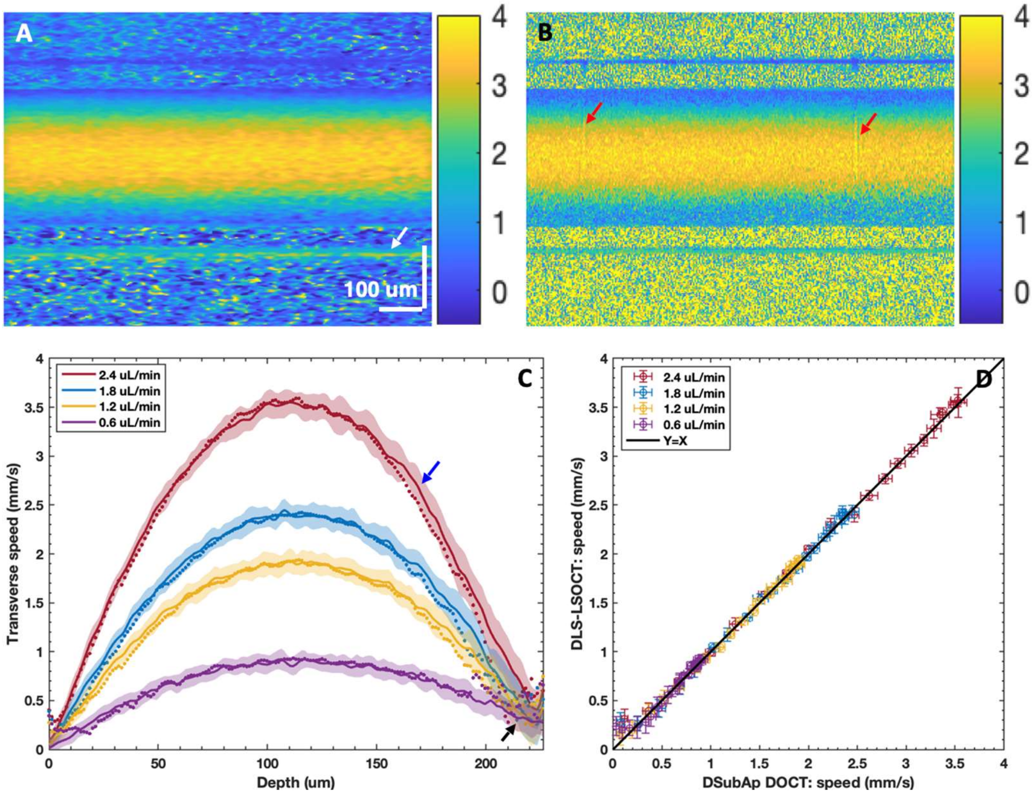

Figure 6.5 Comparison of the localized transverse speed determined by digital subaperture-based (DSubAp) DOCT and DLS-LSOCT. (A) Localized transverse speed $v_y(y,z)$ determined by DSubAp DOCT at the flow rate of 2.4 μL/min. The white arrow indicates the bottom glass-air interface where no flow exists. (B) Localized transverse speed $v_y(y,z)$ determined by DLS-LSOCT at the same flow rate as (A). The red arrows show two discontinuous lines. (C) Comparison of the results of the two methods as a function of depth at different flow rates. The solid lines are the mean speeds determined by DSubAp DOCT and the opacity areas represent the 3-sigma uncertainties. The dot plots are the averaged speed determined by DLS-LSOCT. The black arrow indicates the position of the bottom intralipid-glass interface where the transverse flow speed should be zero. (D) Depth by depth comparison of the speed determined by DLS-LSOCT and DSubAp DOCT.

Figure 6.5 shows a comprehensive comparison of the DLS-LSOCT and DSubAp DOCT performance without axial velocity. Figure 6.5 (A) and (B) show the localized transverse speed $v_y(y,z)$ of the B-scan estimated by DSubAp DOCT and DLS-LSOCT, respectively. Both speed distribution maps suggest that the transverse speed of the intralipid flow is parabolic distributed along the z-direction and is constant along the y-direction. The two results are highly matched except for 4 differences. (1) The large speckles in Figure 6.5 (A) indicate a bad lateral resolution due to small subapertures utilized in DSubAp DOCT. Apart from the speckles, the speed distribution map in Figure 6.5 (A) is smoother than in Figure 6.5 (B). This is because the result of DSubAp DOCT is an average of the 799 adjacent B-scan pairs' results, while the result of DLS-LSOCT is only fitted once though the temporal autocorrelation is determined with 800 repeated B-scans. (2) The noise in the air and glass regions in Figure 6.5 (B) suggests that the DLS-LSOCT is not robust when there is no scattering or reflecting signal. The fast decorrelation of the noise is interpreted as a high speed thus a binary mask generated by the OCT or OCTA image is needed to block out the noise-only regions. (3) The white arrow in Figure 6.5 (A) shows the fake speed signal located at the bottom glass-air interface as a result of the extra phase signal accumulated due to multi-scattering. The fake speed signal appears at the same location in Figure 6.5 (B) but with smaller values. The possible reasons for the fake signal in DLS-LSOCT include mechanical vibrations, abnormal resolution parameters, and low SNR. Whether and how multi-scattering plays a role in generating the fake signal in DLS-LSOCT needs further investigation. (4) The red arrows in Figure 6.5 (B) indicate two discontinuities that come from the defects of the top glass surface directly above the two discontinuous locations. The DSubAp DOCT is not affected since the two selected subapertures are away from the center. Figure 6.5 (C) shows depth resolved transverse speeds $v_y(z)$ at different flow rates. The solid line and the opacity areas indicate the mean speeds determined by DSubAp DOCT and their 3-sigma uncertainty respectively. The dot plots show the mean speeds of DLS-LSOCT. The results of the two methods are excellently correlated in the depth range $z \in [5,160]$ μm. The DLS-LSOCT method cannot detect translational velocity under 0.3 mm/s precisely because of the mechanical motions and vibrations induced extra decorrelation. Thus, the lower flow speed detection limit of the DLS-LSOCT method can be claimed as 0.3 mm/s. In the depth range $z \in [160,200]$ μm, the speeds estimated by DLS-LSOCT are lower than those of DSubAp OCT except for the result at the flow rate of 0.6 μL/min, as indicated by the blue arrow. As we already know that the DSubAp DOCT method accumulates extra phase at deeper depth due to higher possibility of multi-scattering thus its results are higher than the actual flow speed, this finding might suggest that DLS-LSOCT's results are closer to the true speed when the light penetrates deep into scattering media. At the depth range z > 200 μm, the DLS-LSOCT's results are disordered as the SNR is too low. Figure 6.5 (D) shows the depth by depth comparison of the speeds determined by DLS-LSOCT and DSubAp

DOCT. All the dots are located at the Y=X line within the error bar except for the speeds under 0.3 mm/s. This is consistent with what has been observed in Figure 6.5 (C).

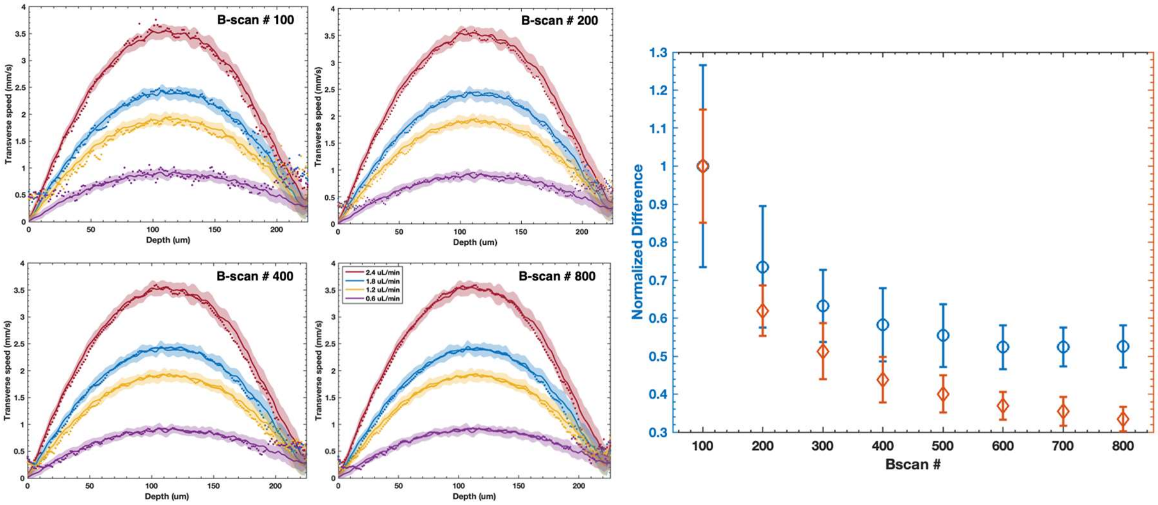

Figure 6.6 Influence of B-scan number on the precision and robustness of DLS-LSOCT. (Left) DLS-LSOCT results estimated using different numbers of B-scans. The DSubAp DOCT results are shown by the solid lines as a reference. (Right) Normalized precision (blue) and robustness (orange) as a function of B-scan number.

We then investigate the influence of repeated B-scans numbers on the performance of DLS-LSOCT. Too few B-scans cannot extract the true autocorrelation function, while too many are not necessary since the accuracy cannot be improved at a certain level due to the noise induced by inevitable mechanical motions. Figure 6.6 (Left) shows the DLS-LSOCT results at different flow rates using the autocorrelation calculated with 100, 200, 400, and 800 repeated B-scans, respectively. The results calculated using 100 B-scans are most disordered. The performance improves with an increase of the B-scan number, although the improvement from 400 to 800 is not significant. In order to provide a quantitative analysis of the relationship of the precision and robustness with the B-scan number, we define the precision and robustness of the DLS-LSOCT as:

$$\begin{aligned} P &= \sum_i \left| \overline{v}_y(z_i) - v_{y,r}(z_i) \right| \\ R &= \sum_i \frac{1}{12-1} \sum_l^{12} \left(v_y(l,z_i) - \overline{v}_y(z_i) \right)^2 \end{aligned} \qquad (6.57)$$

where $\overline{\mathrm{v}_{\mathrm{y}}}(z_i) = \langle v_y(l, z_i) \rangle_l$ is the average of the DLS-LSOCT's results of the 12 sub-tomograms, $v_{y,r}(z_i)$ is the mean speed of the DSubAp DOCT, and $z_i \in [0,110]$ μm. The precision and robustness at the 4 different flow rates are calculated and the normalized precision and robustness as a function of

B-scan number is shown in Figure 6.6 (Right). As it can be seen, both the precision and robustness improve a lot from a B-scan number of 100 to 600, and the performance improvement is limited after 600. Thus, 600 repeated B-scans are utilized in the subsequent studies.

6.4.2 DLS-LSOCT performance with axial velocity gradient and defocus

It has been realized that the axial velocity gradient ∇v_z will results in an extra phase in DSubAp DOCT [184] and additional decorrelation terms in DLS-OCT [171,188]. The transverse speeds estimated by both methods are distorted unless special care is taken to account for these artifacts. The influence of axial velocity gradient on the performance of DLS-LSOCT is investigated by comparing its results with the phase-based methods. As shown in Figure 6.7 (A), the axial velocity gradient was introduced by tilting the glass capillary about the x-axis such that the Doppler angle is set as 87.9°, 85.3°, and 83.1°. The axial position of the glass capillary was set ~ 50 μm away from the location where the top glass-intralipid interface's single in the center of y-direction reached the highest. Figure 6.7 (B)-(D) shows the localized transverse speed $v_y(y, z)$ maps determined by DOCT, DSubAp DOCT, and DLS-LSOCT at the flow rate of 1.8 μL/min with a Doppler angle of 85.3°, respectively. The DOCT's performance is the best among the three methods except for the fake velocity signal at the bottom glass-air interface. Figure 6.7 (E)-(G) shows the transverse speeds $v_y(z)$ at different flow rates with a Doppler angle of 87.9°, 85.3°, and 83.1° respectively. The red and blue lines indicate the speeds determined by DOCT and DSubAp DOCT respectively and the opacity areas represent their 3-sigma uncertainties. The black dash lines represent the results of DLS-LSOCT. The DOCT is utilized as the gold standard since the other two methods suffer from the velocity gradient induced distortion. The discontinuity of the DOCT and DSubAp DOCT's result at the flow rate of 2.4 μL/min in Figure 6.7 (G) is due to phase wrapping. The results of DLS-LSOCT and DSubAp DOCT highly coincide with the gold standard at the Doppler angle of 87.9°. However, their performance drops with an increase of Doppler angle, especially for the DLS-LSOCT method at low SNR regions. The speed estimated by DSubAp DOCT is higher than that of DOCT from depth 0 to 100 μm and lower from depth 100 to 220 μm and the difference rise with the increase of flow rate and decrease of the Doppler angle, which agrees with the theoretical prediction [184]. It is surprising that the results of DLS-LSOCT and DSubAp DOCT are still highly overlapped from depth 0 to 100 μm at all different flow rates and Doppler angles, considering the reasons of the two methods' distortions are different. The fidelities of the DLS-LSOCT at the three different Doppler angles are 0.964±0.014, 0.933±0.011, and 0.864±0.076, respectively. Figure 6.7 (H)-(J) show the depth by depth comparison of the speed determined by DLS-LSOCT and DOCT, corresponding to Figure 6.7 (E)-(I) respectively. The speed is overestimated by DLS-LSOCT at the Doppler angle of 85.3° and 83.1°, while the mismatch is negligible with the Doppler angle 87.9° except for the speed under 0.3 mm/s. The mismatch is dependent on the magnitude of velocity gradient instead of the speed itself, as shown by the black arrow in Figure 6.7 (J). The speed estimated by DLS-LSOCT is twice as large as the gold standard around 0.55 mm/s at the flow rate of 2.4 μL/min; however, the gap reduces with a decrease in flow rate as the location of same speed is closer to the capillary's central depth at which the velocity gradient is smaller.

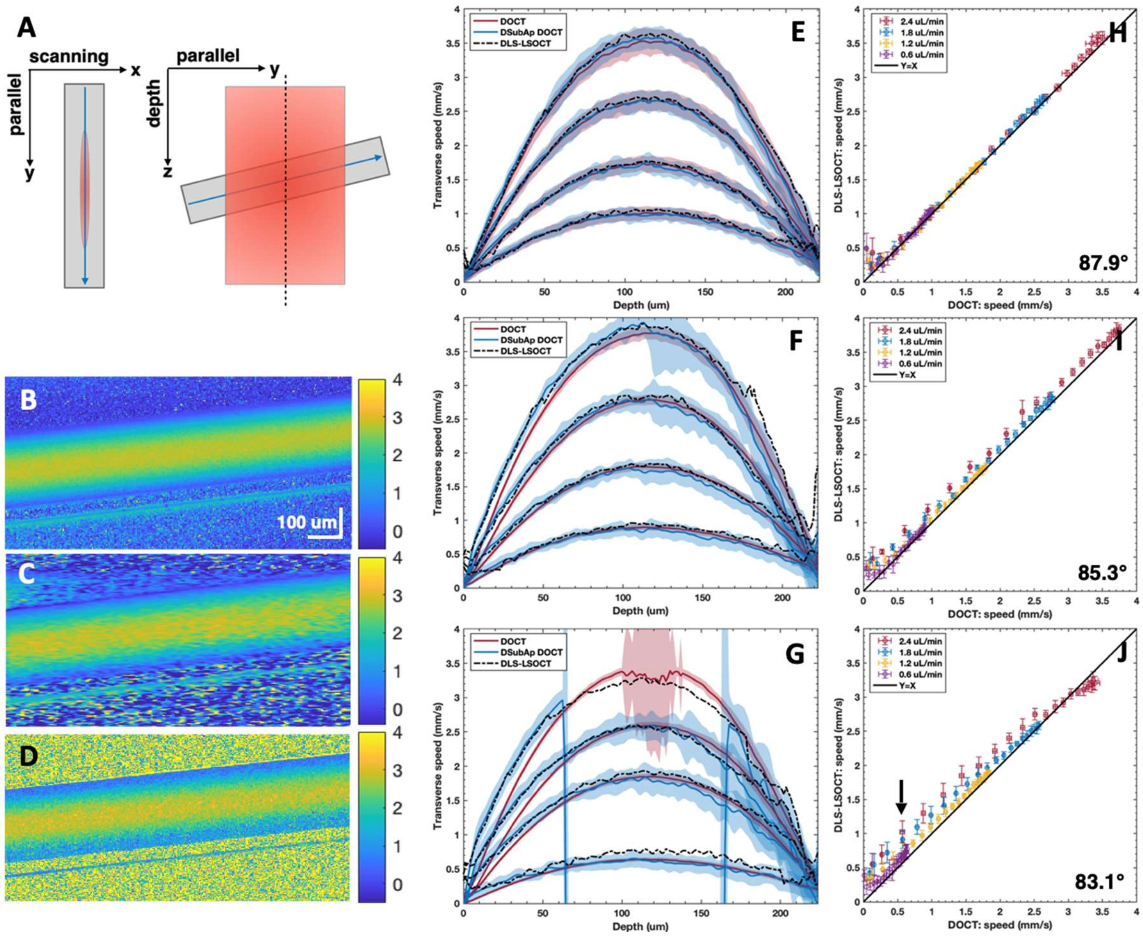

Figure 6.7 Comparison of the results of DOCT, DSubAp DOCT, and DLS-LSOCT at different Doppler angles. (A) Schematic of the illumination plane with respect to the flow direction. (B)-(D) Typical localized transverse speed $v_y(y,z)$ maps determined by DOCT, DSubAp DOCT, and DLS-LSOCT at the flow rate of 1.8 μL/min with a Doppler angle of 85.3°. (E)-(G) Depth resolved transverse speed $v_y(z)$ at different flow rates with a

Doppler angle of 87.9°, 85.3°, and 83.1°, respectively. The red and blue solid lines indicate the speeds determined by DOCT and DSubAp DOCT respectively and the opacity areas represent their 3-sigma uncertainties. The results of DLS-LSOCT are shown by the black dash line. (H)-(J) The depth by depth comparison of the speed determined by DLS-LSOCT and DOCT, corresponding to (E)-(I) respectively.

Although there are many arguments suggest that the decorrelation rate of DLS-OCT is only related to the beam waists and insensitive to the local beam sizes, it has been proven that the local beam sizes play an important role if axial velocity gradients exist [188]. We investigated the performance of the DLS-LSOCT using the same Doppler angle but at three different axial locations such that the local beam sizes are different. Figure 6.8 (A) shows the transverse speeds $v_y(z)$ at different flow rates with a Doppler angle of 86.1°. The axial position of the glass capillary was set ~ 50 μm away from the location where the top glass-intralipid interface's single in the center of y-direction reached the highest. In Figure 6.8 (B) and (C), the glass capillary's orientation was maintained the same, but is position was axially shifted up 100 and 200 μm respectively such that the local beams sizes are significantly different from those in Figure 6.8 (A), considering the Rayleigh range in the y-z plane is about 48 μm. Figure 6.8 (D)-(F) show the depth by depth comparison of the speed determined by DLS-LSOCT and DOCT, corresponding to Figure 6.8 (A)-(C) respectively. The mismatch between the DLS-LSOCT's results and the gold standard from depth 0 to 100 μm increases with an increase of the local beam. The fidelities of the DLS-LSOCT results at the three different axial positions are 0.927 ± 0.004, 0.901 ± 0.011, and 0.884 ± 0.010 respectively. The results in Figure 6.7 and Figure 6.8 qualitatively show that the accuracy of DLS-LSOCT is influenced by the axial velocity gradients as well as the local beam sizes. Nevertheless, its result is highly coincided with the DSubAp DOCT at the high SNR regions. This result is quite interesting because the theoretical distortions of the two methods are different. In DSubAp DOCT, the phase error, $\beta \nabla_y v_z$, comes from the lateral shifts induced by of the two subapertures [184], where β is the axial distance from the focal plane and ∇_y denotes the spatial gradient along the y-direction. In the DLS-LSOCT, the additional decay is a result of the integration of non-uniform motion over the optical volume confined by the local beam size and coherence gate [188]. The index of the additional decorrelation term is proportional to $(\omega_y^2 - {\omega_y}'^2)(\nabla_y v_z)^2$ [188], and other gradient induced terms should be canceled in $G_1(t)$. ω_y and ${\omega_y}'$ are the local beam sizes of the original and low-resolution OCT signals respectively. One reason why the two results coincide might they have been averaged over 12 sub-tomograms and each sub-tomogram's defocus are slightly different since the glass capillary is tilted.

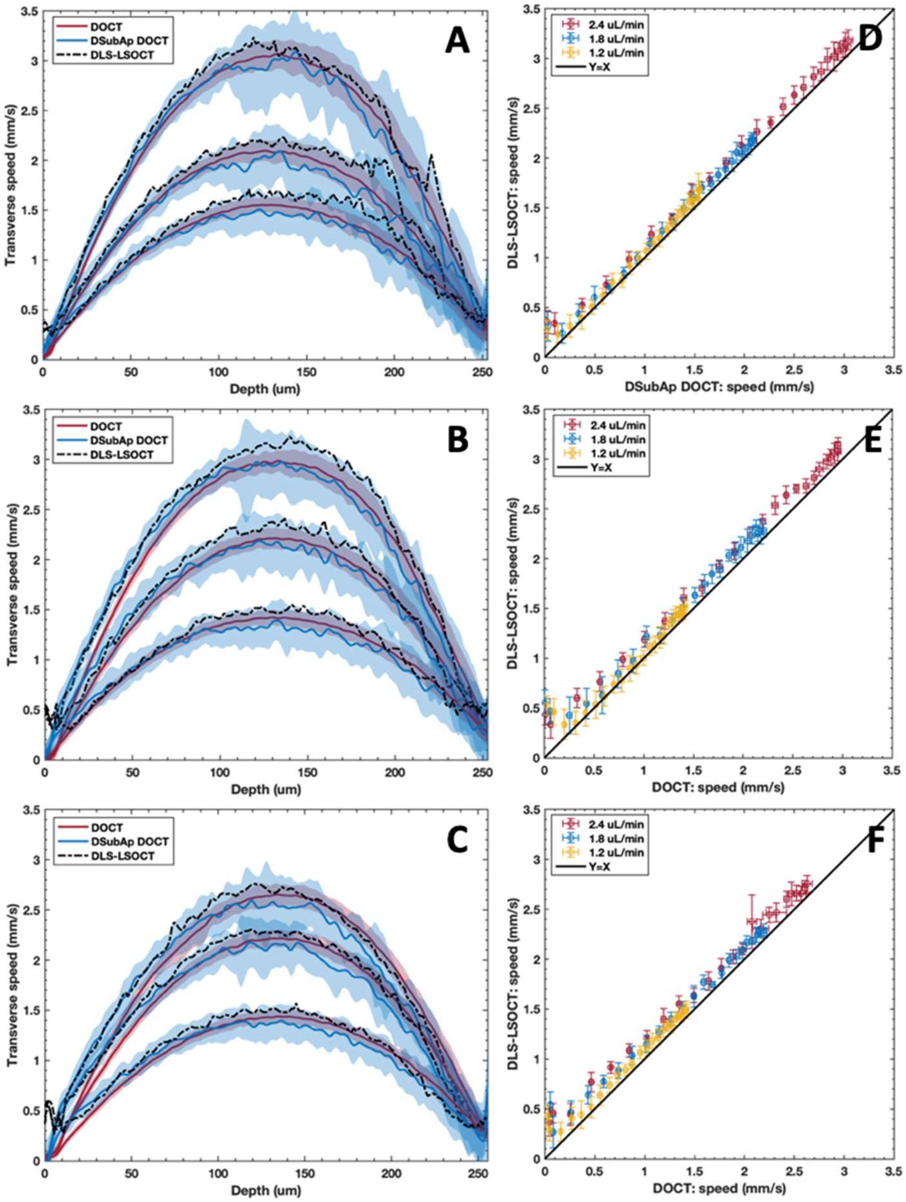

Figure 6.8 Comparison of the results of DOCT, DSubAp DOCT, and DLS-LSOCT at different depths. (A) Depth resolved transverse speed $v_y(z)$ at different flow rates with a Doppler angle of 86.1°. The red and blue solid lines indicate the speeds determined by DOCT and DSubAp DOCT respectively and the opacity areas represent their 3-sigma uncertainties. The results of DLS-LSOCT are shown by the black dash line. (B) and (C) Depth resolved transverse speed $v_y(z)$ measured with the same Doppler angle at two different out of focus depths. (D)-(F) The

depth by depth comparison of the speeds determined by DLS-LSOCT and DOCT, corresponding to (A)-(C) respectively.

In principle, both methods' distortions can be compensated by digitally correcting the defocus aberration across the B-scans. Without defocus, the lateral shifts are eliminated in DSubAp DOCT thus there is no artificial phase. For the DLS-LSOCT, since $\omega_y = \sigma_y$ and $\omega_y' = \sigma_y'$ are constant after defocus aberration correction, the additional decay term can be removed by introducing another low-resolution OCT tomogram whose resolution meets the condition $\sigma_y'' + \sigma_y = 2\sigma_y'$. However, since the phantom’s flow lacks structural contrasts, compensating the aberration using digitally adaptive optics is almost impossible. In addition, eliminating the extra decorrelation term requires a more precise autocorrelation function, which requires higher SNR and more B-scans. Thus, compensating the velocity gradient induced error is still changeling in OCT based flow velocimetry.

6.4.3 Detection of the spatial-resolved velocity in the beam illuminating plane

Figure 6.9 (A) shows a customized PDMS microfluid phantom. The black box indicates a T-shape bifurcated structure at which the 2D transverse velocity distributions are measured. Figure 6.9 (B) shows the magnified ROI in Figure 6.9 (A). The dash and solid lines in red and orange denote the four locations where the B-scans are recorded. The blue arrows indicated the direction of the flow. Figure 6.9 (C) shows the log-scaled B-scan amplitude images of the 4 selected locations. The microfluid phantom is orientated in perpendicular to the beam's propagating direction and the flow rate is set as 7.5 μL/min. The discontinuity of the intralipid-glass interface in Figure 6.9 (C3) and (C4) is the result of a mismatch of the refraction index of the intralipid solution and PDMS material. Figure 6.9 (D) shows the localized transverse velocity $v_y(y, z)$ determined by DLS-LSOCT. A binary mask is applied to block out the noise-only regions. The phase difference determined with DSubAp DOCT using two half subapertures are utilized to determine the direction of v_y. Due to the lower speed detection limit, the transverse speed lower than 0.3 mm/s is overestimated in DLS-LSOCT, which leads to an artificial discontinuity indicated by the black arrow in Figure 6.9 (D1). Figure 6.9 (E) shows the localized transverse velocity $v_y(y, z)$ determined by DSubAp DOCT.

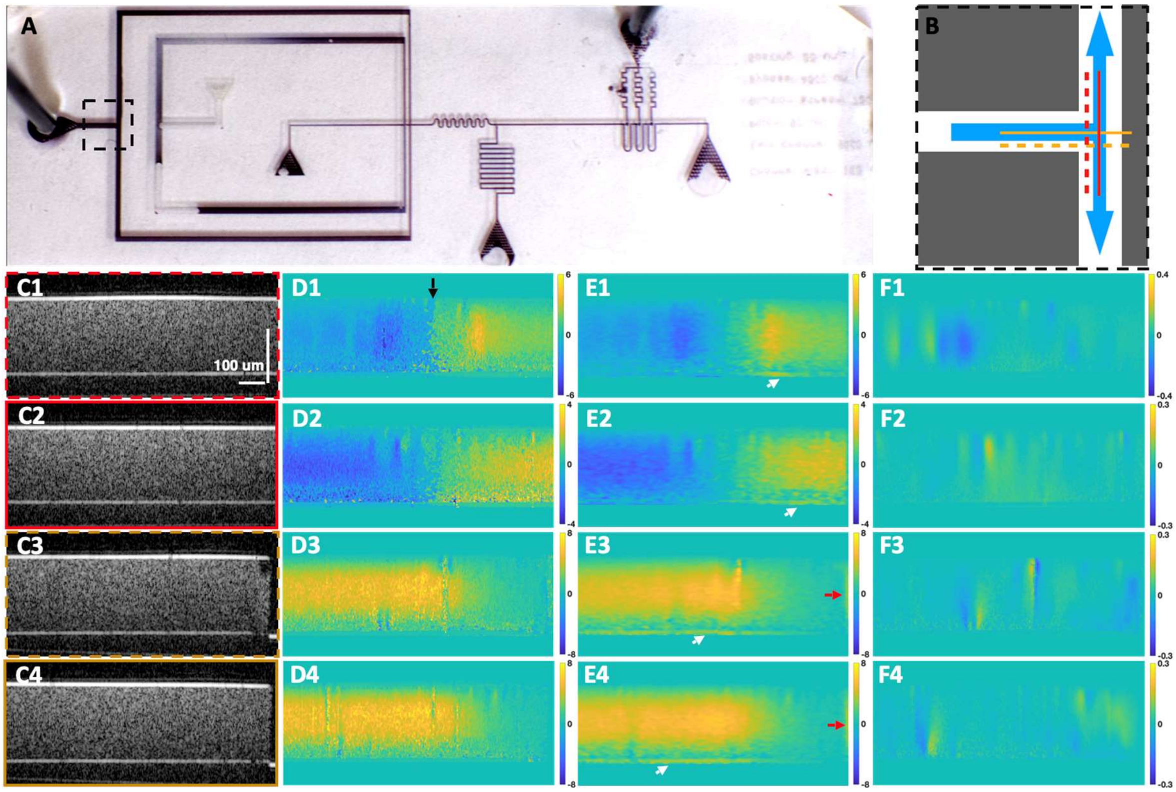

Figure 6.9 Localized velocity detection of a T-shape bifurcated structure in the beam illumination plane. The flow rate is 7.5 μL/min. (A) Image of the customized microfluid phantom. The phantom is filled with black ink for better visualization of the structure. The black box shows the selected ROI. (B) Magnification of the ROI in (A). The solid and dash lines indicate the location of B-scans. The blue arrows show the flow directions. (C) Typical log-scale B-scan images of the 4 locations labelled in (B). (D, E) Transverse flow speed $v_y(y, z)$ determined by DLS-LSOCT and DSubAp DOCT respectively. (F) Axial velocity $v_z(y, z)$ due to phantom surface defects or attached air bubbles.

Besides the low resolution, the results of DSubAp DOCT also show two fake signals indicated by the white and red arrow respectively. The fake signals marked by the white arrows come from the extra phase due to multi-scattering. Since this artifact depends on the possibility of multi-scattering as well as the speed of the scatters above the location of the signal, it is more pronounced as the light penetrates deeper scattering mediums with a higher flow speed. The fake signals at the same location in Figure 6.9 (D) are much smaller than those in Figure 6.9 (E). Thus, DLS-LSOCT seems more robust than DSubAp DOCT in terms of multi-scattering. The other fake signals marked by the red arrow come from the defocus-indued lateral shifts since the subapertures are away from the center. Figure 6.9 (F) shows the localized axial velocity $v_z(y, z)$ which might come from the phantom surface defects or attached air bubbles. The proposed DLS-LSOCT has successfully detected the localized transverse velocity distribution $v_y(y, z)$ of the T-shape bifurcated structure at different locations. Compared to the results of DSubAp-DOCT, DLS-LSOCT shows finer vortex structures and weaker fake signals at the exist of multi-scattering.

6.4.4 Estimating the transverse flow direction

Although it has been shown in Chapter 6.4.1 that the diffusion compensating method is not precise in the current system, it can still be used to determine the direction of the transverse flow at the ensemble level. Consider the situation where the flow velocity is confined in the xy-plane and the angle between the flow and beam illumination is θ, as shown in Figure 6.10 (A). The diffusion compensated autocorrelation and the ratio between the autocorrelation functions of the original and low-resolution OCT signals can be expressed as:

$$\begin{aligned} \tilde{g}_1(n\tau) &= \gamma exp[-(\frac{v_x^2}{\sigma_x^2}+\frac{v_y^2}{\sigma_y^2})n^2\tau^2] \\ &= \gamma exp(-Fn^2) \\ G_1(n\tau) &= exp[-(1/\sigma_y^2-1/\sigma'^2_y)v_y^2 n^2\tau^2] \\ &= exp(-F_y n^2) \end{aligned} \tag{6.58}$$

where $F=-\left(\frac{v_x^2}{\sigma_x^2}+\frac{v_y^2}{\sigma_y^2}\right)\tau^2$ and $F_y=-(1/\sigma_y^2-1/{\sigma_y}'^2)v_y^2\tau^2$ are the dimensionless decorrelation strengths which depend on the localized speeds, resolutions, and time resolution of the system. Together with $\vec{v}=v_0\cos\theta\hat{x}+v_0\sin\theta\hat{y}$ the ratio of F and F_y can be simplified as:

$$\frac{F}{F_y}=\frac{1/\sigma_x^2}{1/\sigma_y^2-1/\sigma'^2_y}\tan^2\theta+\frac{1/\sigma_y^2}{1/\sigma_y^2-1/\sigma'^2_y} \tag{6.59}$$

If the resolution parameters are constants, $\frac{F}{F_y}$ should be independent with its location. Figure 6.10 (B) shows a representative pixel-to-pixel scatter plot of the decorrelation strength maps $F(y, z)$ and $F_y(y, z)$ with θ = 30°. We determine the ratio $\frac{F}{F_y}$ by linear fitting the scatter plot ($|F|>|F_y|>0.005$). The flow is measured with a preset angle from 10° to 60° in 10° steps with the flow rate of 8 μL/min. The ratio $\frac{F}{F_y}$ vs. $\tan^2\theta$ is shown in Figure 6.10 (C). Since the resolution in the x-direction is unavailable, we estimated the two coefficients, $\frac{1/\sigma_x^2}{1/\sigma_y^2-1/{\sigma_y}'^2}$ and $\frac{1/\sigma_y^2}{1/\sigma_y^2-1/{\sigma_y}'^2}$, by linear fitting and then substitute back to estimate the flow direction, as shown in Figure 6.10 (D).

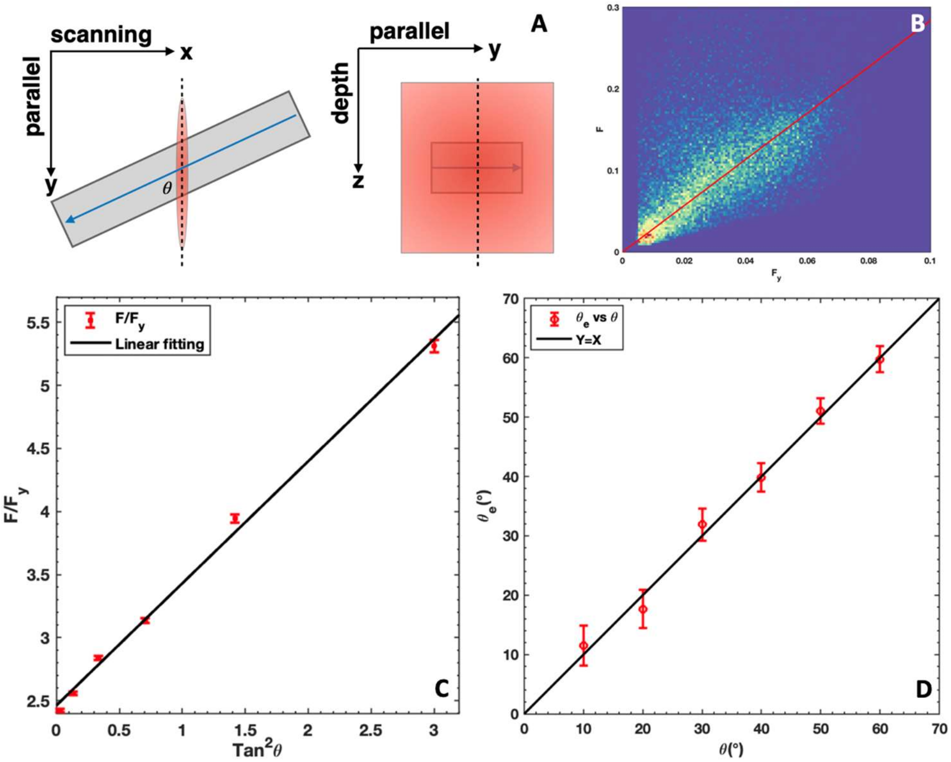

Figure 6.10 Transverse flow direction estimation. (A)Schematic of the illumination plane with respect to the flow direction. (B) Representative pixel-to-pixel scatter plot of common pixels of the decorrelation strength maps $F(y,z)$ and $F_y(y,z)$ with value $|F| > |F_y| > 0.005$. The solid red line shows the linear fitting of the selected data. (C) Fitted ratio F/F_y as a function of $\tan^2\theta$. (D) Estimated transverse flow direction vs. the preset angle.

6.5 Discussion

In this study, we introduce a novel decorrelation-based flow velocimetry method using LS SD-OCT. The effective A-scan acquisition rate of our LS SD-OCT system is 1.5 MHz, which is about 30 times faster than the OCT systems used for DLS-OCT reported in [64,176,188]. Although faster Fourier domain mode locking (FDML) light sources for SS-OCT allows a A-scan rate of several MHz [189–191], the unstable phase and intensity of the sweeping pulse will lead to additional decorrelation. We take advantage of the phase stability within the same B-scan of the LS SD-OCT and digitally generate a low-resolution tomogram. The normalized temporal autocorrelation functions $\tilde{g}_1(t)$ and $\tilde{g}_1{}'(t)$ are calculated by normalization of the inverse Fourier transforming the power spectral density of the axial phase error corrected OCT signals $f_{corr}(y,z,t)$ and $f_{corr}{}'(y,z,t)$ instead of following the autocorrelation definition which is time-consuming. The ratio $G_1(t) = \frac{\tilde{g}_1(t)}{\tilde{g}_1{}'(t)}$, in principle, does not depend on the diffusional motion, translational motions perpendicular to the y-direction, and the noise-induced distortion of the autocorrelation relating to the local SNR.

We calculate the quasi-localized resolution parameters $\sigma_y(l, z)$ and $\sigma_y{}'(l, z)$ based on the spatial autocorrelation for each dataset separately following the method described in [182]. Since calculating the spatial autocorrelation needs a set of data from different lateral positions, the resolution parameters cannot be spatially resolved along the y-direction. Instead, they are assumed to be constants along the y-direction within each sub-tomogram. Compared with other fitting methods using DLS-OCT, DLS-LSOCT shows extraordinary precision in determining the transverse flow speed in the case where no axial velocity gradient exists. To our best knowledge, this is the first time that the DLS-OCT shows precise velocity distributions based on the temporal autocorrelation of B-scans instead of flow dynamic parameters which are composed of diffusional and translational motions [169,179]. Although some fast point-scan SD-OCT [17,119] can reach to similar B-scan rate of LS SD-OCT with a small A-scan number, the extra decorrelation due to the fast mechanical scanning results in fewer data points above the noise level and must be accounted for [182]. In the case where axial velocity gradient exists, both DLS-LSOCT and DSubAp DOCT methods' results are distorted compared with DOCT. Our results support the theoretical prediction that the local beam sizes, together with the axial velocity gradient, affect the precision of the estimated speed [188].

We show that DLS-LSOCT has several advantages over DSubAp DOCT. Firstly, DLS-LSOCT's lateral resolution is better and can show finer transverse velocity distributions. The DSubAp DOCT's lateral resolution is mainly limited by its subapertures' size. Since finding the effective angle separation of two large subapertures is difficult, we limit the size of two subapertures to 1/10 of the full aperture. Secondly, DLS-LSOCT is more robust to the multi-scattering which occurs more often at deeper location of the samples. The phase-based OCT methods pick additional phase when the photons are multi-scattered by the scatters with translational motions. Thus, artificial velocity signals appear when the optical beam is penetrating deeper scattering mediums. Although the influence of multi-scattering on DLS-OCT have not been theoretically interpreted, our experiment results show the fake velocity signals of DLS-LSOCT are weak compared to those of DSubAp-DOCT at the intralipid-glass interfaces, as long as the SNR of the OCT signal is not too low. Thirdly, the DSubAp DOCT's upper transverse speed detection limit is highly sensitive to the axial velocity since the phase differences between two adjacent B-scans of the two sub-tomograms are composed of both the lateral and axial motions. In the case where axial velocity is close to its upper detection limit (0.44 mm/s in this study), its lateral velocity detection range is greatly reduced. However, DLS-LSOCT's transverse velocity detection range is not affected by a small axial velocity component as long as the axial and lateral resolutions are at the same level. Although the DLS-LSOCT method is proposed to measure transverse velocity, a similar method can be applied to measure the axial velocity and its upper detection limit should be much larger than 0.44 mm/s.

There are still several limitations of our proposed method. First of all, the time required for estimating a precise temporal autocorrelation is much longer than the time needed for phase extraction in phase-based methods and motion contrast extraction OCTA. Based on our analysis, 600 repeated B-scans are needed in order to achieve a credible speed estimation. This limitation comes from the nature of DLS methods since the theoretical autocorrelation is an average of all possible initial positions of the scatters. The total acquisition time for each B-scan location is about 0.2 seconds, which is only able to measure the stable or slowly varying flow speed distribution. By averaging within a 5×5 spatial kennels, the time required for a B-scan location can be reduced to 8 milliseconds, which is comparable with the time required for the M-mode in point-scan DLS-OCT [64,192]. However, the spatial resolutions will be dramatically reduced and cannot be used to measure the flow speed inside small structures.

Secondly, the axial velocity gradient over the line-illuminating direction introduces an additional decorrelation term, leading to a significant distortion of the estimated speed. The integration of the non-uniform translational motions inside the optical beam volume, confined by the local beam size and coherence gate, leads to that the defocus phase cannot completely cancel in the autocorrelation. Nevertheless, the gradient-induced distortion in DLS-LSOCT should be, in principle, smaller than that of the point-scan version. This is because the ratio $G_1(t)$ is only sensitive to the velocity and gradient components in the y-direction. One possible method to eliminate the distortion in a single measurement is to correct the aberrations by digital adaptive optics [43,44,135,136,193], and introduce another low-resolution sub-tomogram digitally. With properly chosen resolutions, $\sigma_y{}'$ and $\sigma_y{}''$, the quadratic gradient contribution can be canceled in the ratio of G_1 and only the velocity contribution remains.

The third limitation is that the system lacks the ability to determine the velocity in the x-direction precisely. Although we can determine the velocity component in y- and z-direction with excellent precision, calculating v_x based on the decorrelation requires an accurate estimation of the overall quadratic velocity contribution, which is quite changeling with current setup. The temporal autocorrelation is significantly distorted by the noise as the beam penetrates the deep flow medium.

The number of autocorrelation data above noise level is limited as the time resolution is low. Therefore, the overall quadratic velocity contribution, linear diffusion contribution, and the noise distortion cannot be determined simultaneously. Increasing the optical beam power and reducing the objective NA might be able to enhance the performance of DLS-OCT DC, which in turn improves the accuracy of v_x. Another method is to deploy optical delay difference in x-direction [165], such that we can measure v_x using SubAp DOCT at the cost of reduced depth scanning range.

Finally, although we have shown that DLS-LSOCT can precisely measure the transverse speed of intralipid flow in y-direction without velocity gradient, it does not necessarily imply similar accuracy can be achieved in *in-vivo* measurement of the blood flow. Besides the fact that DLS-LSOCT can only measure slow varying flows, the departure of the theoretical assumptions and motion-induced extra decorrelation also affect the accuracy. The DLS-OCT theory only considers the point scattering regime under first Born approximation. Given that the size of red blood cells (RBCs) is in the same order as the system's resolutions and its biconcave disk shape, the point scattering assumption is not valid. Also, it has been shown that multi-scattering increases the decorrelation rate [194], although the theoretical model is still unavailable. Next, the simplified model only considered rigid diffusion motion of point-like particles, whereas RBC's diffusion decorrelation is more complex due to orientation changes and membrane fluctuations [195,196]. In addition, the inevitable motions during *in-vivo* imaging create additional decorrelation. Although post-registration can be applied, the signal intensity change due to fringe washout cannot be compensated. Further experiments are needed to compare the results of DLS-LSOCT and some ground truth in *in-vivo* blood flow measurement.

6.6 Conclusion

We demonstrate a novel decorrelation-based localized transverse flow measurement using a LS SD-OCT system. We take advantage of the phase stability within each B-scan and digitally generate a low-resolution tomogram. The ratio of the temporal autocorrelations of the original and low-resolution OCT signals only depends on the system resolution and the flow velocity along the line-illuminating direction and is free from the diffusion motion of the flow particles, translation motion orthogonal to the line-illumination direction, and noise-induced distortion. We validated the proposed method by comparing with the phase-based OCT methods in phantom-based experiments. With the advantage that the ratio is only sensitive to the beam sizes in the line-illuminating direction, we anticipate the proposed method brings new opportunities to accounting for the velocity gradient and multi-scattering induced distortion in DLS-OCT such that accurate quantitative measurements of blood flow is possible.

Chapter 7

Conclusion and Future work

7.1 Conclusion

The results presented in this work show the excellent potential of the broadband LS SD-OCT technology for clinical imaging and biomedical research. By combining a broadband femtolaser (central wavelength of 785 nm and FWMH bandwidth of 129 nm) with an ultrafast area camera, the proposed LS SD-OCT system offers nearly isotropic, a high spatial resolution of ~2.3 μm in free space and a B-scan acquisition rate of up to 3 kHz. The combination of high spatial resolution and rapid image acquisition rate opens the door for various clinical and biomedical imaging applications of the LS SD-OCT technology, specifically where non-invasive, contactless, and volumetric imaging of the cellular structure of biological tissue needs to be visualized and characterized. The rapid image acquisition rate provided by the parallel imaging modality effectively suppresses the motion effects during *in-vivo* imaging, which allows for digital restoration of the diffraction-limited lateral resolution over a large imaging depth. The 3D cellular resolution imaging capability of the LS SD-OCT technology is demonstrated by imaging the healthy human cornea and limbus. The wing cells in the cornea epithelium, sub-basal nerves underneath the basal cells, keratocytes in the stroma, and the endothelium cells are all resolved. *In-vivo* volumetric images of the healthy limbal epithelium cells and the structure of POVs have been *in-vivo* for the first time using OCT. While this thesis includes only LS-SD-OCT images of the healthy human cornea and limbus, the same technology can be easily adapted with minor modifications for other clinical and biomedical imaging applications.

This thesis discusses for the first time the three primary phenomena affecting the spatial resolution in LS SD-OCT images other than monochromatic aberrations: interference-induced phase destruction, spatial-spectral crosstalk, and chromatic aberrations. While the phase loss cannot be recovered, it can be avoided by minimizing the focal plane mismatches. The spatial-spectral crosstalk and chromatic aberrations can be suppressed by independently correcting the monochromatic aberrations in sub-band tomograms and registering spatially and spectrally afterward. The proposed reconstruction method is validated in different phantom and biology tissue studies *ex-vivo*. In addition, we extend the DAO methods with respect to the choice of image quality metric and optimization algorithm. We show that the true Shannon entropy is better associated with the image quality of reflecting signals, and swarm-intelligence optimization methods can find the global optimum of the image metric more robustly than commonly used gradient-based methods.

Finally, the work presented on the novel transverse flow velocimetry, designed specifically for LS SD-OCT, is an extension of the current flow measurement techniques. We take advantage of the phase stability within each B-scan and digitally generate a low-resolution tomogram. The ratio of the temporal autocorrelations of the original and low-resolution OCT signals only depends on the system resolution and the flow velocity along the line-illuminating direction. It is free from the perpendicular translation motion, the diffusion, and the noise-induced distortion of the autocorrelation function. Our phantom experiment results show that the proposed method can precisely determine the transverse flow over the line-illuminating direction if there is no axial velocity gradient. Compared with phase-resolved OCT velocimetry, the proposed method is more robust to multi-scattering.

7.2 Future work

In Chapter 3, it was shown that the digital resolution along the y-direction $\tilde{\delta y}$ and the spectral resolution δk are both not high enough according to the Nyquist–Shannon sampling theorem. In the current setup, $\tilde{\delta y}$ and δk cannot be increased simultaneously because of the contradiction of the sample to camera magnification in the y-direction and beam size entering the spectrometer in the x-direction. This paradox can be avoided by replacing the doublets before the transmission grating with a pair of perpendicularly oriented cylindrical achromatic lenses [123]. Replacing the transmission grating, camera lens, and camera may also help in resolving the problem. Next, due to the Gaussian intensity distribution of the illuminating line, the edge's SNR is lower than the center in the current design. In the case that the power of the light source is limited, the Gaussian line can be shaped into a uniform line by a Powell lens to get a constant SNR across the lateral FOV [121,122]. Another problem that has not been addressed in this thesis is the multiple scattering induced spatial crosstalk within a B-scan. Spatially incoherent light generated with a multimode fiber and sparse sampling using a digital micromirror device might be two promising solutions [55,124,125].

In terms of digitally recovering the diffraction-limited lateral resolutions, more effects should be considered for improving the efficiency of the swarm-intelligence algorithms. Instead of uniformly randomizing the initial starts, the results of non-iterative DAO algorithms can serve as better initial guesses. Balancing the global exploration and local search and parallel computing can also improve the converging rate. Next, a better method of eliminating abnormal aberration coefficients is in demand.

Currently, the abnormal results are rejected with a simple smoothing algorithm. In practice, many abnormal results are due to the lack of scattering contrast or signal artifacts, thus an image content based eliminating method should be considered. Moreover, according to the unified-k theory [161], the 3D CTF of an LS OCT system is not separable. Therefore, the digital dispersion compensation is, in principle, not independent of the digital lateral resolution correction, and a unified 3D resolution correction method should be developed.

Last but not least, the DLS-OCT theory should be extended. Currently, the DLS-OCT only exploits the temporal autocorrelation decay above a threshold, and the decay's oscillating tail is considered 'overwhelmed' by the noise. Finding the relationship of these 'decorrelated' oscillations with the localized velocities is important to extend the LS SD-OCT's speed detection range.

Letters of Copyright Permissions

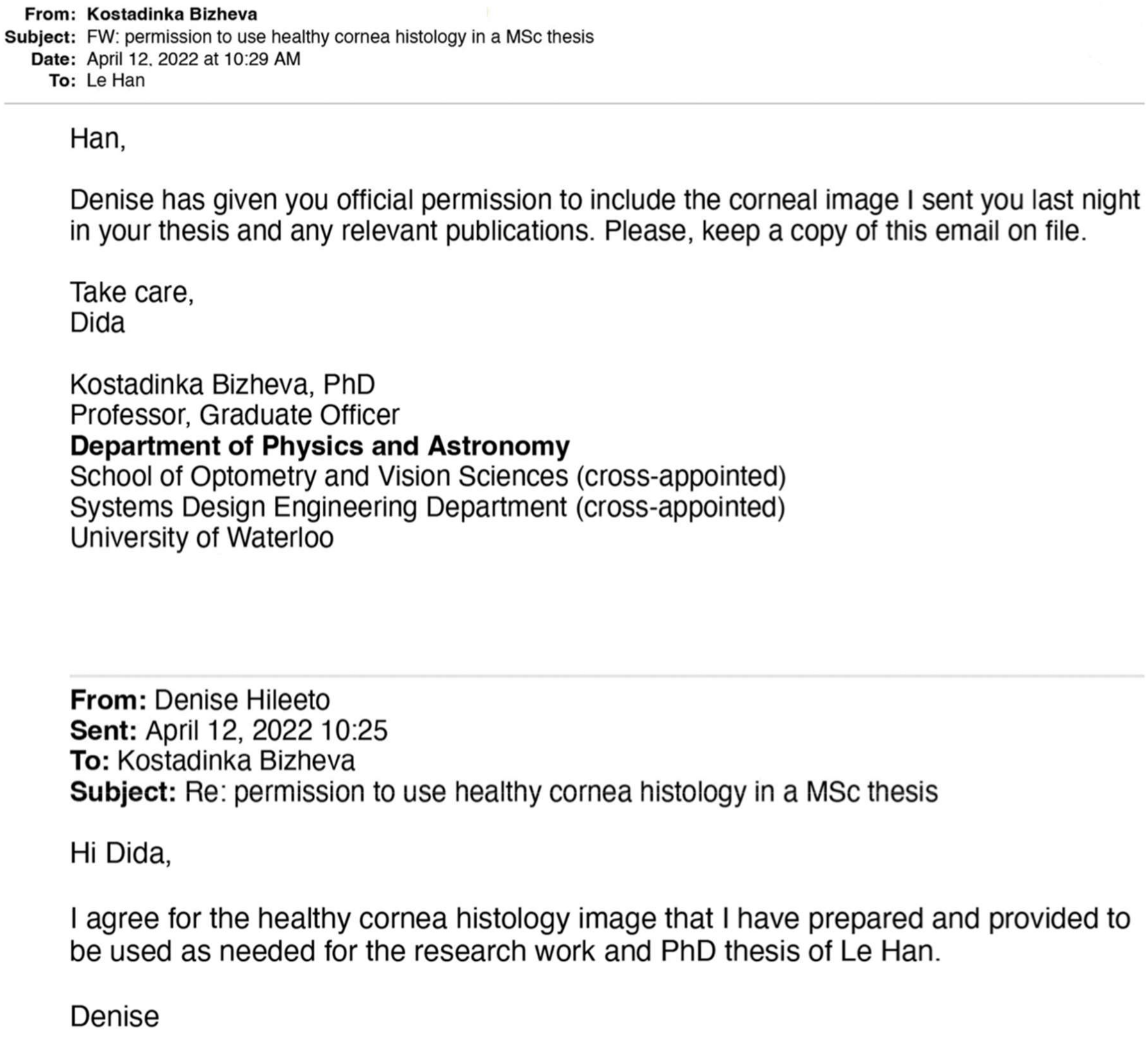

From: **Kostadinka Bizheva**
Subject: FW: permission to use healthy cornea histology in a MSc thesis
Date: April 12, 2022 at 10:29 AM
To: Le Han

Han,

Denise has given you official permission to include the corneal image I sent you last night in your thesis and any relevant publications. Please, keep a copy of this email on file.

Take care,
Dida

Kostadinka Bizheva, PhD
Professor, Graduate Officer
Department of Physics and Astronomy
School of Optometry and Vision Sciences (cross-appointed)
Systems Design Engineering Department (cross-appointed)
University of Waterloo

From: Denise Hileeto
Sent: April 12, 2022 10:25
To: Kostadinka Bizheva
Subject: Re: permission to use healthy cornea histology in a MSc thesis

Hi Dida,

I agree for the healthy cornea histology image that I have prepared and provided to be used as needed for the research work and PhD thesis of Le Han.

Denise

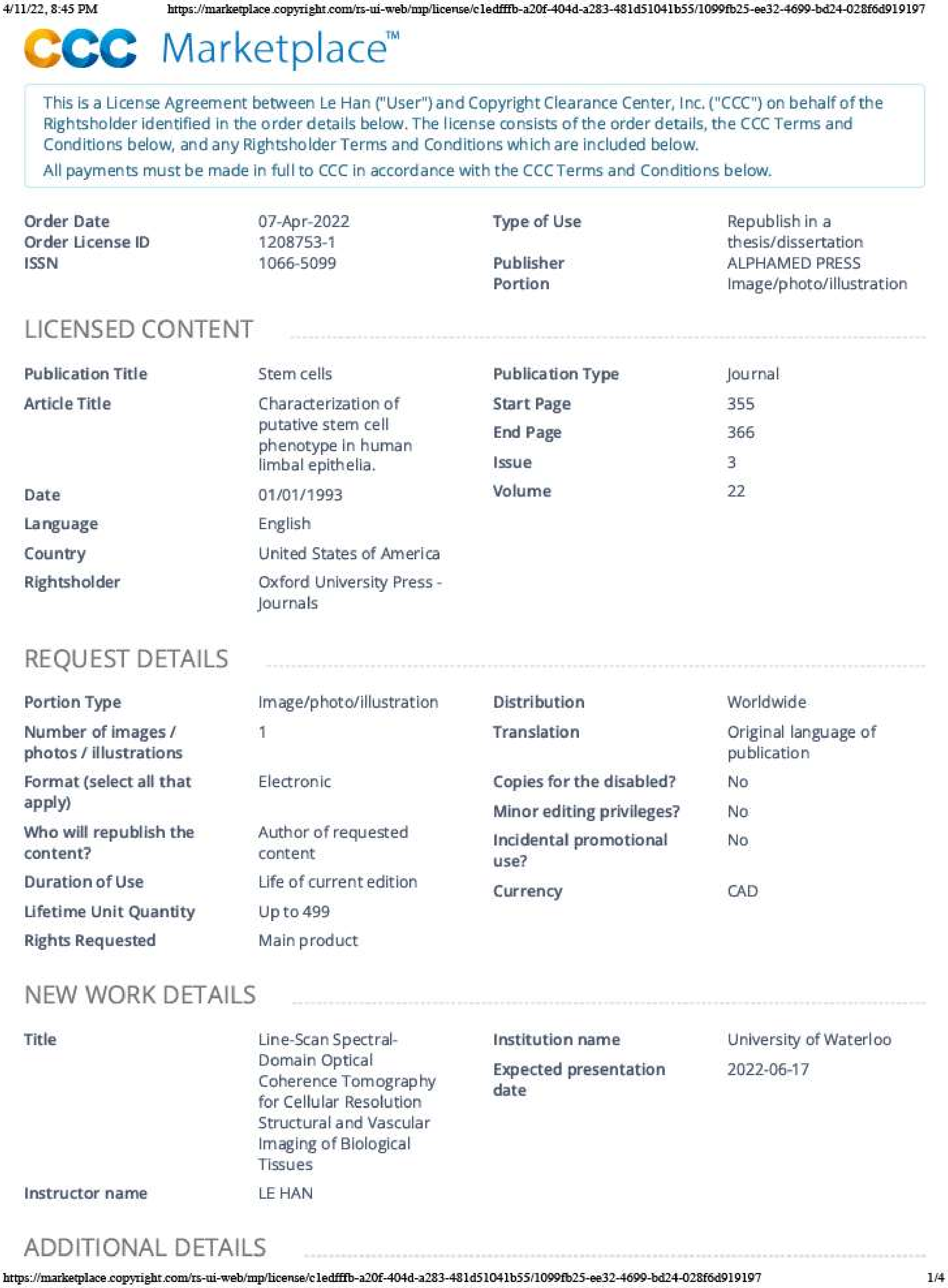

CCC Marketplace™

This is a License Agreement between Le Han ("User") and Copyright Clearance Center, Inc. ("CCC") on behalf of the Rightsholder identified in the order details below. The license consists of the order details, the CCC Terms and Conditions below, and any Rightsholder Terms and Conditions which are included below.

All payments must be made in full to CCC in accordance with the CCC Terms and Conditions below.

Order Date	07-Apr-2022	**Type of Use**	Republish in a thesis/dissertation
Order License ID	1208753-1	**Publisher**	ALPHAMED PRESS
ISSN	1066-5099	**Portion**	Image/photo/illustration

LICENSED CONTENT

Publication Title	Stem cells	**Publication Type**	Journal
Article Title	Characterization of putative stem cell phenotype in human limbal epithelia.	**Start Page**	355
		End Page	366
		Issue	3
Date	01/01/1993	**Volume**	22
Language	English		
Country	United States of America		
Rightsholder	Oxford University Press - Journals		

REQUEST DETAILS

Portion Type	Image/photo/illustration	**Distribution**	Worldwide
Number of images / photos / illustrations	1	**Translation**	Original language of publication
Format (select all that apply)	Electronic	**Copies for the disabled?**	No
		Minor editing privileges?	No
Who will republish the content?	Author of requested content	**Incidental promotional use?**	No
Duration of Use	Life of current edition	**Currency**	CAD
Lifetime Unit Quantity	Up to 499		
Rights Requested	Main product		

NEW WORK DETAILS

Title	Line-Scan Spectral-Domain Optical Coherence Tomography for Cellular Resolution Structural and Vascular Imaging of Biological Tissues	**Institution name**	University of Waterloo
		Expected presentation date	2022-06-17
Instructor name	LE HAN		

ADDITIONAL DETAILS

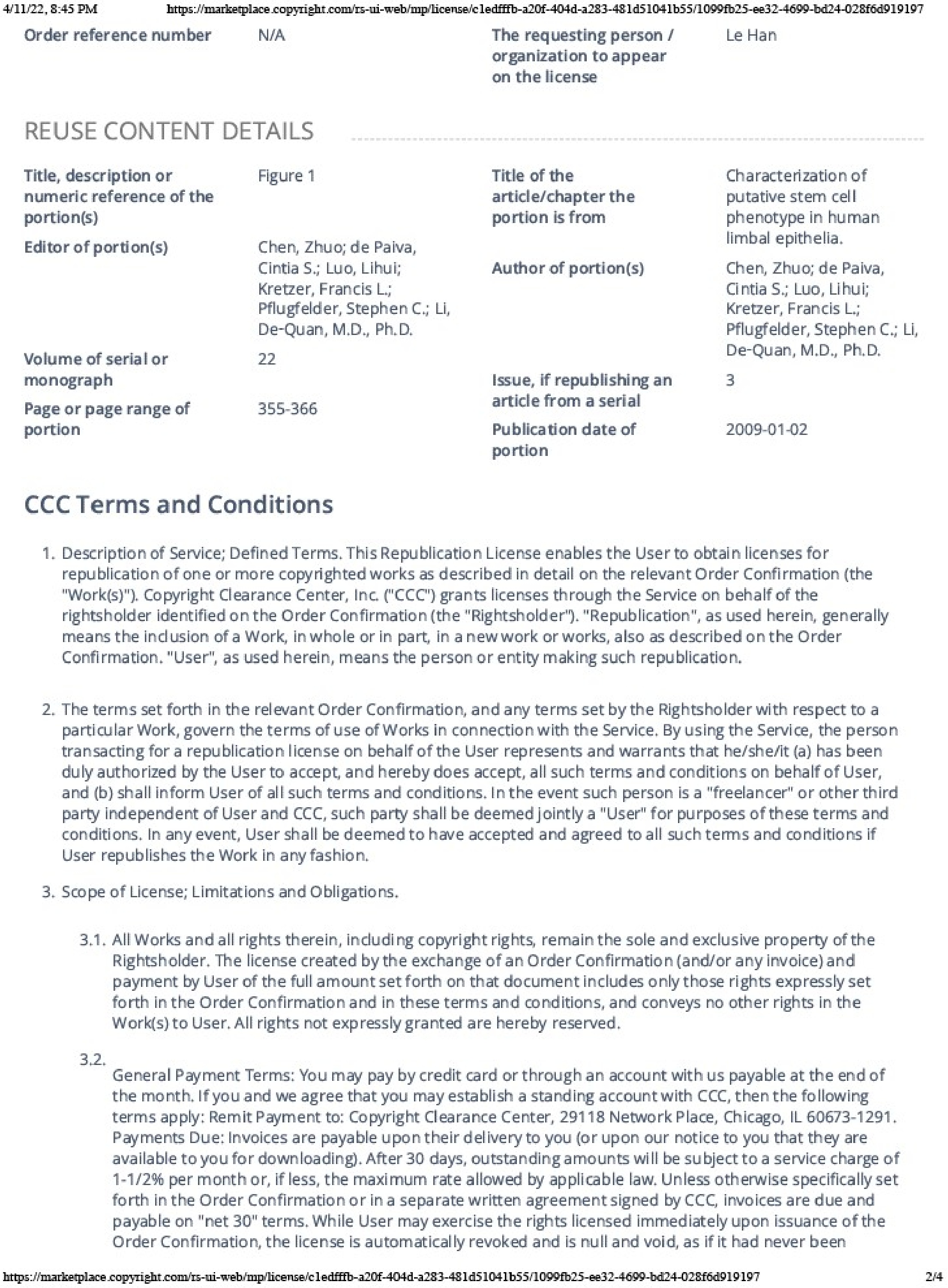

Order reference number	N/A	**The requesting person / organization to appear on the license**	Le Han

REUSE CONTENT DETAILS

Title, description or numeric reference of the portion(s)	Figure 1	**Title of the article/chapter the portion is from**	Characterization of putative stem cell phenotype in human limbal epithelia.
Editor of portion(s)	Chen, Zhuo; de Paiva, Cintia S.; Luo, Lihui; Kretzer, Francis L.; Pflugfelder, Stephen C.; Li, De-Quan, M.D., Ph.D.	**Author of portion(s)**	Chen, Zhuo; de Paiva, Cintia S.; Luo, Lihui; Kretzer, Francis L.; Pflugfelder, Stephen C.; Li, De-Quan, M.D., Ph.D.
Volume of serial or monograph	22	**Issue, if republishing an article from a serial**	3
Page or page range of portion	355-366	**Publication date of portion**	2009-01-02

CCC Terms and Conditions

1. Description of Service; Defined Terms. This Republication License enables the User to obtain licenses for republication of one or more copyrighted works as described in detail on the relevant Order Confirmation (the "Work(s)"). Copyright Clearance Center, Inc. ("CCC") grants licenses through the Service on behalf of the rightsholder identified on the Order Confirmation (the "Rightsholder"). "Republication", as used herein, generally means the inclusion of a Work, in whole or in part, in a new work or works, also as described on the Order Confirmation. "User", as used herein, means the person or entity making such republication.

2. The terms set forth in the relevant Order Confirmation, and any terms set by the Rightsholder with respect to a particular Work, govern the terms of use of Works in connection with the Service. By using the Service, the person transacting for a republication license on behalf of the User represents and warrants that he/she/it (a) has been duly authorized by the User to accept, and hereby does accept, all such terms and conditions on behalf of User, and (b) shall inform User of all such terms and conditions. In the event such person is a "freelancer" or other third party independent of User and CCC, such party shall be deemed jointly a "User" for purposes of these terms and conditions. In any event, User shall be deemed to have accepted and agreed to all such terms and conditions if User republishes the Work in any fashion.

3. Scope of License; Limitations and Obligations.

    3.1. All Works and all rights therein, including copyright rights, remain the sole and exclusive property of the Rightsholder. The license created by the exchange of an Order Confirmation (and/or any invoice) and payment by User of the full amount set forth on that document includes only those rights expressly set forth in the Order Confirmation and in these terms and conditions, and conveys no other rights in the Work(s) to User. All rights not expressly granted are hereby reserved.

    3.2. General Payment Terms: You may pay by credit card or through an account with us payable at the end of the month. If you and we agree that you may establish a standing account with CCC, then the following terms apply: Remit Payment to: Copyright Clearance Center, 29118 Network Place, Chicago, IL 60673-1291. Payments Due: Invoices are payable upon their delivery to you (or upon our notice to you that they are available to you for downloading). After 30 days, outstanding amounts will be subject to a service charge of 1-1/2% per month or, if less, the maximum rate allowed by applicable law. Unless otherwise specifically set forth in the Order Confirmation or in a separate written agreement signed by CCC, invoices are due and payable on "net 30" terms. While User may exercise the rights licensed immediately upon issuance of the Order Confirmation, the license is automatically revoked and is null and void, as if it had never been

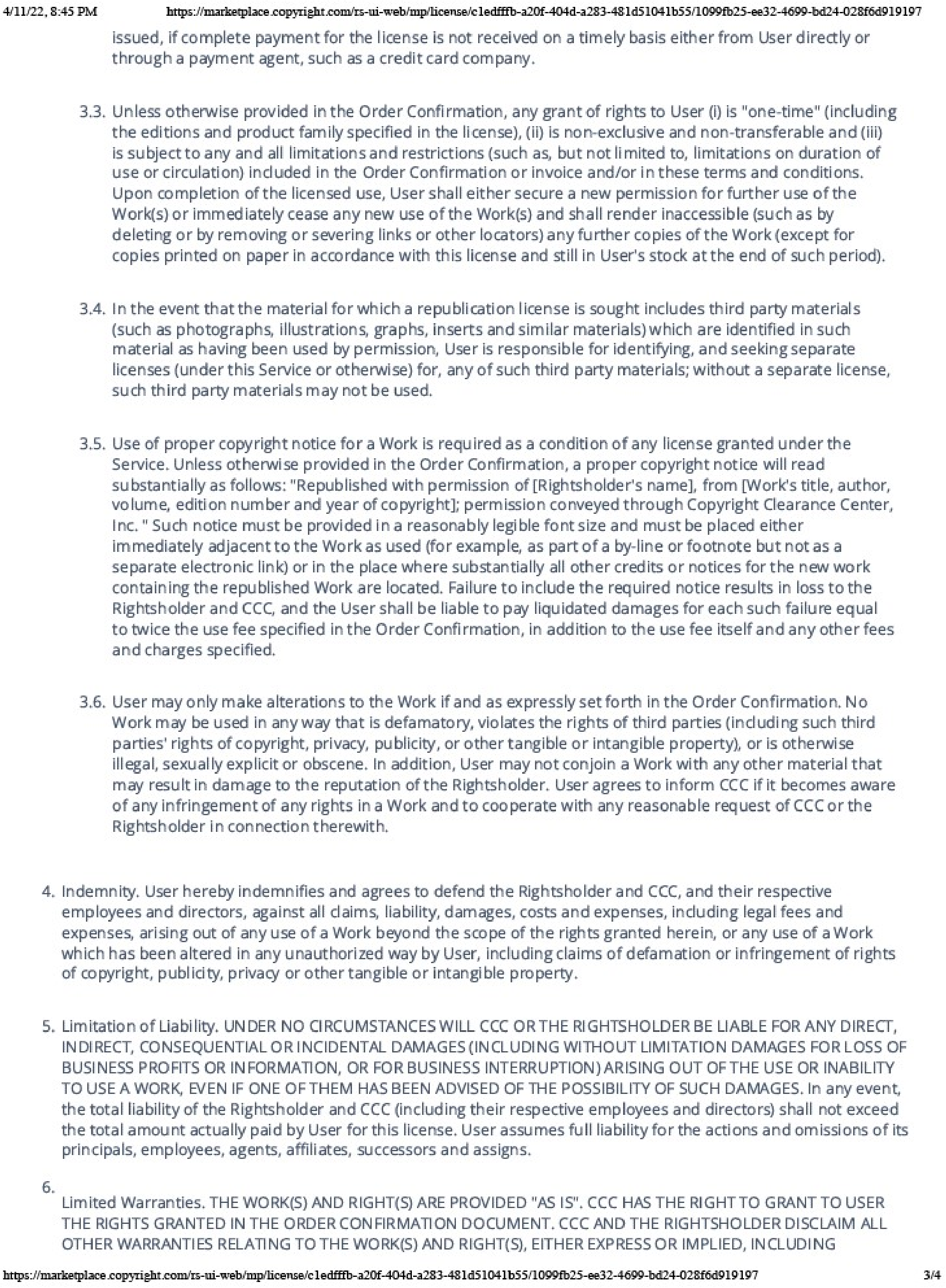

issued, if complete payment for the license is not received on a timely basis either from User directly or through a payment agent, such as a credit card company.

3.3. Unless otherwise provided in the Order Confirmation, any grant of rights to User (i) is "one-time" (including the editions and product family specified in the license), (ii) is non-exclusive and non-transferable and (iii) is subject to any and all limitations and restrictions (such as, but not limited to, limitations on duration of use or circulation) included in the Order Confirmation or invoice and/or in these terms and conditions. Upon completion of the licensed use, User shall either secure a new permission for further use of the Work(s) or immediately cease any new use of the Work(s) and shall render inaccessible (such as by deleting or by removing or severing links or other locators) any further copies of the Work (except for copies printed on paper in accordance with this license and still in User's stock at the end of such period).

3.4. In the event that the material for which a republication license is sought includes third party materials (such as photographs, illustrations, graphs, inserts and similar materials) which are identified in such material as having been used by permission, User is responsible for identifying, and seeking separate licenses (under this Service or otherwise) for, any of such third party materials; without a separate license, such third party materials may not be used.

3.5. Use of proper copyright notice for a Work is required as a condition of any license granted under the Service. Unless otherwise provided in the Order Confirmation, a proper copyright notice will read substantially as follows: "Republished with permission of [Rightsholder's name], from [Work's title, author, volume, edition number and year of copyright]; permission conveyed through Copyright Clearance Center, Inc. " Such notice must be provided in a reasonably legible font size and must be placed either immediately adjacent to the Work as used (for example, as part of a by-line or footnote but not as a separate electronic link) or in the place where substantially all other credits or notices for the new work containing the republished Work are located. Failure to include the required notice results in loss to the Rightsholder and CCC, and the User shall be liable to pay liquidated damages for each such failure equal to twice the use fee specified in the Order Confirmation, in addition to the use fee itself and any other fees and charges specified.

3.6. User may only make alterations to the Work if and as expressly set forth in the Order Confirmation. No Work may be used in any way that is defamatory, violates the rights of third parties (including such third parties' rights of copyright, privacy, publicity, or other tangible or intangible property), or is otherwise illegal, sexually explicit or obscene. In addition, User may not conjoin a Work with any other material that may result in damage to the reputation of the Rightsholder. User agrees to inform CCC if it becomes aware of any infringement of any rights in a Work and to cooperate with any reasonable request of CCC or the Rightsholder in connection therewith.

4. Indemnity. User hereby indemnifies and agrees to defend the Rightsholder and CCC, and their respective employees and directors, against all claims, liability, damages, costs and expenses, including legal fees and expenses, arising out of any use of a Work beyond the scope of the rights granted herein, or any use of a Work which has been altered in any unauthorized way by User, including claims of defamation or infringement of rights of copyright, publicity, privacy or other tangible or intangible property.

5. Limitation of Liability. UNDER NO CIRCUMSTANCES WILL CCC OR THE RIGHTSHOLDER BE LIABLE FOR ANY DIRECT, INDIRECT, CONSEQUENTIAL OR INCIDENTAL DAMAGES (INCLUDING WITHOUT LIMITATION DAMAGES FOR LOSS OF BUSINESS PROFITS OR INFORMATION, OR FOR BUSINESS INTERRUPTION) ARISING OUT OF THE USE OR INABILITY TO USE A WORK, EVEN IF ONE OF THEM HAS BEEN ADVISED OF THE POSSIBILITY OF SUCH DAMAGES. In any event, the total liability of the Rightsholder and CCC (including their respective employees and directors) shall not exceed the total amount actually paid by User for this license. User assumes full liability for the actions and omissions of its principals, employees, agents, affiliates, successors and assigns.

6. Limited Warranties. THE WORK(S) AND RIGHT(S) ARE PROVIDED "AS IS". CCC HAS THE RIGHT TO GRANT TO USER THE RIGHTS GRANTED IN THE ORDER CONFIRMATION DOCUMENT. CCC AND THE RIGHTSHOLDER DISCLAIM ALL OTHER WARRANTIES RELATING TO THE WORK(S) AND RIGHT(S), EITHER EXPRESS OR IMPLIED, INCLUDING

WITHOUT LIMITATION IMPLIED WARRANTIES OF MERCHANTABILITY OR FITNESS FOR A PARTICULAR PURPOSE. ADDITIONAL RIGHTS MAY BE REQUIRED TO USE ILLUSTRATIONS, GRAPHS, PHOTOGRAPHS, ABSTRACTS, INSERTS OR OTHER PORTIONS OF THE WORK (AS OPPOSED TO THE ENTIRE WORK) IN A MANNER CONTEMPLATED BY USER; USER UNDERSTANDS AND AGREES THAT NEITHER CCC NOR THE RIGHTSHOLDER MAY HAVE SUCH ADDITIONAL RIGHTS TO GRANT.

7. Effect of Breach. Any failure by User to pay any amount when due, or any use by User of a Work beyond the scope of the license set forth in the Order Confirmation and/or these terms and conditions, shall be a material breach of the license created by the Order Confirmation and these terms and conditions. Any breach not cured within 30 days of written notice thereof shall result in immediate termination of such license without further notice. Any unauthorized (but licensable) use of a Work that is terminated immediately upon notice thereof may be liquidated by payment of the Rightsholder's ordinary license price therefor; any unauthorized (and unlicensable) use that is not terminated immediately for any reason (including, for example, because materials containing the Work cannot reasonably be recalled) will be subject to all remedies available at law or in equity, but in no event to a payment of less than three times the Rightsholder's ordinary license price for the most closely analogous licensable use plus Rightsholder's and/or CCC's costs and expenses incurred in collecting such payment.
8. Miscellaneous.
    - 8.1. User acknowledges that CCC may, from time to time, make changes or additions to the Service or to these terms and conditions, and CCC reserves the right to send notice to the User by electronic mail or otherwise for the purposes of notifying User of such changes or additions; provided that any such changes or additions shall not apply to permissions already secured and paid for.
    - 8.2. Use of User-related information collected through the Service is governed by CCC's privacy policy, available online here:https://marketplace.copyright.com/rs-ui-web/mp/privacy-policy
    - 8.3. The licensing transaction described in the Order Confirmation is personal to User. Therefore, User may not assign or transfer to any other person (whether a natural person or an organization of any kind) the license created by the Order Confirmation and these terms and conditions or any rights granted hereunder; provided, however, that User may assign such license in its entirety on written notice to CCC in the event of a transfer of all or substantially all of User's rights in the new material which includes the Work(s) licensed under this Service.
    - 8.4. No amendment or waiver of any terms is binding unless set forth in writing and signed by the parties. The Rightsholder and CCC hereby object to any terms contained in any writing prepared by the User or its principals, employees, agents or affiliates and purporting to govern or otherwise relate to the licensing transaction described in the Order Confirmation, which terms are in any way inconsistent with any terms set forth in the Order Confirmation and/or in these terms and conditions or CCC's standard operating procedures, whether such writing is prepared prior to, simultaneously with or subsequent to the Order Confirmation, and whether such writing appears on a copy of the Order Confirmation or in a separate instrument.
    - 8.5. The licensing transaction described in the Order Confirmation document shall be governed by and construed under the law of the State of New York, USA, without regard to the principles thereof of conflicts of law. Any case, controversy, suit, action, or proceeding arising out of, in connection with, or related to such licensing transaction shall be brought, at CCC's sole discretion, in any federal or state court located in the County of New York, State of New York, USA, or in any federal or state court whose geographical jurisdiction covers the location of the Rightsholder set forth in the Order Confirmation. The parties expressly submit to the personal jurisdiction and venue of each such federal or state court.If you have any comments or questions about the Service or Copyright Clearance Center, please contact us at 978-750-8400 or send an e-mail to support@copyright.com.

v 1.1

References

1. K. Bizheva, L. Haines, E. Mason, B. MacLellan, B. Tan, D. Hileeto, and L. Sorbara, "In Vivo Imaging and Morphometry of the Human Pre-Descemet's Layer and Endothelium With Ultrahigh-Resolution Optical Coherence Tomography.," Invest Ophth Vis Sci 57(6), 2782–7 (2016).
2. M. S. Sridhar, "Anatomy of cornea and ocular surface.," Indian journal of ophthalmology 66(2), 190–194 (2018).
3. S. Feizi, M. R. Jafarinasab, F. Karimian, H. Hasanpour, and A. Masudi, "Central and Peripheral Corneal Thickness Measurement in Normal and Keratoconic Eyes Using Three Corneal Pachymeters," J Ophthalmic Vis Res 9(3), 296–304 (2014).
4. K. M. Meek and C. Knupp, "Corneal structure and transparency," Progress in Retinal and Eye Research 49, 1–16 (2015).
5. N. C. Joyce, "Proliferative capacity of corneal endothelial cells," Exp Eye Res 95(1), 16–23 (2012).
6. N. Polisetti and N. C. Joyce, "The culture of limbal stromal cells and corneal endothelial cells.," Methods Mol Biology Clifton N J 1014, 131–9 (2013).
7. D. V. Patel, T. Sherwin, and C. N. McGhee, "Laser Scanning In Vivo Confocal Microscopy of the Normal Human Corneoscleral Limbus," Investigative Opthalmology & Visual Science 47(7), 2823 (2006).
8. A. Miri, M. Al-Aqaba, A. Otri, U. Fares, D. G. Said, L. Faraj, and H. S. Dua, "In vivo confocal microscopic features of normal limbus," British Journal of Ophthalmology 96(4), 530 (2012).
9. G. Yazdanpanah, Z. Haq, K. Kang, S. Jabbehdari, M. l Rosenblatt, and A. R. Djalilian, "Strategies for reconstructing the limbal stem cell niche," The Ocular Surface 17(J Cataract Refract Surg 37 2011), 230–240 (2019).
10. R. M. Lavker, S. Tseng, and T.-T. Sun, "Corneal epithelial stem cells at the limbus: looking at some old problems from a new angle," Experimental Eye Research 78(3), 433–446 (2004).
11. G. Cotsarelis, S.-Z. Cheng, G. Dong, T.-T. Sun, and R. M. Lavker, "Existence of slow-cycling limbal epithelial basal cells that can be preferentially stimulated to proliferate: Implications on epithelial stem cells," Cell 57(2), 201–209 (1989).
12. A. W. Joe and S. N. Yeung, "Concise Review: Identifying Limbal Stem Cells: Classical Concepts and New Challenges," STEM CELLS Translational Medicine 3(3), 318–322 (2014).

13. Y. Hayashi, M. K. Call, C.-Y. Liu, M. Hayashi, G. Babcock, Y. Ohashi, and W. W.-Y. Kao, "Monoallelic Expression of Krt12 Gene during Corneal-type Epithelium Differentiation of Limbal Stem Cells," Investigative Opthalmology Vis Sci 51(9), 4562 (2010).

14. H. S. Dua and A. Azuara-Blanco, "Limbal Stem Cells of the Corneal Epithelium," Surv Ophthalmol 44(5), 415–425 (2000).

15. Z. Chen, C. S. de Paiva, L. Luo, F. L. Kretzer, S. C. Pflugfelder, and D. Li, "Characterization of Putative Stem Cell Phenotype in Human Limbal Epithelia," STEM CELLS 22(3), 355–366 (2004).

16. S. Mathews, J. D. Chidambaram, S. Lanjewar, J. Mascarenhas, N. V. Prajna, V. Muthukkaruppan, and G. P. Chidambaranathan, "In Vivo Confocal Microscopic Analysis of Normal Human Anterior Limbal Stroma," Cornea 34(4), 464–470 (2015).

17. B. Tan, Z. Hosseinaee, L. Han, O. Kralj, L. Sorbara, and K. Bizheva, "250 kHz, 1.5 µm resolution SD-OCT for in-vivo cellular imaging of the human cornea.," Biomedical optics express 9(12), 6569–6583 (2018).

18. K. Bizheva, B. Tan, B. MacLelan, O. Kralj, M. Hajialamdari, D. Hileeto, and L. Sorbara, "Sub-micrometer axial resolution OCT for in-vivo imaging of the cellular structure of healthy and keratoconic human corneas.," Biomedical optics express 8(2), 800–812 (2017).

19. B. MacLellan, B. Tan, D. Hileeto, E. Mason, K. Bizheva, L. Sorbara, and Z. Hosseinaee, "In-vivo imaging of the palisades of Vogt and the limbal crypts with sub-micrometer axial resolution optical coherence tomography," Biomedical Optics Express 8(9), 4141–4151 (2017).

20. P. Xiao, V. Mazlin, K. Grieve, J.-A. Sahel, M. Fink, and C. A. Boccara, "In vivo high-resolution human retinal imaging with wavefront-correctionless full-field OCT," Optica 5(4), 409 (2018).

21. V. Mazlin, P. Xiao, J. Scholler, K. Irsch, K. Grieve, M. Fink, and C. A. Boccara, "Real-time non-contact cellular imaging and angiography of human cornea and limbus with common-path full-field/SD OCT," Nat Commun 11(1), 1868 (2020).

22. L. Vabre, A. Dubois, and A. C. Boccara, "Thermal-light full-field optical coherence tomography.," Opt Lett 27(7), 530–2 (2002).

23. B. Laude, A. D. Martino, B. Drévillon, L. Benattar, and L. Schwartz, "Full-field optical coherence tomography with thermal light.," Appl Optics 41(31), 6637–45 (2002).

24. I. A. Joseph, C. A. Michael, and D. Al-Hafeez, "Theory of Optical Coherence Tomography," in Optical Coherence Tomography: Technology and Application (Springer, 2015), pp. 65–94.

25. E. Auksorius, D. Borycki, P. Stremplewski, K. Liżewski, S. Tomczewski, P. Niedźwiedziuk, B. L. Sikorski, and M. Wojtkowski, "In vivo imaging of the human cornea with high-speed and high-resolution Fourier-domain full-field optical coherence tomography," Biomed Opt Express 11(5), 2849 (2020).

26. A. F. Fercher, K. Mengedoht, and W. Werner, "Eye-length measurement by interferometry with partially coherent light.," Opt Lett 13(3), 186–8 (1988).

27. D. Huang, E. Swanson, C. Lin, J. Schuman, W. Stinson, W. Chang, M. Hee, T. Flotte, K. Gregory, C. Puliafito, and al. et, "Optical coherence tomography," Science 254(5035), 1178–1181 (1991).

28. M. Choma, M. Sarunic, C. Yang, and J. Izatt, "Sensitivity advantage of swept source and Fourier domain optical coherence tomography," Opt Express 11(18), 2183 (2003).

29. R. Leitgeb, C. Hitzenberger, and A. Fercher, "Performance of fourier domain vs. time domain optical coherence tomography," Optics Express 11(8), 889 (2003).

30. B. Vakoc, S. Yun, J. de Boer, G. Tearney, and B. Bouma, "Phase-resolved optical frequency domain imaging," Opt Express 13(14), 5483 (2005).

31. R. A. Leitgeb, R. M. Werkmeister, C. Blatter, and L. Schmetterer, "Doppler Optical Coherence Tomography," Progress in Retinal and Eye Research 41, 26–43 (2014).

32. F. Zhang, K. Kurokawa, A. Lassoued, J. A. Crowell, and D. T. Miller, "Cone photoreceptor classification in the living human eye from photostimulation-induced phase dynamics.," Proceedings of the National Academy of Sciences of the United States of America 116(16), 7951–7956 (2019).

33. M. Azimipour, D. Valente, K. V. Vienola, J. S. Werner, R. J. Zawadzki, and R. S. Jonnal, "Optoretinogram: optical measurement of human cone and rod photoreceptor responses to light," Opt Lett 45(17), 4658 (2020).

34. V. P. Pandiyan, A. Maloney-Bertelli, J. A. Kuchenbecker, K. C. Boyle, T. Ling, Z. C. Chen, B. H. Park, A. Roorda, D. Palanker, and R. Sabesan, "The optoretinogram reveals the primary steps of phototransduction in the living human eye," Sci Adv 6(37), eabc1124 (2020).

35. H. Spahr, C. Pfäffle, S. Burhan, L. Kutzner, F. Hilge, G. Hüttmann, and D. Hillmann, "Phase-sensitive interferometry of decorrelated speckle patterns.," Scientific reports 9(1), 11748 (2019).

36. P. Zhang, R. J. Zawadzki, M. Goswami, P. T. Nguyen, V. Yarov-Yarovoy, M. E. Burns, and E. N. Pugh, "In vivo optophysiology reveals that G-protein activation triggers osmotic swelling and

increased light scattering of rod photoreceptors.," P Natl Acad Sci Usa 114(14), E2937–E2946 (2017).

37. K. Bizheva, R. Pflug, B. Hermann, B. Povazay, H. Sattmann, P. Qiu, E. Anger, H. Reitsamer, S. Popov, J. R. Taylor, A. Unterhuber, P. Ahnelt, and W. Drexler, "Optophysiology: depth-resolved probing of retinal physiology with functional ultrahigh-resolution optical coherence tomography.," P Natl Acad Sci Usa 103(13), 5066–71 (2006).
38. B. F. Kennedy, P. Wijesinghe, and D. D. Sampson, "The emergence of optical elastography in biomedicine," Nat Photonics 11(4), 215–221 (2017).
39. A. Nair, M. Singh, S. R. Aglyamov, and K. V. Larin, "Heartbeat OCE: corneal biomechanical response to simulated heartbeat pulsation measured by optical coherence elastography," J Biomed Opt 25(05), 1 (2020).
40. C. Apelian, F. Harms, O. Thouvenin, and A. C. Boccara, "Dynamic full field optical coherence tomography: subcellular metabolic contrast revealed in tissues by interferometric signals temporal analysis," Biomed Opt Express 7(4), 1511–1524 (2016).
41. A. H. Kashani, C.-L. Chen, J. K. Gahm, F. Zheng, G. M. Richter, P. J. Rosenfeld, Y. Shi, and R. K. Wang, "Optical coherence tomography angiography: A comprehensive review of current methods and clinical applications," Prog Retin Eye Res 60, 66–100 (2017).
42. S. G. Adie, B. W. Graf, A. Ahmad, S. P. Carney, and S. A. Boppart, "Computational adaptive optics for broadband optical interferometric tomography of biological tissue," Proc National Acad Sci 109(19), 7175–7180 (2012).
43. A. Kumar, W. Drexler, and R. A. Leitgeb, "Subaperture correlation based digital adaptive optics for full field optical coherence tomography.," Optics express 21(9), 10850–66 (2013).
44. D. Hillmann, H. Spahr, C. Hain, H. Sudkamp, G. Franke, C. Pfäffle, C. Winter, and G. Hüttmann, "Aberration-free volumetric high-speed imaging of in vivo retina.," Scientific reports 6, 35209 (2016).
45. L. Ginner, A. Kumar, D. Fechtig, L. M. Wurster, M. Salas, M. Pircher, and R. A. Leitgeb, "Noniterative digital aberration correction for cellular resolution retinal optical coherence tomography in vivo," Optica 4(8), 924–931 (2016).
46. L. V. Wang and H. Wu, "Optical Coherence Tomography," in Biomedical Optics: Principles and Imaging (Wiley Interscience, 2012), pp. 181–218.

47. M. Wojtkowski, A. Kowalczyk, R. Leitgeb, and A. F. Fercher, "Full range complex spectral optical coherence tomography technique in eye imaging," Opt Lett 27(16), 1415 (2002).

48. B. Baumann, M. Pircher, E. Götzinger, and C. K. Hitzenberger, "Full range complex spectral domain optical coherence tomography without additional phase shifters.," Opt Express 15(20), 13375–87 (2007).

49. W. Song, L. Chen, L. Han, A. R. Martinez, and K. Bizheva, "400kHz, 1 μm axial resolution SD-OCT for ophthalmic applications," Ophthalmic Technologies Xxxii 3 (2022).

50. M. Münter, M. Pieper, T. Kohlfaerber, E. Bodenstorfer, M. Ahrens, C. Winter, R. Huber, P. König, G. Hüttmann, and H. Schulz-Hildebrandt, "Microscopic optical coherence tomography (mOCT) at 600 kHz for 4D volumetric imaging and dynamic contrast.," Biomed Opt Express 12(10), 6024–6039 (2021).

51. W. Wieser, B. R. Biedermann, T. Klein, C. M. Eigenwillig, and R. Huber, "Multi-Megahertz OCT: High quality 3D imaging at 20 million A-scans and 4.5 GVoxels per second," Opt Express 18(14), 14685–704 (2010).

52. A. Zuluaga and R. Richards-Kortum, "Spatially resolved spectral interferometry for determination of subsurface structure.," Optics letters 24(8), 519–21 (1999).

53. B. Považay, A. Unterhuber, B. Hermann, H. Sattmann, H. Arthaber, and W. Drexler, "Full-field time-encoded frequency-domain optical coherence tomography," Opt Express 14(17), 7661 (2006).

54. E. Auksorius, D. Borycki, and M. Wojtkowski, "Crosstalk-free volumetric in vivo imaging of a human retina with Fourier-domain full-field optical coherence tomography," Biomed Opt Express 10(12), 6390 (2019).

55. E. Auksorius, D. Borycki, and M. Wojtkowski, "Multimode fiber enables control of spatial coherence in Fourier-domain full-field optical coherence tomography for in vivo corneal imaging," Opt Lett 46(6), 1413 (2021).

56. D. Hillmann, T. Bonin, C. Lührs, G. Franke, M. Hagen-Eggert, P. Koch, and G. Hüttmann, "Common approach for compensation of axial motion artifacts in swept-source OCT and dispersion in Fourier-domain OCT," Opt Express 20(6), 6761 (2012).

57. A. Dubois, K. Grieve, G. Moneron, R. Lecaque, L. Vabre, and C. Boccara, "Ultrahigh-resolution full-field optical coherence tomography," Appl Optics 43(14), 2874 (2004).

58. A. Dubois, O. Levecq, H. Azimani, D. Siret, A. Barut, M. Suppa, V. del Marmol, J. Malvehy, E. Cinotti, P. Rubegni, and J.-L. Perrot, "Line-field confocal optical coherence tomography for high-resolution noninvasive imaging of skin tumors," Journal of Biomedical Optics 23(10), 106007 (2018).

59. Z. Ding, Y. Zhao, H. Ren, J. S. Nelson, and Z. Chen, "Real-time phase-resolved optical coherence tomography and optical Doppler tomography," Opt Express 10(5), 236 (2002).

60. R. M. Werkmeister, N. Dragostinoff, M. Pircher, E. Götzinger, C. K. Hitzenberger, R. A. Leitgeb, and L. Schmetterer, "Bidirectional Doppler Fourier-domain optical coherence tomography for measurement of absolute flow velocities in human retinal vessels," Optics Letters 33(24), 2967 (2008).

61. R. Haindl, W. Trasischker, B. Baumann, M. Pircher, and C. K. Hitzenberger, "Three-beam Doppler optical coherence tomography using a facet prism telescope and MEMS mirror for improved transversal resolution," J Mod Optic 62(21), 1781–1788 (2014).

62. H. Spahr, C. Pfäffle, P. Koch, H. Sudkamp, G. Hüttmann, and D. Hillmann, "Interferometric detection of 3D motion using computational subapertures in optical coherence tomography.," Optics express 26(15), 18803–18816 (2018).

63. L. Ginner, A. Wartak, M. Salas, M. Augustin, M. Niederleithner, L. M. Wurster, and R. A. Leitgeb, "Synthetic subaperture-based angle-independent Doppler flow measurements using single-beam line field optical coherence tomography in vivo," Opt Lett 44(4), 967 (2019).

64. J. Lee, W. Wu, J. Y. Jiang, B. Zhu, and D. A. Boas, "Dynamic light scattering optical coherence tomography," Opt Express 20(20), 22262–22277 (2012).

65. P. Andretzky, M. W. Lindner, J. M. Herrmann, A. Schultz, M. Konzog, F. Kiesewetter, and G. Haeusler, "Optical coherence tomography by spectral radar: dynamic range estimation and in-vivo measurements of skin," Opt Imaging Techniques Biomonitoring Iv 78–87 (1999).

66. M. Wojtkowski, R. Leitgeb, A. Kowalczyk, T. Bajraszewski, and A. F. Fercher, "In vivo human retinal imaging by Fourier domain optical coherence tomography," J Biomed Opt 7(3), 457–463 (2002).

67. M. Wojtkowski, V. Srinivasan, T. Ko, J. Fujimoto, A. Kowalczyk, and J. Duker, "Ultrahigh-resolution, high-speed, Fourier domain optical coherence tomography and methods for dispersion compensation.," Optics express 12(11), 2404–22 (2004).

68. S. Yun, G. Tearney, J. de Boer, N. Iftimia, and B. Bouma, "High-speed optical frequency-domain imaging," Opt Express 11(22), 2953 (2003).

69. S. Yun, G. Tearney, B. Bouma, B. Park, and J. de Boer, "High-speed spectral-domain optical coherence tomography at 1.3 µm wavelength," Optics Express 11(26), 3598 (2003).

70. R. J. Zawadzki, B. Cense, Y. Zhang, S. S. Choi, D. T. Miller, and J. S. Werner, "Ultrahigh-resolution optical coherence tomography with monochromatic and chromatic aberration correction," Opt Express 16(11), 8126 (2008).

71. M. Pircher and R. J. Zawadzki, "Review of adaptive optics OCT (AO-OCT): principles and applications for retinal imaging [Invited]," Biomedical Optics Express 8(5), 2536 (2017).

72. F. A. South, K. Kurokawa, Z. Liu, Y.-Z. Liu, D. T. Miller, and S. A. Boppart, "Combined hardware and computational optical wavefront correction," Biomed Opt Express 9(6), 2562 (2018).

73. V. Mazlin, K. Irsch, M. Paques, J.-A. Sahel, M. Fink, and C. A. Boccara, "Curved-field optical coherence tomography: large-field imaging of human corneal cells and nerves," Optica 7(8), 872 (2020).

74. F. Zhang, K. Kurokawa, M. T. Bernucci, H. W. Jung, A. Lassoued, J. A. Crowell, J. Neitz, M. Neitz, and D. T. Miller, "Revealing How Color Vision Phenotype and Genotype Manifest in Individual Cone Cells," Invest Ophth Vis Sci 62(2), 8–8 (2021).

75. O. P. Kocaoglu, T. L. Turner, Z. Liu, and D. T. Miller, "Adaptive optics optical coherence tomography at 1 MHz.," Biomedical optics express 5(12), 4186–200 (2014).

76. B. Povazay, K. Bizheva, A. Unterhuber, B. Hermann, H. Sattmann, A. F. Fercher, W. Drexler, A. Apolonski, W. J. Wadsworth, J. C. Knight, P. S. J. Russell, M. Vetterlein, and E. Scherzer, "Submicrometer axial resolution optical coherence tomography.," Opt Lett 27(20), 1800–2 (2002).

77. R. Yadav, K.-S. Lee, J. P. Rolland, J. M. Zavislan, J. V. Aquavella, and G. Yoon, "Micrometer axial resolution OCT for corneal imaging," Biomedical Optics Express 2(11), 3037–3046 (2011).

78. R. M. Werkmeister, S. Sapeta, D. Schmidl, G. Garhöfer, G. Schmidinger, V. Santos, G. C. Aschinger, I. Baumgartner, N. Pircher, F. Schwarzhans, A. Pantalon, H. Dua, and L. Schmetterer, "Ultrahigh-resolution OCT imaging of the human cornea.," Biomedical optics express 8(2), 1221–1239 (2017).

79. K. Grieve, M. Paques, A. Dubois, J. Sahel, C. Boccara, and J.-F. L. Gargasson, "Ocular tissue imaging using ultrahigh-resolution, full-field optical coherence tomography.," Invest Ophth Vis Sci 45(11), 4126–31 (2004).

80. K. Grieve, D. Ghoubay, C. Georgeon, O. Thouvenin, N. Bouheraoua, M. Paques, and V. Borderie, "Three-dimensional structure of the mammalian limbal stem cell niche.," Experimental eye research 140, 75–84 (2015).

81. S. R. Ellis and L. Stark, "Eye Movements during the Viewing of Necker Cubes," Perception 7(5), 575–581 (1978).

82. J. Ito, A. R. Nikolaev, M. Luman, M. F. Aukes, C. Nakatani, and C. van Leeuwen, "Perceptual Switching, Eye Movements, and the Bus Paradox," Perception 32(6), 681–698 (2002).

83. D. Valente, K. V. Vienola, R. J. Zawadzki, and R. S. Jonnal, "Kilohertz retinal FF-SS-OCT and flood imaging with hardware-based adaptive optics," Biomed Opt Express 11(10), 5995 (2020).

84. M. Szkulmowski, S. Tamborski, and M. Wojtkowski, "Spectrometer calibration for spectroscopic Fourier domain optical coherence tomography," Biomed Opt Express 7(12), 5042 (2016).

85. J. A. Izatt and M. A. Choma, "Theory of Optical Coherence Tomography," Optical Coherence Tomography 47–72 (2008).

86. X. Attendu, R. M. Ruis, C. Boudoux, T. G. van Leeuwen, and D. J. Faber, "Simple and robust calibration procedure for k-linearization and dispersion compensation in optical coherence tomography," J Biomed Opt 24(5), 056001 (2019).

87. Y. Yasuno, Y. Hong, S. Makita, M. Yamanari, M. Akiba, M. Miura, and T. Yatagai, "In vivo high-contrast imaging of deep posterior eye by 1-μm swept source optical coherence tomography and scattering optical coherence angiography," Opt Express 15(10), 6121 (2007).

88. H. C. Hendargo, R. P. McNabb, A.-H. Dhalla, N. Shepherd, and J. A. Izatt, "Doppler velocity detection limitations in spectrometer-based versus swept-source optical coherence tomography," Biomed Opt Express 2(8), 2175–2188 (2011).

89. M. S. Oliva, T. Schottman, and M. Gulati, "Turning the tide of corneal blindness," Indian J Ophthalmol 60(5), 423–427 (2012).

90. R. L. Niederer and C. N. J. McGhee, "Clinical in vivo confocal microscopy of the human cornea in health and disease," Prog Retin Eye Res 29(1), 30–58 (2010).

91. W. Drexler, "Ultrahigh-resolution optical coherence tomography," J Biomed Opt 9(1), 47–74 (2004).

92. M. Ang, M. Baskaran, R. M. Werkmeister, J. Chua, D. Schmidl, V. A. dos Santos, G. Garhöfer, J. S. Mehta, and L. Schmetterer, "Anterior segment optical coherence tomography," Prog Retin Eye Res 66, 132–156 (2018).

93. R. M. Werkmeister, A. Alex, S. Kaya, A. Unterhuber, B. Hofer, J. Riedl, M. Bronhagl, M. Vietauer, D. Schmidl, T. Schmoll, G. Garhöfer, W. Drexler, R. A. Leitgeb, M. Groeschl, and L. Schmetterer, "Measurement of Tear Film Thickness Using Ultrahigh-Resolution Optical Coherence Tomography," Investigative Opthalmology Vis Sci 54(8), 5578 (2013).

94. P. Tankam, Z. He, Y.-J. Chu, J. Won, C. Canavesi, T. Lepine, H. B. Hindman, D. J. Topham, P. Gain, G. Thuret, and J. P. Rolland, "Assessing microstructures of the cornea with Gabor-domain optical coherence microscopy: pathway for corneal physiology and diseases," Opt Lett 40(6), 1113 (2015).

95. S. Chen, X. Liu, N. Wang, X. Wang, Q. Xiong, E. Bo, X. Yu, S. Chen, and L. Liu, "Visualizing Micro-anatomical Structures of the Posterior Cornea with Micro-optical Coherence Tomography," Sci Rep-uk 7(1), 10752 (2017).

96. X. Yao, K. Devarajan, R. M. Werkmeister, V. A. dos Santos, M. Ang, A. Kuo, D. W. K. Wong, J. Chua, B. Tan, V. A. Barathi, and L. Schmetterer, "In vivo corneal endothelium imaging using ultrahigh resolution OCT," Biomed Opt Express 10(11), 5675 (2019).

97. A. Dubois, L. Vabre, A.-C. Boccara, and E. Beaurepaire, "High-resolution full-field optical coherence tomography with a Linnik microscope.," Appl Optics 41(4), 805–12 (2002).

98. R. A. Leitgeb, "En face optical coherence tomography: a technology review [Invited].," Biomed Opt Express 10(5), 2177–2201 (2019).

99. M. Akiba, N. Maeda, K. Yumikake, T. Soma, K. Nishida, Y. Tano, and K. P. Chan, "Ultrahigh-resolution imaging of human donor cornea using full-field optical coherence tomography," J Biomed Opt 12(4), 041202-041202–7 (2007).

100. W. Ghouali, K. Grieve, S. Bellefqih, O. Sandali, F. Harms, L. Laroche, M. Paques, and V. Borderie, "Full-Field Optical Coherence Tomography of Human Donor and Pathological Corneas," Curr Eye Res 40(5), 526–534 (2015).

101. V. Mazlin, P. Xiao, E. Dalimier, K. Grieve, K. Irsch, J.-A. A. Sahel, M. Fink, and A. C. Boccara, "In vivo high resolution human corneal imaging using full-field optical coherence tomography.," Biomedical optics express 9(2), 557–568 (2018).

102. T. Bonin, G. Franke, M. Hagen-Eggert, P. Koch, and G. Hüttmann, "In vivo Fourier-domain full-field OCT of the human retina with 1.5 million A-lines/s.," Opt Lett 35(20), 3432–4 (2010).

103. D. Hillmann, H. Spahr, H. Sudkamp, C. Hain, L. Hinkel, G. Franke, and G. Hüttmann, "Off-axis reference beam for full-field swept-source OCT and holoscopy.," Opt Express 25(22), 27770–27784 (2017).

104. P. Stremplewski, E. Auksorius, P. Wnuk, Ł. Kozoń, P. Garstecki, and M. Wojtkowski, "In vivo volumetric imaging by crosstalk-free full-field OCT," Optica 6(5), 608 (2019).

105. A. Kumar, W. Drexler, and R. A. Leitgeb, "Numerical focusing methods for full field OCT: a comparison based on a common signal model," Opt Express 22(13), 16061 (2014).

106. A. Kumar, T. Kamali, R. Platzer, A. Unterhuber, W. Drexler, and R. A. Leitgeb, "Anisotropic aberration correction using region of interest based digital adaptive optics in Fourier domain OCT," Biomed Opt Express 6(4), 1124–1134 (2015).

107. D. Borycki, E. Auksorius, P. Węgrzyn, and M. Wojtkowski, "Computational aberration correction in spatiotemporal optical coherence (STOC) imaging.," Opt Lett 45(6), 1293–1296 (2020).

108. "ANSI Z80.36-2016 - Ophthalmics - Light Hazard Protection for Ophthalmic Instruments," https://webstore.ansi.org/standards/vc%20(asc%20z80)/ansiz80362016.

109. R. Watkins, "OpticStudio models of the human eye," https://support.zemax.com/hc/en-us/articles/1500005575082-OpticStudio-models-of-the-human-eye.

110. F. C. Delori, R. H. Webb, and D. H. Sliney, "Maximum permissible exposures for ocular safety (ANSI 2000), with emphasis on ophthalmic devices," J Opt Soc Am 24(5), 1250 (2007).

111. M. J. Hogan, J. A. Alvarado, and J. E. Weddell, Histology of the Human Eye: An Atlas and Textbook (Saunders, 1971).

112. E. M. V. Buskirk, "The anatomy of the limbus," Eye 3(2), 101–108 (1989).

113. J. G. Lawrenson and G. L. Ruskell, "The structure of corpuscular nerve endings in the limbal conjunctiva of the human eye.," J Anat 177, 75–84 (1991).

114. P. A. R. Meyer, "The circulation of the human limbus," Eye 3(2), 121–127 (1989).

115. E. B. Papas, "The limbal vasculature," Contact Lens Anterior Eye 26(2), 71–76 (2003).

116. H. S. Dua, V. A. Shanmuganathan, A. O. Powell-Richards, P. J. Tighe, and A. Joseph, "Limbal epithelial crypts: a novel anatomical structure and a putative limbal stem cell niche," Brit J Ophthalmol 89(5), 529 (2005).

117. M. F. Goldberg and A. J. Bron, "Limbal palisades of Vogt.," T Am Ophthal Soc 80, 155–71 (1982).

118. A. Wartak, M. S. Schenk, V. Bühler, S. A. Kassumeh, R. Birngruber, and G. J. Tearney, "Micro-optical coherence tomography for high-resolution morphologic imaging of cellular and nerval corneal micro-structures," Biomed Opt Express 11(10), 5920 (2020).

119. M. Münter, H. Schulz-Hildebrandt, M. Pieper, P. König, and G. Hüttmann, "4D microscopic optical coherence tomography imaging of ex vivo mucus transport," Opt Coherence Imaging Techniques Imaging Scatt Media Iii 11078, 1107811-1107811–5 (2019).

120. Y.-T. Chen, C.-Y. Tsai, Y.-K. Chiu, T.-W. Hsu, L. W. Chen, W.-L. Chen, and S.-L. Huang, "En Face and Cross-sectional Corneal Tomograms Using Sub-micron spatial resolution Optical Coherence Tomography," Sci Rep-uk 8(1), 14349 (2018).

121. I. Powell, "Design of a laser beam line expander," Appl Optics 26(17), 3705 (1987).

122. Z. Al-Qazwini, Z. Ko, K. Mehta, and N. Chen, "Ultrahigh-speed line-scan SD-OCT for four-dimensional in vivo imaging of small animal models.," Biomedical optics express 9(3), 1216–1228 (2018).

123. V. P. Pandiyan, X. Jiang, A. Maloney-Bertelli, J. A. Kuchenbecker, U. Sharma, and R. Sabesan, "High-speed adaptive optics line-scan OCT for cellular-resolution optoretinography," Biomed Opt Express 11(9), 5274 (2020).

124. A.-H. Dhalla, J. V. Migacz, and J. A. Izatt, "Crosstalk rejection in parallel optical coherence tomography using spatially incoherent illumination with partially coherent sources," Optics Letters 35(13), 2305 (2010).

125. J. Lu, B. Gu, X. Wang, and Y. Zhang, "High speed adaptive optics ophthalmoscopy with an anamorphic point spread function.," Optics express 26(11), 14356–14374 (2018).

126. J. Zhu, H. R. Freitas, I. Maezawa, L. Jin, and V. J. Srinivasan, "1700 nm optical coherence microscopy enables minimally invasive, label-free, in vivo optical biopsy deep in the mouse brain," Light Sci Appl 10(1), 145 (2021).

127. R. A. Leitgeb, M. Villiger, A. H. Bachmann, L. Steinmann, and T. Lasser, "Extended focus depth for Fourier domain optical coherence microscopy," Opt Lett 31(16), 2450 (2006).

128. P. J. Marchand, A. Bouwens, D. Szlag, D. Nguyen, A. Descloux, M. Sison, S. Coquoz, J. Extermann, and T. Lasser, "Visible spectrum extended-focus optical coherence microscopy for label-free sub-cellular tomography.," Biomedical optics express 8(7), 3343–3359 (2017).

129. J. Zhao, Y. Winetraub, E. Yuan, and A. de la Zerda, "Needle-shaped beam by a novel diffractive optical element for the extended depth-of-focus of optical coherence tomography," Opt Coherence Tomogr Coherence Domain Opt Methods Biomed Xxv 50 (2021).

130. K. C. Zhou, R. Qian, S. Degan, S. Farsiu, and J. A. Izatt, "Optical coherence refraction tomography," Nature Photonics 1–9 (2019).

131. K. C. Zhou, R. P. McNabb, R. Qian, S. Degan, A.-H. Dhalla, S. Farsiu, and J. A. Izatt, "Computational 3D microscopy with optical coherence refraction tomography," Arxiv (2022).

132. Y. Yasuno, J. Sugisaka, Y. Sando, Y. Nakamura, S. Makita, M. Itoh, and T. Yatagai, "Non-iterative numerical method for laterally superresolving Fourier domain optical coherence tomography," Opt Express 14(3), 1006 (2006).

133. T. S. Ralston, D. L. Marks, P. S. Carney, and S. A. Boppart, "Interferometric synthetic aperture microscopy," Nat Phys 3(2), 129–134 (2007).

134. D. Fechtig, A. Kumar, B. Grajciar, A. S. Singh, W. Drexler, and R. A. Leitgeb, "Line field off axis swept source OCT utilizing digital refocusing," spie 91293S-91293S–7 (2014).

135. P. Pande, Y.-Z. Liu, F. A. South, and S. A. Boppart, "Automated computational aberration correction method for broadband interferometric imaging techniques," Opt Lett 41(14), 3324 (2016).

136. A. Kumar, S. Georgiev, M. Salas, and R. A. Leitgeb, "Digital adaptive optics based on digital lateral shearing of the computed pupil field for point scanning retinal swept source OCT," Biomed Opt Express 12(3), 1577 (2021).

137. N. D. Shemonski, S. G. Adie, Y.-Z. Liu, F. A. South, S. P. Carney, and S. A. Boppart, "Stability in computed optical interferometric tomography (Part I): Stability requirements," Opt Express 22(16), 19183–97 (2014).

138. N. D. Shemonski, A. Ahmad, S. G. Adie, Y.-Z. Liu, F. A. South, S. P. Carney, and S. A. Boppart, "Stability in computed optical interferometric tomography (Part II): in vivo stability assessment," Opt Express 22(16), 19314–26 (2014).

139. A. Kumar, L. M. Wurster, M. Salas, L. Ginner, W. Drexler, and R. A. Leitgeb, "In-vivo digital wavefront sensing using swept source OCT.," Biomed Opt Express 8(7), 3369–3382 (2017).

140. N. D. Shemonski, S. S. Ahn, Y.-Z. Liu, F. A. South, S. P. Carney, and S. A. Boppart, "Three-dimensional motion correction using speckle and phase for in vivo computed optical interferometric tomography," Biomed Opt Express 5(12), 4131 (2014).

141. E. J. Fernández, A. Unterhuber, B. Považay, B. Hermann, P. Artal, and W. Drexler, "Chromatic aberration correction of the human eye for retinal imaging in the near infrared," Opt Express 14(13), 6213 (2006).

142. L. Wang, Q. Xiong, X. Ge, E. Bo, J. Xie, X. Liu, X. Yu, X. Wang, N. Wang, S. Chen, X. Wu, and L. Liu, "Cellular resolution corneal imaging with extended imaging range," Opt Express 27(2), 1298 (2019).

143. L. Han, L. K. Chen, Z. Hosseinaee, and K. Bizheva, "In-vivo, non-contact, cellular resolution imaging of the human cornea with line-field SD-OCT at 2.5 kHz frame rate (Conference Presentation)," Opt Coherence Tomogr Coherence Domain Opt Methods Biomed Xxiv 18 (2020).

144. S. Ruder, "An overview of gradient descent optimization algorithms," Arxiv (2016).

145. R. Hooke and T. A. Jeeves, "`` Direct Search'' Solution of Numerical and Statistical Problems," J Acm Jacm 8(2), 212–229 (1961).

146. J. A. Nelder and R. Mead, "A Simplex Method for Function Minimization," Comput J 7(4), 308–313 (1965).

147. S. Kirkpatrick, C. D. Gelatt, and M. P. Vecchi, "Optimization by Simulated Annealing," Science 220(4598), 671–680 (1983).

148. B. Hajek and G. Sasaki, "Simulated annealing — to cool or not," Syst Control Lett 12(5), 443–447 (1989).

149. B. Hajek, "Cooling Schedules for Optimal Annealing," Math Oper Res 13(2), 311–329 (1988).

150. W. S. Cleveland and S. J. Devlin, "Locally Weighted Regression: An Approach to Regression Analysis by Local Fitting," J Am Stat Assoc 83(403), 596–610 (2012).

151. M. Guizar-Sicairos, S. T. Thurman, and J. R. Fienup, "Efficient subpixel image registration algorithms," Opt Lett 33(2), 156 (2008).

152. M. Guizar, Efficient Subpixel Image Registration by Cross-Correlation (MATLAB Central File Exchange, 2022).

153. J. Fienup and J. Miller, "Aberration correction by maximizing generalized sharpness metrics," J Opt Soc Am 20(4), 609 (2003).

154. L. Zhang, J. Sheng, J. Duan, M. Xing, Z. Qiao, and Z. Bao, "Translational motion compensation for ISAR imaging under low SNR by minimum entropy," Eurasip J Adv Sig Pr 2013(1), 33 (2013).

155. D. P. Kingma and J. Ba, "Adam: A Method for Stochastic Optimization," Arxiv (2014).

156. X.-S. Yang, S. Deb, and S. Fong, "Accelerated particle swarm optimization and support vector machine for business optimization and application," Comm Com Inf Sc 53–66 (2011).

157. X. Yu, X. Liu, J. Gu, D. Cui, J. Wu, and L. Liu, "Depth extension and sidelobe suppression in optical coherence tomography using pupil filters," Optics Express 22(22), 26956–26966 (2014).

158. X.-S. Yang and S. Deb, "Cuckoo Search via LÉvy Flights," 2009 World Congr Nat Biologically Inspired Comput Nabic 210–214 (2009).

159. W. M. Harmening, P. Tiruveedhula, A. Roorda, and L. C. Sincich, "Measurement and correction of transverse chromatic offsets for multi-wavelength retinal microscopy in the living eye," Biomed Opt Express 3(9), 2066–2077 (2012).

160. F. A. South, Y.-Z. Liu, P.-C. Huang, T. Kohlfarber, and S. A. Boppart, "Local wavefront mapping in tissue using computational adaptive optics OCT.," Opt Lett 44(5), 1186–1189 (2019).

161. K. C. Zhou, R. Qian, A.-H. Dhalla, S. Farsiu, and J. A. Izatt, "Unified k-space theory of optical coherence tomography," Adv Opt Photonics 13(2), 462 (2021).

162. N. Leartprapun and S. G. Adie, "Resolution-enhanced OCT and expanded framework of information capacity and resolution in coherent imaging," Arxiv (2021).

163. "Optical Coherence Tomography, Technology and Applications," (2015).

164. B. Braaf, M. G. O. Gräfe, N. Uribe-Patarroyo, B. E. Bouma, B. J. Vakoc, J. F. de Boer, S. Donner, and J. Weichsel, "OCT-Based Velocimetry for Blood Flow Quantification," in High Resolution Imaging in Microscopy and Ophthalmology, New Frontiers in Biomedical Optics (2019), pp. 161–179.

165. C. J. Pedersen, D. Huang, M. A. Shure, and A. M. Rollins, "Measurement of absolute flow velocity vector using dual-angle, delay-encoded Doppler optical coherence tomography," Optics Letters 32(5), 506 (2007).

166. J. Kalkman, A. V. Bykov, D. J. Faber, and T. G. van Leeuwen, "Multiple and dependent scattering effects in Doppler optical coherence tomography," Opt Express 18(4), 3883 (2010).

167. B. J. Berne and R. Pecora, Dynamic Light Scattering: With Applications to Chemistry, Biology, and Physics (Dover Publications, 2000).

168. W. Zhou, O. Kholiqov, S. P. Chong, and V. J. Srinivasan, "Highly parallel, interferometric diffusing wave spectroscopy for monitoring cerebral blood flow dynamics," Optica 5(5), 518 (2018).

169. V. J. Srinivasan, H. Radhakrishnan, E. H. Lo, E. T. Mandeville, J. Y. Jiang, S. Barry, and A. E. Cable, "OCT methods for capillary velocimetry," Biomed Opt Express 3(3), 612–629 (2012).

170. J. Tang, D. D. Postnov, K. Kilic, S. E. Erdener, B. Lee, J. T. Giblin, T. L. Szabo, and D. A. Boas, "Functional Ultrasound Speckle Decorrelation-Based Velocimetry of the Brain," Adv Sci 7(18), 2001044 (2020).

171. N. Weiss, T. G. van Leeuwen, and J. Kalkman, "Localized measurement of longitudinal and transverse flow velocities in colloidal suspensions using optical coherence tomography," Phys Rev E 88(4), 042312 (2013).

172. N. Uribe-Patarroyo, M. Villiger, and B. E. Bouma, "Quantitative technique for robust and noise-tolerant speed measurements based on speckle decorrelation in optical coherence tomography," Opt Express 22(20), 24411–24429 (2014).

173. M.-T. Tsai, T.-T. Chi, H.-L. Liu, F.-Y. Chang, C.-H. Yang, C.-K. Lee, and C.-C. Yang, "Microvascular Imaging Using Swept-Source Optical Coherence Tomography with Single-Channel Acquisition," Appl Phys Express 4(9), 097001 (2011).

174. S. Wei and J. U. Kang, "Optical flow optical coherence tomography for determining accurate velocity fields," Opt Express 28(17), 25502 (2020).

175. T. W. Taylor and C. M. Sorensen, "Gaussian beam effects on the photon correlation spectrum from a flowing Brownian motion system," Appl Optics 25(14), 2421 (1986).

176. N. Weiss, T. G. van Leeuwen, and J. Kalkman, "Simultaneous and localized measurement of diffusion and flow using optical coherence tomography," Opt Express 23(3), 3448–3459 (2015).

177. I. Popov and A. Vitkin, "Dynamic light scattering by flowing Brownian particles measured with optical coherence tomography: impact of the optical system," J Biomed Opt 21(1), 017002–017002 (2016).

178. W. Choi, E. M. Moult, N. K. Waheed, M. Adhi, B. Lee, C. D. Lu, T. E. de Carlo, V. Jayaraman, P. J. Rosenfeld, J. S. Duker, and J. G. Fujimoto, "Ultrahigh-Speed, Swept-Source Optical Coherence Tomography Angiography in Nonexudative Age-Related Macular Degeneration with Geographic Atrophy," Ophthalmology 122(12), 2532–2544 (2015).

179. S. B. Ploner, E. M. Moult, W. Choi, N. K. Waheed, B. Lee, E. A. Novais, E. D. Cole, B. Potsaid, L. Husvogt, J. Schottenhamml, A. Maier, P. J. Rosenfeld, J. S. Duker, J. Hornegger, and J. G. Fujimoto, "TOWARD QUANTITATIVE OPTICAL COHERENCE TOMOGRAPHY ANGIOGRAPHY," Retin 36(NA;), S118–S126 (2016).

180. D. P. Chowdhury, C. M. Sorensen, T. W. Taylor, J. F. Merklin, and T. W. Lester, "Application of photon correlation spectroscopy to flowing Brownian motion systems," Appl Optics 23(22), 4149 (1984).

181. S. Makita, F. Jaillon, I. Jahan, and Y. Yasuno, "Noise statistics of phase-resolved optical coherence tomography imaging: single-and dual-beam-scan Doppler optical coherence tomography," Opt Express 22(4), 4830 (2014).

182. K. Kurokawa, S. Makita, Y.-J. Hong, and Y. Yasuno, "Two-dimensional micro-displacement measurement for laser coagulation using optical coherence tomography," Biomed Opt Express 6(1), 170–190 (2015).

183. M. Courtney, X. Chen, S. Chan, T. Mohamed, P. P. N. Rao, and C. L. Ren, "Droplet Microfluidic System with On-Demand Trapping and Releasing of Droplet for Drug Screening Applications," Anal Chem 89(1), 910–915 (2017).

184. H. Spahr, C. Pfäffle, G. Hüttmann, and D. Hillmann, "Artifacts in speckle tracking and multi-aperture Doppler OCT imaging of lateral motion," Opt Lett 44(6), 1315 (2019).

185. A. Bouwens, D. Szlag, M. Szkulmowski, T. Bolmont, M. Wojtkowski, and T. Lasser, "Quantitative lateral and axial flow imaging with optical coherence microscopy and tomography," Opt Express 21(15), 17711 (2013).

186. J. Kalkman, R. Sprik, and T. G. van Leeuwen, "Path-Length-Resolved Diffusive Particle Dynamics in Spectral-Domain Optical Coherence Tomography," Phys Rev Lett 105(19), 198302 (2010).

187. V. M. Kodach, D. J. Faber, J. van Marle, T. G. van Leeuwen, and J. Kalkman, "Determination of the scattering anisotropy with optical coherence tomography," Opt Express 19(7), 6131 (2011).

188. N. Uribe-Patarroyo and B. E. Bouma, "Velocity gradients in spatially resolved laser Doppler flowmetry and dynamic light scattering with confocal and coherence gating," Phys Rev E 94(2), 022604 (2016).

189. J. V. Migacz, I. Gorczynska, M. Azimipour, R. Jonnal, R. J. Zawadzki, and J. S. Werner, "Megahertz-rate optical coherence tomography angiography improves the contrast of the choriocapillaris and choroid in human retinal imaging," Biomed Opt Express 10(1), 50 (2018).

190. T. Pfeiffer, M. Göb, W. Draxinger, S. Karpf, J. P. Kolb, and R. Huber, "Flexible A-scan rate MHz-OCT: efficient computational downscaling by coherent averaging," Biomed Opt Express 11(11), 6799 (2020).

191. B. Tan, R. McNabb, F. zheng, Y. C. Sim, X. Yao, M. Ang, Q. Hoang, A. Kuo, and L. Schmetterer, "Ultrawide Field, Distortion-Corrected Ocular Shape Estimation with MHz Optical Coherence Tomography (OCT)," Biomed Opt Express (2021).

192. J. Lee, H. Radhakrishnan, W. Wu, A. Daneshmand, M. Climov, C. Ayata, and D. A. Boas, "Quantitative Imaging of Cerebral Blood Flow Velocity and Intracellular Motility using Dynamic Light Scattering–Optical Coherence Tomography," J Cereb Blood Flow Metabolism 33(6), 819–825 (2013).

193. D. Hillmann, C. Pfäffle, H. Spahr, S. Burhan, L. Kutzner, F. Hilge, and G. Hüttmann, "Computational adaptive optics for optical coherence tomography using multiple randomized subaperture correlations.," Optics letters 44(15), 3905–3908 (2019).

194. N. G. Ferris, T. M. Cannon, M. Villiger, B. E. Bouma, and N. Uribe-Patarroyo, "Forward multiple scattering dominates speckle decorrelation in whole-blood flowmetry using optical coherence tomography," Biomed Opt Express 11(4), 1947 (2020).

195. Y. Park, M. Diez-Silva, D. Fu, G. Popescu, W. Choi, I. Barman, S. Suresh, and M. S. Feld, "Static and dynamic light scattering of healthy and malaria-parasite invaded red blood cells," J Biomed Opt 15(2), 020506-020506–3 (2010).

196. M. Meinke, G. Müller, J. Helfmann, and M. Friebel, "Empirical model functions to calculate hematocrit-dependent optical properties of human blood," Appl Optics 46(10), 1742 (2007).

Glossary

Axial phase error	OCT signal's phase discontinuity along the scanning direction induced by the axial bulk motion.
Bulk motion	Rigid translation of the imaged subject.
Digitally adaptive optics	A category of post-processing methods that corrects the monochromatic optical aberrations in interferometric imaging techniques.
Digital refocusing	Correcting the defocus aberration using post-processing methods.
Digital resolution	Spatial interval of a single pixel.
Phase stability	An OCT system is phase stable if the axial phase error between successive or adjacent measurements is confined in the range $(-\pi, \pi)$.
Phase destruction	LS SD-OCT signal's phase information loss because of the misalignment of the sample and reference signals along the axial direction.
Spatial-spectral crosstalk	Different wavelengths of the sample light scattered from the same location are projected to different spatial coordinate on the camera.
Signal decorrelation	OCT signal's temporal autocorrelation reduces due to the motion of the imaged subject.
Sub-band	A narrower spectrum which is digitally filtered from the full spectrum of the OCT light source.
Virtual interference pinhole	A oversimplified model describing the LS SD-OCT signal strength because of the overlapping of sample and reference electrical field.